

Interphase Debonding in High Temperature Ceramic Composites

Contract Number: F49620-96-C-0026
Final Report

DISTRIBUTION STATEMENT A

Approved for Public Release
Distribution Unlimited

Prepared for:

Dr. J. Fuller
Air Force Office of Scientific Research
Directorate of Aerospace and Materials Science
110 Duncan Avenue, Suite B115
Bolling AFB, DC 20332-8080

Prepared by:

David B. Marshall
Janet B. Davis
Rockwell Scientific
1049 Camino Dos Rios
Thousand Oaks, CA 91360

September 13, 2001
Contractor's Reference No. SC71123

20011026 007

Copy No: 2

Reproduced From
Best Available Copy

 **ROCKWELL
SCIENTIFIC**

REPORT DOCUMENTATION PAGE

Public reporting burden for this collection of information is estimated to average 1 hour per response, including the time for reviewing instructions, searching existing data sources, gathering and maintaining the data needed, and completing and reviewing this collection of information. Send comments regarding this burden estimate or any other aspect of this collection of information, including suggestions for reducing this burden, to Washington Headquarters Services, Directorate for Information Operations and Reports (0704-014302). Respondents should be aware that notwithstanding any other provision of law, no person shall be subject to any penalty for failing to provide any information if it does not contain a valid OMB control number. PLEASE DO NOT RETURN YOUR FORM TO THE ABOVE ADDRESS.

AFRL-SR-BL-TR-01-

0534

1. REPORT DATE (DD-MM-YYYY)		2. REPORT TYPE Final Report		PERIOD COVERED (From - To) 6/15/1996 - 6/14/1999	
4. TITLE AND SUBTITLE Interphase Debonding in High Temperature Ceramic Composites				5a. CONTRACT NUMBER F49620-96-C-0026	
				5b. GRANT NUMBER	
				5c. PROGRAM ELEMENT NUMBER	
				5d. PROJECT NUMBER	
6. AUTHOR(S) David B. Marshall Janet B. Davis				5e. TASK NUMBER	
				5f. WORK UNIT NUMBER	
				8. PERFORMING ORGANIZATION REPORT NUMBER	
7. PERFORMING ORGANIZATION NAME(S) AND ADDRESS(ES) Rockwell Scientific Company 1049 Camino Dos Rios Thousand Oaks, CA 91360				10. SPONSOR/MONITOR'S ACRONYM(S) AFOSR/NA	
9. SPONSORING / MONITORING AGENCY NAME(S) AND ADDRESS(ES) Air Force Office of Scientific Research Directorate of Aerospace and Materials Science 110 Duncan Avenue, Suite B115 Bolling AFB, DC 20332-8080				11. SPONSOR/MONITOR'S REPORT NUMBER(S)	
12. DISTRIBUTION / AVAILABILITY STATEMENT Approved for public release; distribution is unlimited.					
13. SUPPLEMENTARY NOTES					
<p style="text-align: right;">AIR FORCE OFFICE OF SCIENTIFIC RESEARCH (AFOSR) NOTICE OF TRANSMITTAL DTIC. THIS TECHNICAL REPORT HAS BEEN REVIEWED AND IS APPROVED FOR PUBLIC RELEASE LAW AFR 190-12. DISTRIBUTION IS UNLIMITED.</p>					
14. ABSTRACT Studies aimed at understanding the role of the interphase in providing a nonlinear response in oxide composites are described. Debonding and sliding of single crystal and eutectic oxide fibers coated with La-monazite caused intense plastic deformation of the LaPO ₄ at room temperature. Such plastic deformation mechanisms could be critical for preventing the development of very high stresses during constrained sliding of rough interfaces. A new class of machinable two-phase ceramics based on the debonding and deformation characteristics of rare-earth phosphates was demonstrated. Multilayered composites, consisting of various zirconia-based materials alternating with layers of LaPO ₄ , were fabricated for studies of compatibility and debonding mechanisms. The stability of La-monazite in high-temperature water-containing environments typical of combustion gases was demonstrated. Mechanics analyses were developed for debonding along an irregular interface and for sliding at closed cracks with friction at their surfaces.					
15. SUBJECT TERMS					
16. SECURITY CLASSIFICATION OF:			17. LIMITATION OF ABSTRACT UL	18. NUMBER OF PAGES 131	19a. NAME OF RESPONSIBLE PERSON D.B. Marshall
a. REPORT Unclassified	b. ABSTRACT Unclassified	c. THIS PAGE Unclassified			19b. TELEPHONE NUMBER (include area code) 805.373.4170



INTERPHASE DEBONDING IN HIGH TEMPERATURE CERAMIC COMPOSITES

Contract Number: F49620-96-C-0026
Final Report

Prepared for

Dr. J. Fuller
Air Force Office of Scientific Research

Prepared by

David B. Marshall
Janet B. Davis

Rockwell Scientific Company
1049 Camino Dos Rios
Thousand Oaks, CA 91360

September 2001

ABSTRACT

Studies aimed at understanding the role of the interphase in providing a nonlinear response in oxide composites are described. Debonding and sliding of single crystal and eutectic oxide fibers coated with La-monazite caused intense plastic deformation of the LaPO_4 at room temperature. Such plastic deformation mechanisms could be critical for preventing the development of very high stresses during constrained sliding of rough interfaces. A new class of machinable two-phase ceramics based on the debonding and deformation characteristics of rare-earth phosphates was demonstrated. Multilayered composites, consisting of various zirconia-based materials alternating with layers of LaPO_4 , were fabricated for studies of compatibility and debonding mechanisms. The stability of La-monazite in high-temperature water-containing environments typical of combustion gases was demonstrated. Mechanics analyses were developed for debonding along an irregular interface and for sliding at closed cracks with friction at their surfaces

Table of Contents

1.0	Summary	1
2.0	Publications, Personnel and Technical Presentations	3
2.1	Personnel	3
2.2	Awards.....	3
2.3	Publications	3
2.4	Technical Presentations	5
3.0	The Influence of Interfacial Roughness on Fiber Sliding In Oxide Composites with La-Monazite Interphases	7
4.0	Stability of LaPO_4 Systems in High Temperature Environments containing H_2O vapor	8
5.0	Oxide Composites of Al_2O_3 and LaPO_4	11
6.0	The Weak Interface Between Monazites and Refractory Ceramic Oxides	12
7.0	Recent Advances in Oxide-Oxide Composite Technology	13
8.0	Machinable Ceramics Containing Rare-Earth Phosphates	14
9.0	Debonding in Multilayered Composites of Zirconia and LaPO_4	15
10.0	Nonlinear Stress-Strain Curves for Solids Containing Closed Cracks with Friction	16
11.0	Analysis of Debonding at Interface Cusps.....	17
12.0	Processing and Hardness of Single Crystal Al_2O_3 Films Containing Nano- ZrO_2 Inclusions Produced by Chemical Solution Deposition	20

1.0 Summary

Our aim in this contract was to gain a basic understanding of the design requirements for interphases in weakly bonded, high temperature ceramic composites: the mechanisms and mechanics of debonding; and the roles of various microstructural parameters that affect the debonding mechanism and the resulting bridging traction law (which is the constitutive relation that determines the macroscopic stress-strain response of the composite). We seek to understand the role of the interphase in providing a nonlinear response *after* the initiation of debonding: What are the optimum debond/damage mechanisms? How do we control debonding and damage by microstructural design?

The work focused on oxide composites, which address the Air Force need for high temperature, oxidation-resistant components for hot structures, thermal protection systems for space re-entry vehicles, gas turbine engines, and rocket engines. Oxides have the clear advantage over non-oxide composites in that they are stable in oxidizing conditions and thus do not need protective coatings. However, their development is far less mature: advances are needed in developing interphases that give the desired constitutive response and in developing suitable methods for fabricating the composites.

Results from the work are described in sections 3 to 11. Some of the key results are as follows:

(1) Debonding and sliding mechanisms were studied in model composites consisting of fully dense Al_2O_3 matrices with LaPO_4 -coated single crystal and eutectic oxide fibers with varied interface topologies and residual stresses. These studies showed that LaPO_4 is compatible with, and enables debonding at all of the fibers (Al_2O_3 , YAG, ZrO_2 , and mullite). They also revealed that sliding of these fibers causes intense plastic deformation of the LaPO_4 coating by twinning and dislocation motion at low temperatures and that these plastic deformation mechanisms could be critical for preventing the development of very high stresses during constrained sliding of rough interfaces in oxide composites.

(2) During the initial debonding of the fibers and coating in the above experiments, the debond cracks were found to follow the interface faithfully, even when cusps due to grain boundary diffusion existed at the interface. A mechanics analysis was developed to define conditions that allow a debond crack to follow an irregular interface rather than deflect into the fiber coating. The analysis extends the earlier classical work of He and Hutchinson on debond criteria.

(3) The stability of LaPO_4 systems in high-temperature water-containing environments typical of combustion gases was demonstrated. Reactions were found from volatile species originating from silica and alumina furnace tubes; in the case of alumina a very thin protective layer of lanthanum aluminate formed on the surface. However, no reactions were detected with the water vapor.

(4) A new class of machinable two-phase ceramics based on the debonding and deformation characteristics of rare-earth phosphates was demonstrated. These materials have application temperatures more than 600°C higher than those of existing glass-ceramic machinable ceramics. Potential applications for the Air Force would include high temperature abradable seals.

(5) Multilayered composites, consisting of various zirconia-based materials alternating with layers of LaPO_4 , were fabricated for studies of compatibility and debonding mechanisms. Mechanisms responsible for damage tolerance were identified: these included distributions of characteristic microcracking within the LaPO_4 layers, as well as debonding at the layer interfaces.

(6) An analytical mechanics analysis was developed to obtain the stress-strain response of a body containing closed cracks with friction at their surfaces. The resultant nonlinear stress-strain curves exhibit cyclic hysteresis linked to microstructural variables. The analysis offers the prospect of accounting for fatigue properties of composites, via attrition of the frictional resistance at sliding crack surfaces.

2.0 Publications, Personnel and Technical Presentations

2.1 Personnel

The principal investigator was Dr. D. B. Marshall. Co-investigators from Rockwell Science Center were Dr. J. Davis, Dr. P. E. D. Morgan and Dr. R. Housley. The program benefited greatly from several collaborations at universities and government laboratories: collaboration funded from this contract with Dr. M. He at UCSB and informal collaborations with Dr. R. Hay at WPAFB, Dr. B. Opila and Dr. A. Sayir at NASA Glenn, Prof. F. Lange at UCSB, and Dr. B. Lawn at NIST.

2.2 Awards

Sosman Memorial Lecture Award, 1998, David Marshall, from Basic Science Division of The American Ceramic Society "In recognition of his outstanding contribution to Ceramic Science," to Present Sosman Memorial Lecture

John Jeppson Award, 1996, David Marshall, Award of The American Ceramic Society "For outstanding scientific and technical contributions to the field of mechanical properties of ceramics"

"Shell Distinguished Lecturer" award, 1999, David Marshall, from Northwestern University,

2.3 Publications

(a) Published

Davis, J.B., Marshall, D.B and Morgan, P.E.D., "Oxide Composites of Al_2O_3 and LaPO_4 " J. European Ceram. Soc. 19 2421-2426 (1999)

Morgan, P.E.D., Marshall, D.B., Davis, J.B. and Housley R.M., "The Weak Interface Between Monazites and Refractory Ceramic Oxides," in Computer Aided Design of High-Temperature Materials, Eds. A. Pechenik, R. K. Kalia, and P. Vashishta, pp 229-243, Oxford University Press, New York, 1999

Evans, A. G., Marshall, D. B., Zok, F., Levi, C., "Recent Advances in Oxide-Oxide Composite Technology," *Advanced Composite Materials*, 8[N1] 17-23 (1999)

Davis, J.B., Marshall, D.B., Housley, R. M., and Morgan, P.E.D. "Machinable Ceramics Containing Rare-Earth Phosphates," *J. Amer. Ceram. Soc.* 81[8] 2169-75 (1998)

Marshall, D.B., Morgan, P.E.D. and Housley, R. M., "Debonding in Multilayered Composites of Zirconia and LaPO_4 ," *J.Amer. Ceram Soc.*, 80[7] 1677-83 (1997)

S. M. Johnson, Y. Blum, C. Kanazawa, H-J. Wu, J. R. Porter, P. E. D. Morgan, D. B. Marshall and D. Wilson, "Processing and Properties of an Oxide/Oxide Composite," *Key Engineering Materials*, Vols.127-131, pp 231-238 (1997)

Lawn, B.R. and Marshall, D.B., "Nonlinear Stress-Strain Curves for Solids Containing Closed Cracks with Friction," *J. Mech. Phys. Solids*, 46[1] 85-113 (1998)

McNally, F. Lange, F. F. and Marshall, D. B., "Processing and Hardness of Single Crystal Al_2O_3 Films Containing Nano- ZrO_2 Inclusions Produced by Chemical Solution Deposition" *Phys. Stat. Sol. (a)* 166 231 (1998) - Major part of work supported at UCSB by contract F49620-96-1-003 (Prof. F. F. Lange); collaboration at Rockwell supported by this contract.

(b) in preparation

Davis, J. B., Hay, R. S., Marshall, D. B., Morgan, P.E.D., and Sayir, A., "The Influence of Interfacial Roughness on Fiber Sliding In Oxide Composites with La-Monazite Interphases," for *J. Am. Ceram. Soc.*

Davis, J. B., Marshall, D. B. and Opila, B., "Stability of LaPO_4 Systems in High Temperature Environments containing H_2O vapor" in preparation for publication in the *Journal of the American Ceramic Society*

M. He and D. B. Marshall "Analysis of Debonding at Interface Cusps," in preparation for publication in the *Journal of the American Ceramic Society*.

2.4 Technical Presentations

a. Invited

Sosman Memorial Lecture, "Fibrous Composites" by D. B. Marshall, American Ceramic Society Annual meeting, Cincinnati, May 1998

"Recent Developments in Ceramic Composites" Shell Lecture, Northwestern University, March 1999

"Interfacial Adhesion in Oxide Composites," International Symposium on Interfaces, Seville, September, 1999.

"Deformation and Fracture of Oxide Composites," Symposium on Processing, Microstructure and Properties of Exotic Materials, Stuttgart, July 1999.

"Ceramic Composites for Aerospace." Seminar, California Institute of Technology, May, 1999.

"Interfacial Fracture and Mechanical Properties of Oxide Composites" Third International Symposium on Synergy Ceramics, Osaka, Japan, February 1999.

"New Possible Ceramics Utilizing Monazite, LaPO_4 ," 2nd international Symposium on the Science of Engineering Ceramics, Osaka, Japan, September 1998.

"Oxide Composites," International Conference: New Developments in High Temperature Ceramics, Istanbul, August 1998.

"Oxide composites containing La-Monazite," International workshop on Oxide-Oxide Composites, Irsee, Germany, June 1998.

"Oxide Composites," International Workshop on Ultra-high temperature Ceramics, University of Colorado, Boulder, May 1998.

"Properties of Ceramics," National Materials Advisory Board, Workshop on Structural Materials Research Advancements, Washington, March 1998.

"Design of Composites for High Temperature Oxidizing Environments," International Meeting on Composites, Lake Louise, Canada, October 1997.

"The Interface Between Monazites and High Temperature Ceramics" Conference on Computer Aided Design of High-Temperature Materials, Santa Fe, July 1997.

"The Future of Structural Ceramics." National Science Foundation Workshop on Fundamental Research Needs in Ceramics," Washington, June 1997.

"Interface Materials for Oxide Composites" International Conference on Ceramic and Metal Matrix Composites, San Sebastian, September , 1996, Plenary Lecture.

"Design and Properties of Multilayered Ceramic Composites," Third International Workshop on Interfaces, Santiago, September 1996.

"Design of Interfaces for Oxidation-Resistant Composites," Gordon Research Conference on Solid State Studies in Ceramics, Aug. 1996.

b. Contributed

American Ceramic Society Annual meeting, Cincinnati, April 1998 (2 presentations)

American Ceramic Society Annual Meeting, April 1999

American Ceramic Society Annual meeting, Cincinnati, April 1997

Society of Engineering Science, 33rd Annual Meeting, Tempe, October 1996

3.0 The Influence of Interfacial Roughness on Fiber Sliding In Oxide Composites with La-Monazite Interphases

by Davis, J. B., Hay, R. S., Marshall, D. B., Morgan, P.E.D., and Sayir, A.

The following section is a draft of a paper being prepared for publication in the Journal of the American Ceramic Society.

The Influence of Interfacial Roughness on Fiber Sliding In Oxide Composites with La-Monazite Interphases

J. B. Davis,* R. S. Hay,** D. B. Marshall,* P.E.D. Morgan*
and A. Sayir***

*Rockwell Science Center
1049 Camino Dos Rios
Thousand Oaks, CA 91360

** Air Force Research Laboratory
Materials Directorate
WPAFB, OH 45433

***NASA Glenn Research Center / CWRU
NASA Glenn Research Center
21000 Brookpark Road
Cleveland, OH 44135

ABSTRACT

Room temperature debonding and sliding of La-monazite coated fibers is assessed using a composite with a polycrystalline alumina matrix and fibers of several different single crystal (mullite, sapphire) and eutectic ($\text{Al}_2\text{O}_3/\text{Y}_3\text{Al}_5\text{O}_{12}$ and $\text{Al}_2\text{O}_3/\text{Y-ZrO}_2$) compositions. These fibers provide a range of residual stresses and interfacial roughnesses. Sliding occurred over a debond crack at the fiber-coating interface when the sliding displacement and surface roughness were relatively small. At large sliding displacements with relatively rough interfaces, the monazite coatings were deformed extensively by fracture, dislocations and occasional twinning, whereas the fibers were undamaged. Dense, fine-grained (10 nm) microstructures suggestive of dynamic recrystallization were also observed in the coatings. Frictional heating during sliding is assessed. The possibility of low temperature recrystallization is discussed in the light of the known resistance of monazite to radiation damage. The ability of La-monazite to undergo plastic deformation relatively easily at low temperatures may be enabling for its use as a composite interface.

1. INTRODUCTION

Rare-earth orthophosphates (monazite and xenotime) are of interest for fiber-matrix interphases that enable interfacial debonding and damage tolerance in oxide composites.¹⁻

⁸ They are refractory materials (LaPO_4 melting point 2070°C), compatible in high temperature oxidizing environments with many oxides that are either currently available as reinforcing fibers or of interest for future development as fibers and matrices. They are also relatively soft for such refractory materials (LaPO_4 hardness 5GPa). Studies of several combinations of oxides and rare-earth phosphates ($\text{LaPO}_4\text{-Al}_2\text{O}_3$, $\text{LaPO}_4\text{-ZrO}_2$, $\text{CePO}_4\text{-ZrO}_2$, $\text{YPO}_4\text{-Al}_2\text{O}_3$ and $\text{NdPO}_4\text{-Al}_2\text{O}_3$) have shown that the oxide-phosphate interfacial bond is sufficiently weak that debonding occurs whenever a crack approaches an interface from within the phosphate.^{1,9-11} The most detailed studies have involved the $\text{LaPO}_4\text{-Al}_2\text{O}_3$ system. Other studies have shown that debonding and sliding occurs in fiber push-out tests with model composites consisting of LaPO_4 -coated single crystal fibers of Al_2O_3 and $\text{Y}_3\text{Al}_5\text{O}_{12}$ (YAG) in polycrystalline Al_2O_3 matrices.^{1,12}

Damage-tolerant behavior in ceramic composites requires sliding and pullout of fibers in addition to interfacial debonding. Recent calculations suggest that such pullout would be strongly suppressed in fully dense oxide composites by misfit stresses generated during sliding of fibers with rough interfaces or with minor fluctuations in diameter.¹³ For given strain mismatch, these misfit stresses are expected (assuming elastic accommodation) to be larger in high-stiffness oxide systems than in non-oxide composites, which typically contain turbostratic carbon or boron nitride interphases with low transverse elastic modulus. However, the misfit stresses could potentially be reduced by plastic deformation of the interphase. The higher elastic modulus in oxide interphases also results in larger residual thermal stresses in systems with matrix and fibers of different thermal expansion coefficients.

In this study, we investigate the debonding and sliding behavior of four La-monazite coated fibers (single-crystal alumina and mullite, directionally solidified eutectics of $\text{Al}_2\text{O}_3/\text{YAG}$ and $\text{Al}_2\text{O}_3/\text{Y-ZrO}_2$), chosen to provide different residual stress states and

interface topology. The coated fibers were surrounded with a matrix of polycrystalline Al_2O_3 . Debonding and sliding were assessed using indentation fracture and push-out techniques. Damage in the coating, including plastic deformation, was identified by scanning and transmission electron microscopy (SEM and TEM).

2. EXPERIMENTAL

Four different single crystal or directionally solidified eutectic oxide fibers, grown at NASA Glenn by a laser-heated float zone technique,^{14,15} were coated with LaPO_4 by dipping in a slurry of rhabdophane (hydrated LaPO_4). The coated fibers were embedded in α -alumina powder (Sumitomo AKP50) and hot pressed in graphite dies for 1 h at 1400°C . Uncoated fibers were included in the same specimen for reference. The fibers were arranged in rows within the one hot-pressed disk, with separation between fibers ~ 2 mm, thus ensuring identical processing conditions for all fibers. In an earlier study, the same rhabdophane slurry yielded pure La-monazite, with no excess La or P being detectable either by EDS analysis of the monazite or by reaction of the monazite with sapphire fibers after long-term heat treatment (200 h at 1600°C).³

The fibers had different surface textures and thermal expansion coefficients, thus allowing assessment of the effects of interfacial topology and residual stress on debonding and sliding mechanisms. The fibers were as follows:

(1) Directionally solidified $\text{Al}_2\text{O}_3/\text{ZrO}_2$ eutectic fibers with a two-phase microstructure of alumina and cubic zirconia (stabilized with Y_2O_3).⁴³ Dimensions of the individual phases were $\sim 0.5\ \mu\text{m}$. The starting composition of the feed rod was 60.8 mole % Al_2O_3 ; 39.2 mole % ZrO_2 (9.5 mole % Y_2O_3)) with purity levels 99.995 % or better. X-ray and SEM/TEM analysis did not show any third phase, indicating that all of the Y_2O_3 was in solid solution in the ZrO_2 phase. The surfaces of the fibers were rough on the scale of the microstructure (Fig. 1(a)). The fiber diameters were $\sim 100\ \mu\text{m}$ with fluctuations of $\sim 2\ \mu\text{m}$ over lengths of $\sim 200\ \mu\text{m}$. Thermal mismatch during cooling of the composite caused tensile radial stresses normal to the fiber surface (Table1).

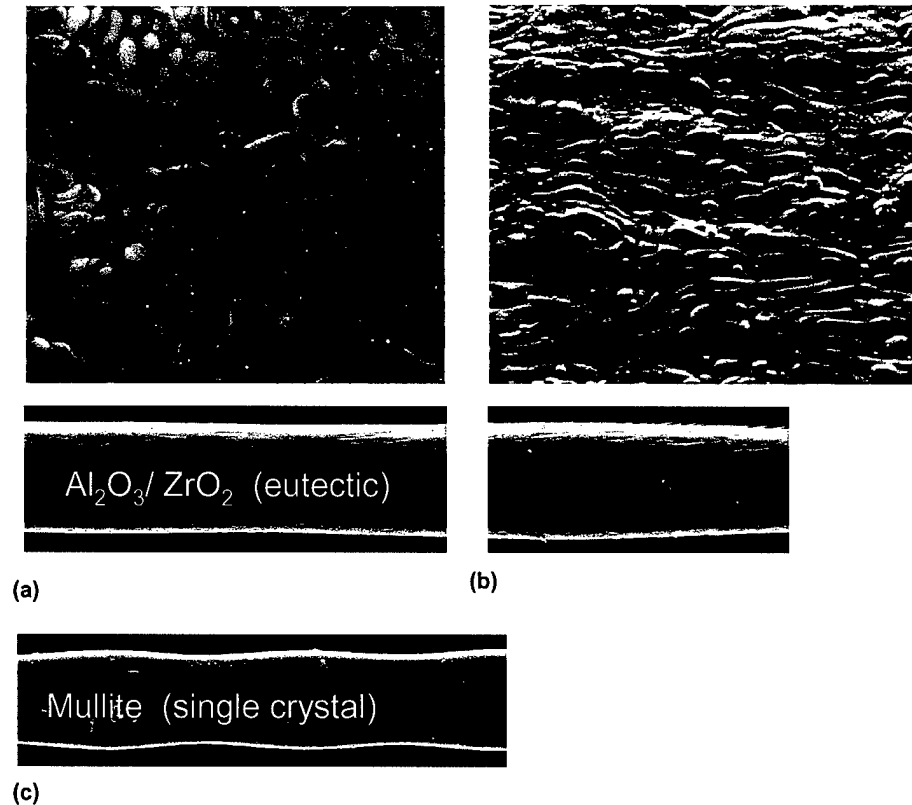


Figure 1. Scanning electron micrographs of fiber surfaces: (a) $\text{ZrO}_2/\text{Al}_2\text{O}_3$ eutectic fiber, (b) $\text{Al}_2\text{O}_3/\text{YAG}$ eutectic fiber, and (c) mullite single crystal fiber.

(2) Directionally solidified $\text{Al}_2\text{O}_3/\text{YAG}$ eutectic fibers,^{44,45} with a two-phase microstructure of dimensions $\sim 0.5 \mu\text{m}$ and surface roughness on the scale of the microstructure (Fig. 1(b)). The fiber diameters were $\sim 100 \mu\text{m}$, with fluctuations of $< 1 \mu\text{m}$ over lengths of $\sim 1 \text{ mm}$. Thermal mismatch stresses were of the same sign as for the $\text{Al}_2\text{O}_3/\text{ZrO}_2$ fibers but were smaller in magnitude (Table 1).

(3) Mullite single-crystal fibers formed from a source rod of high purity (99.99%) polycrystalline alumina powder (CERAC) and 99.99 % pure SiO_2 (Alpha Products), which gave 2:1 mullite as described in Ref.15. In the as-grown condition the fibers had smooth surfaces but relatively large fluctuations in diameter ($50 \pm 5 \mu\text{m}$, Fig. 1 (c)) with period $\sim 100 \mu\text{m}$. Thermal mismatch caused large compressive radial stress in the coating and at the fiber-coating and coating-matrix interfaces, with tensile circumferential stress in the coating and matrix (Table1).

(4) Sapphire fibers, which had smooth surfaces (as-grown) and relatively uniform diameter ($100 \pm 1 \mu\text{m}$). These were included for comparison with previous studies of this system.^{1,3} All residual stresses except the circumferential (and axial) tension in the coating are small.

TABLE 1 Representative* residual stresses in composites of monazite-coated fibers in polycrystalline Al_2O_3 matrix. Stresses in MPa.

Stress component	Fiber			
	Sapphire	Mullite	$\text{Al}_2\text{O}_3/\text{YAG}$	$\text{Al}_2\text{O}_3/\text{ZrO}_2$
Radial (coating/fiber)	15	-720	130	240
Radial (matrix/coating)	25	-630	140	240
Circumferential (coating)	300	420	290	280
Axial (fiber)	7	-1160	240	420

*Values in this table are intended only as rough guide for relative stresses. They were calculated using a coaxial cylinder analysis, assuming a temperature change of $\Delta T = 1000^\circ\text{C}$, coating thickness $2 \mu\text{m}$, zero volume fraction of fibers, and the following Young's moduli and thermal expansion coefficients (nominal isotropic, temperature-independent values): polycrystalline Al_2O_3 (400 GPa, $8 \times 10^{-6} \text{ }^\circ\text{C}^{-1}$); sapphire (400 GPa, $8 \times 10^{-6} \text{ }^\circ\text{C}^{-1}$); mullite (200 GPa, $4 \times 10^{-6} \text{ }^\circ\text{C}^{-1}$);⁴⁶ $\text{Al}_2\text{O}_3/\text{ZrO}_2$ (300 GPa, $9 \times 10^{-6} \text{ }^\circ\text{C}^{-1}$); and $\text{Al}_2\text{O}_3/\text{YAG}$ (350 GPa, $8.5 \times 10^{-6} \text{ }^\circ\text{C}^{-1}$).^{16,17}

The hot-pressed disk was cut into slices (thickness ~ 0.3 to 2mm) normal to the fibers. The surfaces of the slices were polished using diamond paste and some of the polished slices were thermally etched. The thicker slices were used for indentation cracking experiments, which involved placing Vickers indentations (10 kg load) in the polycrystalline alumina matrix near the fibers. The indenter was oriented so that one of the median/radial cracks grew towards the fiber to test for interfacial debonding. The thinner slices were used for fiber push-out experiments, which involved loading a flat punch (truncated Vickers indenter) onto the end of each fiber while the slice was supported in a fixture with a gap beneath the fiber. Some specimens were fractured after

the push-out test to separate the debonded interface. The indented and pushed out specimens were examined by optical and scanning electron microscopy (SEM).

Specimens used for fiber push-out were also sectioned parallel and perpendicular to the fiber axes and examined by TEM (Phillips CM20 FEG operating at 200kV) to allow identification of damage within the LaPO_4 coating caused by debonding and sliding. Four $\text{Al}_2\text{O}_3/\text{YAG}$ fibers were examined in the parallel section; one mullite and one $\text{Al}_2\text{O}_3/\text{ZrO}_2$ were examined in the axial section. The TEM foils were prepared by impregnating the specimens with epoxy, tripod polishing to thickness of 10 μm , followed by ion milling (Gatan model 691 operating at 4.5 kV).¹⁸

3. RESULTS

3.1 Microstructural Observations

All of the coated fibers were surrounded with a continuous layer of LaPO_4 and a fully dense matrix of polycrystalline Al_2O_3 . The coating thicknesses were nonuniform (between $\sim 1 \mu\text{m}$ and $5 \mu\text{m}$) and largest at the positions where the fiber surfaces were parallel to the hot pressing direction. No reactions were observed between the LaPO_4 and any of the fibers. Occasionally an elongated La-magnetoplumbite ($\text{LaAl}_{11}\text{O}_{19}$) grain was observed along the coating-matrix interface. Despite the presence of substantial tensile residual stresses in all of the LaPO_4 coatings (~ 300 to 400 MPa , table 1), no evidence of cracking was detected by SEM examination of polished or thermally etched cross-sections. The grain sizes were ~ 0.5 to $1 \mu\text{m}$ in the monazite and ~ 2 to $10 \mu\text{m}$ in the alumina matrix.

3.2 Interfacial Debonding

The LaPO_4 coatings protected all of the fibers from penetration of indentation cracks, whereas uncoated fibers were always penetrated. Examples are shown for the $\text{Al}_2\text{O}_3/\text{YAG}$, $\text{ZrO}_2/\text{Al}_2\text{O}_3$ and mullite fibers in Figs. 2 to 4. The indentation cracks

generally extended from the matrix into the LaPO_4 coatings then arrested and caused debonding at the coating/fiber interface. In a few cases with the $\text{ZrO}_2/\text{Al}_2\text{O}_3$ fibers debonding occurred at both interfaces (matrix/coating and coating /fiber). The former response was observed previously with coated sapphire fibers and was shown to be consistent with the debond criterion of He and Hutchinson and the measured fracture toughnesses of the fibers, coating, and interface.¹ Although the fracture toughnesses of the YAG/ LaPO_4 and mullite/ LaPO_4 interfaces have not been measured, the present observations suggest that they are similar to that of the alumina/ LaPO_4 interface ($\sim 4.5 \text{ J/m}^2$). It is noteworthy that the fibers were protected from cracking even when the contact area of the Vickers indentation was close enough to the fiber to overlap the coating (Fig. 3(b)). In that case the residual stress from the indentation (compressive normal to the interface, tensile on the prospective crack plane into the fiber) would tend to inhibit debonding and favor fiber penetration.

The interfacial roughnesses for both of the eutectic fibers were similar to the surface roughnesses of the as-formed fibers, with amplitude $\sim 100 - 300 \text{ nm}$ and period $\sim 500 \text{ nm}$ (Figs. 2(a) and 3(a)). This roughness amplitude is greater than that of the interfaces at the single-crystal mullite and sapphire fibers. These initially smooth fibers developed cusps during hot pressing where grain boundaries of the monazite coating intersected the fiber surface. Measurements of the cusp profiles on sapphire fibers by atomic force microscopy have been reported elsewhere.^{19,20} The cusp heights were typically $\sim 50 \text{ nm}$ and the angular distortions of the surface were small ($\leq 20^\circ$). The cusps on the mullite surfaces are very similar.

Some insight into the effect of interfacial roughness on fiber sliding and pullout can be gained from the observations of Figs. 2 to 4. As the debond grows around the circumference of the fiber, the loading on the crack tip due to the indentation stress field is initially mostly shear (although the loading eventually changes to tension if the crack grows sufficiently). Since fiber pullout also involves shear loading of a debond crack, the initial region of growth of the deflected cracks in Figs. 2-4 should be representative of the behavior during the corresponding stage of pullout.

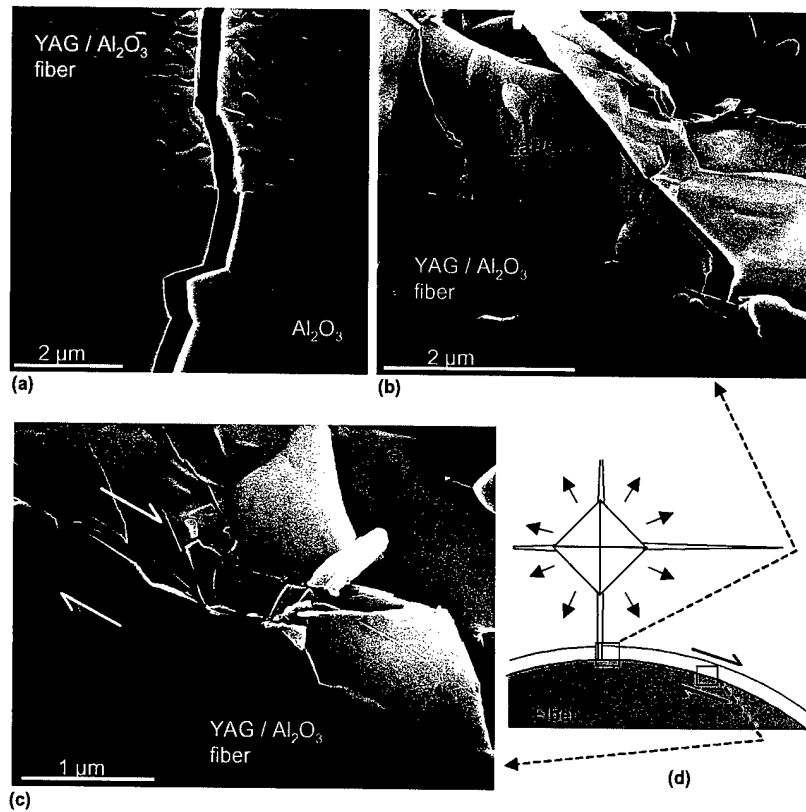


Figure 2. Scanning electron micrographs showing interactions of indentation cracks with $\text{Al}_2\text{O}_3/\text{YAG}$ eutectic fibers: (a) uncoated fiber in alumina matrix (indentation located out of field of view below the region shown); (b) fiber coated with LaPO_4 (indentation located out of field of view, as indicated in (d)); (c) same fiber as in (b) but showing region further along the debonded interface (arrows indicate magnitude of sliding displacement across debond crack); (d) schematic showing locations of (b) and (c).

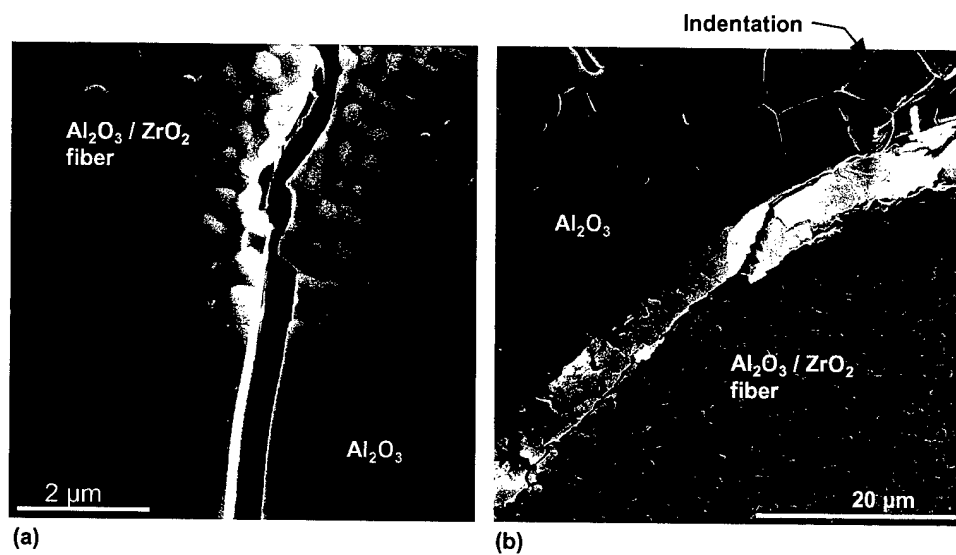


Figure 3. Scanning electron micrographs showing interactions of indentation cracks with $\text{ZrO}_2/\text{Al}_2\text{O}_3$ eutectic fibers: (a) uncoated fiber in alumina matrix (indentation located out of field of view below the region shown); (b) fiber coated with LaPO_4 (indentation located at top of field of view).

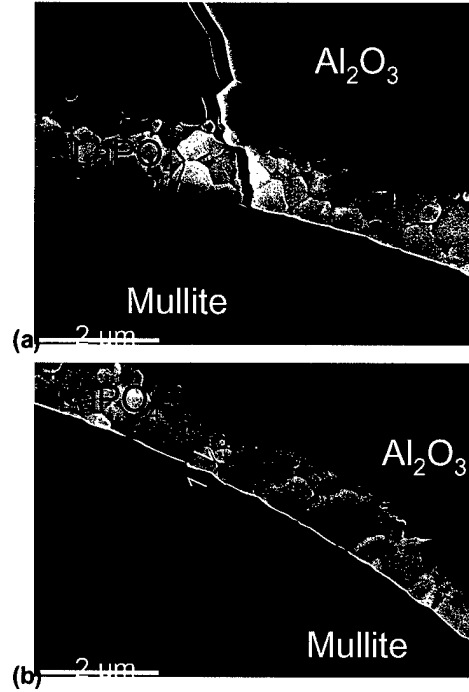


Figure 4. Scanning electron micrographs showing interaction of indentation crack with single crystal mullite fiber (coated with LaPO_4 in alumina matrix): (a) intersection of indentation crack with interface and debonding (indentation located out of field of view above the region shown); (b) same fiber as in (a) but showing region further to the right along the debonded interface (arrows indicate magnitude of sliding displacement across debond crack).

In all cases, the initial debond crack followed the fiber-matrix interface closely, even when the interface was rough. For the mullite fibers (Fig. 4) the sliding displacement of the debond crack surfaces (~ 250 nm, i.e., opening displacement of initial indentation crack) is smaller than the average spacing between the interfacial cusps (~ 600 nm). Sliding caused separation of the debonded surfaces to accommodate their misfit (Fig. 4(b)), despite the constrained configuration with large residual compressive normal stress (~ 700 MPa, Table 1). The misfit was apparently accommodated by elastic strains, with no irreversible deformation of the mullite fiber or LaPO_4 coating discernable by SEM. In contrast, sliding of the eutectic fibers caused extensive damage in the LaPO_4 coating (Fig. 2 (c)), without discernable damage in the fibers. The damage included cracks across the full width of the coating, aligned at $\sim 45^\circ$ to the interface on planes of maximum tension,

similar to previous observations of cracking in layers of LaPO_4 sandwiched between polycrystalline Al_2O_3 ¹. More intense local damage is evident at individual asperities, as in Fig. 2(c). The damage included cracking and fine lamellar features, which could be cracks or twins.

3.3 Fiber Push-out

All of the fibers debonded during the push-out experiments. Sliding occurred unstably over distances of ~ 5 to $10\ \mu\text{m}$ at a critical load between 10 and 20 N. The average shear stress (load divided by fiber surface area) at the critical load was $130 \pm 10\ \text{MPa}$ for the sapphire fiber, $200 \pm 20\ \text{MPa}$ for the mullite fiber, $190 \pm 20\ \text{MPa}$ for the $\text{Al}_2\text{O}_3/\text{YAG}$ fiber, and $255 \pm 30\ \text{MPa}$ for the $\text{Al}_2\text{O}_3/\text{ZrO}_2$ fiber.

Sliding of the sapphire fiber occurred at the fiber-coating interface, as reported previously. Grain boundary cusps were observed along the separated interfaces by SEM and AFM, although no damage was visible in either the fiber or the coating.

Extensive wear tracks were observed in the LaPO_4 coating on both eutectic fibers, indicating that sliding involved plastic deformation (Fig. 5). The plane of sliding was mostly adjacent to the fiber-matrix interface, although smeared fragments of the LaPO_4 coating remained on the fiber surface. In some regions (such as Fig. 5) sliding occurred near the matrix-coating interface.

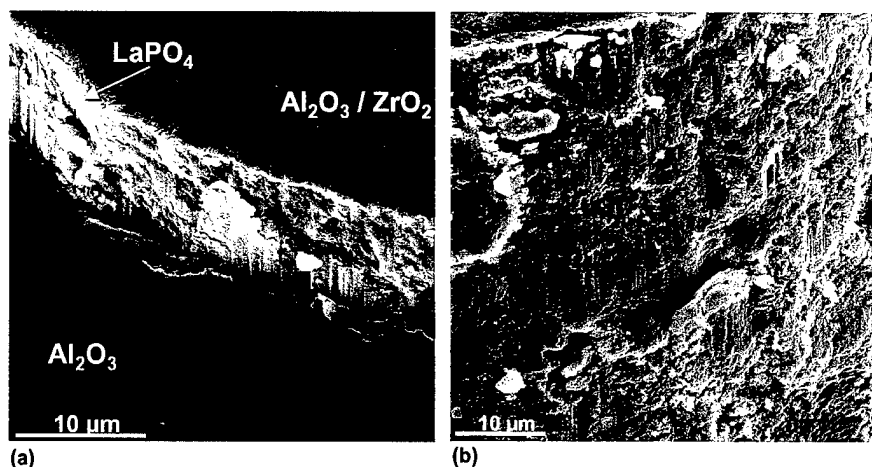


Figure 5. Scanning electron micrographs showing $\text{ZrO}_2/\text{Al}_2\text{O}_3$ eutectic fiber after push-out: (a) bottom of push-out specimen (monazite-coated eutectic fiber, polycrystalline Al_2O_3 matrix); (b) surface of monazite remaining attached to fiber, showing deformation due to sliding.

TEM observations from a typical region of a sectioned specimen containing a $\text{Al}_2\text{O}_3/\text{YAG}$ fiber are shown in Fig. 6. Sliding occurred along a debond crack adjacent to the fiber. A very thin layer of the LaPO_4 coating within ~ 200 nm of the plane of sliding, is heavily deformed, whereas the coating further from the sliding plane is free of defects. The $\text{Al}_2\text{O}_3/\text{YAG}$ fiber surface is also undamaged. The deformed microstructure in the LaPO_4 coating consists of tangled dislocations, lamellar feature resembling twins, microcracks, and very fine crystallites of LaPO_4 with diameter as small as 10 nm (Fig. 6b). The latter features are usually characteristic of recrystallized microstructures in other materials. The intensity of deformation generally decreased with distance from the debond crack.

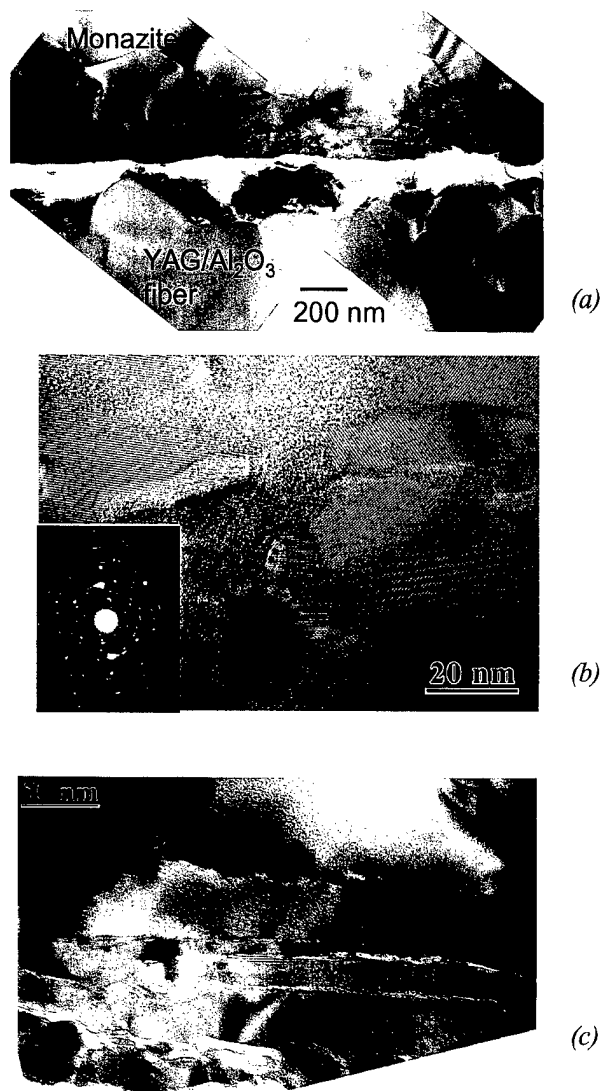
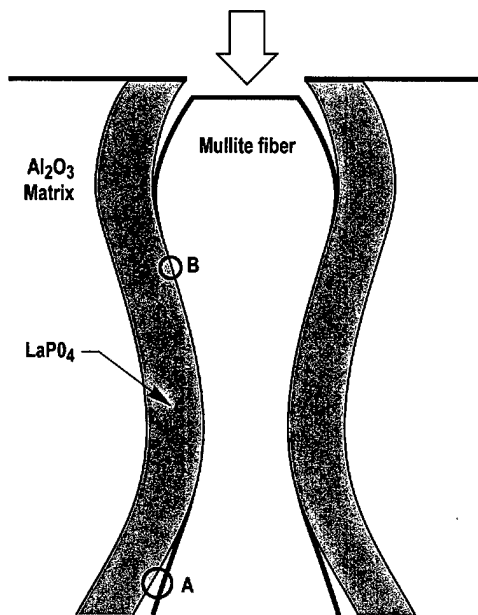


Figure 6. TEM micrographs from monazite-coated $\text{Al}_2\text{O}_3/\text{YAG}$ eutectic fiber after push-out: (a) bright field image showing damage in monazite either side of the sliding plane (b) high resolution lattice image from region of heavily deformed monazite in (a); (c) region of lightly deformed monazite from (a).

Sliding of the mullite fibers occurred predominantly at the interface between the fiber and coating. SEM observations of the separated interface revealed plastic deformation of the LaPO_4 coating in regions where the sliding displacements caused increasing misfit due to the variable fiber diameter (region A in Fig. 7). (Note that the sliding displacements are smaller than the period of the fluctuations in fiber diameter and larger than the spacing of cusps associated with grain boundaries in the LaPO_4 coating.) On the other hand, in regions where the fluctuating fiber diameter led to decreasing misfit during sliding (region B in Fig. 7), the separated interface was very similar to that of the sapphire fiber,

with grain boundary cusps, clean separation at the interface, and no evidence for damage in either the fiber or the coating.



RSC0828 090501

Figure 7. Schematic of fiber sliding for monazite-coated mullite fiber.

Direct correlation of the changes in coating damage with fiber diameter fluctuation by TEM was difficult, because only limited areas were observed. Nevertheless, some trends are evident. Deformation was distributed, often non-uniformly, throughout the entire coating thickness, rather than being localized in a thin layer adjacent to the fiber as for the YAG-alumina. In some places the monazite adjacent to the fiber was undeformed, while in others plastic deformation was confined to an isolated grain. Extensive microcracking was distributed throughout the coating, often at $\pm 45^\circ$ to the fiber surface.

In regions of coating inferred to have been compressed during sliding, almost the entire coating was microcracked and plastically deformed. Extensive dislocations were evident, with variability in density from grain to grain. Some grains were twinned parallel to the fiber-matrix interface, the orientation of maximum shear stress due to pushout of the fiber. Microcracking at $\sim 45^\circ$ to the fiber surface, was extensive, with crack spacings as

small as ~50 nm and an abundance of planar segments consistent with cleavage on (100), (010), and (001), as reported previously.

4.0 DISCUSSION

4.1 Effects of residual stress

The residual stresses noted in Table 1 might be expected to influence whether or not interfacial debonding occurs. Therefore, it is necessary to establish whether or not the debonding response is affected significantly by differences in residual stress state and crack orientation in the model experiments discussed here and those normally encountered in a composite.

In the analysis of He and Hutchinson,^{21,22} the presence of residual stresses shifts the debond criterion by an amount that depends on the parameters η_p and η_d :

$$\eta_p = \sigma_p a^{1/2} / K, \quad \eta_d = \sigma_d a^{1/2} / K \quad (1)$$

where σ_p and σ_d are the residual stresses normal to the potential crack paths penetrating the fiber or along the interface, K is the applied stress intensity factor for the incident crack and a is a characteristic defect size. In the case of a crack oriented on a radial plane propagating towards the fiber from within the coating, as in the indentation cracking experiments of Sect. 3.2, the residual stresses (radial and circumferential stresses at the surface of the fiber) are equal. With η_p and η_d thus being equal, the residual stress would not be expected to affect the debond condition significantly. On the other hand, for a crack oriented normal to the fiber axis (the most important case for a composite) the relevant stresses are the axial stress in the fiber (for penetration) and the radial stress at the fiber surface (for debonding). From Table 1 it is evident that the magnitude of the axial stress is about double that of the radial stress for all of the fibers, with both being compressive for the mullite fibers and tensile for the others. Therefore, in this case the residual stresses would be expected to bias the response towards debonding in the case of

mullite fibers and towards penetration in the case of both eutectic fibers. However, this result is sensitive to the volume fraction of fibers. Calculations for a fiber volume fraction of 0.5, a value typical for structural composites, indicate that the magnitudes of the axial stresses decrease by a factor of about 2, to a level similar to the radial stresses. Therefore, in that case the residual stress does not affect the condition for debonding and the observations of the debonding response of a crack oriented on a radial plane are representative of the response of transverse cracks in the composite. The use of indentation cracks provides a conservative indication, since the residual stress field associated with the indentation itself tends to favor penetration of the crack into the fiber, as discussed in the previous section.

4.2 Effects of misfit stresses

The sliding of fibers caused misfit stresses on two different length scales, one at the level of either the grain size in the monazite coating (in the case of single crystal fibers) or the fiber microstructure (eutectic fibers), and the other due to longer-range fluctuations in fiber diameter. The sliding displacements in the push-out experiments exceeded the microstructural dimensions by a factor of about 5 to 10 but were smaller than the period of the diameter fluctuations by factors of 10 to 100. Consequently, the misfit strains in all except the mullite fibers were dominated by the microstructural roughness (Table 2). In the mullite fibers the superposition of misfit strains due to thermal expansion mismatch (Table 1) and diameter fluctuations would give compressive radial misfit stresses as high as 5.2 GPa in some regions and separation of the interface in others. This maximum compressive stress is higher than the hardness of LaPO_4 (5 GPa^1) suggesting that plastic deformation should occur throughout the thickness of the coating in regions such as area A in Fig7., as observed.

TABLE 2. Misfit strains and stresses

	Fiber			
	Sapphire	Mullite	YAG/Al ₂ O ₃	ZrO ₂ /Al ₂ O ₃
Fiber radius (R/ μ m)	50	25	50	50
Microstructural roughness				
δr (μ m)	0.05	0.05	0.2	0.2
λ_r (μ m)	2	2	1	1
$\delta r/R$	0.001	0.002	0.004	0.004
σ_r (MPa)**	-200	-300	-770	-730
Fiber diameter fluctuation				
ΔR (μ m)	0.5	2.5	0.5	1
λ_R (μ m)	500	100	1000	400
$(\Delta R/R) (\pi z_{\max}/\lambda_R)^*$	0.0006	0.03	0.0003	0.0015
σ_R (MPa)**	-120	-4500	-60	-270

* z_{\max} is the maximum sliding displacement ($\sim 10 \mu$ m)

** Nominal radial misfit stresses intended only as rough guide for comparisons: stresses calculated as in Table 1 but with radial misfit strains $\delta r/R$ and $(\Delta R/R) (\pi z_{\max}/\lambda_R)$, the latter being the maximum misfit strain for sinusoidal diameter fluctuation.

For all of the other fibers the maximum radial mismatch strains due to fluctuations in fiber diameter are similar in magnitude and opposite in sign to the thermal expansion mismatch strains. Therefore, whether or not deformation of the coating occurs in these cases would be expected to depend on the microstructural roughness (both the profile of the roughness and the magnitude of the mismatch strain, $\delta r/R$). A clear distinction was seen between the single crystal fibers, for which the mismatch strains were small ($\delta r/R < 0.002$) and sliding occurred along a single interfacial debond over displacements up to ~ 5 to 10 times the period of the microstructural roughness, and the eutectic fibers, for which the mismatch strains were larger ($\delta r/R \sim 0.004$) and extensive deformation of the coating occurred when the sliding displacements exceeded the dimensions of the microstructural roughness.

The oxide fibers currently available in quantities sufficient to fabricate composites are polycrystalline alumina and mullite, with diameter $\sim 12 \mu$ m and grain size about 50 to 100 nm.^{23,24} These fibers have smooth surfaces in the as-produced state. However,

during processing with a matrix, surface diffusion leads to increased roughness due to grain boundary grooving, with amplitude approaching half of the grain size (~20 - 50 nm). Although this roughness amplitude is smaller than that of the eutectic fibers, the mismatch strain is similar or larger ($\delta r/R \sim 0.003$ to 0.008). Therefore, deformation of the coating might be expected if these fibers were to be embedded in a matrix with stiffness similar to that used in this study. However, in a composite with a porous matrix the response would be mitigated by the reduced constraint owing to the lower elastic stiffness of the matrix.

The maximum temperature capability of oxide composites is limited by the stability of currently available polycrystalline fibers. Directionally solidified eutectic fibers have the potential to provide large increases in use temperature through their greater microstructural stability, creep resistance, and strength retention.⁴³⁻⁴⁵ However, substantial development would be needed for economical production of fibers of smaller diameter suitable for composite reinforcements.

4.3 Plastic deformation of LaPO_4

It is clear from Figs. 5 and 6a that plastic deformation of the monazite coating is caused by the sliding of rough interfaces over distances that are large compared with the roughness dimensions. Plastic deformation of monazite, in the form of twins and dislocations, has also been observed in other experiments involving quasi-static contact with spherical indenters at room temperature.²⁵⁻²⁷ The occurrence of twinning and dislocations is not surprising in the light of other studies of ceramic materials such as Al_2O_3 , in which mechanical twinning and dislocations have been observed at low temperatures in loading configurations with hydrostatic confining pressure.²⁸⁻³² However, the microstructure that appears to be recrystallized is at first sight unexpected for room-temperature deformation of a refractory material such as LaPO_4 . This raises the question of whether local temperature rises due to frictional heating might have occurred in these experiments.

Local heating effects

Several approaches, based on different assumptions about dissipative mechanisms, may be taken to estimate limits on local temperature rises during sliding. If we assume that deformation occurs quasi-statically and continuously, an upper (adiabatic) limit may be obtained by assuming that all of the work done by the sliding asperities is dissipated as heat within the deformed zone (~200nm thickness in Fig. 6a). With further assumptions about the uniformity of the heat generation within this zone and the relative cross-sectional areas of the sliding asperities and the deformation zone, such calculations give values between 800 °C and 2000 °C, depending on whether analysis is performed for individual asperities or for an average contact area (Appendix A). With the uncertainty in some of the parameters in these analyses, either of these numbers could vary by a factor of 2. Nevertheless, it is clear that large temperature rises might be expected if the heating were to be adiabatic.

However, adiabatic heating requires a sliding velocity sufficiently large that conduction of heat away from the deformation zone during the period of sliding is negligible. Although the sliding velocity was not measured during these experiments, we can calculate a very conservative upper bound for the relative velocity of the fiber and matrix. Comparison of the corresponding sliding time with an estimate of the time taken for a given temperature increase in the deformation zone to dissipate by conduction (from standard transient heat flow solutions) suggests that the upper-bound sliding velocity is several orders of magnitude smaller than that required for adiabatic heating under these conditions (Appendix A).

A similar conclusion is drawn from application of analyses from the literature on frictional sliding (e.g., Bowden³³ and Tabor,³⁴ Jaeger, Ashby³⁵), in which the assumption is made that work done by frictional forces is dissipated as heat at the interface between the sliding surfaces. Solutions for the interface temperature as a function of the sliding velocity are then obtained from analysis of heat flow into the materials either side of the interface. Solutions are available at a macroscopic level (average) and at an asperity contact level for transient and steady-state conditions (Appendix A). In both cases the

calculated temperature rises corresponding to the upper-bound sliding velocity in these experiments are small ($\sim 0.5^{\circ}\text{C}$ for the asperity calculation and $\sim 5^{\circ}\text{C}$ for the average calculation).

These calculations indicate that significant temperature rises could not have occurred in these experiments as long as the basic assumptions that the deformation occurred in a quasistatic, continuous manner were valid. Two mechanisms could conceivably invalidate these assumptions. One is the occurrence of stick slip motion, giving rise to local sliding velocities significantly larger than the average sliding velocity.³⁶ However, this appears unlikely, for the local velocity would need to exceed the maximum upper-bound average velocity by a factor of 100 in order to approach adiabatic conditions. The other mechanism is a sequence of damage events involving extensive localized fragmentation by cracking (termed cataclastic flow in the geological literature) followed by plastic deformation of the debris. If the debris is not in perfect contact with surrounding material during deformation, the conduction of heat to the surroundings is reduced and adiabatic conditions might be more closely approached. Unfortunately, it is not straightforward to assess this effect quantitatively.

Annealing of radiation damage

Possible recrystallization of monazite may be related to the resistance of monazite to radiation damage, and in particular to recent observations of room-temperature annealing of radiation damage in LaPO_4 . That monazites are extremely resistant to amorphization by radiation damage, and are thus ideal crystal hosts for containment of actinide or transuranic elements is well established.³⁷ Natural monazites, despite having large concentrations of radioactive thorium and uranium substituted in the crystal structure, are always found in a crystalline state rather than as an amorphous or metamict mineral. Studies using synthetic monazite crystals have shown that this occurrence is due to the ability of monazite to recover readily from displacive damage events at near-ambient temperatures.^{38,39}

In a recent study by Meldrum, Boatner and Ewing⁴⁰ radiation damage in LaPO_4 and several related ABO_4 -type phosphates and silicates were monitored as a function of temperature *in-situ* in a transmission electron microscope. Fundamental differences in the amorphization and recrystallization kinetics between the phosphates and silicates were observed; the critical temperature above which amorphization could not be induced (i.e., recrystallization processes were faster than damage accumulation) was only 35°C for LaPO_4 , but more than 700°C for zircon. This difference was tentatively attributed to the higher stability of isolated PO_4 tetrahedra than isolated SiO_4 units, with less bond breaking being required to form the crystal structure from the amorphous structure. Similar arguments might apply for recrystallization from a microstructure subjected to intense mechanical deformation.

5. CONCLUSIONS

The results of the previous sections confirm that La-monazite is compatible with mullite, YAG, ZrO_2 and Al_2O_3 and that interfaces between La-monazite and these materials are sufficiently weak to allow debonding when a crack approaches the interface from within the monazite. This conclusion holds even in the presence of substantial residual compressive stresses normal to the interface, as in the case of the mullite fiber in an alumina matrix.

All of the monazite-coated fibers studied (single crystal mullite, alumina, eutectic $\text{Al}_2\text{O}_3/\text{YAG}$ and eutectic $\text{ZrO}_2/\text{Al}_2\text{O}_3$ fibers, all embedded in a fully dense alumina matrix) underwent sliding in single fiber push-out experiments. Debonding and sliding occurred by a single interfacial debond when the sliding displacements were small and/or the fiber surfaces were relatively smooth. At larger sliding displacements the eutectic fibers, which had rougher interfaces, caused extensive damage in the LaPO_4 coating. The damage mechanisms included fracture, twinning and dislocations. The ability of La-monazite to undergo plastic deformation at low temperatures, without causing any damage to the fibers, may be critical for its use as a composite interface because of the need to accommodate sliding of constrained rough surfaces.

TEM observations showed evidence suggesting that recrystallization may have occurred within the intensely deformed monazite. Several analyses indicated that significant frictional heating during sliding was unlikely unless stick-slip motion caused large increases in local sliding velocities. The absence of significant heating would imply that recrystallization of heavily deformed monazite is possible at room temperature, an unusual behavior for such a refractory material. However, such behavior might be consistent with observations of recrystallization from radiation damage in La-monazite at much lower temperatures than in other minerals.

ACKNOWLEDGEMENTS

Funding for this work at Rockwell was provided by the U.S. Air Force Office of Scientific Research under contract F49620-96-C-0026 monitored by Dr. A. Pechenik.

The work related on the development of new fibers at NASA Glenn was supported by the U.S. Air Force Office of Scientific Research under contract number F49620-00-1-0048 and National Aeronautics and Space Administration contract number NCC3-372.

REFERENCES

1. P. E. D. Morgan and D. B. Marshall, "Ceramic Composites of Monazite and Alumina," *J Am Ceram Soc*, **78** 1553-63 (1995).
2. P. E. D. Morgan, D. B. Marshall and R. M. Housley, "High Temperature Stability of Monazite-Alumina Composites," *J. Mat. Sci. Eng.*, **A195** 215 - 222 (1995).
3. D. B. Marshall, P. E. D. Morgan, R. M. Housley and J. T. Cheung, "High temperature Stability of the Al_2O_3 - LaPO_4 System," *J. Am. Ceram. Soc.*, **81**[4] 951-56 (1998).
4. D. B. Marshall, J. B. Davis, P. E. D. Morgan and J. R. Porter, "Interface Materials for Damage-Tolerant Oxide Composites," *Key Engineering Materials*, **127-131** 27-36 (1997).
5. J. B. Davis, D. B. Marshall and P. E. D. Morgan, "Oxide Composites of Al_2O_3 and LaPO_4 ," *J. European Ceram. Soc.*, **19** 2421-2426 (1999).
6. J. B. Davis, D. B. Marshall and P. E. D. Morgan, "Monazite Containing Oxide-Oxide Composites," *J. Eur. Ceram. Soc.*, **20**[5] 583 - 587 (2000).
7. K. A. Keller, T.-I. Mah, E. E. Boakye and T. A. Parthasarathy, "Gel-Casting and Reaction Bonding of Oxide-Oxide Minicomposites with Monazite Interphase," *Ceramic Engineering and Science Proceedings*, **21**[4] 525-534 (2000).
8. T. A. Parthasarathy, E. Boakeye, M. K. Cinibulk and M. D. Perry, "Fabrication and Testing of Oxide/Oxide Microcomposites with Monazite and Hiconite as Interlayers," *J. Amer. Ceram. Soc.*, **82**[12] 3575-3583 (1999).
9. D. B. Marshall, P. E. D. Morgan and R. M. Housley, "Debonding in Multilayered Composites of Zirconia and LaPO_4 ," *J. Am. Ceram. Soc.*, **80**[7] 1677-83 (1997).
10. D.-H. Kuo and W. M. Kriven, "Characterization of Yttrium Phosphate and a Yttrium Phosphate/Yttrium Aluminate Laminate," *J. Am. Ceram. Soc.*, **78**[11] 3121-3124 (1995).
11. M. G. Cain, R. L. Cain, A. Tye, P. Rian, M. H. Lewis and J. Gent, "Structure and Stability of Synthetic Interphases in CMCs," *Key Engineering Materials*, **127-131** 37-49 (1997).
12. D.-H. Kuo, W. M. Kriven and T. J. Mackin, "Control of interfacial Properties Through Fiber Coatings: Monazite Coatings in Oxide-Oxide Composites," *J. Am. Ceram. Soc.*, **80**[12] 2987-96 (1997).
13. R. J. Kerans and T. A. Parthasarathy, "Debond Crack Roughness, Interface Properties and Fiber Coating Design in Ceramic Composites," *Key Engineering Materials*, **127-131** 51-62 (1997).

14. A. Sayir, Ed. (1999). Directional Solidification of Eutectic Ceramics. Computer Aided Design of High Temperature Materials. Oxford, Oxford University Press.
15. A. Sayir and S. C. Farmer, "Directionally Solidified Mullite Fibers," *Mat. Res. Soc. Proc.*, **365** 11-21 (1995).
16. Y. S. Touloukian, R. K. Kirby, R. E. Taylor and T. Y. R. Lee, Thermal Expansion - Non Metallic Solids. New York, Plenum (1977).
17. S. Geller, G. P. Espinosa and P. B. Crandall, "Thermal Expansion of Yttrium and Gadolinium Iron, Gallium and Aluminum Garnets," *J. Appl. Crystallography*, **2** 86-88 (1969).
18. R. S. Hay, J. R. Welch and M. K. Cinibulk, "TEM Specimen Preparation and Characterization of Ceramic Coatings on Fiber Tows," *Thin Solid Films*, **308-309** 389-392 (1997).
19. D. B. Marshall, J. B. Davis, P. E. D. Morgan, J. R. Waldrop and J. P. Porter, "Properties of La-Monazite as an Interphase in Oxide Composites," *Zeitschrift fur Metallkunde*, **90**[12] 1048-1052 (1999).
20. D. B. Marshall, J. R. Waldrop and P. E. D. Morgan, "Thermal Grooving at the Interface Between alumina and Monazite," *Acta Mat.*, (in press).
21. M.-Y. He and J. W. Hutchinson, "Crack Deflection at an Interface Between Dissimilar Materials," *Int. J. Solids Struct.*, **25** 1053-1067 (1989).
22. M.-Y. He, A. G. Evans and J. W. Hutchinson, "Crack Deflection at an Interface Between Dissimilar Elastic Materials: Role of Residual Stresses," *Int. J. Solids Structures*, **31**[24] 3443-3455 (1994).
23. R. S. Hay, E. Boakeye, M. D. Petry, Y. Berta, K. Von Lehmden and J. Welch, "Grain Growth and Tensile Strength of 3-M Nextel 720TM after Thermal Exposure," *Ceramic Engineering and Science Proceedings*, **20**[3] 165-172 (1999).
24. D. M. Wilson and L. R. Visser, "Nextel 650 Ceramic Oxide Fiber: New Alumina-based Fiber for High Temperature Composite Reinforcement," *Ceramic Engineering and Science Proceedings*, **21**[4] 363-373 (2000).
25. J. B. Davis, D. B. Marshall, P. E. D. Morgan and R. M. Housley, "Machinable Ceramics Containing Rare-Earth Phosphates," *J. Am. Ceram. Soc.*, **81**[8] 2169-75 (1998).
26. R. S. Hay, "Monazite and Scheelite Deformation Mechanisms," *Ceramic Engineering and Science Proceedings*, **21**[4] 203-228 (2000).
27. R. S. Hay, J. B. Davis and D. B. Marshall, "Mechanical twinning in La-monazite," (unpublished).

28. B. J. Hockey, "Plastic Deformation of Aluminum Oxide by Indentation and Abrasion," *J. Am. Ceram. Soc.*, **54**[5] 223-31 (1971).
29. A. H. Heuer, "Deformation Twinning in Corundum," *Philos. Mag. A*, **13**[122] 379-93 (1966).
30. R. M. Cannon, "Structure and Properties of MgO and Al₂O₃"; pp 818-38 in Advances in Ceramics. Ed. W. D. Kingery. Columbus, Ohio, The American Ceramic Society. **10**, 1984.
31. H. M. Chan and B. R. Lawn, "Indentation Deformation and Fracture of Sapphire," *J. Am. Ceram. Soc.*, **71**[1] 29-35 (1988).
32. K. P. D. Lagerlof, A. H. Heuer, J. Castaing, J. P. Riviere and T. E. Mitchell, "Slip and Twinning in Sapphire (a-Al₂O₃)," *J. Am. Ceram. Soc.*, **77**[2] 385-97 (1994).
33. F. P. Bowden and D. Tabor, Friction and Lubrication of Solids, Parts I and II. Oxford, U.K., Clarendon Press (1964).
34. J. C. Jaeger, *Jour. & Proc. Roy. Soc. NSW*, **76** 203 (1942).
35. M. F. Ashby, J. Abulawi and H. S. Kong, "Temperature Maps For Frictional Heating in Dry Sliding," *Tribology Transactions*, **34**[4] 577-587 (1991).
36. S. Brown, "Frictional Heating on Faults: Stable Sliding versus Stick-Slip," *J. Geophys. Res.*, **103**[B4] 7413-7420 (1998).
37. L. A. Boatner and B. C. Sales, "Monazite"; in Radioactive Waste Forms for the Future. Eds W. Lutze and R. C. Ewing. New York, North-Holland. **Chapter 8**, 1988.
38. F. G. Karioris, K. A. Gowda and L. Cartz, "Heavy Ion Bombardment of Monoclinic ThSiO₄, ThO₂ and Monazite," *Radiation Effects Letters*, **58** 1-3 (1981).
39. T. C. Ehlert, K.A. Gowda, F. G. Karioris and L. Cartz, "Differential Scanning Calorimetry of Heavy Ion Bombarded Synthetic Monazite," *Radiation Effects*, **70** 173-181 (1983).
40. A. Meldrum, L. A. Boatner and R. C. Ewing, "A Comparison of Radiation Effects in Crystalline ABO₄-type Phosphates and Silicates," *Mineralogical Magazine*, **64**[2] 185-194 (2000).
41. Y. Hikichi, T. Nomura, Y. Tanimura and S. Suzuki, "Sintering and Properties of Monazite-type CePO₄," *J. Am. Ceram. Soc.*, **73**[12] 3594-3596 (1990).
42. Y. S. Touloukian, R. W. Powell, C. Y. Ho and P. G. Klemens, Thermal Conductivity - Non Metallic Solids. New York, Plenum (1970).

43. A. Sayir and S. C. Farmer, "The Effect of the Microstructure on Mechanical Properties of Directionally Solidified $\text{Al}_2\text{O}_3/\text{ZrO}_2(\text{Y}_2\text{O}_3)$ Eutectic," *Acta Mater.*, 48 (2000) 000-000.
44. A. Sayir and L. E. Matson, "Growth and Characterization of Directionally Solidified $\text{Al}_2\text{O}_3/\text{Y}_3\text{Al}_5\text{O}_{12}$ (YAG) Eutectic Fibers," in "HITEMP Review. Advanced High Temperature Engine Materials Technology Program," *Proc. of the 2nd Ann. HITEMP Rev.*, [83] (1991) pp.1-14.
45. L. E. Matson and N. Hecht, "Microstructural Stability and Mechanical Properties of Directionally Solidified Alumina/YAG Eutectic Monofilaments," *J. of. the European Ceram. Soc.*, [19] (1999) 2487-2503.
46. W. M. Kriven, J. W. Palko, S. Sinogeikin, J. D. Bass, A. Sayir, G. Brunauer, H. Boysen, F. Frey and J. Schneider, "High Temperature Single Crystal Properties of Mullite" *J. Europ. Ceram. Soc.*, 19 (1999) 2529 – 2541.

Appendix A: Estimates of Heating due to fiber sliding

Several approaches, based on different assumptions about dissipation mechanisms, may be taken to estimate limits on local temperature rises during fiber sliding. Some results from these analyses are summarized below

Adiabatic sliding

If we assume that the work done by the sliding friction is dissipated entirely by uniform adiabatic heating within the zone of deformed monazite adjacent to the plane of sliding, the temperature rise is given by

$$\Delta T = \tau_s \delta / (\rho c_p h), \quad (\text{A1})$$

where τ_s is the sliding friction stress, δ is the sliding displacement, h is the thickness of the deformation zone, and ρ and c_p are the density and specific heat of the monazite. For the sliding experiment corresponding to Fig. 6, the measured parameters are: $\tau_s \sim 200$ MPa, $\delta = 5 \mu\text{m}$ and $h \sim 0.2 \mu\text{m}$. With $\rho = 5 \text{ g/cm}^3$ and $c_p = 500 \text{ J/kg.K}$,⁴¹ Eq. (A1) gives $\Delta T = 2000^\circ\text{C}$.

An alternative estimate based on incremental sliding of individual asperities, as depicted in Fig A1, gives the temperature rise:

$$\Delta T = H A_a / (\rho c_p A_b), \quad (\text{A2})$$

where H is the hardness of the monazite, A_a is the cross-sectional area of the asperity and A_b is the cross-sectional area of the plastic deformation zone created by the asperity as it slides (the sliding force acting on the asperity being set equal to $H A_a$). If we take H equal to the room temperature hardness of monazite ($\sim 5 \text{ GPa}$)¹ and $A_a/A_b \sim 2$ (from Fig. 6) Eq. (A2) gives $\Delta T = 1000^\circ\text{C}$.

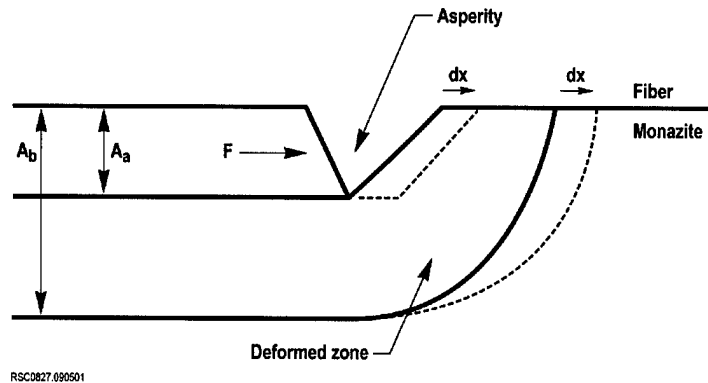


Figure A1. Schematic showing asperity sliding and associated deformation zone.

Both of these estimates are subject to considerable uncertainty (a factor of ~ 2) associated with the parameters h and A_a/A_b as well as the assumption of uniform heating within the

zone. Nevertheless, they indicate that large local temperature rises can occur if the sliding velocity is sufficiently large to allow adiabatic conditions.

Estimated sliding velocity and transient heating effects

The time in transient heat conduction problems always appears normalized by the characteristic time, τ :

$$\tau = \rho c_p d^2 / k, \quad (A3)$$

where k is the thermal conductivity and d is a characteristic diffusion distance. In the fiber sliding problem, d is the depth of the deformation zone and the conditions are close to adiabatic only if the time, t_h , taken to inject heat into the deformation zone is small compared with τ . If we assume that heat is conducted only into the monazite ($k \sim 2$ W/m.K)⁴¹ the characteristic diffusion time for a zone of depth $\sim 0.2 \mu\text{m}$ is $\tau \sim 10^{-7}$ s. The time t_h is given by $t_h = \delta / v$, where δ is the sliding distance and v is the sliding velocity.

The sliding velocity was not measured in the experiments described in section 2. However we can estimate a very conservative upper bound. The experiments involved loading the indenter on the end of the fiber using a fixed weight lowered slowly (velocity less than 10^{-4} m/s) via a viscous dash-pot. When debonding occurred, the sliding fiber accelerated unstably until the indenter was arrested by contacting the matrix. The magnitude of the acceleration was determined by the resultant force acting on the fiber (the difference between the combined weight of the loading mass, indenter, and fiber and the opposing forces due to sliding friction and the dash-pot). An upper bound for this acceleration, corresponding to zero resistance from sliding and the dash-pot, is simply the gravitational acceleration, g . This acceleration acting over the measured sliding displacement ($\sim 5 \mu\text{m}$) would result in a maximum velocity of 10^{-2} m/s. A less conservative overestimate obtained with the assumption that the sliding friction remains constant during the test gives a value smaller by a factor of 15.

With the upper-bound velocity of 10^{-2} m/s and the sliding distance $\delta = 5 \mu\text{m}$ for the average analysis of Eq. (A1), the lower bound estimate for the heat input time is $t_h \sim 5 \times 10^{-4}$ s. This is more than 3 orders of magnitude larger than the value of τ estimated above, indicating that adiabatic conditions are not approached. For the asperity sliding analysis (Eq. (A2)), the relevant sliding distance is smaller (equal to the dimensions of the asperity, $\sim 0.5 \mu\text{m}$) giving a smaller heat input time, although still far from adiabatic conditions ($t_h / \tau \sim 10^2$).

It is worth noting the role of asperity size in the above analysis. Since both d in Eq. (A3) and the sliding distance δ that determines the sliding time (t_h) scale with the asperity size, the ratio t_h / τ increases with decreasing asperity size. Therefore, if the damage observed in Fig. 6 was caused by sequential sliding of asperities of various sizes, the conditions for the smaller asperities would have been further from adiabatic. Given the

conservative nature of these estimates it appears unlikely that large temperature increases could have occurred in these experiments.

Frictional sliding analyses

In the literature on frictional sliding (e.g., Bowden and Tabor,³³ Jaeger,³⁴ Ashby³⁵) the assumption is made that work done by frictional forces is dissipated as heat at the interface between the sliding surfaces. Solutions for the interface temperature as a function of the sliding velocity are then obtained from analysis of heat flow into the materials either side of the interface. Solutions are available at a macroscopic level (average) and at an asperity contact level for transient and steady state conditions. These solutions can be written in the general form³⁵

$$\Delta T = (F_s v / A) (k_1/\ell_1 + k_2/\ell_2)^{-1}, \quad (\text{A4})$$

where ΔT is the difference between the interface temperature and the remote temperature, F_s is the sliding force, v the velocity, A the contact area, k_1 and k_2 are the thermal conductivities of materials 1 and 2 either side of the interface, and ℓ_1 and ℓ_2 are functions of the contact geometry, thermal diffusivities (α) and the time over which the heat is applied. We note that a limitation of these models is that ΔT increases without limit as the sliding velocity increases (i.e. as adiabatic conditions are approached), a consequence of the assumption that the heat is dissipated at the interface rather than in a deformation zone of finite volume.

For the analysis of sliding asperities, a convenient solution for ℓ_1 and ℓ_2 is that of a Gaussian heat source applied for a time t over a circular contact area of radius r_0 .³⁵

$$\ell = r_0 \pi^{-1/2} \tan^{-1}(4 t \alpha / r_0^2)^{1/2}. \quad (\text{A5})$$

An upper bound for the sliding force on an asperity is given by taking the contact pressure equal to the hardness of the monazite and a friction coefficient of unity, so that $F_s/A = H$. For asperity contact times between the limits $\sim r_0/v$ and δ/v , the temperature rise estimated from Eq. (A4) for a $\text{Al}_2\text{O}_3/\text{YAG}$ asperity with $r_0 = 0.2 \mu\text{m}$, $\alpha \sim 0.05 \text{ cm}^2/\text{s}$, $k \sim 20 \text{ W/m.K}$,⁴² and other parameters as defined above is $\sim 0.5^\circ\text{C}$. An alternative analysis based on the measured sliding force and uniform contact gave $\Delta T \sim 5^\circ\text{C}$.

4.0 Stability of LaPO_4 Systems in High Temperature Environments containing H_2O vapor

The following is a summary of a paper in preparation for publication in the Journal of the American Ceramic Society, by J. B. Davis, D. B. Marshall, and B. Opila (NASA Glen)

We previously demonstrated the long-term stability and compatibility of the $\text{LaPO}_4/\text{Al}_2\text{O}_3$ system in a closed air-containing environment at temperatures up to at least 1600°C . However, combustion environments with flowing water vapor can be more aggressive because the formation of volatile OH-containing species, even at very low partial pressures, can lead to degradation over long times. Recent studies have emphasized the importance of this with systems such as SiC that rely on a protective layer of SiO_2 for oxidation resistance.

To assess the stability of LaPO_4 in such environments, test specimens were exposed to flowing gas consisting of 90% H_2O / 10% O_2 at 1 atm. in a tube furnace at 1400°C for periods up to 500 hours. The test specimens were polycrystalline LaPO_4 formed by sintering powders synthesized in our laboratories. Some specimens contained a few percent of dispersed AlPO_4 particles formed by adding Al nitrate during processing to act as a buffer for P-rich precursors. Others contained a few percent of Al_2O_3 particles, while another was pure LaPO_4 made from stoichiometric powder. Key results are as follows:

- (1) In tests using a silica furnace tube significant microstructural changes were observed, with formation of porosity throughout and $\text{La}_2\text{Si}_2\text{O}_7$ near the surface, to depth ~ 60 to $100\ \mu\text{m}$. After the testing there were also isolated traces of a La-Si-Al containing glass in the interior (these specimens initially contained AlPO_4 inclusions). However all weight changes were accounted for by the reaction of LaPO_4 with silica vapors ($\text{SiO}(\text{OH})$, $\text{Si}(\text{OH})_3$ etc.) arising from reaction of water vapor with the silica furnace tube. These results suggest that additional direct reaction of LaPO_4 with water vapor under these conditions is negligible.
- (2) In tests using a high purity alumina furnace tube a thin protective layer of LaAlO_3 and $\text{LaAl}_{11}\text{O}_{18}$ formed on the surfaces of the test specimens in regions exposed directly to the flowing gas (Fig. 1). In the interior of the specimen, and at surfaces not directly exposed to the

flow (i.e., the bottom surface of the sample resting on an Al_2O_3 plate, Fig. 2) there was no detectable change to the LaPO_4 microstructure. In particular, there was no evidence for formation of La-rich compounds that would be evidence for loss of P due to reaction with water vapor. All weight changes were accounted for by observed reaction with volatile species (Al oxy-hydroxides) that originated from reaction of water vapor with the furnace tube, again suggesting that additional direct reaction of LaPO_4 with water vapor under these conditions is negligible. For applications in composites of LaPO_4 and Al_2O_3 it is worth noting the protective nature of the LaAlO_3 layer that formed on the surface exposed directly to the flow. Moreover, if the interior of such a composite were to be exposed to the environment through matrix cracks or porosity, the concentration of volatilized Al-containing species would be many orders of magnitude lower than in these experiments, even on the bottom surface of the plate where no reaction was observed (Fig. 2). The experiments indicate a very high stability of LaPO_4 in water-containing environments (possibly greater than alumina).

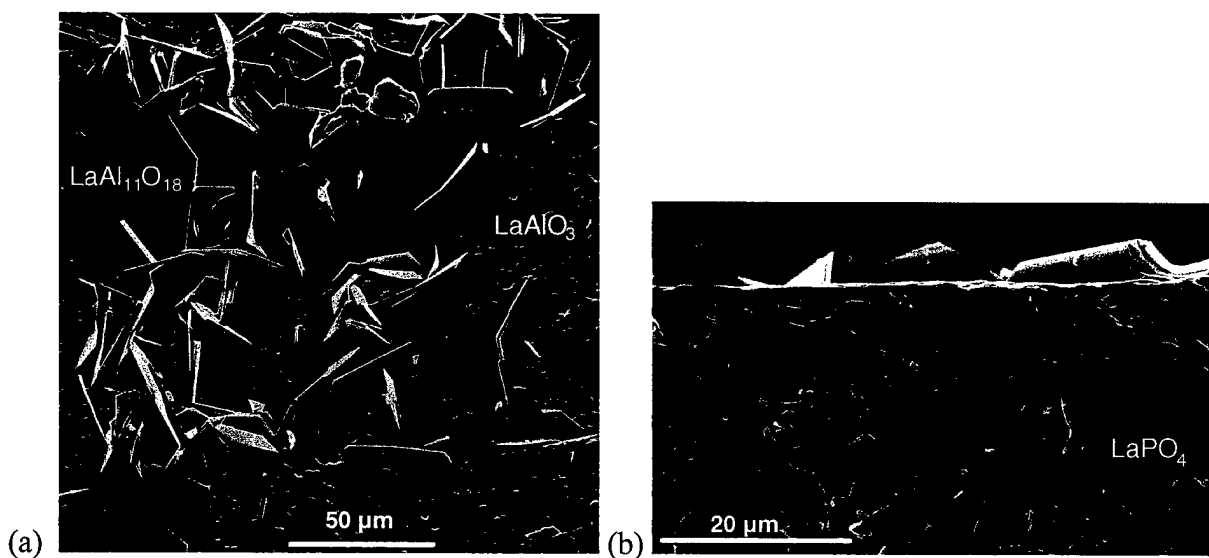
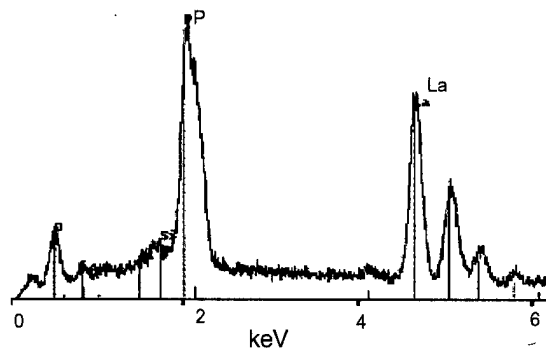
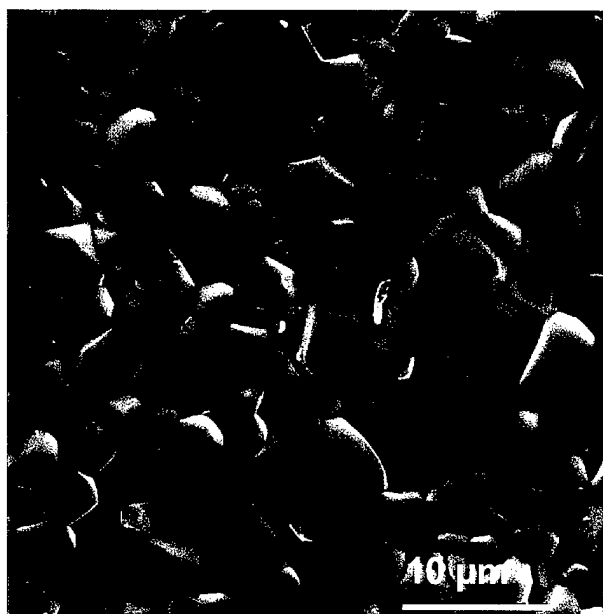


Fig. 1. Top surface of LaPO_4 exposed to 90% H_2O /10% O_2 flowing at 0.75 cm/s at 1400°C for 250h in Al_2O_3 furnace tube. (b) Fractured cross section from specimen in (a). showing thin LaAlO_3 surface layer and underlying LaPO_4 .



(a)

(b)

Fig. 2. (a) Bottom surface of LaPO_4 specimen, which rested on an Al_2O_3 support plate while being exposed at 1200°C to $90\%\text{H}_2\text{O}/10\%\text{O}_2$ flowing at 0.75 cm/s in Al_2O_3 furnace tube. (b) EDS analysis from (a), showing only LaPO_4 .

5.0 Oxide Composites of Al_2O_3 and LaPO_4

by Davis, J.B., Marshall, D.B and Morgan, P.E.D.

The following section is a paper published in the Journal of the J. European Ceram. Soc. 19
2421-2426 (1999)

Oxide Composites of Al_2O_3 and LaPO_4

J. B. Davis,* D. B. Marshall and P. E. D. Morgan

Rockwell Science Center, 1049 Camino Dos Rios, Thousand Oaks, CA 91360, USA

Abstract

Some properties of oxide composites based on Al_2O_3 and LaPO_4 (La-monazite) are examined. A composite consisting of woven Al_2O_3 fibers with a porous matrix of Al_2O_3 and LaPO_4 is shown to be damage tolerant and notch insensitive. The feasibility of achieving fiber sliding and pullout in a composite with a fully dense matrix is investigated using a small hot-pressed composite of sapphire fibers and LaPO_4 matrix. © 1999 Elsevier Science Ltd. All rights reserved.

Keywords: LaPO_4 , composites, fibres, mechanical properties, Al_2O_3 .

1 Introduction

Damage-tolerant, nonlinear behavior in ceramic composites requires weak surfaces or phases that decouple fracture processes in the matrix and the fiber reinforcements. This can be achieved in composites with a weak interphase separating strong fibers from a strong matrix, such as in glass-matrix/SiC-fiber composites with a weak carbon interphase.^{1–3} It can also be achieved in composites consisting of strong fibers in a porous, weak matrix, such as in carbon-matrix composites.^{4,5} Until fairly recently, all ceramic composites relied on either carbon or BN for the weak phase. As a result, they suffered from limited oxidation resistance.

During the past 5 years, several analogous oxide systems have been identified, with potential for long-term stability in oxidizing environments. Composites with weak porous matrices of $\text{SiO}_2/\text{Al}_2\text{O}_3$,⁶ Al_2O_3 ,⁷ $\text{Al}_2\text{O}_3/\text{mullite}$,^{8,9} and AlPO_4 ¹⁰ have been reported with room temperature mechanical properties very similar to carbon-carbon composites. These oxide composites were fabricated by infiltration of slurries into preforms of woven fibers (small-diameter, polycrystalline alumina or mullite fibers) followed by sintering. In the absence of a separate weak interphase between the

fibers and matrix, the porous matrix bonds strongly to the fibers. However, because of the low elastic stiffness and fracture toughness resulting from the porosity, cracks do not readily pass from the matrix to the fibers, and tensile loading causes extensive damage in the matrix before failure of the fibers. Failure ultimately involves pullout of fibers, mainly in tows, and the fracture strength is relatively insensitive to the presence of stress concentrators such as notches and holes.⁹ The high temperature limitations of such composites are expected to come from several sources: microstructural stability of fine grained fibers, coarsening of the matrix, and inter-diffusion of the matrix and fibers.

In fully dense systems, two classes of oxides that allow debonding have recently been identified. One relies on layered crystal structures such as micas,¹¹ β -aluminas,¹² magnetoplumbites^{12,13} and perovskites,¹⁴ with intrinsically weak cleavage planes. The other is a group of refractory mixed oxides (rare-earth orthophosphates with the monazite^{15–18} or xenotime¹⁹ structures, and several tungstates²⁰ and vanadates²¹), which have been shown to form weak interfaces with other oxides such as Al_2O_3 , YAG, ZrO_2 , and mullite. In the case of La-monazite (LaPO_4), long-term stability with sapphire fibers has been demonstrated at 1600°C,¹⁸ thus indicating the prospect of fabricating dense-matrix composites with better stability than the porous matrix systems presently available. However, most studies of these systems have involved model specimen configurations designed to assess interfacial debonding. With the exception of some multi-layered composites,¹⁷ fully dense composites have not been formed, mainly because of the difficulty of processing such composites without degrading the oxide fibers that are presently available.

In this paper we present some properties of an oxide composite that combines a porous matrix and a weak fiber-matrix interface to give enhanced nonlinear behavior and potentially improved stability at high temperatures. The composite consists of polycrystalline Al_2O_3 fibers in a porous, two-phase matrix of LaPO_4 and Al_2O_3 . We also report some preliminary experiments to test the ability of LaPO_4 to facilitate fiber debonding and pullout in fully dense systems.

*To whom correspondence should be addressed.

2 Experiments

A porous matrix composite was fabricated by infiltrating woven fabric of polycrystalline alumina fibers (3M company, Nextel 610, 8-harness satin weave) with a slurry of $\text{Al}_2\text{O}_3/\text{LaPO}_4$. The slurry contained dispersed α -alumina powder (Sumitomo, AKP50) and solution precursor for LaPO_4 . Individual layers of fabric, $15 \times 15 \text{ cm}^2$, were infiltrated, stacked (10 layers), dried while vacuum bagging and warm pressing, then sintered at 1100°C in air for 1 h. The resulting composite plate was $\sim 2 \text{ mm}$ thickness. Double-edge-notched tensile test specimens, with dimensions $\sim 15 \times 1 \text{ cm}$ aligned parallel to the weave direction, were cut from the plate using a diamond saw (Fig. 1). The saw cuts that formed the notches were of $\sim 150 \mu\text{m}$ width. The specimens were loaded in tension using wedge grips and tabs glued to the ends. The gauge section extension was measured using a clip gauge attached 12.5 mm above and below the mid plane, which contained the notches.

A composite with a fully dense LaPO_4 matrix and sapphire fiber reinforcement was fabricated by hot pressing. Since the sole purpose of this composite was to test whether debonding and fiber pullout occur in this system under tensile loading parallel to the fibers, the simplest possible fabrication route, making use of available hot pressing facilities, was used. Sapphire fibers were chosen to allow hot pressing at sufficiently high temperature to densify the matrix (1400°C) without damaging the fibers (polycrystalline fibers would degrade at

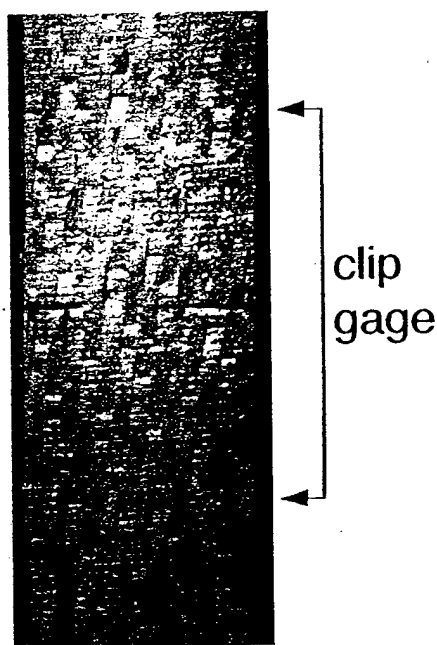


Fig. 1. Double-edge-notched tensile test specimen of composite consisting of woven Al_2O_3 fibers and porous Al_2O_3 - LaPO_4 matrix.

this temperature). Approximately 200 fibers of length 40 mm were coated individually with a thick layer of rhabdophane (hydrated LaPO_4) powder and stacked together along a diameter of a 50 mm cylindrical graphite die. The remainder of the die was filled with Al_2O_3 powder to prevent direct contact between the graphite die and the LaPO_4 . The compact was hot pressed at 1400°C for 1 h, to form an alumina disk with a small embedded sapphire/ LaPO_4 composite, of cross-section dimensions $\sim 2 \times 2 \text{ mm}$, along its diameter.

The test specimen shown schematically in Fig. 2 was cut from the hot pressed disc and loaded in four-point bending with the embedded composite in tension. The hole drilled adjacent to the embedded composite served to reduce the gradient of tensile bending stress across the composite and to allow cracking of the ligament of material between the hole and the edge of the specimen without fracturing the entire beam.

3 Results

3.1 Porous $\text{Al}_2\text{O}_3/\text{LaPO}_4$ matrix composites

The microstructure of the $\text{Al}_2\text{O}_3/\text{LaPO}_4$ matrix composite is shown in the scanning electron microscope (SEM) image of Fig. 3. The matrix consists of a two-phase mixture of Al_2O_3 and LaPO_4 grains, both with dimensions smaller than approximately $0.5 \mu\text{m}$, with fine-scale porosity between the grains. The alumina grains in the matrix are always separated from the fibers by a thin layer of LaPO_4 . The composites consisted of approximately 40 vol% of fibers (20% in each of the 0 and 90° orientations), 40 vol% matrix (Al_2O_3 and LaPO_4 in the ratio approximately 2:1) and 20 vol% porosity (as estimated from weight measurements).

The tensile response of a test specimen with notch depth greater than half of the test section ($a/w = 0.54$) is shown in Fig. 4. The net section stress during testing (load divided by the remaining cross-sectional area between the ends of the notches) is plotted as a function of the extension measured from the clip gauge. Also shown along the top border is the average strain calculated from the

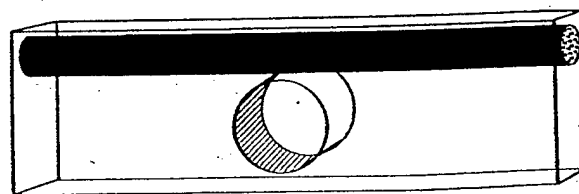


Fig. 2. Test specimen (Al_2O_3) with embedded composite of sapphire fibers and LaPO_4 matrix.

extension measurements; however, the strain is very nonuniform within the gauge area. The stress-strain curve shows substantial nonlinearity in the loading portion and continuously decreasing load beyond the peak. Test specimens without notches showed similar stress-strain curves, with strengths, in the range 200 to 220 MPa.

The nonlinear response is associated with extensive pullout of fibers, as seen from the separated ends of the test specimen in Fig. 5. Failure of the specimen occurred by separation of the matrix along an approximately planar section between the ends of the two notches and pullout of individual fibers over lengths up to ~ 1 cm from both sides of the fracture plane. Small but finite loads were supported by these bridging fibers at crack opening displacements of several mm. Examples of intact specimens loaded beyond the peak in the stress-strain curve are shown in Fig. 6: at a crack opening of ~ 1 mm in Fig. 6(a), (showing bridging fibers) and at a crack opening of ~ 3 mm in Fig. 6(b) (*in-situ* micrograph with net section stress 8 MPa).

3.2 Fully dense LaPO_4 -matrix composite

The microstructure of the hot pressed LaPO_4 -matrix composite is shown in the polished cross-section of Fig. 7. The matrix contains a few isolated pores, but is mostly fully dense LaPO_4 . There is no apparent degradation of the sapphire fibers or reaction with the matrix.

Micrographs of the specimen depicted in Fig. 2 after loading to failure are shown in Fig. 8. Pullout of the sapphire fibers occurred over lengths of several mm, with most fibers pulling out from one side of the fracture surface. Although extensive crack-

ing occurred in the LaPO_4 matrix, and pieces of the matrix pulled out with the fibers as in Fig. 8(a), higher magnification micrographs such as Fig. 8(b) show that debonding and sliding occurred at the fiber-matrix interface [scratch marks due to fiber sliding can be seen in the LaPO_4 matrix in Fig. 8(b), in the hole left behind after pulling out the fiber].

4 Discussion

Under tensile loading parallel to the 0 or 90° weave direction, the $\text{Al}_2\text{O}_3/\text{LaPO}_4$ matrix composite shows nonlinear stress-strain response, with the nonlinear component of strain at the peak load being several times the linear elastic strain extrapolated from low loads. Failure is non-catastrophic, with fiber pullout over distances of ~ 1 cm. Strengths, in the range 200–250 MPa, are unaffected by the presence of severe notches. These characteristics differ from the responses reported

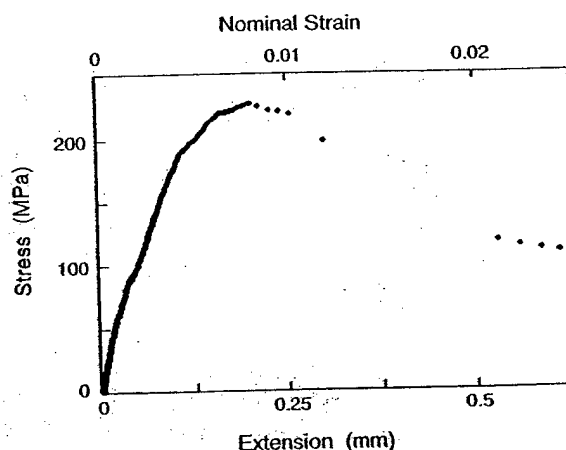


Fig. 4. Tensile test results from composite of Fig. 1.

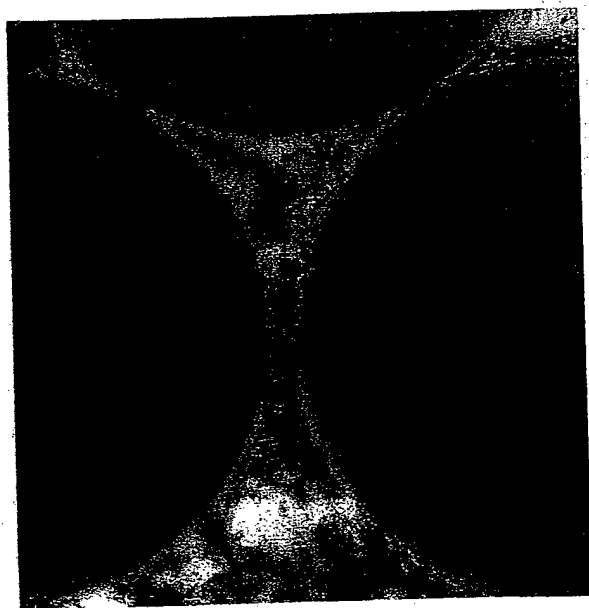


Fig. 3. Microstructure of composite from Fig. 1 (secondary electron image).

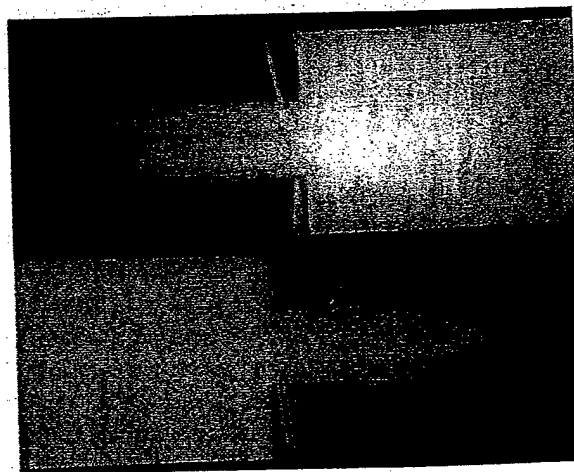


Fig. 5. Separated test specimen from test in Fig. 4.

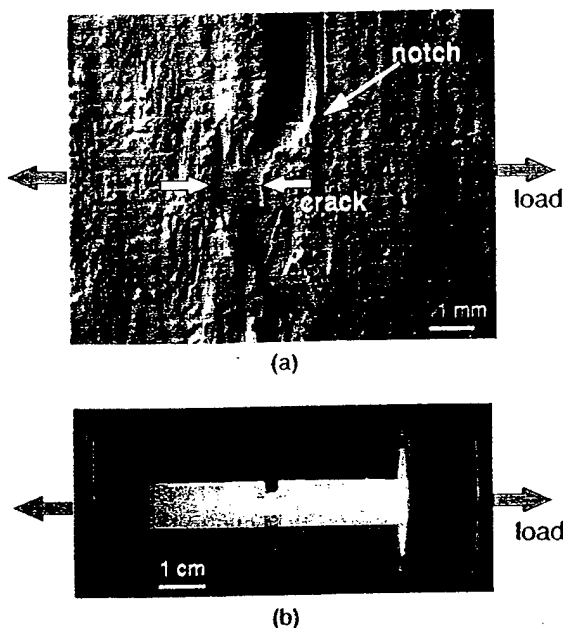


Fig. 6. (a) Bridging fiber tows in test specimen loaded as in Fig. 4, interrupted before complete separation. (b) *In-situ* optical micrograph from test as in Fig. 4 at net section stress of 8 MPa.

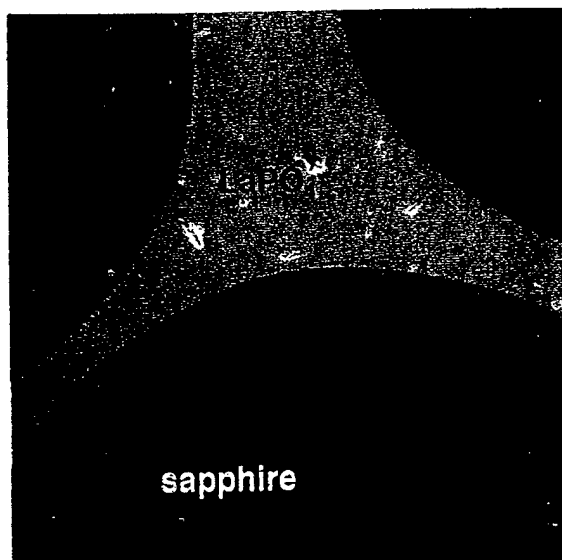


Fig. 7. Cross-section of hot-pressed LaPO₄-matrix composite (secondary electron image).

for other porous matrix composites in systems where strong local bonding between matrix and fibers would be expected (SiO₂/Al₂O₃,⁶ Al₂O₃/mullite,^{8,9} AlPO₄¹⁰). The strengths of such composites under loading parallel to the 0 or 90° directions have been reported in the same range, while notch-insensitivity along with nonlinear stress-strain response and noncatastrophic failure have been reported under flexural loading and under tensile loading in a direction at 45° to the 0/90

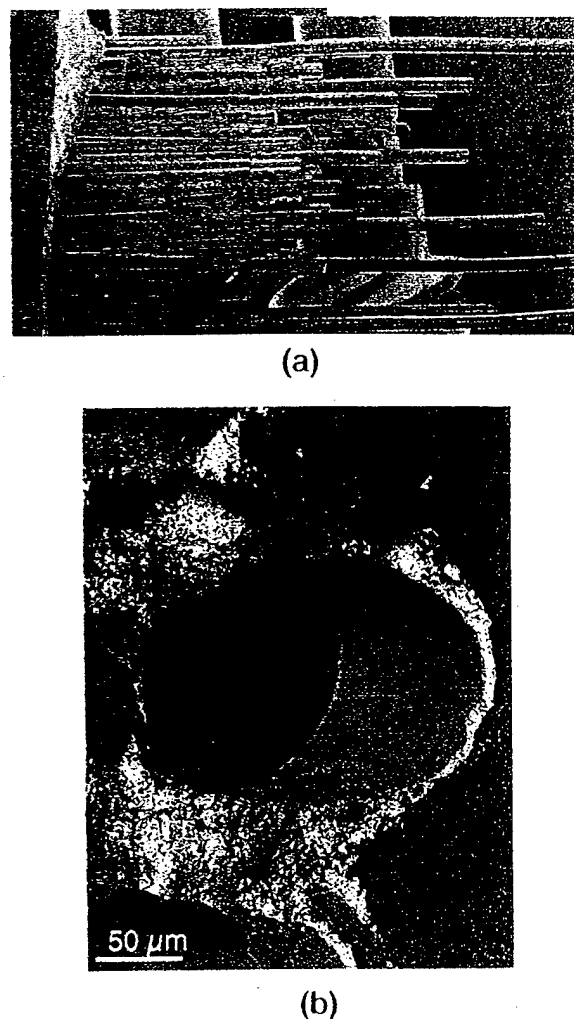


Fig. 8. (a) Fractured test piece of LaPO₄ matrix composite. (b) Higher magnification of region of fracture surface from same specimen as (a). Dark circular area is fracture surface of sapphire fiber. Smooth light region is LaPO₄ coating in cylindrical hole (going into page from right to left) remaining after pull-out of the other half of the fractured fiber.

weave direction.⁹ However, the large nonlinear response has not been observed in tensile loading parallel to the 0 or 90° weave directions. In this case, the composites may show a very small nonlinearity before the peak load (nonlinear component of strain less than 10% of the total strain) and a jagged fracture surface associated with some pullout of fiber tows. However, failure is catastrophic and the extensive pullout of individual fibers, such as in Fig. 5, is not observed. Therefore, it is evident that, while the porous nature of the matrix in the Al₂O₃/LaPO₄ composite most likely contributes to the nonlinear response, the presence of the weakly bonded LaPO₄ phase at the fiber-matrix interface greatly enhances the damage-tolerant behavior of the composite.

Although porous-matrix composites may be adequate for many applications, certain uses bene-

fit from, or require a fully dense matrix (e.g., extremely corrosive environments, need for hermetic seal). Previous studies of $\text{LaPO}_4/\text{Al}_2\text{O}_3$ interfaces have demonstrated that debonding occurs in a variety of cracking configurations in fully dense systems.¹⁵⁻¹⁸ However, damage-tolerant behavior requires sliding and pullout of fibers in addition to debonding. Fiber sliding after debonding would be expected to be more difficult in fully dense systems than in composites with porous matrices, because the higher stiffness of the matrix would be less accommodating for the misfit caused by the sliding motion of any irregularities at the interface.²²

Fiber sliding was demonstrated previously in pushout experiments involving isolated sapphire fibers with LaPO_4 coatings in a fully dense Al_2O_3 matrix.¹⁵ The interface in these experiments contained irregularities in the form of grain boundary grooves and cusps with height ~ 50 nm. Sliding occurred without permanent deformation, implying that the misfitting asperities were accommodated by elastic strains during sliding. The LaPO_4 -matrix composite examined in the present study was prepared using the same starting materials and nominally identical processing conditions as the composite used in the previous pushout experiments.¹⁵ The results in Figs. 7 and 8 demonstrate the feasibility of achieving fiber pullout in fully dense systems.

The development of oxide composites with fully dense matrices is presently limited by our ability to densify the matrix under conditions that do not degrade the fibers. Processing temperatures for composites containing polycrystalline Al_2O_3 and mullite fibers are limited to ~ 1200 – 1300°C (lower if pressure is used to aid densification). Such composites require development of either higher temperature fibers (e.g. eutectic or single crystal fibers) or methods, currently being examined, for promoting densification of the matrix at lower temperatures.

5 Conclusions

An oxide composite consisting of woven Al_2O_3 fibers and a porous matrix of Al_2O_3 and LaPO_4 was found to exhibit much greater nonlinear response and notch insensitivity than other porous matrix composites. The enhanced properties were attributed to weak bonding between the fibers and the LaPO_4 phase, which allowed extensive fiber pullout.

The feasibility of achieving fiber pullout in fully dense Al_2O_3 - LaPO_4 composites was demonstrated using a hot pressed composite with sapphire fibers.

Acknowledgements

Funding for this work was provided by the U.S. Air Force Office of Scientific Research under contract F49620-96-C-0026 monitored by Dr. A. Pechenik (work on fully dense matrix composites) and the U.S. Office of Naval Research under contract N00014-95-C-0057 monitored by Dr. S. Fishman (work on porous matrix composite).

References

1. Prewo, K. M. and Brennan, J. J., High strength silicon carbon fiber reinforced glass matrix composites. *J. Mater. Sci.*, 1980, 15(2), 463–468.
2. Brennan, J. J. and Prewo, K. M., Silicon carbide fiber reinforced glass-ceramic matrix composites exhibiting high strength and toughness. *J. Mater. Sci.*, 1982, 17(8), 2371–2383.
3. Sun, E. Y., Nutt, S. R. and Brennan, J. J., Fiber coatings for SiC-fiber-reinforced BMAS glass-ceramic composites. *J. Am. Ceram. Soc.*, 1997, 80(1), 264.
4. Turner, K. R., Speck, J. S. and Evans, A. G., Mechanisms of deformation and failure in carbon-matrix composites subject to tensile and shear loading. *J. Am. Ceram. Soc.*, 1995, 78(7), 1841–1848.
5. Buckley, J. D., Carbon-carbon, an overview. *Am. Ceram. Soc. Bull.*, 1988, 67(2), 364–368.
6. Harrison, M. G., Millard, M. L. and Szveda, A., Fiber reinforced ceramic matrix composite member and method for making. U.S. Patent No. 5 306 554; UK Patent No. 2 230 259 (1994).
7. Tu, W. C., Lange, F. F. and Evans, A. G., Concept for a damage-tolerant ceramic composite with 'strong' interfaces. *J. Am. Ceram. Soc.*, 1996, 79(2), 417–424.
8. Levi, C. G., Yang, J. Y., Dalgleish, B. J., Zok, F. W. and Evans, A. G., Processing and performance of an all-oxide ceramic composite. *J. Am. Ceram. Soc.*, 1998, 81(8), 2077–2086.
9. Lange, F. F., Tu, W.-C. and Evans, A. G., Processing of damage-tolerant, oxidation-resistant ceramic-matrix composites by a precursor infiltration and pyrolysis method. *Mater. Sci. Eng.*, 1995, A195, 145–150.
10. Keith, W. P. and Kedward, K. T., Shear damage mechanisms in a woven, nicalon reinforced ceramic matrix composite. *J. Am. Ceram. Soc.*, 1997, 80(2), 357–364.
11. Cooper, R. F. and Hall, P. C., Reactions between synthetic mica and simple oxide compounds with application to oxidation-resistant ceramic composite. *J. Am. Ceram. Soc.*, 1993, 76(5), 1265–1273.
12. Morgan, P. E. D. and Marshall, D. B., Functional interfaces in oxide-oxide composites. *J. Mat. Sci. Eng.*, 1993, A162(1–2), 15–25.
13. Cinibulk, M. K., Magnetoplumbite compounds as a fiber coating for oxide-oxide composites. *Ceram. Eng. and Sci. Proc.*, 1994, 15(5), 721–728.
14. Petuskey, W. T. (private communication).
15. Morgan, P. E. D. and Marshall, D. B., Ceramic composites of monazite and alumina. *J. Am. Ceram. Soc.*, 1995, 78(6), 1553–1563.
16. Morgan, P. E. D., Marshall, D. B. and Housley, R. M., High temperature stability of monazite-alumina composites. *J. Mat. Sci. Eng.*, 1995, A195, 215–222.
17. Marshall, D. B., Morgan, P. E. D. and Housley, R. M., Debonding in multilayered composites of zirconia and LaPO_4 . *J. Am. Ceram. Soc.*, 1997, 80(7), 1677–1683.
18. Marshall, D. B., Morgan, P. E. D., Housley, R. M. and Cheung, J. T., High temperature stability of the Al_2O_3 - LaPO_4 system. *J. Am. Ceram. Soc.*, 1998, 81(4), 951–956.

19. Kuo, D.-H. and Kriven, W. M., Characterization of yttrium phosphate and a yttrium phosphate/yttrium aluminate laminate. *J. Am. Ceram. Soc.*, 1995, **78**(11), 3121-3124.
20. Goettler, R. W., Sambasivan, S. and Dravid, V. P., Isotropic complex oxides as fiber coatings for oxide-oxide CFCC. *Ceramic Engineering and Science Proceedings*, 1997, **18**, 279-286.
21. Cain, M. G., Cain, R. L., Tye, A., Rian, P., Lewis, M. H. and Gent, J., Structure and stability of synthetic interphases in CMCs. *Key Engineering Materials*, 1997, **127-131**, 37-49.
22. Kerans, R. J., The role of coating compliance and fiber/matrix interfacial topography on debonding in ceramic composites. *Scripta Metall Mater.*, 1995, **32**, 505-509.

6.0 The Weak Interface Between Monazites and Refractory Ceramic Oxides

by Morgan, P.E.D., Marshall, D.B., Davis, J.B. and Housley R.M.

The following section is a paper published in Computer Aided Design of High-Temperature Materials, Eds. A. Pechenik, R. K. Kalia, and P. Vashishta, pp 229-243, Oxford University Press, New York, 1999

THE WEAK INTERFACE BETWEEN MONAZITES AND REFRACTORY CERAMIC OXIDES

PETER E.D. MORGAN, DAVID B. MARSHALL, JANET B. DAVIS
AND ROBERT M. HOUSLEY

Rockwell Science Center
1049 Camino Dos Rios
Thousand Oaks, CA 91360

High-temperature, oxidation-resistant, ceramic matrix composites (CMCs), with (La)-monazite (LaPO_4) serving as a weakly bonded interphase, have been invented. Monazite is stable and phase compatible with several other ceramic oxides at temperatures to at least as high as 1750°C in air. The chemical and morphological stability and debonding characteristics of monazite-alumina interfaces are examined at temperatures of 1400°C and 1600°C . Especially important for use in high toughness composites, the monazite-alumina and other interfaces are shown to be sufficiently weak that interfacial debonding prevents cracks from growing from monazite into alumina. Observations of the fracture behavior and compatibility of LaPO_4 coatings in alumina and alumina-zirconia systems are discussed, and property measurements are presented for composites consisting of alumina fibers in a two-phase matrix of alumina and LaPO_4 . Weak interfaces also lead to machinable ceramics in two phase systems of monazite or xenotime and useful oxides such as mullite, alumina and zirconia. More surprisingly, it was discovered that pure monazite is machinable.

1. Introduction

CMCs are considered for many uses in engines, filters, etc. in attempts to wrest a few percent more useful energy from, oil, coal and gas. Previous ceramic composites have relied on carbon or boron nitride fiber coatings to prevent brittle failure and are thus severely limited by degradation in high temperature oxidizing environments. In recent attempts to overcome this limitation, several all-oxide composite systems (such as aluminum oxide fibers and matrix) have been explored¹⁻⁴.

For a coating on alumina fibers to operate successfully in an alumina matrix composite at high temperature we need: 1) chemical compatibility, 2) morphological compatibility, 3) refractoriness, 4) stability in oxidizing and preferably also in slightly reducing atmosphere, 5) stability in water vapor and carbon dioxide

environments and, perhaps, other even more corrosive situations and 6) weak interfaces capable of debonding; this is an extremely demanding set of requirements.

Alumina, an amphoteric (exhibiting both basic and acidic properties) oxide, is phase compatible (viz., does not chemically react) with very few simple oxides. It readily reacts with either basic or acidic oxides, ruling out simple oxides of elements on the left- or right-hand sides of the conventional periodic table. This leaves only a few oxides of elements towards the lower center of the table, such as SnO_2 , ZrO_2 (and HfO_2), TiO_2 (below 1420°C), and a few other more complicated choices, such as the β -alumina/magnetoplumbite family¹. In this group we observed¹ some, perhaps surmountable, morphological problems; this system has since attracted the attention of others^{2,9}.

A few choices exist, however, in other mixed oxides, especially where an element from the left (basic) side of the periodic table and an element from the right (acidic) side form a neutral mixed oxide. During preliminary scoping tests of this kind of idea, it rapidly became apparent that (La)-monazite, originally discussed in ref. 1 and hereinafter referred to simply as monazite, was in a class of its own in terms of its favorable physical properties and the nature of its interface with alumina. Monazite is non-toxic; almost completely insoluble in water, dilute acids and bases; refractory, MP $2072 \pm 20^\circ\text{C}$ ¹⁰ (higher than alumina) with no decomposition up to the melting point; and is not as easily reduced as SnO_2 ¹¹, which also suffers from volatility at high temperature.

LaPO_4 is monoclinic¹². Phosphorus is 4-coordinated in a distorted tetrahedral environment; La is nine-coordinated by O in an unusual arrangement; while O is 3- or 4-coordinated to 2 or 3 La and 1 P. It is a well-known, commercially important mineral; its occurrence in rocks has been discussed earlier¹³.

Although nature has performed innumerable phase stability experiments, only recently have a few studies of monazite phase diagrams been done by few people.¹⁴⁻¹⁶ "Phase Diagrams for Ceramists"¹⁷ contains less than a handful of diagrams involving monazite, part of a dearth of diagrams for rare earth oxide systems in general; this seems a curious oversight for such refractory materials with possible uses. The potential use of monazite as a radioactive waste encapsulant has not, however, escaped attention¹⁴. The sintering and some thermophysical properties of (Ce)-monazite (CePO_4) for possible high temperature applications have been reported by Hikichi et al¹⁹.

We have also found that LaPO_4 is a suitable oxidation resistant interphase for ceramic composites containing alumina as both the matrix and the reinforcement.^{1,13} In a "closed" system, monazite is believed to be phase compatible with alumina up to the eutectic melting point, which appears to be $> 1750^\circ\text{C}$ in air. Fully dense, fine grained, diphasic, mixtures of refractory oxides (e.g., Al_2O_3 , ZrO_2 , nullite) and rare-earth phosphates (e.g., LaPO_4 , CePO_4), should be machinable as

easy material removal should occur by formation and linking of cracks at the weak interfaces between the two phases. As these materials are all stable to very high temperatures in oxidizing environments ($>1600^{\circ}\text{C}$), they offer the potential to tailor microstructures with ranges of hardness, elastic properties, and thermal conductivity way beyond the ranges achievable with other machinable ceramics.

2. Potential Interphase Systems

2.1 LAYERED OXIDE CRYSTAL STRUCTURES

The use of crystal structures with easy cleavage planes has been explored as interphases that allow debonding. The first attempts used fluorophlogopite mica.⁷ Although adequate debonding was achieved, high temperature stability was compromised by reactions of the fluorophlogopite with alumina and mullite. Of more interest were the β -alumina/magnetoplumbite family of layer structures, which are compatible with alumina and stable to temperatures up to 1800°C .¹

Debonding and compatibility have been demonstrated in several systems^{1,2,7,20-23} (e.g., Na(Li)- β "-alumina, $\text{BaMg}_2\text{Al}_6\text{O}_{27}$, $\text{KMg}_2\text{Al}_5\text{O}_{25}$, $\text{LaAl}_{11}\text{O}_{18}$ and $\text{CaAl}_{12}\text{O}_{19}$). The main obstacles remaining involve morphology. Some success has been achieved in grain alignment;^{2,7,20-22} the degree of alignment must be perfect over distances equal to the required pull-out length (isolated grains oriented normal to a fiber have been observed to grow into the fiber and act as effective sites for deflecting a debond crack into the fiber).

2.2 WEAK INTERFACES

Two systems have been found in which the bond between the interphase and the fibers is intrinsically weak, with toughnesses sufficiently low that debonding prevents growth of a crack across the interface. One is tin dioxide, which has been shown to provide a diffusion barrier and weak interface between glass or alumina materials and alumina fibers (both polycrystalline and single crystal).^{4,5} However, a limitation of this system is that it could never be exposed to an even slightly reducing environment as the eutectic melting point of the Sn-SnO₂ system is low (1080°C).¹³

The other group of interphases are the rare earth phosphates that form the monazite and xenotime structures. The interfaces between these compounds and various refractory oxides are sufficiently weak to allow debonding^{13,24-26}. This, combined with their phase compatibility, high melting points (many over 2000°C) and corrosion resistance, make them appealing as components of refractory oxide composites. Material combinations for which weak bonding and phase compatibility have been demonstrated (at least in closed systems) include: (1) $\text{LaPO}_4/\text{Al}_2\text{O}_3$, the first monazite-based system for which debonding was observed^{13,26} (provided the

stoichiometry of the LaPO_4 is 1:1, this system has been shown to be phase compatible and morphologically stable for long periods at temperatures at least as high as 1600°C ; (2) LaPO_4 with Y-stabilized zirconia,²⁵ (3) CePO_4 with Ce-stabilized zirconia²⁶; (4) LaPO_4 with mullite²⁷, and (5) YPO_4 with YAG.^{28,29} Very recently a few other ABO_4 structures such as CaWO_4 (scheelite)³⁰ have been proposed as weak interfaces and look promising for lower temperature uses.

2.3 POROUS INTERPHASES OR POROUS MATRIX

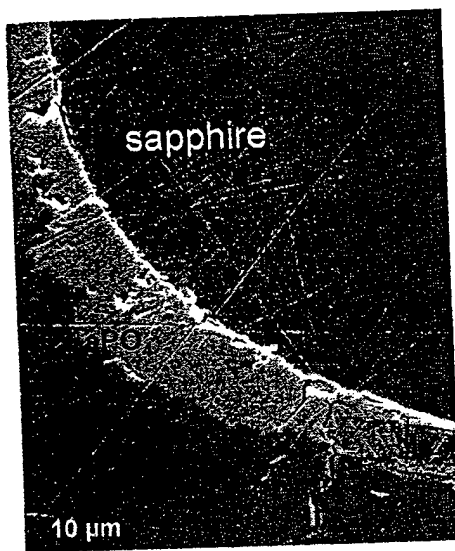
Several research groups are exploring an approach that relies on debonding within a weak fiber coating rather than at an interface, with the weakness being induced by controlled porosity within the coating.^{6,31-35} In this case, the interphase material itself may bond strongly to the matrix and fiber. Examples include porous interphases of ZrO_2 or Al_2O_3 in composites consisting of Al_2O_3 fibers and Al_2O_3 matrix. Although debonding has been demonstrated in such systems, several concerns remain. One is the extent to which fiber strength is degraded by regions of coating that bond strongly to the fiber and by impurities that form other phases which affect this or cause defects in the fibers. Another relates to the roughness of the debonded region and the degree of pull out achievable. Both are in principle controllable to some extent by controlling the size scale and volume fraction of the porosity. However, a limitation of very fine scale porosity is its tendency to coarsen at high temperatures. Some success has been achieved with oxide composites with porous matrices, in which the notion of requiring debonding of individual fibers is abandoned, and instead damage tolerance and notch insensitivity are achieved by splitting within the porous matrix, in regions that are matrix-rich, i.e., between fiber tows in woven composites and in regions with random fluctuations of fiber density in unidirectional composites.^{8,34} Less-catastrophic, wood-like fracture has been observed in such composites (examples include composites with Al_2O_3 fibers and porous mullite, alumina, silicon nitride, or AlPO_4 matrices).

3. Interfacial Debonding

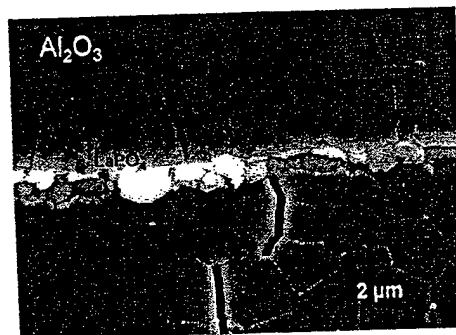
3.1 OBSERVATIONS OF DEBONDING IN LaPO_4 - CONTAINING SYSTEMS

Examples of debonding associated with LaPO_4 in several systems are shown in Fig. 1. The alumina-sapphire system of Fig. 1(a) was fabricated by packing sapphire fibers that had been slurry coated with LaPO_4 in alumina powder and hot pressing at 1400°C . The cracks at the bottom of the micrograph were generated by a Vickers indentation located in the matrix just beneath the field of view. In Fig. 1(b) a thin layer of LaPO_4 sandwiched between polycrystalline alumina shows that debonding occurs even for relatively irregular interfaces that must exist in polycrystalline systems. Fig. 1(c) shows a Vickers indentation in a multilayered composite consisting of alternating layers of LaPO_4 and two-phase alumina/yttria-partially stabilized zirconia. The composite was fabricated by sequential slip casting,

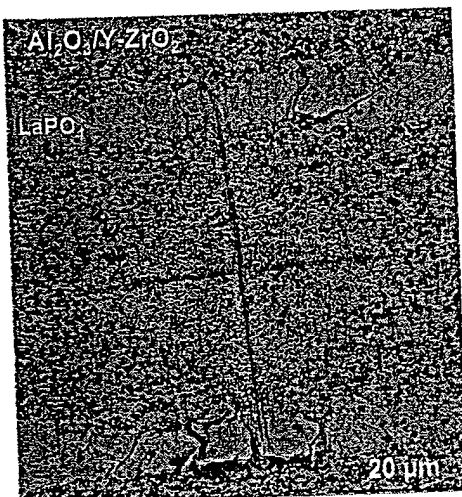
followed by sintering at 1600°C. The LaPO_4 layers are evidently able to contain very severe damage due to indentation.



(a)



(b)



(c)

Fig. 1. Scanning electron micrographs showing: (a) Debonding at LaPO_4 - sapphire interface. Coated sapphire fiber in polycrystalline alumina matrix, hot pressed 1400°C for 1 h. Crack produced by Vickers indentation located below the field of view, from ref. 13. (b) Debonding at thin layer of LaPO_4 in polycrystalline alumina, from ref. 25. (c) Cracking and debonding in layers of LaPO_4 in polycrystalline, diphasic $\text{Al}_2\text{O}_3/\text{Y-ZrO}_2$, from ref. 25.

3.2 MECHANICS OF DEBONDING

A general observation is that cracks are able to pass from alumina or zirconia-based materials into LaPO_4 without causing interfacial debonding. However, cracks growing in the opposite direction cause debonding and are unable to cross the interface. This behavior, which is clearly evident in Figs. 1(a) and (c), is consistent with measured toughnesses and the debonding behavior predicted by the analysis of He and Hutchinson.³⁶ They define a critical value of the ratio of the toughnesses of the interface and the material into which the crack is about to grow (Fig. 2). If the toughness ratio for a particular system falls above the critical value, the cracks grow through the interface, whereas if the toughness ratio falls below the critical value, debonding occurs. The critical value depends on the elastic mismatch parameter, $\alpha = (E'_2 - E'_1)/(E'_2 + E'_1)$, where E'_1 and E'_2 are the plane-strain Young's moduli for the two materials, as shown in Fig. 2.

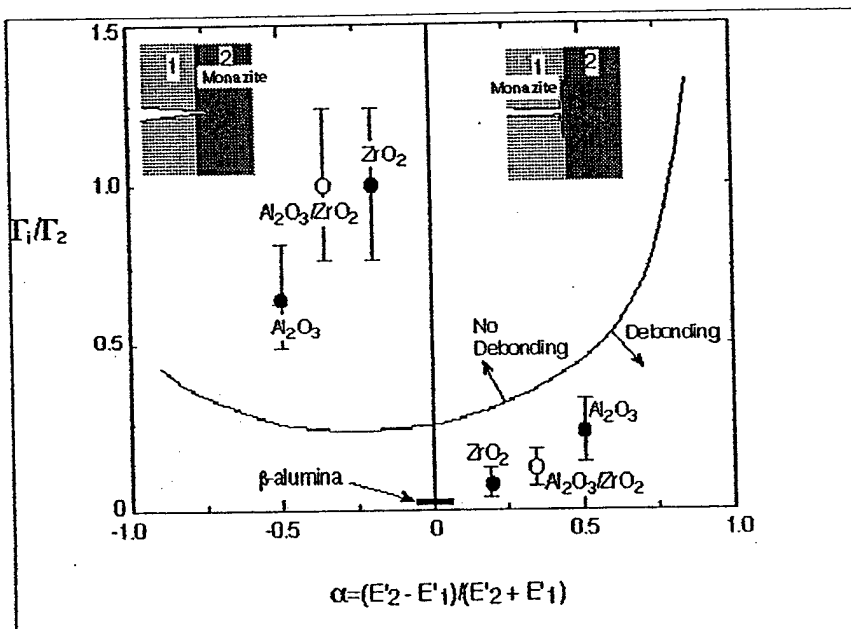


Fig. 2. Comparison of measured fracture toughnesses with the debond criterion of He and Hutchinson,³⁶ from ref. 25.

Measured values of the toughness ratio for various combinations of materials (LaPO_4 with Al_2O_3 , Y-ZrO_2 and $\text{Al}_2\text{O}_3/\text{Y-ZrO}_2$) are shown in Fig. 2. Values on the right half of this figure (i.e., positive α), which fall below the critical curve, correspond to cracks growing from LaPO_4 to the other material, while values to the left (negative α), which fall above the critical curve, correspond to cracks growing from the other material to the LaPO_4 . The measured values used in these calculations are given in Table 1. The results are in agreement with the observed cracking behavior.

Table I - Material Properties

Material	Young's Modulus E (GPa)	Fracture Energy (J/m ²)	Interface Fracture Energy (J/m ²)
LaPO ₄	133	7	
Al ₂ O ₃	400	20	4
Y-ZrO ₂	200	110	7
Al ₂ O ₃ /Y-ZrO ₂ (1:1)	300	80	7

Also shown for comparison in Fig. 2 is an estimated toughness ratio for a β -alumina coating in alumina. The toughnesses in this case were estimated from measurements on single crystal specimens, using the lengths of indentation cracks growing normal and parallel to the weak layers in polished cross sections normal to the weak layers. The toughness ratio estimated in this manner (0.01) is much lower than for the LaPO₄ based systems. The difficulties associated with alignment of the β -alumina grains along the fibers and continued debonding and sliding, have been addressed by others.²¹

A complete analysis of debonding in these systems would also include analysis of the influence of residual stresses, which have the effect of shifting the critical curve in Fig. 2.³⁶ This requires knowledge of component geometry, and is also dependent on the presence of flaws in the layers and interfaces. Nevertheless, qualitative trends can be easily estimated from known thermal expansion coefficients. Since the thermal expansion coefficient of LaPO₄ is almost identical to that of ZrO₂ and higher than that of Al₂O₃, the stresses parallel to a LaPO₄ coating in alumina-containing systems are tensile in the LaPO₄ and compressive in the other material. Therefore, the tendency for a crack to penetrate the interface when growing towards the LaPO₄ layer is enhanced (i.e. the critical curve in Fig. 2 for $\alpha < 0$ is lowered), whereas the tendency for debonding is enhanced when the crack approaches the interface from within the LaPO₄ layer (i.e., the critical curve for $\alpha > 0$ is raised).

4. Composites of LaPO₄ and Al₂O₃

Several research groups are developing methods for coating fibers with LaPO₄ using CVD, PVD and liquid precursors. Here we present composite fabrication studies using aqueous solution precursors with polycrystalline alumina tow fibers.

Processing temperatures for composites containing currently available polycrystalline alumina fibers are limited to $< 1200^\circ\text{C}$ in order to avoid grain growth and strength loss in the fibers. After heat treatments to these temperatures, for times up to several hours, various monazite precursors have been found to sinter to fine grained (~ 100 to 300 nm) polycrystalline films, as shown in Fig. 3(a).

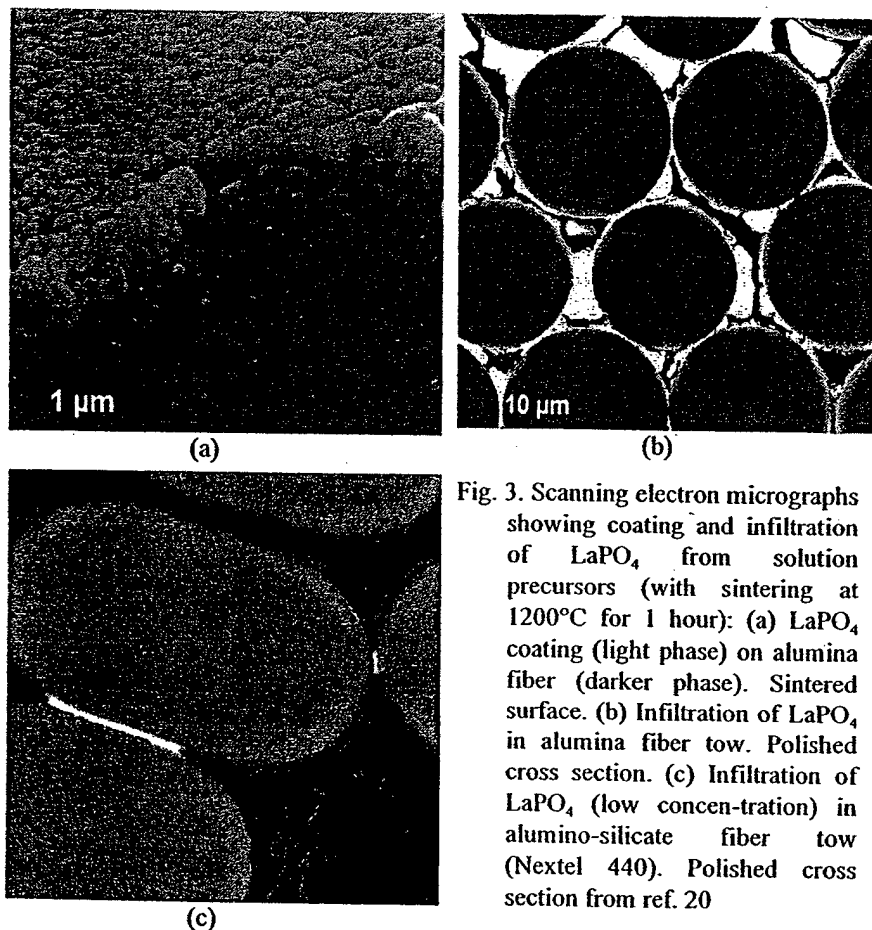


Fig. 3. Scanning electron micrographs showing coating and infiltration of LaPO_4 from solution precursors (with sintering at 1200°C for 1 hour): (a) LaPO_4 coating (light phase) on alumina fiber (darker phase). Sintered surface. (b) Infiltration of LaPO_4 in alumina fiber tow. Polished cross section. (c) Infiltration of LaPO_4 (low concentration) in alumino-silicate fiber tow (Nextel 440). Polished cross section from ref. 20

When infiltrating fiber tows, the amount of monazite within the tows can be varied over a wide range by controlling the concentration of the solution and the infiltration conditions (Fig. 3(b)). However, the fibers are invariably separated by a layer of monazite after heat treatment, even when the concentration of monazite is very low. An example is shown in Fig. 3(c): monazite film thicknesses as small as 50 nm have been observed, whereas examples of touching fibers could not be found.

Fiber tows and fabrics (Nextel 610 from 3M Company) have also been infiltrated with slurries consisting of dispersed alumina (99.99% α -alumina, AKP30, from Sumitomo) and monazite precursor solutions. The resulting two-phase alumina-monazite matrix, after sintering at 1200°C for 1 h, consists of separate grains of alumina and monazite, both with dimensions smaller than 500 nm, with fine scale porosity between the grains (Fig. 4(a)). The alumina grains in the matrix

are apparently always separated from the fibers by monazite, in the same manner as the fibers are separated from each other, as in Fig. 4(b).

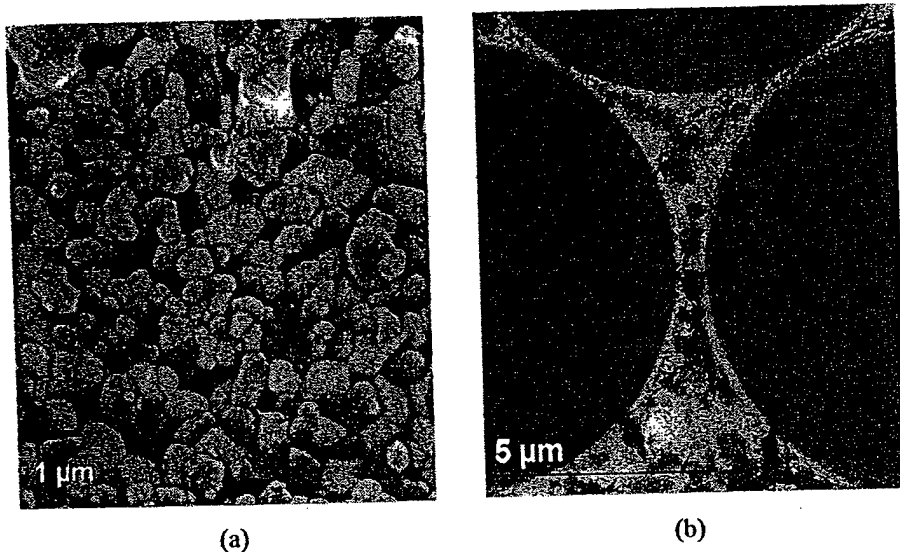
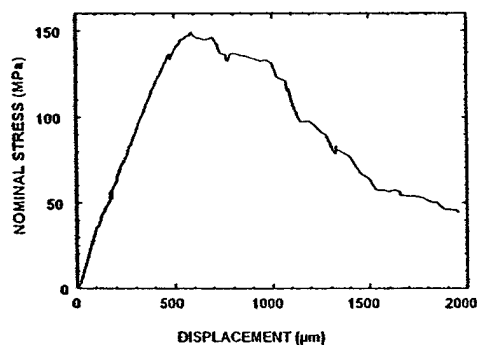


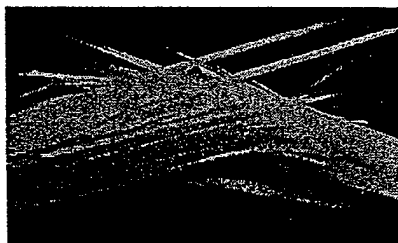
Fig. 4. Scanning electron micrographs from composite containing alumina fibers and alumina-monazite matrix (back-scattered electron images: lighter phase is monazite): (a) As-sintered surface of matrix and (b) Polished cross-section from ref. 20

Unidirectional composites with the alumina-monazite matrix have been formed by filament winding, with the alumina fiber tows passing through the slurry immediately before being wound onto a drum. After drying, the composite was sintered at 1200°C in air for 1 h. Beams of the composite (5x4x60 mm) were loaded in flexure using four-point loading spans of 50 mm and 5 mm. The resulting load-deflection curve is non-linear with a gradual load drop beyond the peak (Fig. 5(a)). The nominal tensile stress corresponding to the peak load in Fig. 5(a) is, within a rough estimate, consistent with the tensile strength having been dictated by the fiber bundle strength: the fiber volume fraction is approximately 10%, while the early experimental batch of Nextel 610 fiber bundle strength measured independently was approximately 1.5 Gpa, strengths of current production fibers are higher.^{37,38}

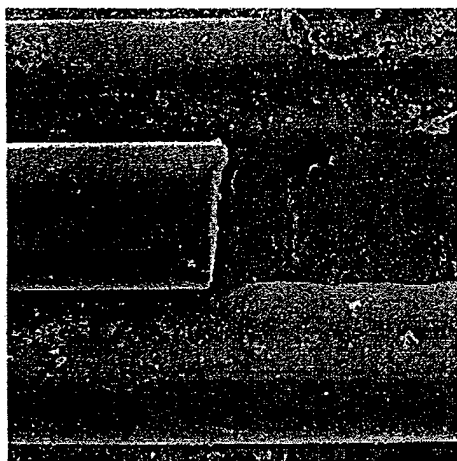
The damage in the composite of Fig. 5 involved extensive cracking and chipping of the matrix, leaving a fibrous, brush-like damage zone. The beam remained intact even after the load had dropped to less than 10% of the peak load (Fig. 5(b)). Debonding and sliding of individual fibers was evident throughout the damage zone (Fig. 5(c)).



(a)



(b)



(c)

Fig. 5. (a) Nominal stress-strain response of alumina-monazite matrix composite in flexure; (b) Test specimen from (a) and (c) Scanning electron micrograph from (b) showing fiber debonding and sliding from ref. 25.

5. Machinability

All the mixtures of refractory oxides, Al_2O_3 , ZrO_2 and mullite with the rare-earth phosphates LaPO_4 and CePO_4 could be drilled using tungsten-carbide drills as anticipated. With less phosphate, drilling forces increased and drilling rates decreased for a fixed load. A clear increase in drilling rate with volume fraction of CePO_4 was evident for the $\text{Ce-ZrO}_2/\text{CePO}_4$ composites. For a given volume fraction of rare-earth phosphate, the ease of drilling is greatest in the $\text{Ce-ZrO}_2/\text{CePO}_4$ system, intermediate in the alumina/ LaPO_4 system, and least in the mullite/ LaPO_4 system. Most of the results showed a nonlinear dependence of drilling rate on force.

In all of the materials containing CePO_4 and LaPO_4 , departure from a linear Hertzian response occurs at pressures substantially below the Vickers hardness and is similar to previously published measurements on ceramic materials, including machinable glass ceramics, that experience distributed damage,³⁹⁻⁴³ with a permanent

depression left at the contact site similar to observations of Lawn and co-workers^{42,43} in materials that contain heterogeneities and weak interphase boundaries.

6. Discussion

Naturally the basic question arises as to why monazite bonds so weakly to some other oxides. At this early stage, we may offer only qualitative conjectures. Firstly, inspection of a model of the monazite crystal structure indicates that it has open irregular oxygen crystal planes, which show no readily apparent epitaxial relationship with those of the nearly close-packed oxygens of most conventional oxides; interfaces with good fits seem to be ruled out.

Secondly, we may resort to a (novel?) use of Pauling's second crystal rule. In the bulk all the oxygens in monazite are bonded to 1 phosphorus and 2 or 3 lanthanums. Because of their higher polarizability, which can reduce the surface free energy, we speculate that oxygens are likely to terminate the surface, remaining bonded to the 1 phosphorus with a bond valence of $5/4$ (valence of phosphorus divided by coordination). With likely attachment also to at least 1 lanthanum, a further bond valence of $3/9$ is contributed. This adds up to 1.58, a substantial portion of the desired valence bond of 2. In reality, bonds near the surface would shorten to increase the valence bond further and attachment to another lanthanum, which sometimes appears possible from the crystal structure, would essentially almost satisfy the oxygen requirement.

We conjecture that the weak bonding across the interface to some oxides may be related to the particular crystal structure, with a lack of epitaxy and the presence of the high valent ion, P^{5+} , with a low coordination of 4, which alone can satisfy a large portion of the valence bond to interface oxygen from within the monazite. The fact that xenotime and scheelite seem also to work may support this idea.

7. Conclusions

Several potentially viable approaches exist for introducing damage-tolerant behavior in oxide composites: fiber coatings of monazite, fiber coatings of layered oxides, or porous coatings (or porous matrix). All have been shown to allow the necessary fiber debonding; while damage-tolerant fiber reinforced composites have been demonstrated in monazite-alumina systems and in several porous matrix systems. Monazite-based systems are especially appealing in view of their long-term, high-temperature microstructural stability. Such composites are at an early stage of development, and advances are needed in fiber coating methods, development of improved oxide fibers (especially creep resistance) and development of methods of matrix fabrication.

Evidence for the possibility that, in two-phase mixtures of oxides and rare earth phosphates, easy material removal should occur by formation and linking of cracks at the weak interfaces between the two phases, and that this should lead to machinability, was found. Alumina, zirconia, and mullite can be rendered "machinable" by the addition of finely dispersed rare-earth phosphates, in amounts at least as small as 20 volume percent. But, as nominally single-phase LaPO_4 was also found to be machinable, interfacial debonding cannot be the only mechanism involved. Another possible mechanism is that associated with the deformation observed within individual grains of LaPO_4 beneath Hertzian contacts.

Acknowledgments

Work on α -alumina/monazite and the initial discovery of machinability was funded by the US Office Naval Research, Contract N00014-95-C-0157, monitored by Dr. S. Fishman. Work on zirconia/monazite and later work on the machinability was funded by the Air Force Office of Scientific Research under contract F49620-96-C-0026 monitored by Dr. A. Pechenik.

References

1. P.E.D. Morgan and D.B. Marshall, "Functional Interfaces for Oxide/Oxide Composites," *Mat. Sci. Eng.*, **A162** [1-2] 15-25 (1993).
2. M.K. Cinibulk, "Magnetoplumbite Compounds as a Fiber Coating for Oxide-Oxide Composites," *Ceram. Eng. and Sci. Proc.*, **15** [5] 721-28 (1994).
3. J.B. Davis, J.P.A. Lofvander, A.G. Evans, E. Bischoff and M.L. Emiliani, "Fiber Coating Concepts for Brittle Matrix Composites," *J. Am. Ceram. Soc.* **76** [5] 249-57 (1993).
4. A. Maheshwari, K.K. Chawla and T.A. Michalske, "Behavior of Interface in Alumina/glass Composite," *Mater. Sci. Eng.* **A107** 269-76 (1989).
5. R. Venkatesh and K.K. Chawla, "Effect of Interfacial Roughness on Fiber Pullout in Alumina/ SnO_2 /glass Composites," *J. Mat. Sci. Lett.*, **11** 650-52 (1992).
6. M.H. Jasowiak, J.I. Eldridge, J.B. Hurst and J.A. Setlock, "Interfacial Coatings for Sapphire/ Al_2O_3 ," in *High Temp Review 1991* NASA Conference Publication 10082 (1991) p. 84.
7. R.F. Cooper and P.C. Hall, "Reactions Between Synthetic Mica and Simple Oxide Compounds with Application to Oxidation-Resistant Ceramic Composite," *J. Am. Ceram. Soc.* **76** [5] 1265-73 (1993).
8. W.C. Tu, F.F. Lange and A.G. Evans, "A Novel, Damage-Tolerant Ceramic Composite (Synthetic High Temperature Wood)," *J. Am. Ceram. Soc.* **79** 417-24 (1996).

9. P.W. Brown, "MOCVD of Beta-Alumina," *Ceram. Eng. and Sci. Proc.*, **15** [5] 729-30 (1994).
10. Y. Hikichi and T. Nomura, "Melting Temperatures of Monazite and Xenotime", *J. Am. Ceram. Soc.*, **70** [1] C-252-53 (1987).
11. P.E.D. Morgan and R.M. Housley, "Some Effects of Eutectic Liquid Under Reducing Conditions in the Alumina-Tin Dioxide-Tin Composite System," *J. Am. Ceram. Soc.*, **78** 263-65 (1995).
12. D.F. Mullica, W.O. Milligan, D.A. Grossie, G.W. Beall and L.A. Boatner, "Ninefold Coordination in LaPO_4 : Pentagonal Interpenetrating Tetrahedral Polyhedron," *Inorg. Chim. Acta*, **95** 231-36 (1984).
13. P.E.D. Morgan, and D.B. Marshall, "Ceramic Composites of Monazite and Alumina", *J. Am. Ceram. Soc.* **78** 1553 - 63 (1995).
14. W. Jungowska and T. Znamierowska, "Phase Equilibria in a Portion of the System La_2O_3 - K_2O - P_2O_5 Rich in P_2O_5 ," *Mat. Chem. & Phys.*, **24** 487-94 (1990).
15. W. Jungowska and T. Znamierowska, "The System LaPO_4 - KPO_3 - $\text{La}(\text{PO}_3)_3$," *Mat. Chem. & Phys.*, **27** 109-16 (1991).
16. W. Jungowska and T. Znamierowska, "The System LaPO_4 - $\text{K}_4\text{P}_2\text{O}_7$ - KPO_3 ," *J. Therm. Anal.*, **39** 715-20 (1993).
17. Phase Diagrams for Ceramists, publ. by NIST/Am. Ceram. Soc.
18. L.A. Boatner and B.C. Sales, "Monazite", chapter 8, pp. 495-563 in *Radioactive Waste Forms for the Future*, Eds W. Lutze and R. C. Ewing, North-Holland, New York 1988.
19. Y. Hikichi, T. Nomura, Y. Tanimura and S. Suzuki, "Sintering and Properties of Monazite-type CePO_4 ," *J. Am. Ceram. Soc.*, **73** [12] 3594-96 (1990).
20. P.E.D. Morgan and D.B. Marshall, "Composites of Monazite and Alumina for High Temperature Oxidizing Environments", *J. Am. Ceram. Soc.* in press.
21. M.K. Cinibulk, R.S. Hay, "Textured magnetoplumbite fiber-matrix interphase derived from sol-gel fiber coatings", *J. Am. Ceram. Soc.* **79** 1233-46 (1996).
22. D.B. Marshall, P.E.D. Morgan and R.M. Housley, *J. Am. Ceram. Soc.* (in preparation).
23. M. K. Cinibulk, "Synthesis and characterization of sol-gel derived lanthanum hexaaluminate powders and films", *J. Mater. Res.* **10** 71-76 (1995).
24. M.H. Lewis, M.G. Cain, P. Doleman, A.G. Razzell and J. Gent, "Development of Interfaces in Oxide and Silicate-Matrix Composites", *Ceramic Transactions* **58** 41-52 (1995).
25. D.B. Marshall, P.E.D. Morgan and R.M. Housley, "Debonding in Multilayered Composites of Zirconia and LaPO_4 ", *J. Am. Ceram. Soc.* **80** 1677-83 (1997)

26. P.E.D. Morgan, D.B. Marshall and R.M. Housley, "High Temperature Stability of Monazite-Alumina Composites", *J. Mat. Sci. Eng.* A195 215 - 22 (1995).
27. J. B. Davis, P.E.D. Morgan, D.B. Marshall, R.M. Housley, "Machinable Ceramics Containing Rare Earth Phosphates", *J. Am. Ceram. Soc.* (in press).
28. D.-H. Kuo and W.M. Kriven, "Chemical Stability, Microstructure, and Mechanical Behavior of LaPO_4 -Containing Ceramics" *Materials Science and Engineering* A210 123-34 (1996).
29. D.-H. Kuo and W.M. Kriven, "Characterization of Yttrium Phosphate and a Yttrium Phosphate/Yttrium Aluminate Laminate", *J. Am. Ceram. Soc.* 78 3121-24 (1995).
30. R.W. Goettler, S. Sambasivan and V.P. Dravid, "Isotropic Complex Oxides as Fiber Coatings for Oxide-Oxide CFCC," presented at the 21st Annual Cocoa Beach Conf. on Composites, etc. Cocoa Beach, FL., Jan. 12-16, 1997, in press: *Ceram. Eng. Sci. Proc.*
31. T. Mah, K. Keller and T.A. Parthasarathy, J. Guth, "Fugitive Interface Coating In Oxide-Oxide Composites: A Viability Study", *Ceram. Eng. Sci. Proc.* 12 1802-15 (1991).
32. J.B. Davis, J.P.A. Lofvander, A.G. Evans, E. Bischoff and M.L. Emiliani, "Fiber Coating Concepts For Brittle Matrix Composites", *J. Am. Ceram. Soc.* 76 1249-57 (1993).
33. J.B. Davis, J. Yang and A.G. Evans, "Effects of Composite Processing on the Strength of Sapphire Fiber-reinforced Composites", *Acta Met.* 43 259-68 (1995).
34. F.F. Lange, W.-C. Tu and A. G. Evans, "Processing of Damage-tolerant, Oxidation-resistant, Ceramic Matrix Composites by a Precursor Infiltration and Pyrolysis Method", *Mater. Sci. Eng.* A195 145-50 (1995).
35. W.P. Keith and K.T. Kedward, "Shear Damage Mechanisms in a Woven, Nicalon-Reinforced Ceramic Matrix Composite", *J. Am. Ceram. Soc.* 80 357-64 (1997).
36. M.-Y. He and J. W. Hutchinson, "Crack Deflection at an Interface Between Dissimilar Materials", *Int. J. Solids Struct.* 25 1053-67 (1989).
37. T.L. Tompkins, "Ceramic Oxide Fibers: Building Blocks for New Applications", *Ceramic Industry*, 144 45-50 (1995).
38. Wilson, D.C. Lueneburg and S.L. Lieder, "High Temperature Properties of Nextel 610 alumina-based nanocomposite fibers", *Ceram. Eng. Sci. Proc.* 14 609-21 (1993).
39. F. Guiberteau, N. P. Padture and B. R. Lawn, "Effect of Grain Size on Hertzian Contact in Alumina," *J. Am. Ceram. Soc.*, 77[7] 1825-31 (1994).
40. H. Cai, M. A. S. Kalceff and B. R. Lawn, "Deformation and Fracture of Mica-Containing Glass-Ceramics in Hertzian Contacts," *J. Materials Research*, 9[3] 762-70 (1994).

41. H. H. K. Xu, L. Wei, N. P. Padture and B. R. Lawn, "Effect of Microstructural Coarsening on Hertzian Contact Damage in Silicon Nitride," *J. Mater. Sci.*, in press (1996).
42. N. P. Padture and B. R. Lawn, "Toughness Properties of a Silicon Carbide With an In-Situ-Induced Heterogeneous Grain Structure," *J. Am. Ceram. Soc.*, (in press).
43. B. R. Lawn, N. P. Padture, H. Cai and F. Guiberteau, "Making Ceramics "Ductile"," *Science*, 263 1114-16 (1994).

7.0 Recent Advances in Oxide-Oxide Composite Technology

by Evans, A. G., Marshall, D. B., Zok, F., Levi, C.

The following section is a paper published in Advanced Composite Materials, 8[N1]17-23 (1999)

Recent advances in oxide–oxide composite technology

A. G. EVANS¹, D. B. MARSHALL², F. ZOK³ and C. LEVI³

¹ *Division of Engineering and Applied Sciences, Harvard University, Cambridge, MA 02138, USA*

² *Rockwell International, Thousand Oaks, CA 93610, USA*

³ *Materials, University of California, Santa Barbara, CA 93106, USA*

1. BACKGROUND

It is now well-documented that SiC and C-based ceramic matrix composites (CMCs) are susceptible to embrittlement at intermediate temperatures (700–900°C): the so called 'Pest Effect' (Fig. 1). It is caused by the ingress of moist air through cracks that form upon thermomechanical fatigue (TMF). The consequence is relatively short life above the matrix cracking stress, σ_0 , when the application requires cycling through the pest temperature. There is also evidence that even when operating below σ_0 , overloads can introduce damage that results in life-limiting pest failures. While these problems do not adversely affect performance in either short life application (e.g. in rocket engines) or in space, they substantially limit applications when long life is needed, as in aero and power turbines, etc. Accordingly, for these applications, all-oxide CMCs are being explored.

A substantial technology base generated on SiC-based CMCs provides general benchmarks for assessing the progress being made with oxide materials. The most notable are as follows:

- (i) Thermostructural robustness requires that the material be capable of sustaining considerable inelastic strain locally in the vicinity of strain concentrations, such as holes/notches. These strains redistribute stresses and contribute to desirable CMC notch performance, comparable to that for metals (and much superior to monolithic ceramics, Fig. 2). Inelastic strains in the range 0.5 to 1% achieve this objective (Fig. 2).
- (ii) The inelastic strain is governed by a combination of matrix cracking and frictional slip at the fiber/matrix interfaces. The friction is, in turn, governed by the fiber roughness and the shear properties of the fiber coating.

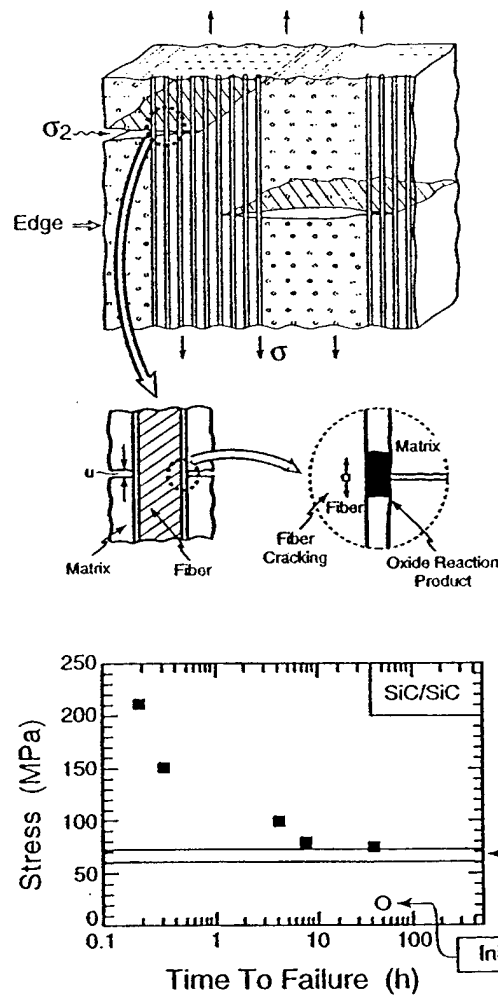


Figure 1. The oxidation embrittlement problem in SiC-based CMCs.

- (iii) Absent environmental embrittlement, the fatigue threshold is a substantial fraction β on the ultimate tensile strength (UTS): typically, $\beta = 0.7-0.8$. Fatigue above the threshold is attributed to changes in internal friction at the fiber/matrix interface.
- (iv) The low interlaminar properties of 2D woven/laminated CMCs limit design flexibility and cause degradation both at attachments and in through-thickness thermal gradients.

2. OXIDE CMC MATERIALS

Two basic approaches have been used to create damage-tolerant, oxide CMCs. One uses a porous matrix with porosity designed to provide a compromise between in-plane damage tolerance and interlaminar strength. The other uses a monazite fiber coating which can be designed to give debonding with frictional slip at the fiber/matrix interface.

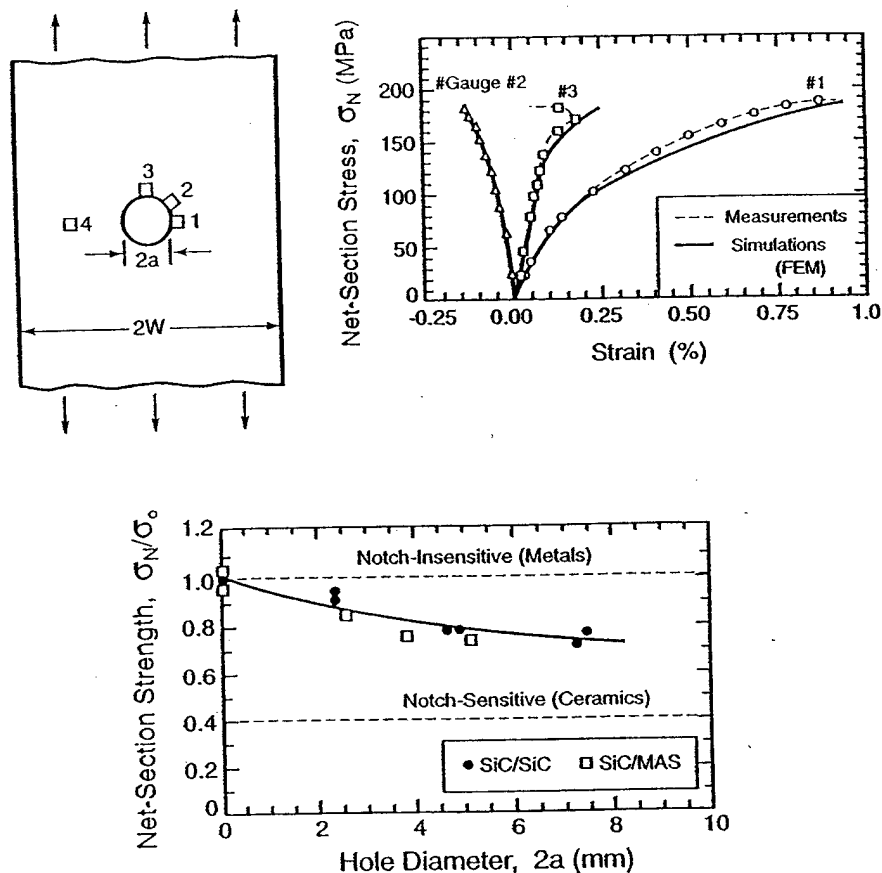


Figure 2. The inelastic deformation and notch tolerance of SiC-based CMCs.

2.1. Porous matrix materials

The matrix microstructure has been designed to have a sufficiently low toughness to enable crack deflection through the matrix while maintaining enough strength for adequate off-axis and interlaminar properties. These seemingly contradictory requirements are achievable by incorporating a controlled amount of fine, uniformly distributed porosity. Acceptable matrix performance dictates a stable and well bonded particle network with substantial void space, $\sim 30\%$, on a scale comparable with the interparticle spacing. Fine matrix particles are preferred to enhance packing density and uniformity within the fiber preform, as well as the nominal strength of the matrix. However, fine particles also reduce the stability of the matrix against densification during processing and service, promoting the formation of undesirable flaws under the constraint imposed by the surrounding fibers.

Mullite emerges as an attractive matrix material owing to its excellent creep resistance, low modulus and, sluggish sintering kinetics below $\sim 1300^\circ\text{C}$. The latter suggests adequate microstructural stability for applications in the gas turbine engine, where initial target wall temperatures are in the range ~ 1000 to $\sim 1200^\circ\text{C}$. However, it presents a challenge in processing. That is, temperatures above $\sim 1300^\circ\text{C}$ are required to achieve the requisite bonding between the matrix particles.

Yet most commercial oxide fibers are susceptible to microstructural degradation at these temperatures.

The matrix design concept is depicted in Fig. 3. Relatively large ($\sim 1 \mu\text{m}$) mullite particles are packed between and within tows to form touching, non-shrinking network. Alumina particles that fit within the void spaces of this network ($\sim 200 \text{ nm}$) are added in a proportion limited primarily by the requisite levels of porosity. Since sub-micron alumina sinters readily above 800°C , the fine particles form bridges between the larger mullite particles, as well as between the mullite particles and the fibers, at processing temperatures which minimize fiber degradation. Interparticle voids may locally open owing to the sintering, but the overall matrix is constrained from shrinking by the rigid mullite network. The matrix is further strengthened by adding material to the alumina 'bridges' using precursor impregnation and pyrolysis.

The damage tolerance of these materials is manifest in their off-axis tensile stress/strain behavior and in the notch performance. That is, they exhibit considerable inelastic strain capability in the $\pm 45^\circ$ orientation (Fig. 3). Accordingly, even though they are essentially linear to failure in the $0/90^\circ$ orientation, these materials exhibit high in-plane damage tolerance. In this regard they are 'fiber dominated' materials, analogous to C-C and polymer matrix composites.

These materials are limited in two ways. (i) They only retain long term damage tolerant behavior up to about 1200°C . At higher temperatures, sintering of the matrix to the fibers causes embrittlement. (ii) The transverse properties are marginal

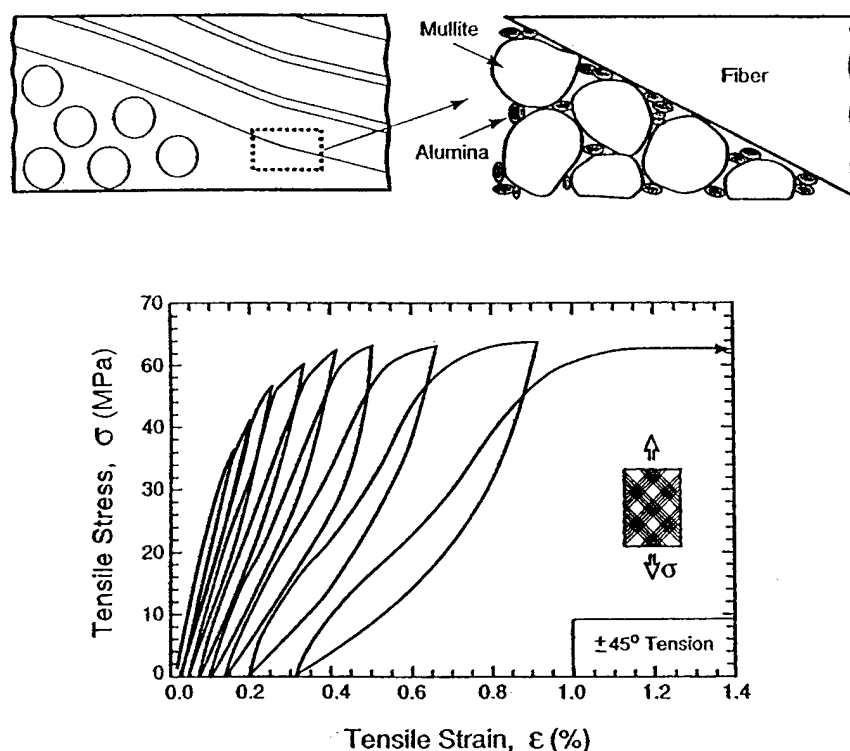


Figure 3. The characteristics of oxide CMCs with a porous matrix.

because of the matrix porosity. A 3D woven architecture is needed to achieve adequate design flexibility.

2.2. Monazite fiber coatings

Monazite is thermochemically stable with Al_2O_3 and mullite and moreover, has a low interface fracture toughness. Accordingly, it has two of the three characteristics required from a fiber coating for an Al_2O_3 fiber-reinforced oxide CMC. By using a combination of mullite and monazite as a matrix, the compliance of the circumventing material provides the third characteristic; namely, the requisite frictional slip response between the fibers and matrix. All oxide CMCs of this type exhibit notch properties comparable to SiC-based CMCs (Fig. 4), while also achieving TMF longevity by eliminating the 'pest' degradation phenomenon. These are the most promising CMCs for long life application.

From an application perspective, oxide CMCs have the disadvantage relative to SiC materials that their thermal conductivity is appreciably lower. Accordingly, in high thermal flux conditions, the material temperatures are higher, placing greater demands on the creep and creep rupture performance. At this stage, these are the limiting properties of oxide CMCs. Efforts to increase the creep resistance by doping with rare earths (notably Y_2O_3) and by using nanoparticles are at the research forefront.

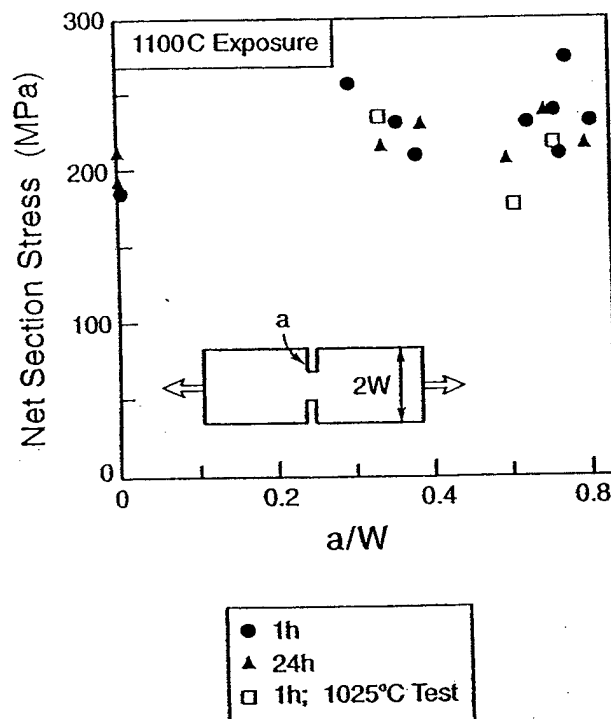


Figure 4. The performance of oxide CMCs with a monazite-based fiber/matrix interface.

3. INTERLAMINAR PERFORMANCE

The inferior interlaminar properties of 2D woven and laminated CMCs pose limitations on design flexibility and hence, on their implementation. The problems are manifest as delaminations that occur at thermomechanically loaded attachments as well as on plane sections subject to through thickness thermal gradients (Fig. 5). The interlaminar properties are controlled by the matrix material, which is designed to have low toughness to enable the fiber/matrix debonding and slip needed for in-plane damage tolerance. They are also subject to weakest link size scaling associated with manufacturing flaws, causing large components to be particularly susceptible to these problems.

The only solution appears to comprise 3D woven architectures: the same solution used for structural C-C composites. The weaving technology is under development for oxide fibers. Its viability has already been demonstrated.

4. SUMMARY

For applications requiring long life, oxide composites comprising Al_2O_3 /mullite fibers with a monazite/mullite matrix have greatest applicability. Architectures

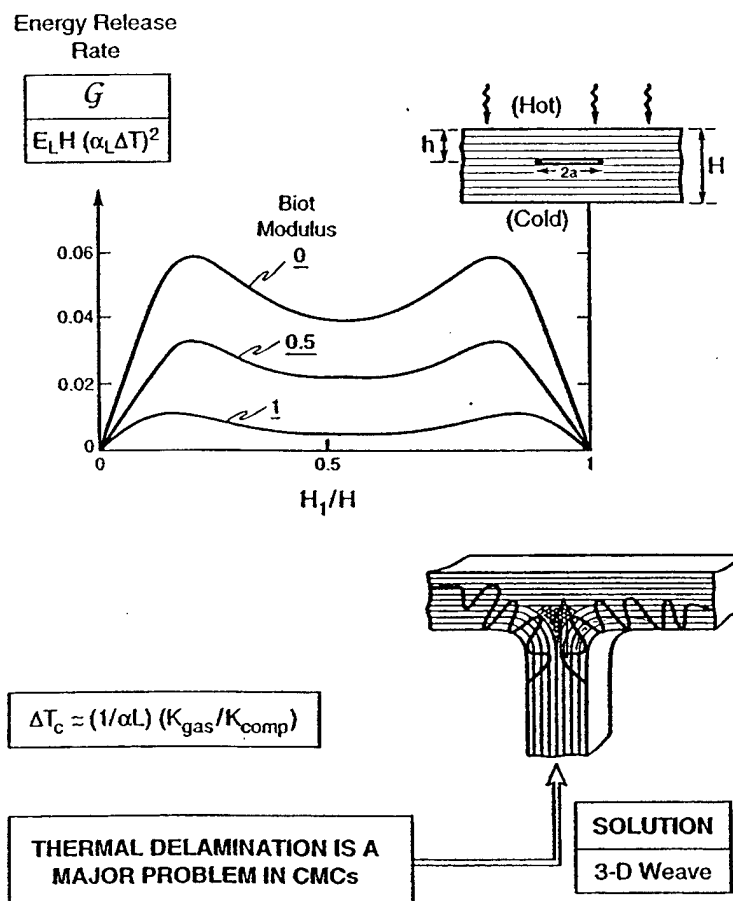


Figure 5. Delamination problems in 2D woven CMCs.

based on local 3D weaving are needed to obviate delamination sensitivity, particularly at joints/attachments and in regions subject to high thermal flux. These materials are presently creep/rupture limited. Research priorities include approaches for enhancing the creep resistance by using dopants or nanoparticles.

For either short life or space applications, C-SiC materials are often preferred because of their high-temperature capability at low oxygen pressures and their relatively high thermal conductivity.

REFERENCES

1. Ceramic Fibers and Coatings. Advanced materials for the twenty-first century, National Materials Advisory Board, National Research Council, Publication NMAB-494, Washington, DC (1998).
2. J. D. French, J. Zhao, M. P. Harmer, G. A. Miller and G. M. Chan, *J. Amer. Ceram. Soc.* **77**, 2857-2866 (1994).
3. T. J. Lu and J. W. Hutchinson, *J. Amer. Ceram. Soc.* **78**, 261 (1995).
4. P. E. D. Morgan and D. B. Marshall, *J. Amer. Ceram. Soc.* **78**, 1553-1563 (1995).
5. P. E. D. Morgan and D. B. Marshall, US Patent No. 5,514,474, May 7 (1996).
6. T. A. Ohji, T. Nakahira, T. Hirano and K. Niihara, *J. Amer. Ceram. Soc.* **77**, 3259-3262 (1994).
7. F. E. Heredia, M. Y. He and A. G. Evans, *Composites Part A* **27A**, 1157-1167 (1996).
8. F. E. Heredia, J. C. McNulty, F. W. Zok and A. G. Evans, *J. Amer. Ceram. Soc.* **78** (8), 2097-2100 (1995).
9. C. G. Levi, J. Y. Yang, B. J. Dalgleish, F. W. Zok and A. G. Evans, *J. Amer. Ceram. Soc.* **78**, 2077 (1998).
10. T. E. Steyer, F. W. Zok and D. P. Walls, *J. Amer. Ceram. Soc.* **78**, 2140 (1998).



8.0 Machinable Ceramics Containing Rare-Earth Phosphates

by Davis, J.B., Marshall, D.B., Housley, R. M., and Morgan, P.E.D.

The following section is a paper published in J. Amer. Ceram. Soc. 81[8] 2169-75 (1998)



Machinable Ceramics Containing Rare-Earth Phosphates

Janet B. Davis,* David B. Marshall,* Robert M. Housley,* and Peter E. D. Morgan*

Rockwell Science Center, Thousand Oaks, California 91360

Two-phase composites consisting of LaPO_4 or CePO_4 and alumina, mullite, or zirconia were found to be machinable; i.e., they can be cut and drilled using conventional tungsten carbide metal-working tools. Single-phase LaPO_4 was also machinable. Measurements of drilling rates, grinding rates, and normal forces are used to compare the ease of machining in these materials and in a conventional machinable glass-ceramic material, and to provide preliminary information on the relation between microstructure and machining properties. In Hertzian contact experiments these materials showed extensive nonlinear behavior associated with a damage zone beneath the contact site, similar to other machinable ceramics. Mechanisms of material removal are discussed.

I. Introduction

MACHINABLE glass-ceramics, consisting of finely dispersed mica platelets in a glass matrix,^{1,2} can be cut and drilled using conventional metal-working tools. The ease of cutting derives from the cleavage of the mica crystals beneath the cutting tool, and material removal by linking of the microcracks. These materials are used in a variety of applications requiring their high-temperature properties, high hardness, electrical or thermal insulation, or dielectric properties, combined with the convenience of machining. However, their high-temperature use is limited by softening of the glass phase or coarsening of the crystallites, usually at temperatures above about 800°C.

Attempts have been made to develop analogous, more refractory systems. Barsoum *et al.*³ showed that Ti_3SiC_2 , consisting of large, plate-shaped, easily cleaved grains, could be drilled and tapped using high-speed steel tools. Padture *et al.*⁴ showed that material removal rates during diamond grinding and drilling of silicon carbide could be substantially increased by incorporating elongated grains, weak interphase boundaries, and high internal stresses into the microstructure. The microstructure consisted of plate-shaped SiC grains with a second phase of yttrium aluminum garnet with relatively weak interphase bonding. Machinability has also been reported in very fine-grained silicon carbide containing porosity and free carbon (Tanimoto *et al.*⁵).

In this paper we report on the fabrication and preliminary testing of another potential class of machinable ceramics, based on two-phase mixtures of refractory oxides (e.g., Al_2O_3 , ZrO_2 , mullite) and rare-earth phosphates (e.g., LaPO_4 , CePO_4). Recent studies have shown that the bonding between these phosphates and oxides is weak.⁶⁻⁸ The rationale for designing these materials as machinable ceramics was that, in a fully dense, fine-grained, two-phase mixture, easy material removal should occur by formation and linking of cracks at the weak interfaces

between the two phases. These materials are all stable to very high temperatures in oxidizing environments (>1600°C)⁷ and offer the potential to tailor microstructures with ranges of hardness, elastic properties, and thermal conductivity beyond the ranges achievable with other machinable ceramics.

II. Experimental Procedure

Two-phase composites consisting of mullite ($3\text{Al}_2\text{O}_3 \cdot 2\text{SiO}_2$) with LaPO_4 , alumina with LaPO_4 , and Ce-ZrO_2 with CePO_4 were fabricated using several techniques. For the mullite/ LaPO_4 composite, an aqueous slurry was prepared with powders of mullite (from Baikowski) and rhabdophane (hydrated $\text{LaPO}_4 \cdot 0.5\text{H}_2\text{O}$ synthesized in our laboratory) in the approximate ratio 4:1. The slurry was mixed ultrasonically, consolidated into a disk of 50 mm diameter and 5 mm thickness by pressure filtration, dried, packed in alumina powder, and then hot-pressed in graphite dies in nitrogen for 1 h at 1500°C.

The $\text{Ce-ZrO}_2/\text{CePO}_4$ composites were fabricated using colloidal consolidation and sintering. Aqueous slurries of Ce-ZrO_2 powder (Tosoh, 12-mol%- CeO_2 -doped ZrO_2) and CePO_4 (All Chemie Ltd.) were dispersed at pH 2, mixed in several predetermined proportions (1:3, 1:1, and 3:1), and consolidated into disks of 50 mm diameter and 10 mm thickness by pressure filtration. After drying, the disks were cold isostatically pressed, then sintered for 2 h at 1600°C in air to greater than 98% of their theoretical densities.

The alumina/ LaPO_4 composite was fabricated by reactive hot pressing, using powders of monoaluminum phosphate (Albright & Wilson Americas), lanthanum carbonate (Alfa Aesar Chemicals), and high-purity alumina (Sumitomo AKP-30). The powders were ball-milled in an aqueous slurry for approximately 24 h, dried, calcined, and hot-pressed at 1400°C for 1 h, giving a composite consisting of alumina and LaPO_4 in the approximate ratio 3:7.

The "machinability" of each composite was tested and compared with other materials using tungsten carbide drills and a diamond grinding wheel as shown schematically in Fig. 1. The drilling tests were done using a standard drill press operating at 450 rpm, with a drop of aqueous based cutting fluid (South Bay Technologies Inc.) placed at the drill tip at the beginning of each run. The drill bits were shaped as in Fig. 1(a), with a uniform section of 1 mm diameter within the first 1 mm from the end, and increasing diameter beyond this section. The composite specimens were mounted on a load cell (Kistler) and tested by manually applying a constant normal force to the drill, while measuring the times taken to drill holes of fixed depth (~1 mm). Two sets of drilling rates (rate of change in hole depth) were obtained in this manner for each material. In the first, a series of holes were drilled at a fixed load of 50 N to investigate the rate of drill wear. In the second set, drilling rates were measured at several different drilling forces. A new drill bit was used at the beginning of each set for each material to avoid systematic effects due to wear of the drill.

The diamond grinding measurements were obtained using a 220 grit, resin-bonded wheel (6 in. diameter, 6 mm width) rotating at 3600 rpm on a standard surface grinding machine using a spray of the same aqueous cutting fluid as used for drilling. Test specimens of uniform width (10 mm) and thickness (3 mm) were mounted in a row on the load cell, so that the

J. E. Ritter—contributing editor

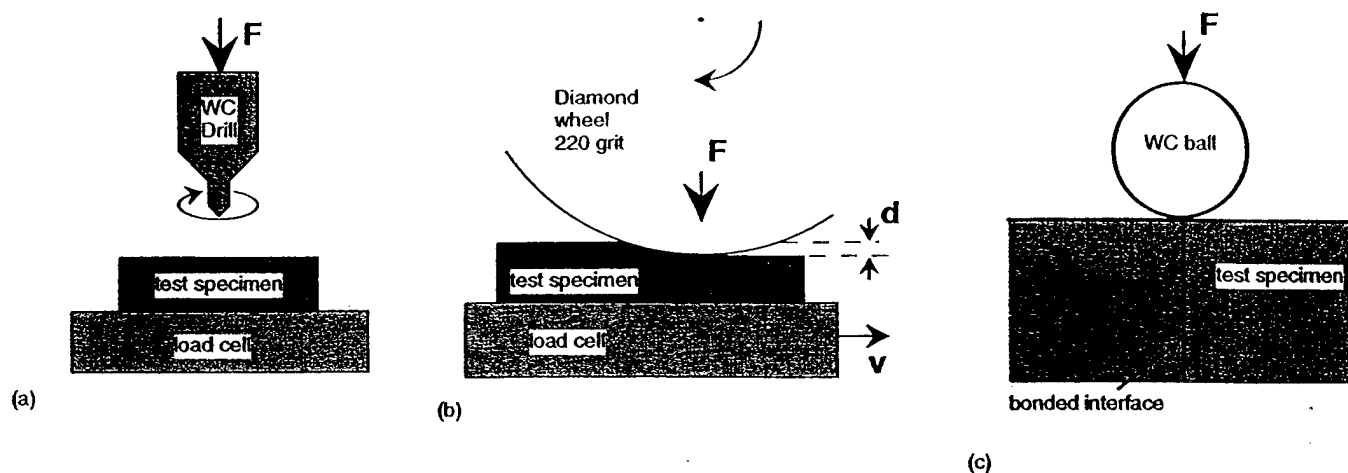


Fig. 1. Schematic diagrams illustrating the test setup for (a) drilling measurements, (b) grinding measurements, and (c) ball indentation measurements using a bonded interface specimen.

grinding wheel passed over each specimen sequentially in a single pass, thereby ensuring common grinding conditions for all of the materials. Measurements of the normal grinding force were obtained for several depths-of-cut using a constant translation speed of ~ 2.8 cm/s.

For reference, several other materials were included in these tests. The diamond grinding measurements were done on a standard machinable glass-ceramic ("Macor" from Corning) as well as single-phase materials of the constituents of the composites: Ce-ZrO₂ fabricated in the same manner as the Ce-ZrO₂/CePO₄ composites; alumina and mullite prepared by hot-pressing the same powders used for the alumina/LaPO₄ and mullite/LaPO₄ composites; and LaPO₄ prepared in a previous study⁶ by hot-pressing commercial powder of LaPO₄ (Strem Chemical) surrounded by alumina at 1200°C in graphite dies (this specimen contained a minor eutectic phase due to potassium impurity⁶). The reference drilling measurements were done only on the Macor and LaPO₄; attempts to drill Ce-ZrO₂, alumina, and mullite were unsuccessful, as might be expected.

The hardnesses and fracture toughnesses were measured in all except two of the materials using Vickers indentations.⁹ Radial cracks were not produced at Vickers indentations in the Ce-ZrO₂ reference material and the Ce-ZrO₂/CePO₄ composite with highest Ce-ZrO₂ content (typical for Ce-ZrO₂ materials^{10,11}). In these two materials the fracture toughnesses were measured using notched beams loaded in bending.¹² The beam dimensions were 2 mm \times 2.5 mm \times 3 mm and the notch width and depth were 200 μ m and 0.8 mm.

The relative susceptibility of each material to the onset of localized damage at contact sites was assessed using the Hertzian contact method introduced recently by Lawn and co-workers.^{13–15} This involved loading tungsten carbide balls of various diameters (in the range 1 to 3 mm) onto polished surfaces of the materials, and calculating the average contact pressure from measurements of the load and contact area. The surfaces were coated with thin layers of gold and carbon to enhance visibility of the contact area after removal of the ball indenter.

Preliminary assessments of damage mechanisms at localized contacts in the monazite/mullite composite and in the monolithic monazite were obtained using the bonded interface technique.^{13–15} This involved preparing a bonded test piece by gluing together polished surfaces of two rectangular blocks of the test material, polishing another surface normal to the bonded interface, and loading a tungsten carbide ball onto the polished surface at the interface (Fig. 1(c)). Damage associated with sliding contact was also examined by dragging a Knoop indenter across the interface, with the sliding direction parallel to the longer indentation diagonal and normal to the interface. The two halves of the test piece were then separated

by dissolving the glue, and the damage zones beneath the contact sites were examined optically and by scanning electron microscopy.

III. Results

(1) Microstructural Observations

The compatibility of the alumina/LaPO₄ system has been reported previously.^{6–8} Provided the overall La-to-P ratio is close to the stoichiometric value of unity, there are no reactions at temperatures up to at least 1600°C. In the reactively hot-pressed material synthesized here the only phases detected by X-ray diffraction were alumina and LaPO₄ (Fig. 2(a)). X-ray diffraction patterns from the other two systems (mullite/LaPO₄ and Ce-ZrO₂/CePO₄) are shown in Fig. 2. The results indicate that both of these systems are also compatible at the fabrication temperatures (1500° and 1600°C, respectively).

Scanning electron micrographs illustrating the microstructures of the three systems are shown in Fig. 3. The two phases in each of the mullite/LaPO₄ and alumina/LaPO₄ composites can be distinguished on polished surfaces because of the higher scattering (for both backscattered and secondary electrons) of the LaPO₄ phase. In the mullite/LaPO₄ composite (Fig. 3(a)), the two phases are well dispersed with grain sizes in the mullite of ~ 2 to 5 μ m and in the LaPO₄ of ~ 1 to 2 μ m. In the alumina/LaPO₄ composite the grain sizes were ~ 0.3 μ m in the alumina and ~ 1 μ m in the LaPO₄. In the Ce-ZrO₂/CePO₄ composite, thermal etching was needed to distinguish the two phases (Fig. 3(c)), since the scattering from both phases was similar; the grain sizes of both phases were ~ 2 to 5 μ m.

(2) Mechanical Property Measurements

The hardnesses and toughnesses of the composites and the reference materials were measured from Vickers indentations. The results are shown in Table I. Toughnesses were calculated using the analysis of Anstis *et al.*⁹ from indentations produced by as wide a range of loads as possible (indicated in a separate column in Table I). However, for some materials the range of loads was small because of chipping; in those cases the toughness results should be treated with caution.

The softer CePO₄ phase dominates the hardness of the Ce-ZrO₂/CePO₄ composites, which is almost constant over the composition range 25% to 75% CePO₄. However, the toughness is more strongly affected by the fractions of the two phases, increasing from 1.6 MPa·m^{1/2} at 25% zirconia to 4.8 MPa·m^{1/2} at 75% zirconia.

(3) Drilling and Grinding Measurements

All of the composites could be drilled using the tungsten carbide tool. A scanning electron micrograph of a typical

drilled hole in the mullite/LaPO₄ composite is shown in Fig. 4. The hole was cleanly drilled, with no evidence of large-scale cracking or chipping. Holes drilled in all of the other composites had similar appearances.

Measurements of drilling rate as a function of drilling distance, at a fixed load of 50 N, are shown in Fig. 5 for several of the materials. Each increment of drilling distance represents a new hole. For materials containing more than 50% of monazite, the drilling rates remained constant within the measurement accuracy, indicating that wear of the drill was not sufficient to affect measurements over this range of drilling distances. In composites with smaller volume fractions of monazite a small decrease in drilling rate was observed, indicating some drill wear.

The measured drilling rates in all of the materials as a function of applied normal load are shown in Fig. 6. The drilling rates for the Macor glass-ceramic are significantly larger than for all of the other materials. Nevertheless, the other drilling rates fall within a useful range. A clear increase in drilling rate with volume fraction of CePO₄ is evident for the Ce-ZrO₂/CePO₄ composites. Most of the results show a nonlinear dependence of drilling rate on force.

A similar general ranking of these materials is evident in the diamond grinding measurements of Fig. 7, with the exception of the alumina/LaPO₄ composite which exhibited the highest grinding force but intermediate drilling force. However, the relative differences between the various machinable composites is considerably smaller in the grinding measurements than in drilling. For example, the normal grinding force in the Ce-ZrO₂/CePO₄ composites was a factor of about 1.5 larger (for a given material removal rate) in the composite containing 25% CePO₄ than in the composite with 75% CePO₄, whereas the ratio of drilling forces for the same pair of composites was about 10. Moreover, the grinding forces for the single-phase

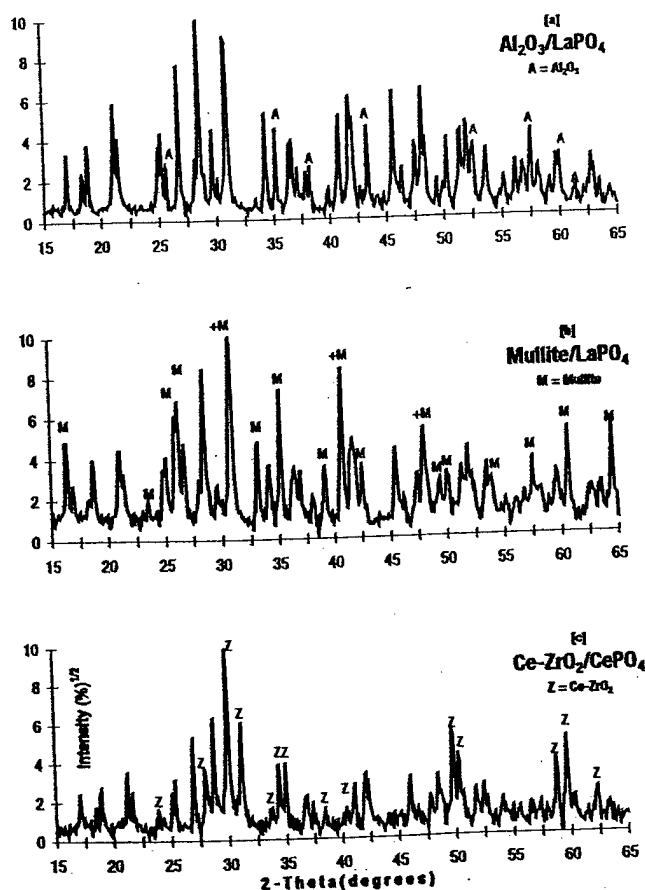


Fig. 2. X-ray diffraction data for (a) alumina/LaPO₄ (b) mullite/LaPO₄ composite, and (c) Ce-ZrO₂/CePO₄ composite.

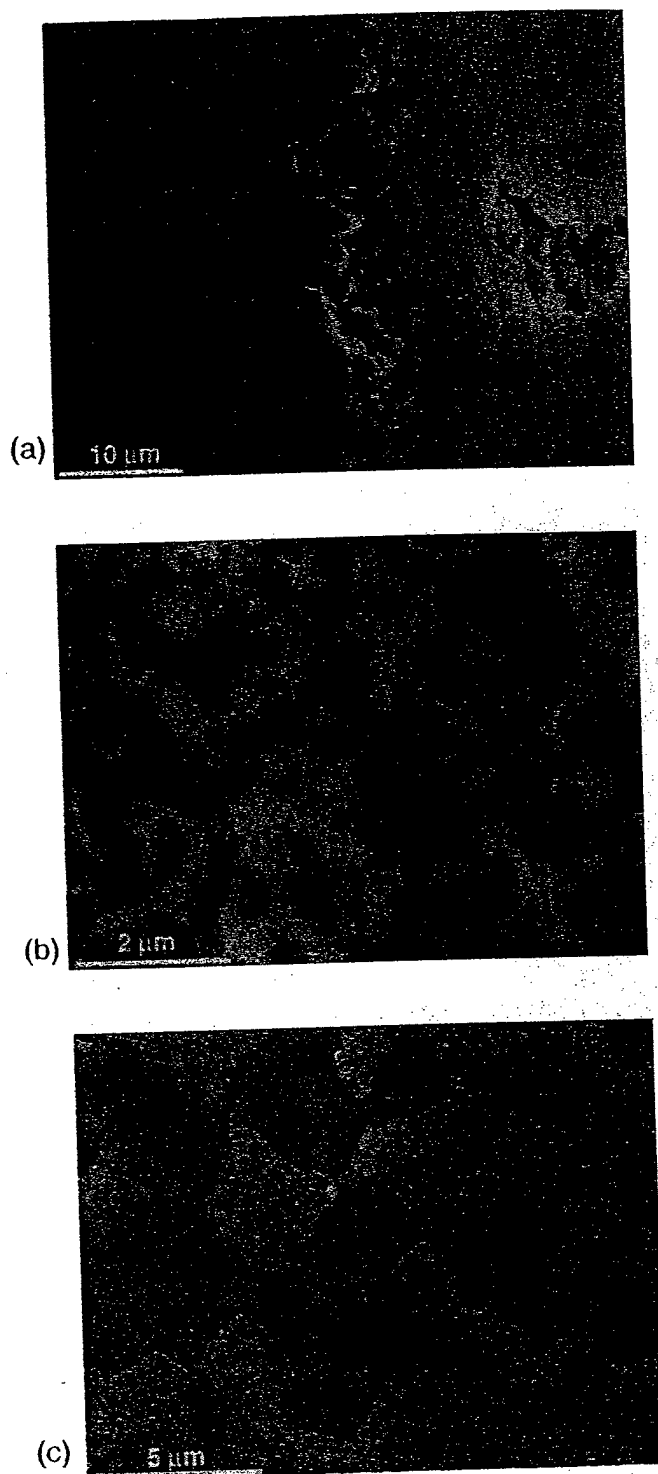


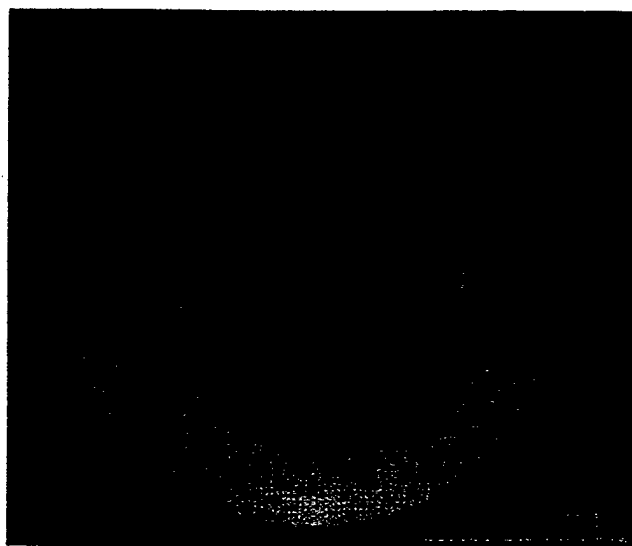
Fig. 3. Scanning electron micrographs from polished surfaces of (a) mullite/LaPO₄ composite (region from edge of drilled hole in Fig. 4; right hand side of micrograph is the drilled surface); (b) alumina/LaPO₄ composite; and (c) Ce-ZrO₂/CePO₄ composite (thermally etched surface).

oxides (zirconia, mullite, and alumina), which cannot be drilled with WC tools, were not consistently larger than for their machinable composite counterparts: in the case of Ce-ZrO₂, the grinding forces were ~30% larger than for the CePO₄-containing composites, whereas the grinding forces for mullite and alumina were smaller than for the corresponding composites containing LaPO₄. For all of the materials tested, the grinding forces were proportional to the material removal rates (i.e., depth-of-cut).

Table I. Hardnesses and Toughnesses of Test Materials

Material [†]	Hardness (GPa)	E (GPa)	Indentation load range (N)	Toughness (MPa·m ^{1/2})	
				Indentation	Notched beam
Mullite/LaPO ₄ (4:1)	11.4	203 [‡]	2–100	1.8 ± 0.1	
Ce-ZrO ₂ /CePO ₄					
CZ/CP (3:1)	6.5	183 [‡]	50–100		4.8 ± 1.1
CZ/CP (1:1)	5.7	167 [‡]	100	3.6 ± 0.1	3.2 ± 0.5
CZ/CP (1:3)	5.0	150 [‡]	50	1.6 ± 0.1	
Alumina/LaPO ₄ (3/7)	9	210 [‡]	3–10	2.3 ± 0.5	
Ce-ZrO ₂	9.5	200	20–200		8 ± 1
Alumina	15	390	20–100	3.9 ± 0.3	
Mullite	14	225	3–100	1.6 ± 0.1	
LaPO ₄	5.5 ^{††}	133 ^{††}	10–100	1.0 ± 0.1 ^{††}	
Macor	3	63 [§]		1.0 ± 0.1 [‡]	

[†]Ratios in parentheses indicate volume fractions of the two phases. [‡]Young's moduli estimated from rule-of-mixtures for two-phase materials. [§]From Ref. 14. ^{††}From Ref. 18. ^{‡†}From Ref. 6.

Fig. 4. Hole drilled in mullite/LaPO₄ composite using WC drill bit.

(4) Damage Observations

(A) **Drilling damage:** Details of the damage associated with drilling in the mullite/LaPO₄ composite are shown in Figs. 3, 4, and 8(a). Results for the Ce-ZrO₂/CePO₄, alumina/LaPO₄, and LaPO₄ systems were similar (Fig. 8(b)). In all cases the drilled surfaces were covered with a layer of smeared material with thickness approximately 0.5 μm. Although the virgin material in Figs. 3(a) and 8(a) consists of mullite and LaPO₄ in separate phases with dimensions ~2–5 μm, separate phases could not be distinguished in the smeared layer by scanning electron microscopy. EDS analysis of the layer is consistent with LaPO₄ and mullite mixed together on a very fine scale. However, confirmation of the microstructure within this layer will require the higher resolution of transmission electron microscopy. In regions where the layer had been removed, an underlying surface of intergranular fracture is visible. Observations of the surface adjacent to the drilled hole (Fig. 3) and cross sections indicate that damage from the drilling is confined to the smeared layer and the underlying layer of grains that had been dislodged (i.e., to a depth of ~2–5 μm). Significant microcracking to larger depths was not observed.

(B) **Indentation Damage:** Results of the ball contact measurements are summarized in Fig. 9 as plots of average contact pressure versus indentation strain (defined as the ratio of the contact radius to the ball radius). In this plotting scheme an elastic Hertzian response falls along a linear curve: a representative curve corresponding to $E = 200$ GPa is shown. The corresponding contact pressures obtained from a Vickers indenter are shown in Table I (i.e., the hardnesses). In all of the

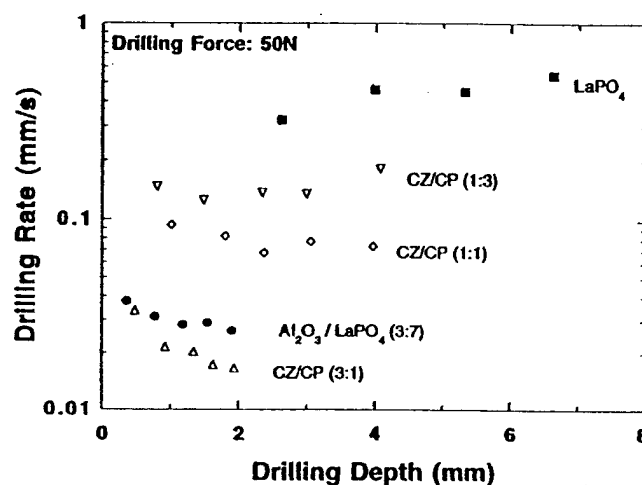


Fig. 5. Measurements of drilling rate as a function of distance at constant normal force to test drill wear. New drill bit used for each material. CZ/CP represents Ce-ZrO₂/CePO₄ composites. Ratios in brackets indicate volume fractions of the two phases.

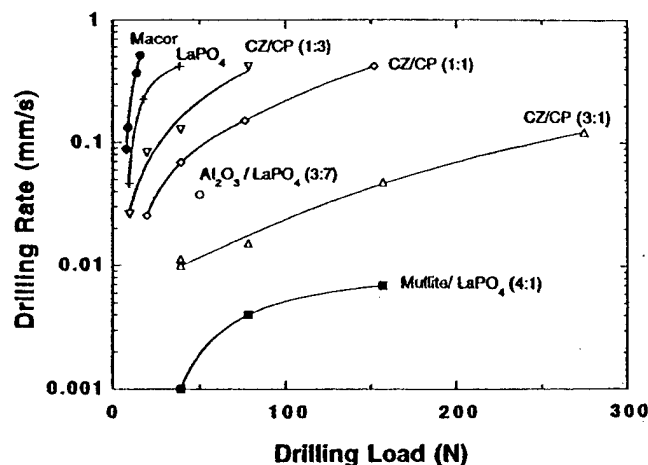


Fig. 6. Measurements of drilling rate as a function of normal force. CZ/CP represents Ce-ZrO₂/CePO₄ composites. Ratios in brackets indicate volume fractions of the two phases.

materials containing Ce-PO₄ and La-PO₄, departure from a linear Hertzian response occurs at pressures substantially below the Vickers hardness. The response in Fig. 9 is similar to previously published measurements on ceramic materials, including machinable glass-ceramics, that experience localized damage controlled by microstructural heterogeneity.^{13–17}

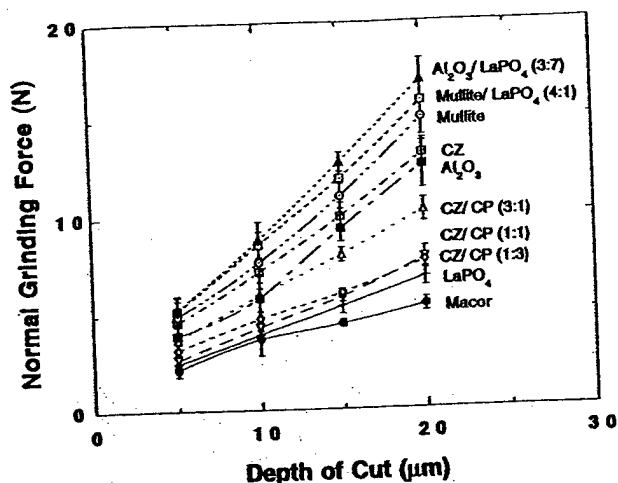


Fig. 7. Measurements of grinding forces. CZ/CP represents $\text{Ce-ZrO}_2/\text{CePO}_4$ composites. Ratios in brackets indicate volume fractions of the two phases.

Contact damage in the mullite/ LaPO_4 composite is shown in Fig. 10; at all loads within the nonlinear region of Fig. 9, a permanent depression was left at the contact site. In the section view after separating the bonded interface specimen, there was extensive cracking and shear faulting beneath the contact sites, similar to observations of Lawn and co-workers^{16,17} in other materials that contain heterogeneities and weak interphase boundaries. Near the periphery of the damage zone, there was microcracking predominantly between the monazite and mullite phases (Fig. 10(b)).

Damage in a bonded interface specimen of LaPO_4 is shown in Fig. 11. Both Hertzian contact and scratching with the Knoop indenter produced extensive cracking within a localized zone beneath the contact site. In both cases there were also many uncracked grains containing parallel sided bands (examples indicated by arrows in Fig. 11) with an appearance similar to that of twinning in other materials (alumina and various minerals) and martensitic transformation bands in zirconia. Martensitic transformation is not known in LaPO_4 . However, mechanical twinning on (001)/(100) might be possible, although the shear angle would be large (12°).

IV. Discussion

The results of this study show that alumina, zirconia, and mullite can be rendered "machinable" by the addition of finely dispersed rare-earth phosphates, in amounts at least as small as 20 vol%. Holes can be drilled in these two-phase composites using a conventional WC drill bit. The ease of diamond grinding is also increased in the case of zirconia by the addition of CePO_4 , although the relative change is much smaller. However, in the case of alumina and mullite, the addition of LaPO_4 did not increase the ease of diamond grinding. Small differences in grinding forces in materials with vastly different drilling characteristics have been observed before in grinding studies of alumina and machinable glass-ceramics.¹⁸ These results suggest either that the controlling material removal mechanisms differ in the single-point cutting action of a drill and the multipoint grinding process or that interactions of the WC and diamond tool materials with the work pieces differ.

The lack of an enhanced grinding response in machinable ceramics is also illustrated by comparing the measured grinding forces with those expected for ceramics with homogeneous, fine-grained microstructures. In such materials, grinding under sufficiently severe conditions involves contact-induced cracking that extends beyond the immediate contact zone. The single-phase alumina and mullite materials in this study are expected to behave in this manner. In that case, the material

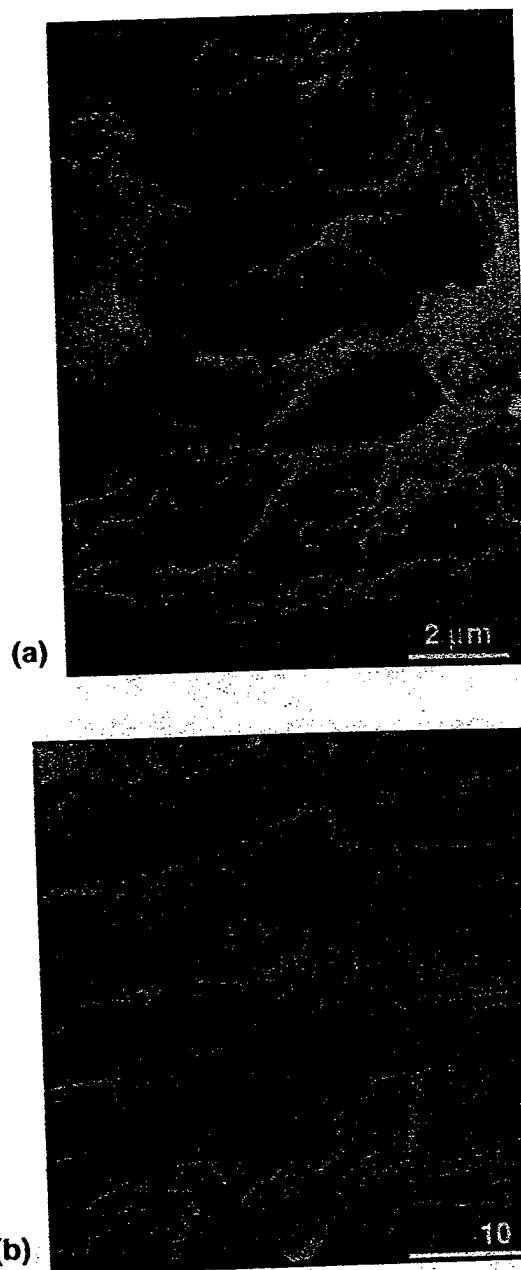


Fig. 8. Scanning electron micrographs from surfaces of drilled holes in (a) mullite/ LaPO_4 composite (showing region from Fig. 3(a) where smeared layer had chipped away) and (b) $\text{Ce-ZrO}_2/\text{CePO}_4$ composite.

removal process has been quantitatively modeled in terms of indentation lateral cracking. The grinding force, P , for a given rate of material removal is related to the macroscopic hardness, H , fracture toughness, K_{IC} , and elastic modulus, E , of the material:¹⁹

$$P \propto \left[\frac{K_{IC}^{1/2} H^{5/8}}{(E/H)^{4/5}} \right]^{8/9} \quad (1)$$

The measured grinding forces for all of the materials of this study at 20 μm depth-of-cut are compared with Eq. (1) in Fig. 12 (using measured values of H and K_{IC} from Table I and values of E for the composites estimated using a rule-of mixtures[†] with known values for the constituents). Despite some scatter,

[†]Better methods are available for estimating elastic moduli of two-phase composites. However, the difference would not affect the comparisons here.

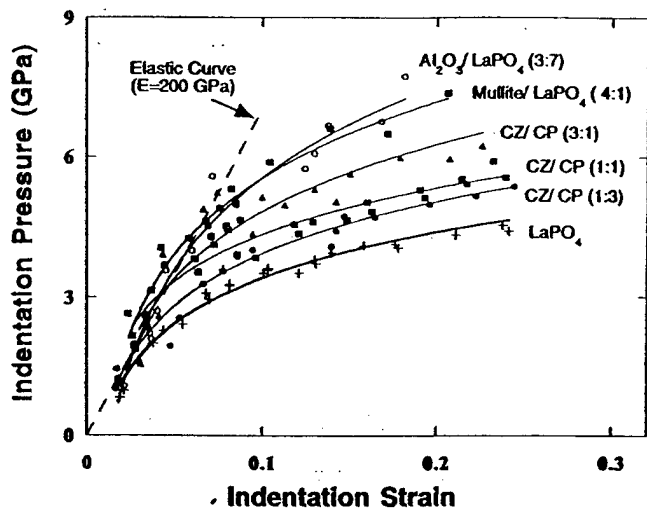
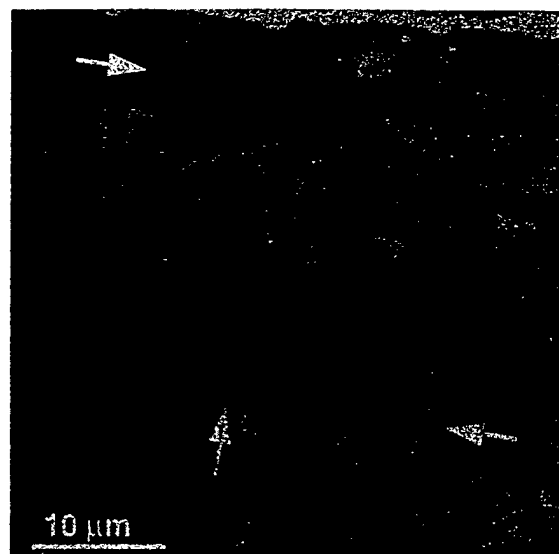
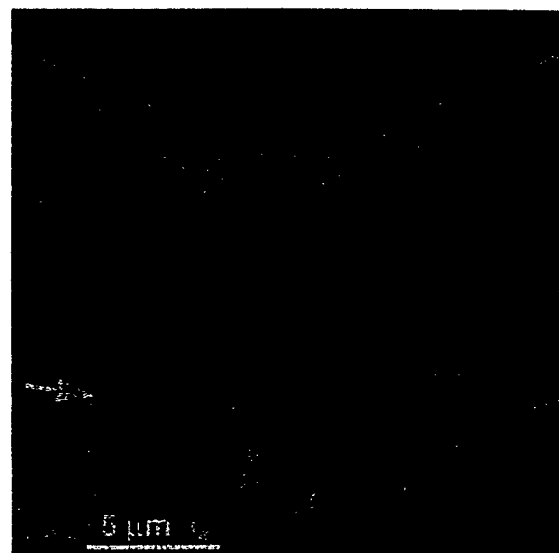


Fig. 9. Indentation stress-strain curves. CZ/CP represents Ce-ZrO₂/CePO₄ composites. Ratios in brackets indicate volume fractions of the two phases.



(a)



(b)

Fig. 11. Cross-section view from bonded interface specimen of LaPO₄ showing: (a) damage zone beneath ball indentation; (b) damage zone beneath scratch produced by dragging Knoop diamond indenter. Arrows indicate deformation bands.

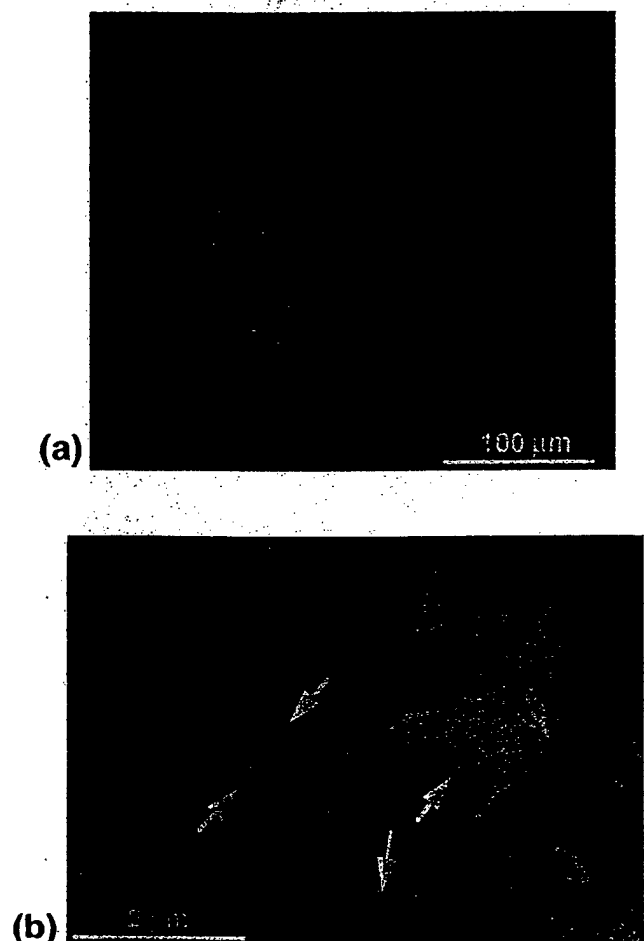


Fig. 10. (a) Surface view of residual impression at site of ball contact (3 mm ball, 300 N load) in mullite/LaPO₄. (b) Cross-section view beneath ball indentation on bonded interface specimen of mullite/LaPO₄ showing microcracking (arrows) near periphery of damage zone beneath contact site.

and some uncertainty in some of the parameters, the data mostly follow the trend predicted by Eq. (1), even though the damage mechanisms and removal processes in machinable materials would be expected to differ from the lateral cracking mechanism. In any case, it is clear that the grinding forces for

the machinable phosphate-containing composites and mica-containing glass-ceramic do not fall below the values expected on the basis of this model.

The present study was initially motivated by the possibility that in two-phase mixtures of oxides and rare-earth phosphates easy material removal should occur by formation and linking of cracks at the weak interfaces between the two phases. Evidence for this mechanism was observed in Fig. 10. However, since nominally single-phase LaPO₄ was also found to be machinable, interfacial debonding cannot be the only mechanism involved. Another possible mechanism is that associated with the deformation bands observed within individual grains of LaPO₄ beneath Hertzian contact sites (Fig. 11).

The presence of residual stresses might be expected to affect material removal processes that involve accumulated damage from microcracking. Large differences in residual stresses are expected in the three systems studied here, based on known thermal expansion coefficients of the constituent phases (approximately 10×10^{-6} for LaPO₄,⁶ CePO₄,²⁰ and zirconia;²¹ 8×10^{-6} for alumina;²¹ and 4×10^{-6} for mullite²¹). Cooling by 1000°C would generate the following residual tensile stresses in an isolated spherical phosphate particle in the three matrices:

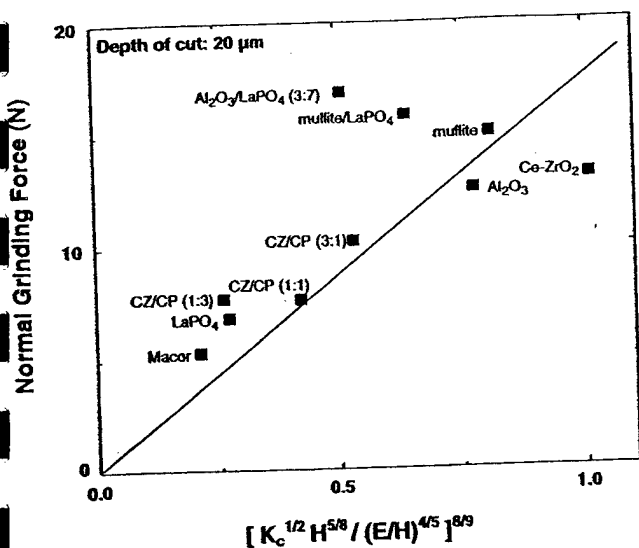


Fig. 12. Comparison of grinding forces at fixed depth-of-cut (20 μm) with Eq. (1). CZ/CP represents Ce-ZrO₂/CePO₄ composites. Ratios in brackets indicate volume fractions of the two phases. Line is representation of Eq. (1), adjusted to fit the data for alumina and mullite.

zero in zirconia, 460 MPa in alumina, and 1140 MPa in mullite.[†] Despite these very large differences in residual stresses, the drilling and grinding forces for these three systems do not differ greatly, suggesting that residual stresses do not play a dominant role.

We should emphasize that the observations concerning mechanisms in this study are preliminary. We have presented data from systems with various constituent phases in order to establish some general trends in behavior, without attempting to ensure equivalent microstructural characteristics or to vary microstructural parameters systematically within a given system. Such experiments will be needed to identify the roles of parameters such as grain size and morphology, residual stress, interfacial fracture properties, and relative fractions of the constituent phases. Effects of machining parameters (tool speed, tool shape, lubrication) are also yet to be determined.

V. Conclusions

Two-phase ceramics consisting of refractory oxides (Ce-ZrO₂, mullite, and Al₂O₃) and rare-earth phosphates (CePO₄ and LaPO₄) with microstructural dimensions in the range 1 to 5 μm can be shaped with conventional WC metal-working tools. The ease of machining increases with increasing volume fraction of the rare-earth phosphate component. Single-phase LaPO₄ was also found to be machinable. Preliminary observations suggest that in the two-phase composites microcracking at the interface between the two phases is involved in the mechanism of material removal. However, other mechanisms must also be involved, including cracking and deformation within the monazite phase. Evidence was presented for planar

deformation features within monazite grains. The formation of a finely crushed, smeared layer of material between the work-piece and tool was observed after drilling all of the machinable materials.

Note added in proof: The presence of (100) twins and dislocations in regions surrounding contact sites such as Fig. 10(a) in LaPO₄ has now been confirmed by transmission electron microscopy (R. S. Hay, personal communication).

Acknowledgments: The initial discovery of machinability in mullite/LaPO₄ was funded by the U.S. Office of Naval Research under Contract No. N00014-95-C-0057. Subsequent study of this and other materials was funded by the U.S. Air Force Office of Scientific Research under Contract No. F49620-96-C-0026.

References

- ¹C. K. Chyung, G. H. Beall, and D. G. Grossman, "Microstructures and Mechanical Properties of Mica Glass-Ceramics"; pp. 1167-94 in *Electron Microscopy and Structure of Materials*, Edited by G. Thomas, R. M. Fulrath, and R. M. Fisher. University of California, Berkeley, CA, 1972.
- ²K. Chyung, G. H. Beall, and D. G. Grossman, "Fluorophlogopite Mica Glass-Ceramics," *Proc. Int. Glass Congr.*, 10th, 33-40 (1974).
- ³M. W. Barsoum and T. El-Raghy, "Synthesis and Characterization of a Remarkable Ceramic: Ti₃SiC₂," *J. Am. Ceram. Soc.*, **79** [7] 1953-56 (1996).
- ⁴N. P. Padture, C. J. Evans, H. H. K. Xu, and B. R. Lawn, "Enhanced Machinability of Silicon Carbide via Microstructural Design," *J. Am. Ceram. Soc.*, **78** [1] 215-17 (1995).
- ⁵T. Tanimoto, T. Morii, M. Okumura, A. Nakazawa, G. Suganuma, G. Sasaki, and K. Niihara, "Mechanical Properties and Nanostructure of Machinable SiC"; pp. 419-24 in *Proceedings of 1st International Symposium on Science of Engineering Ceramics*, Edited by S. Kimura and K. Niihara. The Ceramic Society of Japan, Tokyo, Japan, 1991.
- ⁶P. E. D. Morgan and D. B. Marshall, "Ceramic Composites of Monazite and Alumina," *J. Am. Ceram. Soc.*, **78** [6] 1553-63 (1995).
- ⁷P. E. D. Morgan, D. B. Marshall, and R. M. Housley, "High Temperature Stability of Monazite-Alumina Composites," *Mater. Sci. Eng.*, **A195**, 215-221 (1995).
- ⁸P. E. D. Morgan and D. B. Marshall, "Functional Interfaces in Oxide-Oxide Composites," *Mater. Sci. Eng.*, **A162** [1-2] 15-25 (1993).
- ⁹G. R. Anstis, P. Chantikul, B. R. Lawn, and D. B. Marshall, "A Critical Evaluation of Indentation Techniques for Measuring Fracture Toughness: I, Direct Crack Measurements," *J. Am. Ceram. Soc.*, **64** [9] 533-38 (1981).
- ¹⁰R. H. J. Hannink and M. V. Swain, "Metastability of the Martensitic Transformation in a 12 mol% Ceria-Zirconia Alloy: I, Deformation and Fracture Observations," *J. Am. Ceram. Soc.*, **72** [1] 90-98 (1989).
- ¹¹P. E. Reyes-Morel and I-W. Chen, "Transformation Plasticity of CeO₂-Stabilized Tetragonal Zirconia Polycrystals: I, Stress Assistance and Autocatalysis," *J. Am. Ceram. Soc.*, **71** [5] 343-53 (1988).
- ¹²H. Tada, P. C. Paris, and G. R. Irwin, *The Stress Analysis of Cracks Handbook*. Paris Productions, St. Louis, MO, 1985.
- ¹³F. Guiberteau, N. P. Padture, and B. R. Lawn, "Effect of Grain Size on Hertzian Contact in Alumina," *J. Am. Ceram. Soc.*, **77** [7] 1825-31 (1994).
- ¹⁴H. Cai, M. A. S. Kalceff, and B. R. Lawn, "Deformation and Fracture of Mica-Containing Glass-Ceramics in Hertzian Contacts," *J. Mater. Res.*, **9** [3] 762-70 (1994).
- ¹⁵H. H. K. Xu, L. Wei, N. P. Padture, B. R. Lawn, and R. L. Yeckley, "Effect of Microstructural Coarsening on Hertzian Contact Damage in Silicon Nitride," *J. Mater. Sci.*, **30** [4] 869-78 (1995).
- ¹⁶N. P. Padture and B. R. Lawn, "Toughness Properties of a Silicon Carbide with an *In Situ* Induced Heterogeneous Grain Structure," *J. Am. Ceram. Soc.*, **77** [10] 2518-22 (1994).
- ¹⁷B. R. Lawn, N. P. Padture, H. Cai, and F. Guiberteau, "Making Ceramics 'Ductile,'" *Science*, **263**, 1114-16 (1994).
- ¹⁸D. B. Marshall, B. R. Lawn, and R. F. Cook, "Microstructural Effects in Grinding of Alumina," *J. Am. Ceram. Soc.*, **70** [6] C-139-C140 (1987).
- ¹⁹A. G. Evans and D. B. Marshall, "Wear Mechanisms in Ceramics"; pp. 439 in *Fundamentals of Friction and Wear of Materials*, Edited by D. A. Rigney. American Society of Mechanical Engineers, New York, 1981.
- ²⁰Y. Hikichi, T. Nomura, Y. Tanimura, and S. Suzuki, "Sintering and Properties of Monazite-Type CePO₄," *J. Am. Ceram. Soc.*, **73** [12] 3594-96 (1990).
- ²¹Y. S. Touloukian, R. K. Kirby, R. E. Taylor, and T. Y. R. Lee, *Thermal Expansion Nonmetallic Solids*. Plenum, New York, 1977.
- ²²B. R. Lawn, *Fracture of Brittle Solids*, 2nd ed. Cambridge University Press, Cambridge, U.K., 1993.

[†]For equations giving the residual stress for this configuration, see, for example, Ref. 22.

9.0 Debonding in Multilayered Composites of Zirconia and LaPO_4

by Marshall, D.B., Morgan, P.E.D. and Housley, R. M.

The following section is a paper published in J.Amer. Ceram Soc., 80[7] 1677-83 (1997)

Debonding in Multilayered Composites of Zirconia and LaPO_4

David B. Marshall,* Peter E. D. Morgan,* and Robert M. Housley*

Rockwell Science Center, Thousand Oaks, California 91360

Multilayered composites consisting of LaPO_4 (La-monazite) layers alternating with various ZrO_2 -based materials were fabricated to investigate whether LaPO_4 provides a weakly bonded interface suitable for promoting toughening, as previously observed in the system $\text{LaPO}_4/\text{Al}_2\text{O}_3$. The following ZrO_2 -based materials were assessed: Y-ZrO_2 , $\text{Y-ZrO}_2/\text{Al}_2\text{O}_3$, Ce-ZrO_2 , and $\text{Ce-ZrO}_2/\text{Al}_2\text{O}_3$. Debonding was observed in all cases. The composites containing Y-ZrO_2 and $\text{Y-ZrO}_2/\text{Al}_2\text{O}_3$ were stable, with no reactions, at temperatures up to at least 1600°C . However, in the composites containing Ce-ZrO_2 , interdiffusion of Ce and La occurred, resulting in formation of a pyrochlore-like phase and, in the case of the $\text{Ce-ZrO}_2/\text{Al}_2\text{O}_3$ composite, a $(\text{Ce},\text{La})\text{Al}_2\text{O}_6$ magnetoplumbite phase.

I. Introduction

SEVERAL mechanisms have been used to achieve toughening in multilayered ceramic composites.¹ One involves enhanced transformation toughening in systems containing zirconia with strongly bonded interfaces.²⁻⁴ While large increases in fracture toughness have been achieved in such composites, failure in tensile loading involves growth of a single crack: the composites do not exhibit a large nonlinear behavior or distributed damage. Other mechanisms involve deflection of cracks or secondary cracking caused by the presence of weak layers, weak interfaces, residual stresses, or other microstructural defects.⁵⁻¹⁶ If the degree of crack deflection is sufficient to cause splitting between layers, a damage-tolerant response and distributed damage can be achieved in flexural loading, as demonstrated initially in systems containing layers of carbon or BN.⁹⁻¹¹ However, the usefulness of systems containing carbon and BN is limited by their sensitivity to oxidation.

Attempts have been made recently to avoid this limitation by developing analogous oxide-based systems, using either layers of magnetoplumbite/ β -alumina compounds,^{7,17-19} porous oxide layers,¹² or rare-earth orthophosphates¹³⁻¹⁶ such as LaPO_4 (La-monazite) and YPO_4 (xenotime) to cause debonding. In the system $\text{LaPO}_4\text{-Al}_2\text{O}_3$, the interfacial toughness is sufficiently low to satisfy the criterion of He and Hutchinson²⁰ for a normally incident crack to deflect along the interface rather than cross it.¹³ This system is stable for long periods in air at temperatures at least as high as 1600°C .^{13,14} In this paper, we present a preliminary study of the stability and debonding characteristics of LaPO_4 with several layered zirconia systems. The possibility of achieving toughening from both interlaminar cracking and transformations is also explored.

David J. Green—contributing editor

Manuscript No. 191602. Received August 15, 1996; approved February 10, 1997.
Presented at a Symposium on Microstructure-Property Relations of Advanced Materials, a symposium in honor of Professor Arthur Heuer's 60th birthday, held at Max-Planck-Institut für Metallforschung, Stuttgart, Germany, April 29-30, 1996.
Supported by the Air Force Office of Scientific Research under Contract Numbers F49620-92-C-0028 and F49620-96-C-0026 monitored by Dr. A. Pechenik.
*Member, American Ceramic Society.

II. Experimental Procedure

Laminar composites consisting of alternating layers of LaPO_4 and zirconia were fabricated by colloidal techniques. Four types of composites containing different compositions in the "zirconia" layers were fabricated: one with 3 mol% Y_2O_3 addition (Tosoh 3Y); one with 12 mol% CeO_2 addition (Tosoh 12Ce); one with a mixture (50% by volume) of Al_2O_3 (Sumitomo AKP30) and Y-ZrO_2 ; and one with a mixture of Al_2O_3 (50% by volume) and Ce-ZrO_2 . The layer thicknesses were in the range 5 to 50 μm for the LaPO_4 layers and 20 to 200 μm for the ZrO_2 layers.

The composites were consolidated by sequential centrifuging or vacuum slip casting of colloidal suspensions of the various layers. Use was made of a colloidal technique developed by Velamakanni *et al.*²¹ and Chang and Velamakanni²² in which an aqueous electrolyte (NH_4NO_3) was used (after dispersing the powders at pH 2) to produce short-range repulsive hydration forces and reduce the magnitudes of the longer range electrostatic forces between the suspended particles. Such conditions produce a weakly attractive network of particles, which prevents mass segregation during centrifugation and slip casting, but because of the lubricating action of the short-range repulsive forces, allows particles to pack to high green density. The prevention of mass segregation is especially important for forming uniform two-phase layers such as $\text{Al}_2\text{O}_3\text{-ZrO}_2$ from suspensions containing mixtures of the two types of powder.

The consolidated bodies were cold isostatically pressed at 350 MPa, then sintered in air (in the case of Y-containing composites) or oxygen (Ce-containing composites) at 1600°C for 2 h. Several specimens containing Y-ZrO_2 were packed in alumina powder after the cold-pressing step and hot-pressed in graphite dies at 1400°C for 1 h. Sections were cut, polished, and thermally etched at 1400°C for microstructural analysis.

Microstructural characteristics of the multilayered composites were assessed using X-ray diffraction, electron microprobe analysis, and scanning electron microscopy (SEM). In the SEM, secondary electrons, backscattered electrons, and cathodoluminescence were used for imaging, and elements were identified by energy-dispersive spectroscopy (EDS) of fluorescence X-rays. The response of the cathodoluminescence detector was strongly peaked in the blue wavelengths. The electron microprobe measurements were taken at an operating voltage of 15 kV using standards of lanthanum phosphate, zirconium silicate, and cerium oxide. (Electron microprobe measurements were done at the Geology Department at Caltech, using a JEOL JXA-733 instrument.) In the various imaging modes the following phase distinctions could be readily made: with backscattered and secondary electrons, alumina was darker than zirconia and monazite, while zirconia and monazite were almost indistinguishable; in cathodoluminescence, $(\text{La},\text{Ce})\text{PO}_4$ was bright, while Al_2O_3 and ZrO_2 did not luminesce in the blue and were indistinguishable.

Debonding at the LaPO_4 layers was tested using two methods. One involved forming cracks in a polished surface (normal to the layers) by indenting with a Vickers indenter. The other involved loading rectangular beams in four-point bending and monitoring crack growth *in situ* using an optical microscope. The beams were oriented with the layers normal to the loading direction, so that initial crack growth was normal to the layers. Some beams

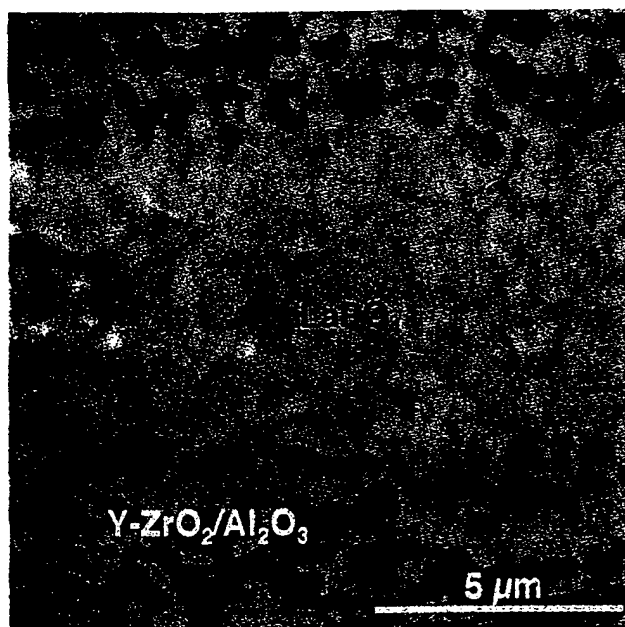


Fig. 1. Layers of LaPO_4 (La-monazite) and $\text{Y-ZrO}_2/\text{Al}_2\text{O}_3$. Backscattered electron image. Thermally etched surface.

were tested with a notch of width 200 μm , cut with a diamond saw normal to the layers on the tensile side of the beam.

III. Results

(1) Microstructures

The composites containing Y-ZrO_2 and $\text{Y-ZrO}_2/\text{Al}_2\text{O}_3$ layers did not exhibit any reactions or interdiffusion with the LaPO_4 layers. In composites that were hot-pressed at 1400°C, both layers appeared fully dense on polished cross sections. A back-scattered electron image showing 5 μm layers of LaPO_4 and $\text{Y-ZrO}_2/\text{Al}_2\text{O}_3$ in a hot-pressed composite is shown in Fig. 1: within the $\text{ZrO}_2/\text{Al}_2\text{O}_3$ layers the grain size is $\sim 0.7 \mu\text{m}$, with the ZrO_2 and Al_2O_3 being well dispersed, while the grain size in the LaPO_4 layer is $\sim 3 \mu\text{m}$. In the composites that were sintered at 1600°C, the ZrO_2 -containing layers were fully dense, although the LaPO_4 layers contained isolated pores with diameters up to 2 μm (see Fig. 7). The grain sizes in both layers are larger than in the hot-pressed composites: 1.5 μm for the $\text{Al}_2\text{O}_3/\text{ZrO}_2$ and ~ 4 to 5 μm for the monazite.

In the composite containing Ce-ZrO_2 layers, there was interdiffusion of La and Ce and precipitation of a second phase within the Ce-ZrO_2 layers (Fig. 2). However, X-ray diffraction measurements indicated that the composite was primarily zirconia and monazite, with only a few small additional diffraction peaks that were consistent with a few percent of a pyrochlore-like structure. The electron microprobe results (Fig. 3) indicate that the LaPO_4 layers had lost $\sim 5\%$ to 10% of the La which had been replaced by Ce, forming the monazite solid solution $\text{La}_{1-x}\text{Ce}_x\text{PO}_4$. In the zirconia layers, the La was in precipitates, which also contained much higher concentration of Ce than the host Ce-ZrO_2 (Fig. 3). These precipitates show as bright spots in Fig. 2(b) and are possibly a pyrochlore-like phase. The ZrO_2 -containing layers are fully dense, while the (La,Ce)-monazite layers contain more porosity than was observed in the La-monazite layers of the Y-ZrO_2 composite (Fig. 2(b)).

The composite containing $\text{Ce-ZrO}_2/\text{Al}_2\text{O}_3$ layers showed substantially more reaction associated with the diffusion of La and Ce. In the centers of the $\text{Ce-ZrO}_2/\text{Al}_2\text{O}_3$ layers there were isolated elongated grains of $(\text{Ce,Lu})\text{Al}_2\text{O}_6$ magnetoplumbite containing approximately equal amounts of Ce and La (Fig. 4). Near the edges of the layers there were larger concentrations of magnetoplumbite and some LaAlO_3 grains.

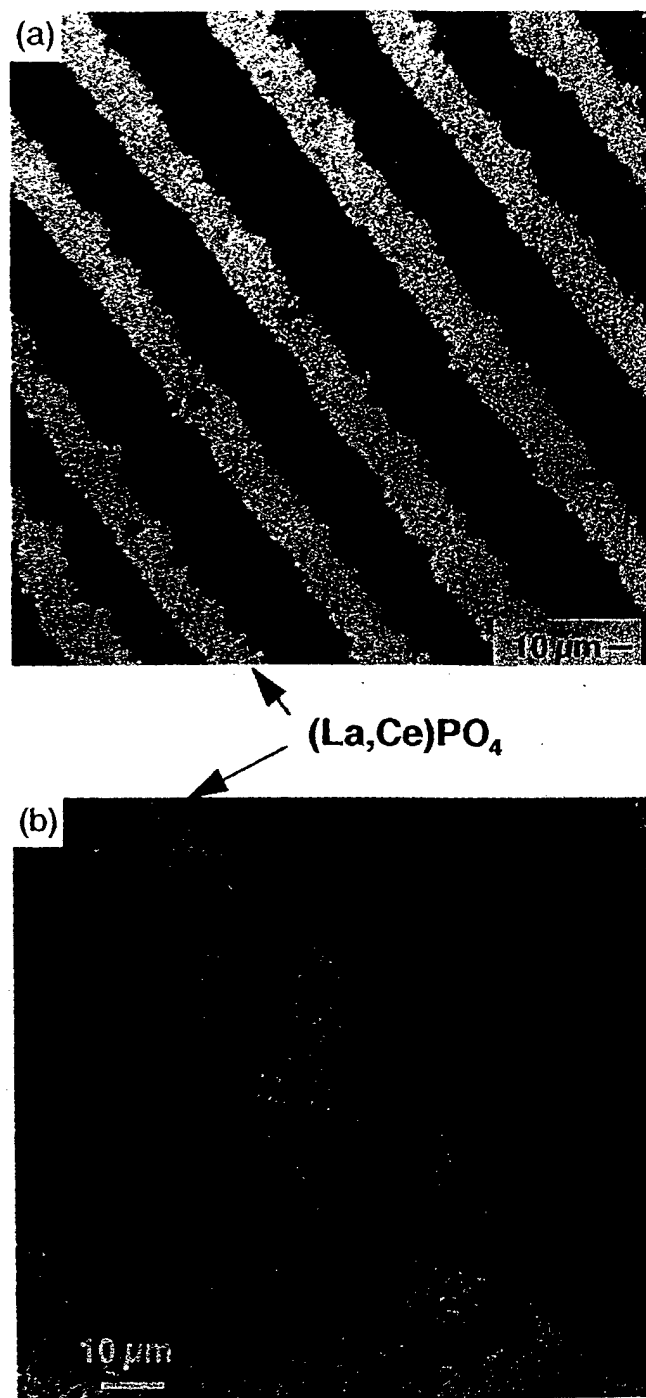


Fig. 2. (a) Cathodoluminescence image of $\text{Ce-ZrO}_2/\text{LaPO}_4$ composite showing overall structure. Bright layers are $(\text{La,Ce})\text{PO}_4$. (b) Backscattered electron image of $\text{Ce-ZrO}_2/\text{LaPO}_4$ composite. Porous layers are single-phase $(\text{La,Ce})\text{PO}_4$.

(2) Fracture and Debonding

(A) Flexural Loading

In all of the composites, flexural loading of notched beams caused delamination and sequential fracture of the layers, with a nonlinear load-deflection response such as shown in Fig. 5(a). A similar response was observed with notch-free beams (Fig. 5(b)) in all cases except for the composite containing $\text{Ce-ZrO}_2/\text{Al}_2\text{O}_3$ layers: in that case failure was catastrophic without debonding. The typical delamination damage can be seen in Fig. 6, which shows a broken beam of the $\text{Ce-ZrO}_2/\text{LaPO}_4$ composite, along with an *in situ* optical micrograph taken during loading and SEM micrographs of the stepped fracture surface after failure. In the *in situ* micrograph of Fig. 6(b), extensive damage is evident in

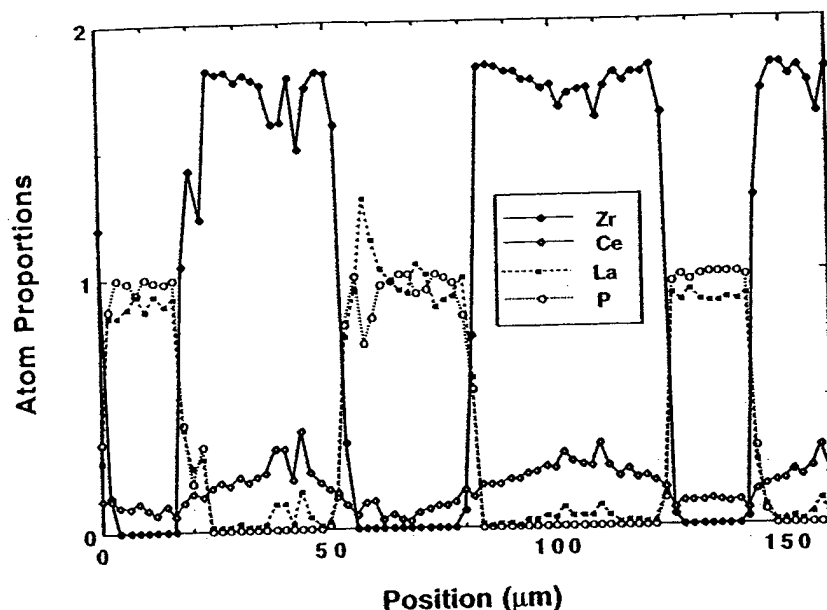


Fig. 3. Electron microprobe measurements along a line traversing several layers in $\text{Ce-ZrO}_2/\text{LaPO}_4$ composite. Atomic proportions are normalized to four oxygen atoms.

the first six LaPO_4 layers past the notch, whereas the ZrO_2 layers in this region are fractured in only one or two places. At this stage of loading there was no damage in any layers beyond the sixth LaPO_4 layer. On the stepped fracture surface (Figs. 6(c) and (d)), cracking in the LaPO_4 layers is seen primarily at or near the interface between the LaPO_4 and Ce-ZrO_2 layers.

Similar results were obtained for the composite consisting of layers of $\text{Y-ZrO}_2/\text{Al}_2\text{O}_3$ and LaPO_4 . Although on the fracture surfaces it appeared that separation of the layers occurred mainly at or near the interfaces between the ZrO_2 and LaPO_4 , there was also substantial cracking within the LaPO_4 layers (Fig. 7). Usually delamination began with simple deflection of the main crack, as in Fig. 7(a) but then continued by forming an array of echelon cracks as in Figs. 7(b) and (c). This mechanism of delamination

has also been observed in $\text{LaPO}_4/\text{Al}_2\text{O}_3$ composites,¹³ as well as in other material systems under shear loading, including unidirectionally reinforced glass matrix composites,^{23,24} brittle adhesive joints between rigid layers,²⁵ and graphite-epoxy composites.^{26,27}

A preliminary observation suggestive of possible combined toughening by martensitic transformation and interlaminar cracking in the $\text{Ce-ZrO}_2/\text{LaPO}_4$ composite is shown in Fig. 8. The Nomarski interference micrograph of Fig. 8(a) shows a zone of uplifted material surrounding the main crack. The uplift is due to the volume increase associated with the tetragonal-to-monoclinic phase transformation in the Ce-ZrO_2 layers. The width of this zone increases as the crack extends from the notch root, as observed previously in multilayered composites of Al_2O_3 and Ce-ZrO_2 ²⁻⁴ in which the layers were strongly bonded. However, in this case there is also cracking in the LaPO_4 layers within the transformation zone, as shown in Fig. 8(b).

(B) Indentation Fracture

In all of the multilayered composites, the LaPO_4 layers were effective in confining the cracking due to adjacent Vickers indentations, as shown in Figs. 9(a) and (b). The damage in the layers at either side of the indentation consists mostly of arrays of echelon cracks, similar to the damage observed in notched beams.

Cracks produced by Vickers indentations located directly on LaPO_4 layers were used to obtain a measure of the interlaminar toughness, as shown in Fig. 9(c). The area of Fig. 9(c) lies within a beam of 4 mm thickness that consisted of $\text{Y-ZrO}_2/\text{Al}_2\text{O}_3$ with three layers of LaPO_4 in the center. The lengths of the indentation cracks growing along the LaPO_4 layer in Fig. 9(c) are about 3 times the length of the crack growing normal to the layer into the $\text{Y-ZrO}_2/\text{Al}_2\text{O}_3$ matrix. The corresponding fracture toughnesses calculated from 10 indentations using the analysis of Anstis *et al.*²⁸ are $\Gamma_i = 8 \pm 4 \text{ J/m}^2$ for the interlaminar crack and $\Gamma_m = 80 \pm 5 \text{ J/m}^2$ for the $\text{Y-ZrO}_2/\text{Al}_2\text{O}_3$ matrix (using a value of 300 GPa for the elastic modulus). The matrix toughness is consistent with values reported in the literature (corresponding to a critical stress intensity factor of $K_{Ic} = 5 \text{ MPa}\cdot\text{m}^{1/2}$); while the interlaminar toughness is similar to values reported for monazite itself.¹³ For the composite with Y-ZrO_2 matrix, the fracture energies were $\Gamma_i = 6 \pm 3 \text{ J/m}^2$, and $\Gamma_m = 110 \pm 10 \text{ J/m}^2$.

This toughness calculation is based on an analysis for a homogeneous isotropic material, whereas the measurements were obtained from composites containing layers of differing elastic moduli (133 GPa for LaPO_4 , 200 GPa for ZrO_2 , and 400 GPa for Al_2O_3). In the configuration of Fig. 9, with a thin layer of

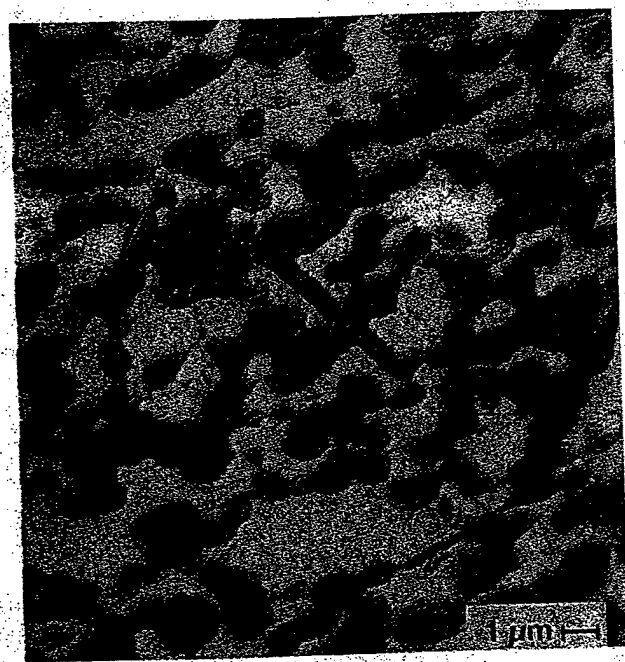


Fig. 4. Backscattered electron image from composite containing $\text{Ce-ZrO}_2/\text{Al}_2\text{O}_3$ and LaPO_4 layers, from region in center of $\text{Ce-ZrO}_2/\text{Al}_2\text{O}_3$ layer, showing presence of elongated Ce-La magnetoplumbite. Thermally etched surface.

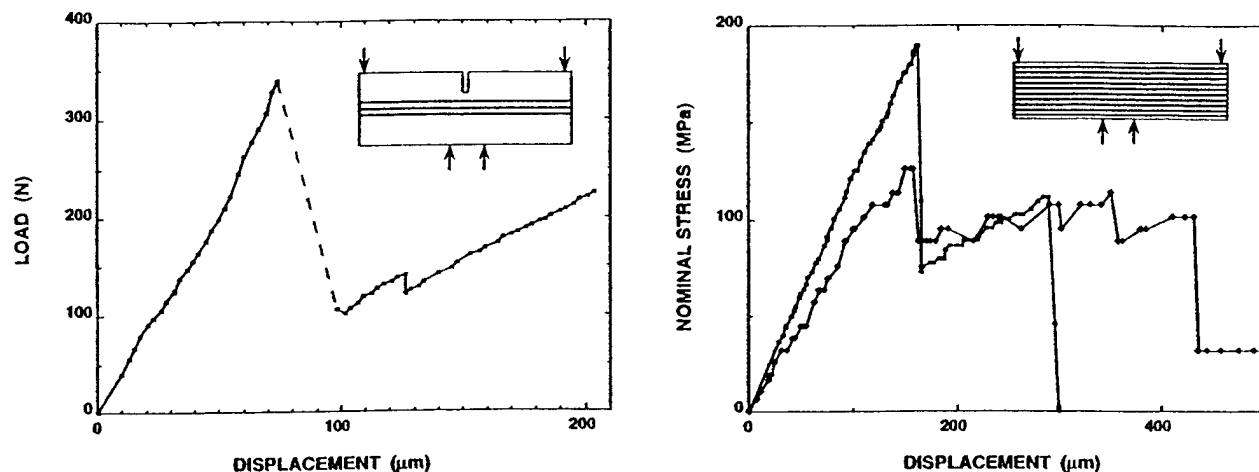


Fig. 5. (a) Load-deflection response of notched beam of Y-ZrO₂ containing three layers of LaPO₄ near its midplane. (b) Flexural loading response of unnotched beams of multilayered Ce-ZrO₂/LaPO₄. (Nominal stress is calculated for undamaged linear elastic beam.)

LaPO₄ sandwiched between relatively thick layers of ZrO₂, the calculation of the crack driving force for a crack growing along the layer (either in the layer or at the interface) in terms of the residual indentation stress field is not affected by the lower elastic modulus of the LaPO₄.²⁹ The lower modulus would affect the crack driving force only through its influence on the magnitude of the indentation stresses, as determined by the inelastic deformation around the indentation. This effect must be small if the indentation is large compared with the monazite layer thickness, as in Fig. 9(c).

The calculated toughnesses are also affected by residual stresses due to thermal expansion mismatch in the layered composites. Since the thermal expansion coefficients for LaPO₄ and ZrO₂ are approximately equal ($\sim 10 \times 10^{-6} \text{ }^\circ\text{C}^{-1}$),¹³ residual stresses are negligibly small in composites containing only those two phases. However, in composites containing mixed Al₂O₃/ZrO₂ layers, the lower thermal expansion coefficient of Al₂O₃ ($\sim 8 \times 10^{-6} \text{ }^\circ\text{C}^{-1}$) leads to tensile stresses within the LaPO₄ layers in the direction parallel to the layers and balancing compressive stresses in the Al₂O₃/ZrO₂ (the latter stress

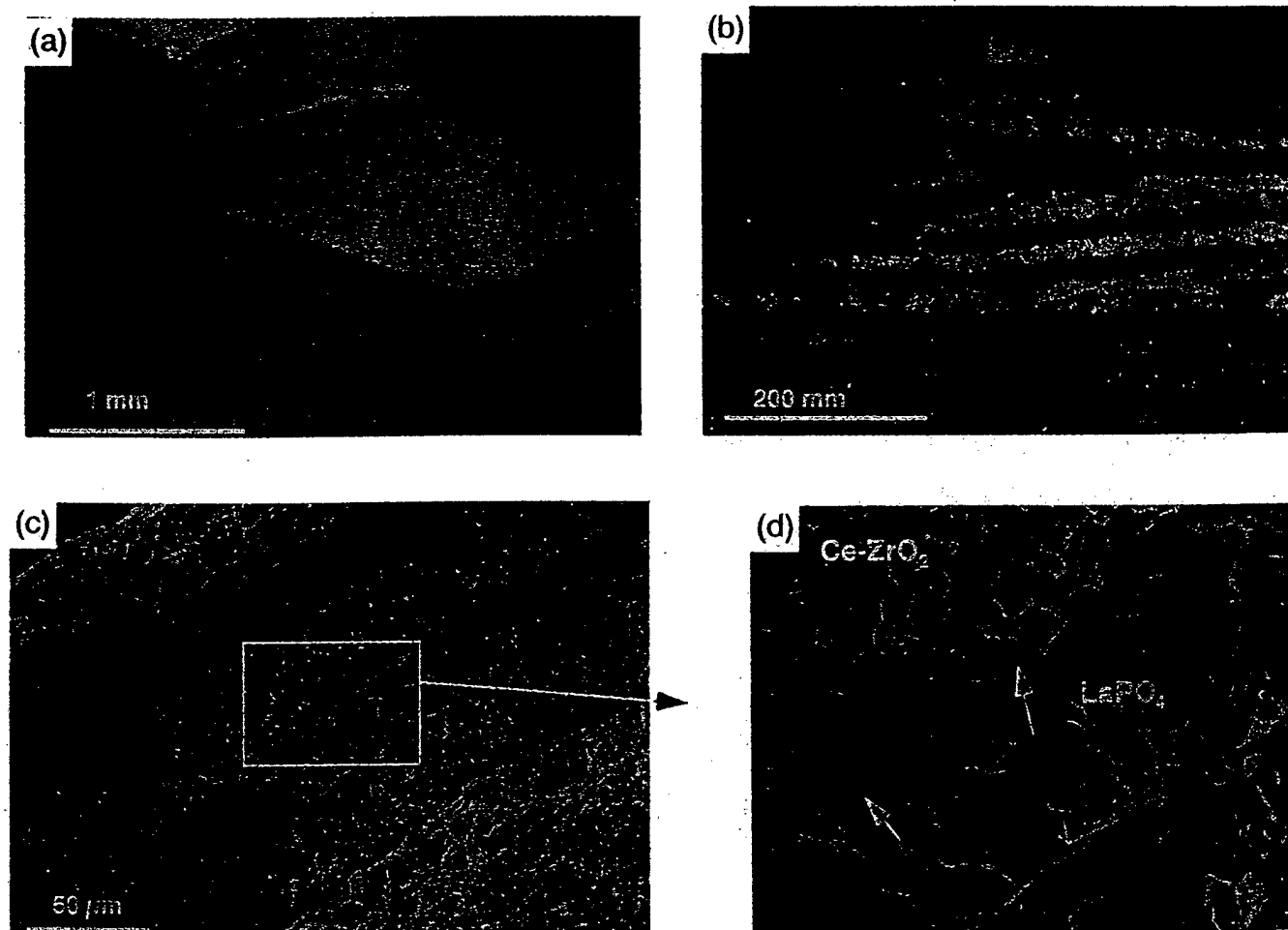


Fig. 6. Fracture of notched beam of multilayered composite of Ce-ZrO₂ and LaPO₄. (a) Overall view after failure. (b) *In situ* optical micrograph during loading. (c) and (d) Fracture surface after failure (arrows indicate cracks).

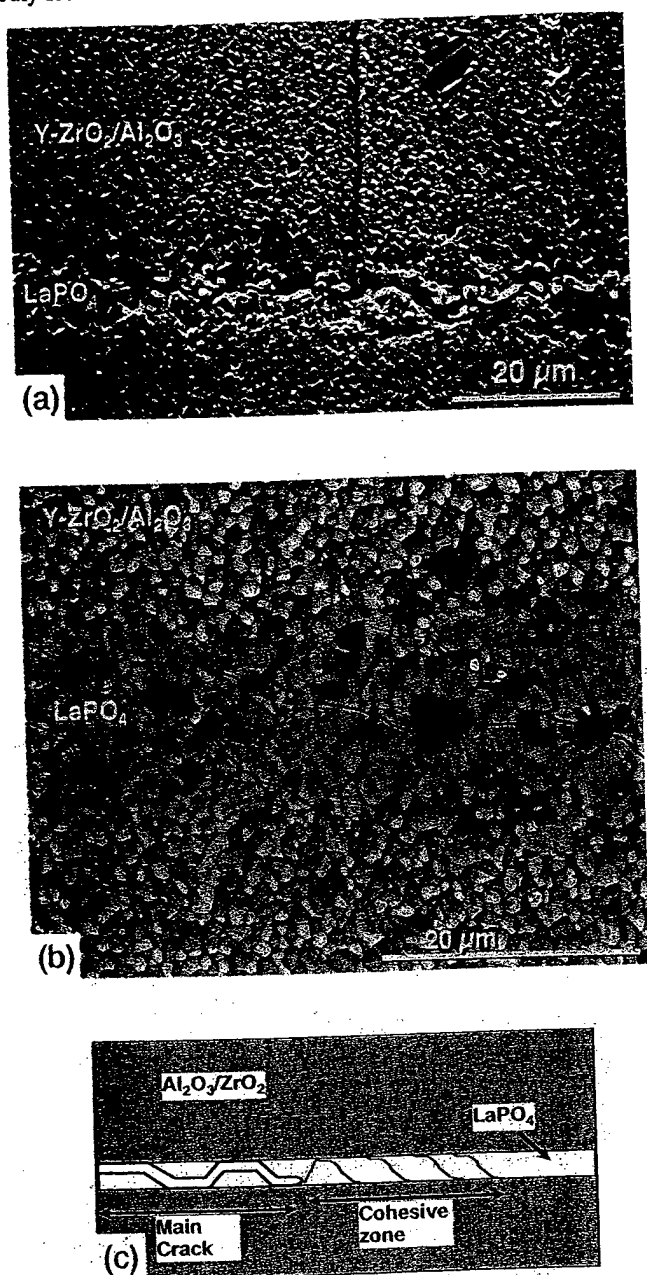


Fig. 7. Fracture of notched beam of multilayered composite of $\text{Y-ZrO}_2/\text{Al}_2\text{O}_3$ and LaPO_4 . (a) Initial debonding after crack from notch was grown to first LaPO_4 layer. (b) Cracking within LaPO_4 layer at position $\sim 200 \mu\text{m}$ to the right of (a). (c) Schematic of debonding mechanism.

being negligibly small in the specimen of Fig. 9(c), which contains a small volume fraction of LaPO_4 layers). In regions near the polished cross-sectional surface, there are also residual stresses in the direction normal to the layers with opposite signs to the corresponding parallel stresses.³⁰ The magnitudes of the normal stresses are maximum at the surface (equal to the magnitudes of the parallel stresses) and decay within a depth approximately equal to the layer thickness. Therefore, the growth of the cracks along the LaPO_4 layer of Fig. 9(c) is opposed by the compressive near-surface stress within the LaPO_4 layer. The magnitude of this stress is approximately 130 MPa. However, since the depth over which the stress acts is small compared with the crack depth, the influence on the crack length is not large: application of the analysis of Lawn and Fuller³¹ indicates that the corresponding overestimate of the interlaminar toughness for the $\text{Al}_2\text{O}_3/\text{ZrO}_2$ composites is no more than 10%.

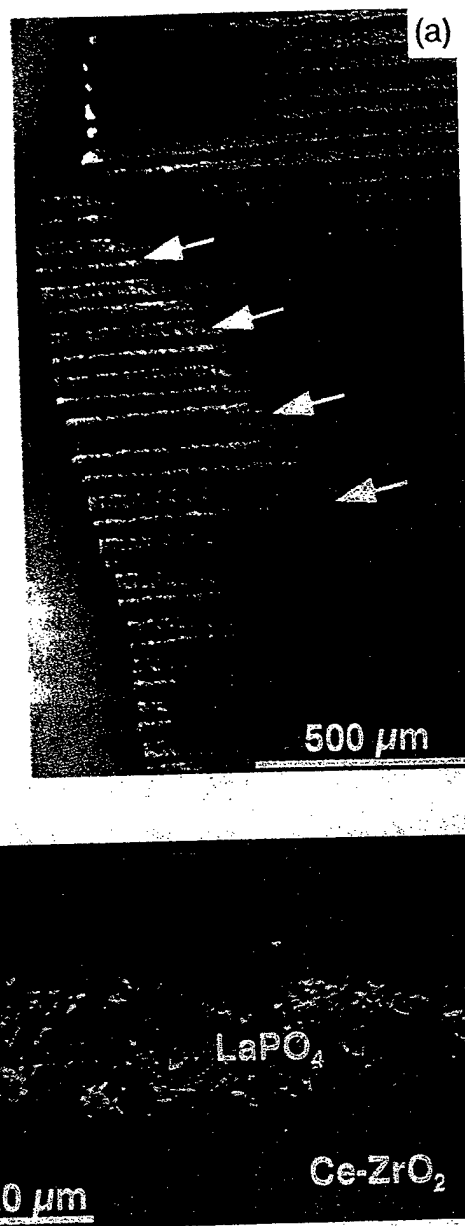


Fig. 8. Broken notched beam of multilayered composite of Ce-ZrO_2 and LaPO_4 showing evidence for both transformation toughening and interlaminar debonding. (a) Nomarski interference micrograph showing surface uplift adjacent to main crack due to tetragonal-to-monoclinic phase transformation in the ZrO_2 layers (boundary of uplifted zone indicated by arrows). (b) SEM micrograph showing cracking within LaPO_4 layers in uplifted region adjacent to main crack.

IV. Discussion

The results of the previous section indicate that, when Ce-stabilized zirconia and LaPO_4 were in contact at 1600°C , some of the Ce diffused into the LaPO_4 , displacing La. The displaced La reacted with the zirconia to form a precipitate phase containing La, Ce, and Zr, possibly a pyrochlore-like structure. When Al_2O_3 was present also in the mixed $\text{Al}_2\text{O}_3/\text{Ce-ZrO}_2$ layers, the displaced La formed a (La,Ce) magnetoplumbite as well as LaAlO_3 . In view of these results, it is likely that CePO_4 , which has the same monazite structure as LaPO_4 and has now been found to be phase-compatible with Ce-ZrO_2 ,³² would be a more suitable debonding phase for CeO_2 -stabilized ZrO_2 .

In contrast, the results indicate that Y, which forms a different (but related) phosphate structure,³³ xenotime, does not diffuse into LaPO_4 at 1600°C , and La does not diffuse out of the LaPO_4 .

The fracture behavior of the $\text{ZrO}_2/\text{LaPO}_4$ layered composites is qualitatively similar to that of $\text{Al}_2\text{O}_3/\text{LaPO}_4$ composites investigated previously.¹³ Specifically, normally incident cracks in a ZrO_2 layer appear to penetrate the ZrO_2 - LaPO_4 interface and to debond either at the LaPO_4 - ZrO_2 interface or within the LaPO_4 layer. The specific location of debonding and damage within the LaPO_4 layers is influenced by the morphology of the interface, which in these composites has roughness on the scale of the grain size (see Fig. 1). Although debonding occurs near the interface, the crack path lies both at the interface and in the LaPO_4 . This observation is consistent with the measured interlaminar toughness being approximately equal to the toughness of LaPO_4 . Despite this complication, useful insight may be gained by comparing the measured toughnesses with the analysis of interfacial debonding by He and Hutchinson.²⁰

Whether a crack approaching an interface between two materials will debond along the interface rather than penetrate into the second material depends on the ratio Γ_1/Γ_2 of the fracture energies of the interface and the second material, as well as the elastic mismatch parameter,²⁰ α , given by

$$\alpha = (E'_2 - E'_1)/(E'_2 + E'_1) \quad (1)$$

where E' is the plane strain Young's modulus. The critical values of Γ_1/Γ_2 calculated by He and Hutchinson²⁰ are shown in Fig. 10. With the toughnesses measured in the previous section, the following parameters are obtained: (1) for a crack about to

grow from LaPO_4 to ZrO_2 , $\alpha = 0.2$ ($E_1 = 133$ GPa (Ref. 9), $E_2 = 200$ GPa) and $\Gamma_1/\Gamma_2 = 0.05$; and (2) for a crack about to grow from LaPO_4 to $\text{Al}_2\text{O}_3/\text{ZrO}_2$, $\alpha = 0.35$ ($E_2 = 300$ GPa) and $\Gamma_1/\Gamma_2 \sim 0.1$. These values fall below the critical condition in Fig. 10 so that debonding is expected, as observed.

For a crack growing in the reverse direction, from zirconia to LaPO_4 , a different response is predicted. In that case, Γ_2 is the fracture energy of LaPO_4 (~ 7 J/m²) and the sign of α is changed, corresponding to interchanging the two materials. The corresponding value of Γ_1/Γ_2 (~ 1) falls above the critical condition, where the crack is predicted to grow into the LaPO_4 , as observed.

The debonding criterion in Fig. 10 is also influenced by residual stresses parallel and normal to the interface. In these composites there are two sources of residual stresses.

(i) *Transformation Stresses:* If the ZrO_2 layers were to undergo the tetragonal-to-monoclinic phase transformation, either during cooling or in the tensile stress field ahead of the incident crack, large residual stresses would be generated. The effect of these stresses can be estimated using the analysis of He et al.,³⁴ who define a normalized residual stress parameter

$$\eta = \sigma_R \sqrt{a/K} \quad (2)$$

where σ_R is the residual stress, either normal to the interface or parallel to the interface in material 2, a is a characteristic flaw

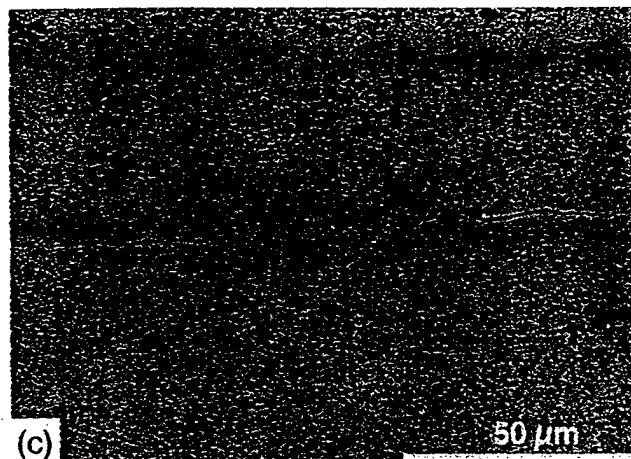
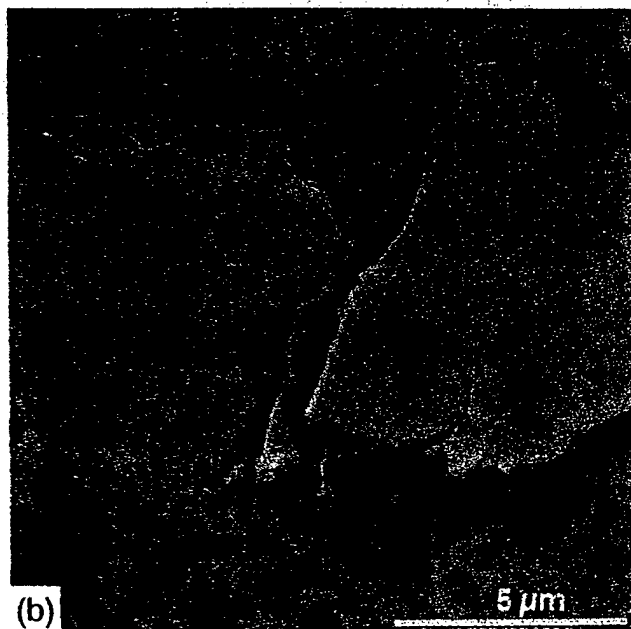
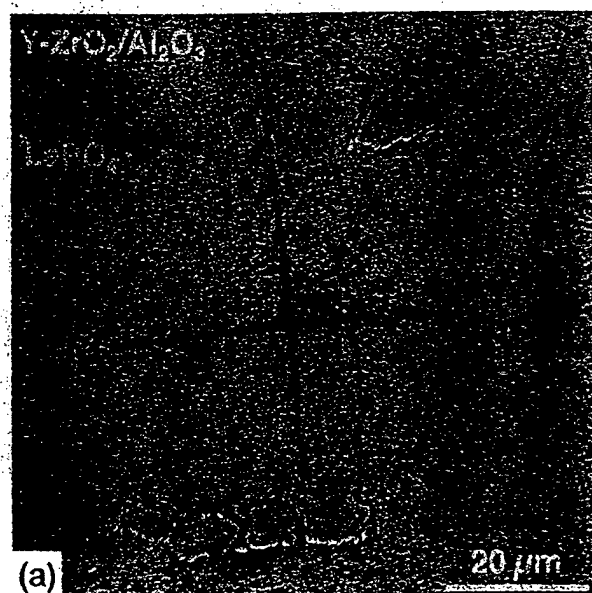


Fig. 9. Vickers indentations in composite of $\text{Y-ZrO}_2/\text{Al}_2\text{O}_3$ and LaPO_4 . (a) and (b) SEM micrographs showing damage within LaPO_4 layers. (c) Comparison of interlaminar crack length and crack length in $\text{Y-ZrO}_2/\text{Al}_2\text{O}_3$ matrix.

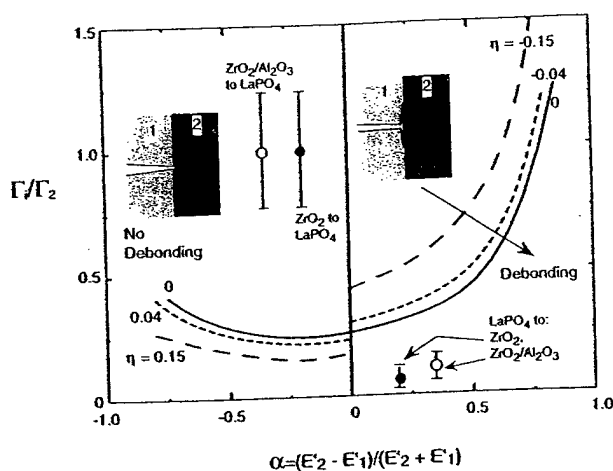


Fig. 10. Comparison of fracture energies with debonding criterion of He and Hutchinson.²⁰ Solid curve is debond criterion for tetragonal zirconia layers (negligible residual stresses). Dashed curves are approximate criteria in the presence of residual stresses:³¹ (1) $\eta = 0.15$, corresponding to ZrO_2 layers that are transformed to the monoclinic structure (residual compression in ZrO_2 layers, tension in LaPO_4 layers) and (2) $\eta = 0.04$ for $\text{ZrO}_2/\text{Al}_2\text{O}_3$ layers. Symbols represent measured properties for $\text{LaPO}_4/\text{Y-ZrO}_2$ and $\text{LaPO}_4/(\text{Y-ZrO}_2, \text{Al}_2\text{O}_3)$ systems.

size, and K is the applied stress intensity factor for the incident crack.⁴ For a composite with equal thickness layers of LaPO_4 and ZrO_2 , and with the ZrO_2 layers fully transformed, the residual stresses are as follows: zero normal to the layers; +800 MPa parallel to the layers within the LaPO_4 layers; and -800 MPa parallel to the layers within the ZrO_2 . Taking the characteristic flaw size to be equal to the grain size ($\sim 1 \mu\text{m}$) and K as the toughness of zirconia ($\sim 6 \text{ MPa}\cdot\text{m}^{1/2}$), we obtain $\eta = +0.15$ for a crack growing from transformed ZrO_2 to LaPO_4 , and $\eta = -0.15$ for a crack growing in the reverse direction. The corresponding positions of the critical debond conditions from the results of He *et al.*³⁴ are shown as broken lines in Fig. 10. For both directions of crack growth, the effect of residual stress makes the response already described more likely.

(ii) **Thermal Expansion Mismatch Stresses:** As discussed in the previous section, residual stresses due to thermal expansion mismatch are present in composites consisting of layers of $\text{Al}_2\text{O}_3\text{-ZrO}_2$ and LaPO_4 (these stresses are negligibly small in composites consisting only of ZrO_2 and LaPO_4). The sign of the mismatch is the same as that of the tetragonal-to-monoclinic transformation. The magnitude of these stresses for the 1:1 Al_2O_3 to ZrO_2 ratio is $\sim 200 \text{ MPa}$, giving $\eta = 0.04$. The corresponding shift in the critical debond condition is shown in Fig. 10; the shift does not change the behavior described above.

V. Conclusions

Lanthanum phosphate forms a weakly bonded interface with Y-stabilized zirconia and $\text{Y-ZrO}_2/\text{Al}_2\text{O}_3$, which is stable at temperatures at least as high as 1600°C . However, with Ce-stabilized ZrO_2 , counter diffusion of Ce and La produces a new pyrochlore-like phase. In the presence of two-phase $\text{Ce-ZrO}_2/\text{Al}_2\text{O}_3$, the formation of a (La,Ce) magnetoplumbite was observed. Despite these reactions, multilayered composites exhibited debonding in the LaPO_4 layers when loaded in bending.

Acknowledgment: We wish to thank Dr. John Armstrong and Paul Carpenter for their assistance with the electron microprobe measurements.

References

- M. P. Harmer, H. M. Chan, and G. A. Müller, "Unique Opportunities for Microstructural Engineering with Duplex and Laminar Ceramic Composites," *J. Am. Ceram. Soc.*, **75** [7] 1715-28 (1992).

- D. B. Marshall, J. J. Ratto, and F. F. Lange, "Enhanced Fracture Toughness in Layered Composites of Ce-ZrO_2 and Al_2O_3 ," *J. Am. Ceram. Soc.*, **74** [12] 2979-87 (1991).
- D. B. Marshall, "The Design of High Toughness Laminar Zirconia Composites," *Am. Ceram. Soc. Bull.*, **71** [6] 969-73 (1992).
- D. B. Marshall and J. J. Ratto, "Crack Resistance Curves in Layered $\text{Ce-ZrO}_2/\text{Al}_2\text{O}_3$ Ceramics," pp. 517-23 in *Science and Technology of Zirconia V*, Edited by S. P. S. Badwal, M. J. Bannister, and R. J. H. Hannink. Technomic, Lancaster, PA, 1993.
- C. J. Russo, M. P. Harmer, H. M. Chan, and G. A. Müller, "Design of a Laminated Ceramic Composite for Improved Strength and Toughness," *J. Am. Ceram. Soc.*, **75** [12] 3396-400 (1992).
- O. Prakash, P. Sarkar, and P. S. Nicholson, "Crack Deflection in Ceramic/Ceramic Laminates with Strong Interfaces," *J. Am. Ceram. Soc.*, **78** [14] 1125-27 (1995).
- P. S. Nicholson, P. Sarkar, and X. Huang, "Electrophoretic Deposition and Its Use to Synthesize $\text{ZrO}_2/\text{Al}_2\text{O}_3$ Micro-Laminate Ceramic/Ceramic Composites," *J. Mater. Sci.*, **28**, 6274-78 (1993).
- J. S. Moya, "Layered Ceramic," *Adv. Mater.*, **7**, 185-89 (1995).
- W. J. Clegg, K. Kendall, N. M. Alford, T. W. Button, and J. D. Birchall, "A Simple Way to Make Tough Ceramics," *Nature (London)*, **347**, 455-57 (1990).
- A. J. Phillips, W. J. Clegg, and T. W. Clyne, "The Correlation of Interfacial and Macroscopic Toughness in SiC Laminates," *Composites*, **24** [2] 166-76 (1993).
- H. Liu and S. M. Hsu, "Fracture Behavior of Multilayer Silicon Nitride/Boron Nitride Ceramics," *J. Am. Ceram. Soc.*, **79** [9] 2452-57 (1996).
- J. B. Davis and W. J. Clegg, "Ceramic Laminates for High Temperature Structural Applications," presented at the 97th Annual Meeting of the American Ceramic Society, Cincinnati, OH, May 3, 1995, Joint Engineering Ceramics and Basic Science Divisions (Paper No. C-37-95).
- P. E. D. Morgan and D. B. Marshall, "Ceramic Composites of Monazite and Alumina," *J. Am. Ceram. Soc.*, **78** [6] 1553-63 (1995).
- P. E. D. Morgan, D. B. Marshall, and R. M. Housley, "High Temperature Stability of Monazite-Alumina Composites," *J. Mater. Sci. Eng. A*, **195**, 215-22 (1995).
- D.-H. Kuo and W. M. Kriven, "Characterization of Yttrium Phosphate and a Yttrium Phosphate/Yttrium Aluminate Laminate," *J. Am. Ceram. Soc.*, **78** [11] 3121-24 (1995).
- D.-H. Kuo and W. M. Kriven, "Chemical Stability, Microstructure and Mechanical Behavior of LaPO_4 -Containing Ceramics," *Mater. Sci. Eng. A*, **210**, 123-34 (1996).
- P. E. D. Morgan and D. B. Marshall, "Functional Interfaces in Oxide-Oxide Composites," *J. Mater. Sci. Eng. A*, **162** [1-2] 15-25 (1993).
- M. K. Cinibulk and R. S. Hay, "Textured Magnetoplumbite Fiber-Matrix Interphase Derived Sol-Gel Fiber Coatings," *J. Am. Ceram. Soc.*, **79** [5] 1233-46 (1996).
- M. H. Lewis, M. G. Cain, P. Doleman, A. G. Razzell, and J. Gent, "Development of Interfaces in Oxide and Silicate-Matrix Composites," pp. 41-52 in *Ceramic Transactions, Vol. 58, High-Temperature Ceramic-Matrix Composites I: Design, Durability, and Performance*. American Ceramic Society, Westerville, OH, 1995.
- M.-Y. He and J. W. Hutchinson, "Crack Deflection at an Interface between Dissimilar Materials," *Int. J. Solids Struct.*, **25**, 1053-67 (1989).
- B. V. Velamakanni, J. C. Chang, F. F. Lange, and D. S. Pearson, "New Method for Efficient Colloidal Particle Packing via Modulation of Repulsive Lubricating Hydration Forces," *Langmuir*, **6** [7] 1323-25 (1990).
- J. C. Chang and B. V. Velamakanni, "Centrifugal Consolidation of Al_2O_3 and $\text{Al}_2\text{O}_3/\text{ZrO}_2$ Composite Slurries vs Interparticle Potentials: Particle Packing and Mass Segregation," *J. Am. Ceram. Soc.*, **74** [9] 2201-204 (1991).
- A. G. Evans, M. D. Thouless, D. P. Johnson-Walls, E. Y. Lu, and D. B. Marshall, "Some Structural Properties of Ceramic Matrix Fiber Composites," pp. 543-53 in *Proceedings of 5th International Conference on Composite Materials*. Metallurgical Society, Warrendale, PA, 1985.
- A. G. Evans, "Engineering Property Requirements for High Performance Ceramics," *Mater. Sci. Eng.*, **71**, 3-21 (1985).
- H. Chai, "Shear Fracture," *Int. J. Fract.*, **37**, 137-59 (1988).
- M. F. Hibbs and W. L. Bradley, "Correlations between Micromechanical Failure Processes and the Delamination Toughness of Graphite Epoxy Systems," pp. 68-97 in *Fractography of Modern Engineering Materials*, ASTM STP 948. Edited by J. E. Masters. American Society for Testing and Materials, West Conshohocken, PA, 1987.
- B. W. Smith and R. A. Grove, "Determination of Crack Propagation Directions in Graphite Epoxy Structures," see Ref. 26, pp. 68-97.
- G. R. Anstis, P. Chantikul, B. R. Lawn, and D. B. Marshall, "A Critical Evaluation of Indentation Techniques for Measuring Fracture Toughness: I. Direct Crack Measurements," *J. Am. Ceram. Soc.*, **64** [9] 533-38 (1981).
- Z. Suo and J. W. Hutchinson, "On Sandwich Test Specimens for Measuring Interface Crack Toughness," *Mater. Sci. Eng. A*, **107**, 135-43 (1989).
- S. Ho, C. Hillman, F. F. Lange, and Z. Suo, "Surface Cracking in Layers under Biaxial Residual Compressive Stress," *J. Am. Ceram. Soc.*, **78** [9] 2353-59 (1995).
- B. R. Lawn and E. R. J. Fuller, "Measurement of Thin-Layer Surface Stresses by Indentation Fracture," *J. Mater. Sci.*, **19**, 4061-67 (1984).
- J. B. Davis, D. B. Marshall, P. E. D. Morgan, and R. M. Housley, "Machineable Ceramics Based on LaPO_4 and CePO_4 ," unpublished work.
- O. Muller and R. Roy, *The Major Ternary Structural Families*. Springer-Verlag, New York, 1974.
- M.-Y. He, A. G. Evans, and J. W. Hutchinson, "Crack Deflection at an Interface between Dissimilar Elastic Materials: Role of Residual Stresses," *Int. J. Solids Struct.*, **31** [24] 3443-55 (1994).

³⁴Equation (2) is an approximate expression, valid as long as the elastic mismatch is not too large.

10.0 Nonlinear Stress-Strain Curves for Solids Containing Closed Cracks with Friction

by Lawn, B.R. and Marshall, D.B

The following section is a paper published in J. Mech. Phys. Solids, 46[1] 85-113 (1998)



Pergamon

J. Mech. Phys. Solids, Vol. 46, No. 1, pp. 85–113, 1998
© 1997 Elsevier Science Ltd
Printed in Great Britain. All rights reserved
0022-5096/97 \$17.00 + 0.00

PII: S0022-5096(97)00036-7

NONLINEAR STRESS-STRAIN CURVES FOR SOLIDS CONTAINING CLOSED CRACKS WITH FRICTION

BRIAN R. LAWN

Materials Science and Engineering Laboratory, National Institute of Standards and Technology,
Gaithersburg, MD 20899, U.S.A.

DAVID B. MARSHALL

Rockwell Science Center, 1049 Camino Dos Rios, Thousand Oaks, CA 91360, U.S.A.

(Received 11 February 1997; in revised form 17 May 1997)

ABSTRACT

Solutions for the uniaxial stress-strain response of a body containing a distribution of non-interacting nonlinear cracks are derived. First, building on energy formalisms outlined by previous workers, general solutions are derived for the body containing cracks with dissipative tractions at their surfaces, in either tension or compression loading. The special case of a body in compression loading with sliding closed cracks governed by a general friction law is then considered as a case study. The friction law contains two shear resistance terms: a “friction coefficient” term proportional to the resolved normal compression stress across the crack plane; and a “cohesion” term representing the intrinsic shear resistance of the closed crack. Inclusion of the latter term is critical to the existence of a well-defined yield point in the stress-strain curve. It is assumed that the cracks do not extend at their ends during the loading-unloading-reloading cycle; they are, however, allowed to undergo reverse sliding during the unloading. Two crack distributions are considered: all cracks aligned, leading to linear expressions for both the elastic and quasi-plastic stress-strain regions; and cracks randomly oriented, with more complex (but nonetheless tractable) expressions for the quasi-plastic regions. The resultant nonlinear stress-strain curves exhibit cyclic hysteresis, to an extent dependent on friction and crack configuration parameters. Illustrative stress-strain curves are generated for selected ranges of these controlling parameters. An outcome of the analysis is the potential link to microstructural variables, via the crack configuration parameter, offering the prospect for predictions of damage accumulation in real microstructures. The model also offers the prospect of accounting for fatigue properties, via attrition of the frictional resistance at the sliding crack surfaces. © 1997 Elsevier Science Ltd. All rights reserved

Keywords: A. fracture mechanisms, A. microcracking, A. microstructures, B. constitutive behavior, B. friction.

1. INTRODUCTION

The class of problems involving ordinarily brittle materials with nonlinear constitutive stress-strain responses has received surprisingly little attention in the mechanics literature. Such nonlinear responses are common in rocks (Jaeger and Cook, 1971; Paterson, 1978) and concretes (Shah, *et al.*, 1995), and even in some ceramics (Lawn *et al.*, 1994a; Padture and Lawn, 1995a,b), under constrained compression loading. In those cases the nonlinearity is attributable to sliding friction at pre-existent internal

crack-like defects (Ashby and Hallam, 1986; Horii and Nemat-Nasser, 1986; Nemat-Nasser and Obata, 1988; Kemeny and Cook, 1991; Myer *et al.*, 1992) or incipient microstructural "shear faults" (Lawn *et al.*, 1994a). Nonlinear responses are also observed in certain otherwise brittle solids under tension loading, e.g. ceramics containing "bridged" cracks where frictional tractions from grains (Mai and Lawn, 1987; Swanson *et al.*, 1987), reinforcing fibers or whiskers (Cox and Marshall, 1991) or metal ligaments (Evans, 1990) restrain crack separation. Experimentally, the nonlinearity is manifested as a departure from ideal elasticity above some threshold "yield" stress in the loading half-cycle, with hysteresis on unloading.

Linear problems, on the other hand, have been widely addressed, especially by those concerned with effective elastic moduli of bodies containing arrays of microscopic cracks. If the cracks do not extend or multiply the loading response remains linear, although with reduced modulus relative to an ideal uncracked solid, and again with possible hysteresis on unloading. A classic example is a compressively loaded body containing an array of identical closed cracks governed by a simple coefficient of sliding friction (Walsh, 1965; Jaeger and Cook, 1971). The load-unload stress-strain curve for this system has three branches: (i) loading branch, linear through the origin, but with reduced modulus owing to continuous frictional sliding at the crack interfaces; (ii) partial unloading branch, linear but with intrinsic modulus corresponding to that of an uncracked solid, reflecting a transient delay in sliding as the friction reverses; (iii) final unloading branch, linear back through the origin, with even lower modulus than during loading, as reverse sliding is activated. Linear solutions are also available for various crack geometries in tension and for various effective media approximations (Budiansky and O'Connell, 1976; Horii and Nemat-Nasser, 1983; Hashin, 1988), for fluid-filled cracks (Budiansky and O'Connell, 1976), and for crack arrays with interactions (Kachanov, 1992; Kachanov, 1994). Nonlinear stress-strain solutions in the loading half-cycle exist only for cases where the cracks are allowed to extend from their ends (Ashby and Hallam, 1986; Horii and Nemat-Nasser, 1986; Nemat-Nasser and Obata, 1988; Kemeny and Cook, 1991; Myer *et al.*, 1992).

In the first part of this paper (Section 2) we derive generalized solutions for an isotropic body containing a random three-dimensional distribution of non-interacting, stationary, nonlinear cracks for use as a basis for damage modelling. We begin by considering the energetics for cracks governed by a nonlinear constitutive displacement-stress relation, and thence present a formulation for the stress-strain response. The stress state is conveniently taken to be uniaxial, tension or compression, but may be readily extended to multiaxial loading.

In the second part of this paper we consider a special nonlinear crack system as an illustrative case study, first a body with a single closed crack (Section 3) and then a body with multiple non-interacting closed cracks (Section 4), in uniaxial compression. The problem is similar to the one described by Walsh (1965), but with sliding governed by a more generalized friction law. Specifically, the friction law includes an additional "cohesion" term, representing the shear resistance of the closed crack interface in the absence of any superimposed normal stress (Bowden and Tabor, 1986; Nemat-Nasser and Obata, 1988), and thereby contains provision for the description of a yield point in the stress-strain curve. Again, it is assumed that the cracks do not extend or increase in density during the loading-unloading cycle, although the number of

actively sliding cracks in the existing population may be a function of load. Due attention is given to the ensuing conditions for forward and reverse crack-interface sliding during loading and unloading, allowing for cyclic hysteresis. Nonlinear stress-strain relations are then derived, and illustrative load-unload curves generated, for a range of crack densities and sizes and friction terms. A key outcome of the analysis is the explicit form of these relations, offering in those cases where the cracks are associated with the microstructure a potential link to characteristic material parameters.

2. GENERAL STRESS-STRAIN RELATIONS FOR BODIES CONTAINING NONLINEAR CRACKS

In this section we derive general stress-strain relations for a body containing a distribution of randomly oriented, non-interacting slit-like cracks. The body is isotropic and linear elastic everywhere but at the crack surface, where irreversible tractions operate. These tractions are assumed to be governed by a nonlinear constitutive relation between applied stresses and crack-opening displacements. The primary source of nonlinearity of interest here is that arising from sliding frictional forces acting between closed crack surfaces in compressive loading. However, other potential sources of nonlinearity, e.g. from bridging ligaments that restrain crack opening in tensile loading, may equally well be considered. For simplicity, we will address the case of uniaxial loading. Extension to more complex, biaxial or triaxial stress states is straightforward (Kachanov, 1992; Kachanov, 1994). Our approach is analogous to that laid out by previous workers (Walsh, 1965; Budiansky and O'Connell, 1976), except that we modify the formulation in such a way as to allow for nonlinearity.

The starting point for the analysis is an expression for the complementary energy density of the cracked body as the sum of two terms: the complementary energy density for the body without cracks, plus the crack energy density W (Appendix A):

$$\int_0^\sigma \epsilon d\sigma = \sigma^2/2E_0 + W, \quad (1)$$

where ϵ is the average strain in the body, σ is the applied stress and E_0 is Young's modulus of the uncracked body. If the cracks are non-interacting, W is the sum over the energies w_i of all cracks contained within the volume V of the body:

$$W = (1/V) \sum_{i=1}^{NV} w_i, \quad (2)$$

where N is the crack number density. Differentiation of (1) yields a general strain-stress relation:

$$\epsilon = \sigma/E_0 + dW/d\sigma. \quad (3)$$

Equation (3) conveniently expresses the strain as the sum of the strain in the uncracked body and the additional nonlinear strain from the cracks.

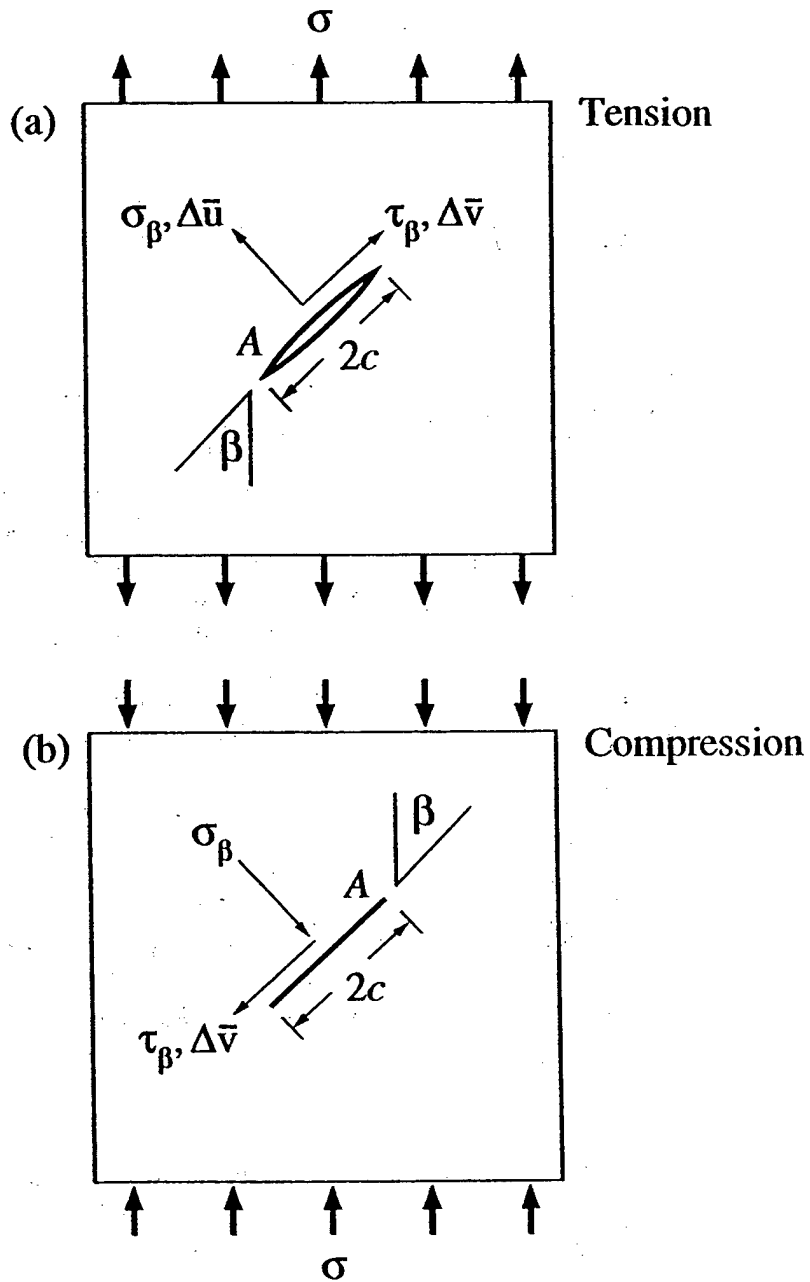


Fig. 1. Body containing crack, area A , characteristic length c ($A = \Omega c^2$), orientation β to applied stress σ : (a) tension, (b) compression. Resolved normal and shear stresses σ_β and τ_β , and corresponding displacements $\Delta\bar{u}(\sigma_\beta)$ and $\Delta\bar{v}(\sigma_\beta)$, indicated.

Now consider the crack energy w for an elastic body containing a single internal crack of area A and orientation β relative to the applied stress σ , either tension [Fig. 1(a)], or compression [Fig. 1(b)]. Resolved normal and tangential stresses σ_β and τ_β on the crack plane are

$$\sigma_\beta = \sigma \sin^2 \beta, \quad (4a)$$

$$\tau_\beta = \sigma \sin \beta \cos \beta, \quad (4b)$$

with corresponding displacement changes averaged over the crack area

$$\Delta \bar{u}(\sigma) = \bar{u}(\sigma) - \bar{u}(0), \quad (5a)$$

$$\Delta \bar{v}(\sigma) = \bar{v}(\sigma) - \bar{v}(0). \quad (5b)$$

In problems involving cracks in reverse loading with irreversible tractions at the crack surfaces, or where cracks are subject to internal residual stresses, nonzero values of $\bar{u}(0)$ and $\bar{v}(0)$ are encountered. The crack energy may be written (Appendix A)

$$\begin{aligned} w(\sigma, \beta) &= 2A \left[\int_0^{\sigma_\beta} \Delta \bar{u}(\sigma_\beta) d\sigma_\beta + \int_0^{\tau_\beta} \Delta \bar{v}(\tau_\beta) d\tau_\beta \right] \\ &= 2A \int_0^\sigma [\Delta \bar{u}(\sigma, \beta) \sin^2 \beta + \Delta \bar{v}(\sigma, \beta) \sin \beta \cos \beta] d\sigma. \end{aligned} \quad (6)$$

Strictly, (6) is restricted to cracks with sliding displacements $\Delta \bar{v}$ parallel to the resolved shear stress τ_β ; this condition is satisfied for any crack with an elliptical front, including the limiting cases of penny and straight-front plane cracks, provided one of the elliptical axes is aligned along the direction of resolved shear stress (Appendix B). For non-aligned elliptical cracks a tensor form of (6) is needed.

Now suppose the body contains a density N of non-interacting randomly oriented cracks. If N is sufficiently large, the sum in (2) may be replaced by an integral over all orientations β (Walsh, 1965; Budiansky and O'Connell, 1976):

$$W(\sigma) = N \int_0^{\pi/2} w(\sigma, \beta) \cos \beta d\beta. \quad (7)$$

Where the cracks are of uniform shape and size, (6) and (7) may be combined to give

$$W(\sigma) = 2NA \int_0^{\pi/2} \int_0^\sigma \sin \beta \cos \beta [\Delta \bar{u}(\sigma, \beta) \sin \beta + \Delta \bar{v}(\sigma, \beta) \cos \beta] d\sigma d\beta. \quad (8)$$

Where cracks are not active over the entire angular range (as in the case for cracks with friction, Section 3), angular limits for β in (8) need to be appropriately restricted.

The combination of (3) and (8) provides a general expression for the stress-strain curve, in terms of the crack-surface displacements $\Delta \bar{u}(\sigma, \beta)$ and $\Delta \bar{v}(\sigma, \beta)$, i.e. in terms of the constitutive behavior of the individual cracks. These two equations provide the basic starting point for the case study of cracks with frictional sliding considered in the following section.

Before concluding this section, two special cases may be noted, as follows. (i) If the angular limits for active cracks, β_1 and β_2 , are independent of σ (linear constitutive law), then (8) may be readily differentiated with respect to σ , as required in (3):

$$dW/d\sigma = 2NA \int_{\beta_1}^{\beta_2} \sin \beta \cos \beta [\Delta \bar{u}(\sigma, \beta) \sin \beta + \Delta \bar{v}(\sigma, \beta) \cos \beta] d\beta, \quad (9)$$

leaving a single integral over a fixed range of β . (ii) If, further, the displacement functions $\Delta\bar{u}(\sigma, \beta)$ and $\Delta\bar{v}(\sigma, \beta)$ are both proportional to σ , (3) and (9) reduce to a linear stress-strain curve. Cases considered previously (Walsh, 1965; Budiansky and O'Connell, 1976; Horii and Nemat-Nasser, 1983; Hashin, 1988; Kachanov, 1992; Kachanov, 1994) are of this form. However, if either of these two conditions is not satisfied, the stress-strain curve is necessarily nonlinear and must be computed from the general form of (3) and (8).

3. STRESS-STRAIN CURVES FOR BODIES IN COMPRESSION LOADING CONTAINING CLOSED CRACKS WITH FRICTIONAL SLIDING: SINGLE-CRACK SOLUTIONS

In this section we consider the special case of a brittle solid containing a single closed crack ["shear fault" (Lawn *et al.*, 1994a)], free of internal residual stresses and with generalized sliding friction between the crack surfaces (Jaeger and Cook, 1971), in uniaxial applied compression σ . The formulation of Section 2 is applicable, with the restriction that, since the cracks are closed, normal displacements across the crack plane are precluded ($\Delta\bar{u} = 0$). Also, since we shall now be concerned exclusively with compression loading, we adopt a sign convention that takes compressive stresses and corresponding displacements as positive.

In the following section we extend the solutions to a body containing specified distributions of cracks.

3.1. Constitutive friction law

Consider a body containing a crack at orientation β [Fig. 1(b)]. Sliding of the crack surfaces is driven by the resolved shear stress τ_β [equation 4(b)] on the crack plane. Let this sliding be resisted by a frictional stress $\tau_f = \tau_c + \mu\sigma_\beta$, where τ_c is a "cohesion stress", μ is a friction coefficient and σ_β is the resolved normal stress [Equation 4(a)] (Horii and Nemat-Nasser, 1986; Nemat-Nasser and Obata, 1988):

$$\tau_f = \tau_c + \mu\sigma \sin^2 \beta. \quad (10)$$

This relationship has been confirmed extensively in direct measurements of friction in rocks and soils (Jaeger and Cook, 1971). Many studies (Walsh, 1965) use a simplified form of (10), with $\tau_c = 0$. We will show later that inclusion of the τ_c term is crucial to certain features of the stress-strain behavior, notably the existence of a yield stress (Nemat-Nasser and Obata, 1988).

3.2. Crack sliding displacements

The average sliding displacements of the closed crack surfaces are proportional to the net shear stresses acting on the crack. The general form is (Walsh, 1965; Budiansky and O'Connell, 1976)

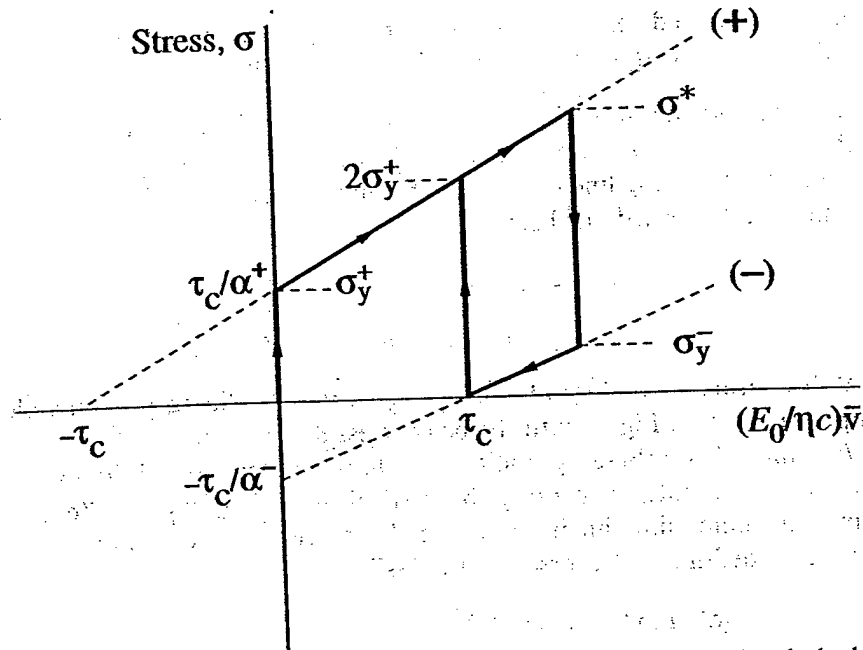


Fig. 2. Constitutive stress-displacement relation for body in compression containing single closed shear crack. Inclined lines represent sliding branches, forward (+) and reverse (-). Vertical lines represent passive non-sliding branches. Solid line segments indicate hysteric load-unload-reload cycle.

$$\bar{v} = \begin{cases} (\eta c/E_0)(\tau_\beta - \tau_t) & \text{(loading),} \\ (\eta c/E_0)(\tau_\beta + \tau_t) & \text{(unloading),} \end{cases} \quad (11a)$$

$$\bar{v} = \begin{cases} (\eta c/E_0)(\tau_\beta - \tau_t) & \text{(loading),} \\ (\eta c/E_0)(\tau_\beta + \tau_t) & \text{(unloading),} \end{cases} \quad (11b)$$

where c is a characteristic crack dimension, related to crack area by $A = \Omega c^2$, with Ω a dimensionless constant and η a dimensionless crack geometry constant (Appendix B): for penny cracks, $\Omega = \pi$ and $\eta = 8(1+\nu)/3\pi$. Note that it is \bar{v} and not $\Delta\bar{v}$ that appears in (11); since friction is involved, provision must be made for nonzero $\bar{v}(0)$ in $\Delta\bar{v} = \bar{v}(\sigma) - \bar{v}(0)$. (Equation (11) is subject to the same restriction mentioned in the preceding subsection, that the displacements must be in the same direction as the resolved shear stresses.) With (4b) and (10), (11) may be written in terms of the applied stress σ :

$$(E_0/\eta c)\bar{v} = \begin{cases} \alpha^+(\beta)\sigma - \tau_c & \text{(loading),} \\ \alpha^-(\beta)\sigma + \tau_c & \text{(unloading),} \end{cases} \quad (12a)$$

$$(E_0/\eta c)\bar{v} = \begin{cases} \alpha^+(\beta)\sigma - \tau_c & \text{(loading),} \\ \alpha^-(\beta)\sigma + \tau_c & \text{(unloading),} \end{cases} \quad (12b)$$

where we define the quantities

$$\alpha^+(\beta) = \sin \beta \cos \beta - \mu \sin^2 \beta, \quad (13a)$$

$$\alpha^-(\beta) = \sin \beta \cos \beta + \mu \sin^2 \beta. \quad (13b)$$

The constitutive relations in (12) are represented in Fig. 2 as a plot of applied stress σ against displacement term $(E_0/\eta c)\bar{v}$ for a load-unload-reload cycle. Two sliding branches (inclined solid lines) are shown: forward (+) branch [equation (12a)], with displacement-axis intercept $-\tau_c$ and stress-axis intercept τ_c/α^+ ; reverse (-) branch

[equation (12b)], with displacement-axis intercept τ_c and stress-axis intercept $-\tau_c/\alpha^-$. We identify the following stages (arrows) in the hysteretic loading cycle:

- (i) *Loading*. During initial loading, the crack faces do not slide until the applied shear stress equals the frictional resistance, corresponding to intersection of the vertical loading line $\bar{v} = 0$ with the upper, forward sliding branch in (12a), defining a "forward yield stress"

$$\begin{aligned}\sigma_y^+ &= \tau_c/\alpha^+(\beta) \\ &= \tau_c/(\sin \beta \cos \beta - \mu \sin^2 \beta).\end{aligned}\quad (14)$$

With continued loading above $\sigma = \sigma_y^+$, forward sliding proceeds along the upper branch in Fig. 2 until the peak stress $\sigma = \sigma^*$ is reached.

- (ii) *Unloading*. On unloading, the friction terms reverse sign. Initially, the crack faces remain stationary along the vertical unloading line $\bar{v} = \bar{v}(\sigma^*)$ in (12a), until this unloading line intersects the lower, reverse sliding branch $\bar{v} = \bar{v}(\sigma_y^-)$ in (12b), defining a "reverse yield stress"

$$\begin{aligned}\sigma_y^- &= [\alpha^+(\beta)\sigma^* - 2\tau_c]/\alpha^-(\beta) \\ &= [\sigma^*(\sin \beta \cos \beta - \mu \sin^2 \beta) - 2\tau_c]/(\sin \beta \cos \beta + \mu \sin^2 \beta).\end{aligned}\quad (15)$$

With continued unloading below $\sigma = \sigma_y^-$, reverse sliding proceeds along the lower branch in Fig. 2, leaving a residual displacement $\bar{v}(0) = \eta c \tau_c/E_0$ at $\sigma = 0$ in (12b). Note that if $\tau_c = 0$ [as taken in previous analyses (Walsh, 1965)], then $\bar{v}(0) = 0$ (the hysteretic cycle closes). Note also that no reverse sliding will occur at all if $\sigma_y^- \leq 0$, corresponding to $\sigma^* \leq 2\tau_c/\alpha^+(\beta)$ [i.e. peak stress less than twice the forward yield stress in (14)].

- (iii) *Reloading*. During reloading, the crack faces remain stationary, at $\bar{v} = \eta c \tau_c/E_0$, until the forward sliding branch is again intersected, at $\sigma = \sigma_y^+$, after which this branch is followed up to σ^* . Further cycling between the same zero and peak loads then repeats the hysteretic unload-reload loop.

This hysteretic formulation lays the groundwork for a consideration of fatigue, by progressive attrition of μ and τ_c , manifested in Fig. 2 as cyclic shifts in the hysteretic loop (Padture and Lawn, 1995b).

3.3. Crack energy and stress-strain curve

For a body containing a crack at orientation β in uniaxial compression σ [Fig. 1(b)], insertion of $\Delta \bar{u} = 0$ into (6) reduces the crack energy to

$$w(\sigma, \beta) = 2A \sin \beta \cos \beta \int_0^\sigma \Delta \bar{v}(\sigma) d\sigma. \quad (16)$$

This integral is evaluated by inserting (12) and (13), in conjunction with (14) and (15), for the various stages of loading, unloading and reloading. The pertinent energies at any given applied stress σ are represented by the shaded areas in the schematic

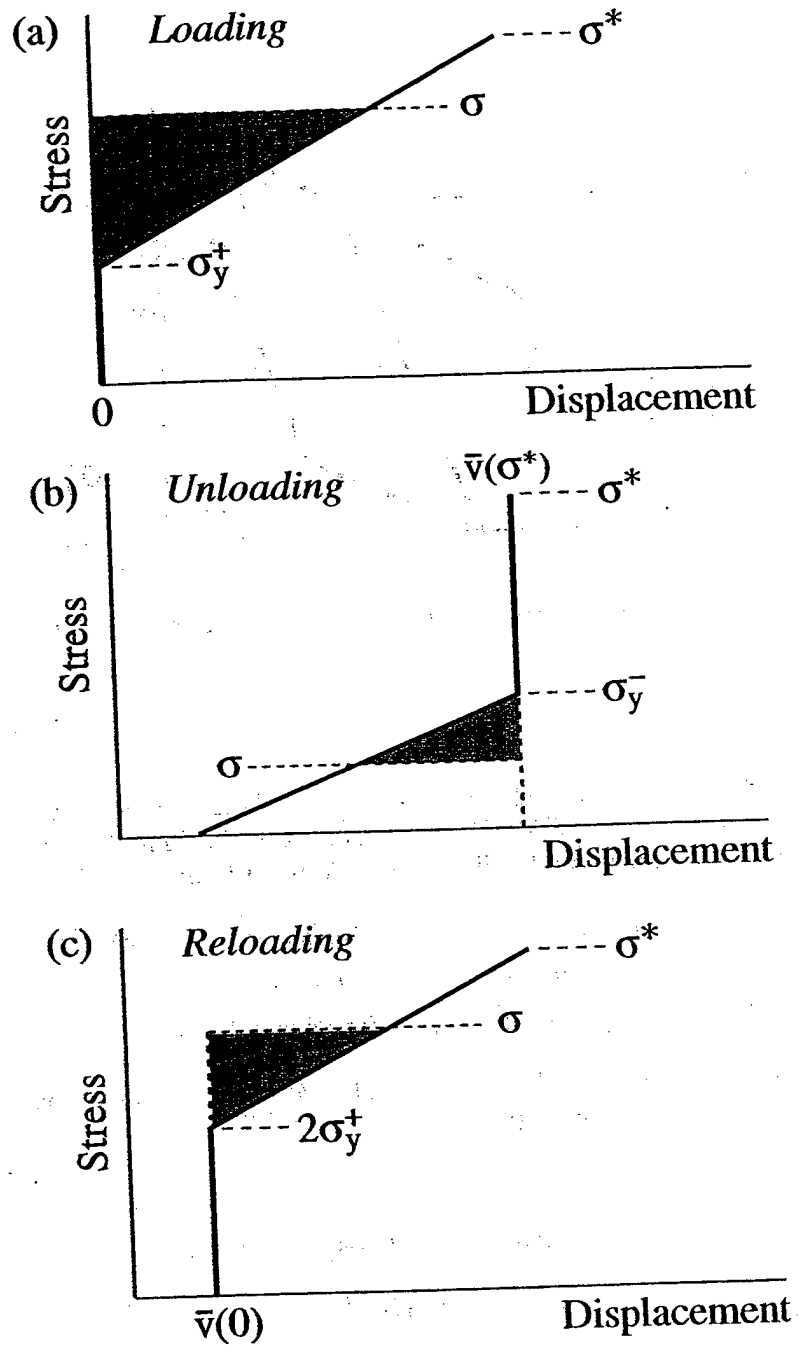


Fig. 3. Stress-displacement diagrams for body with single closed shear crack. Shaded areas represent crack energies associated with crack-surface sliding: (a) loading, (b) unloading (c) reloading.

plots of $\sigma(\bar{v})$ in Fig. 3. Note that there are zero contributions to the energy in the initially passive stages where the crack faces remain stationary: in loading within $0 \leq \sigma \leq \sigma_y^+$, unloading within $\sigma_y^- \leq \sigma \leq \sigma^*$, and reloading within $0 \leq \sigma \leq 2\sigma_y^+$. Note

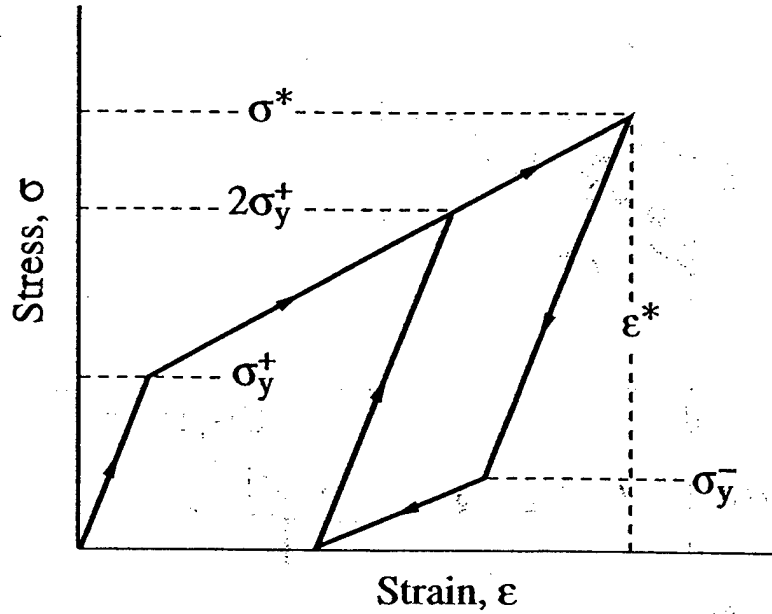


Fig. 4. Stress-strain curve for body with single closed shear crack, showing load-unload-reload cycle. Note linear segments.

also that the displacement changes used to calculate the energies, and thence the strains, are measured relative to the displacements at the beginning of sliding in each of the loading, unloading and reloading segments. Integration then gives:

$$w(\sigma, \beta) = \begin{cases} (\Omega \eta c^3 / E_0) g^+(\beta) [\sigma - \sigma_y^+(\beta)]^2 & (\text{loading}, \sigma_y^+ \leq \sigma \leq \sigma^*), \end{cases} \quad (17a)$$

$$\begin{cases} (\Omega \eta c^3 / E_0) g^-(\beta) [\sigma_y^-(\beta) - \sigma]^2 & (\text{unloading}, 0 \leq \sigma \leq \sigma_y^-), \end{cases} \quad (17b)$$

$$\begin{cases} (\Omega \eta c^3 / E_0) g^+(\beta) [\sigma - 2\sigma_y^+(\beta)]^2 & (\text{reloading}, 2\sigma_y^+ \leq \sigma \leq \sigma^*), \end{cases} \quad (17c)$$

where again we write crack area A in terms of a characteristic linear dimension c , $A = \Omega c^2$, and we define the quantities

$$\begin{aligned} g^+(\beta) &= \alpha^+(\beta) \sin \beta \cos \beta \\ &= \sin \beta \cos \beta (\sin \beta \cos \beta - \mu \sin^2 \beta), \end{aligned} \quad (18a)$$

$$\begin{aligned} g^-(\beta) &= \alpha^-(\beta) \sin \beta \cos \beta \\ &= \sin \beta \cos \beta (\sin \beta \cos \beta + \mu \sin^2 \beta). \end{aligned} \quad (18b)$$

It is instructive to construct the stress-strain curve $\sigma(\epsilon)$ for this single-crack system, as in Fig. 4. During the stages of loading, unloading and reloading where the cracks remain closed and passive, branch slopes are governed by the intrinsic modulus E_0 of the uncracked body. Forward and reverse sliding occurs along the upper and lower sliding branches, with consequent reductions in effective modulus. On these sliding

branches, the slopes of the functions $\sigma(\epsilon)$ are determined by substituting (17) into (3), with $W = w/V$ in (2):

$$(d\sigma/d\epsilon) = \begin{cases} E_0/[1 + 2\Omega\eta c^3 g^+(\beta)/V] & (\text{loading, reloading}), \\ E_0/[1 + 2\Omega\eta c^3 g^-(\beta)/V] & (\text{unloading}), \end{cases} \quad (19a)$$

which are independent of σ , and hence are constants. The hysteric cycle comprises linear segments in Fig. 4. Note again that a residual strain remains after unloading through the first complete cycle, and that subsequent reload/unload curves form a repeatable closed hysteresis loop (provided the friction parameters μ and τ_c do not degrade in successive cycles).

4. STRESS-STRAIN CURVES FOR BODIES IN COMPRESSION LOADING CONTAINING CLOSED CRACKS WITH FRICTIONAL SLIDING: MULTIPLE-CRACK SOLUTIONS

Now let us extend the analysis to a brittle solid containing a distribution of many cracks governed by the friction relation described in the previous section. To do this, we integrate the energy expressions for single cracks to determine the energies for the multiple crack system, from which the stress-strain curves may be calculated. Here, we consider two distributions: first, all cracks commonly aligned; second, cracks randomly oriented.

Before carrying out the energy and stress-strain analyses, consider the allowable crack orientation range for sliding under any given set of loading conditions.

4.1. Angular limits for sliding activity

In a body with many crack orientations, sliding activity is confined within limited ranges of β , in accordance with the conditions for forward and reverse sliding defined by the functions $\sigma_y^+(\beta)$ and $\sigma_y^-(\beta)$ in (14) and (15). These functions are plotted schematically in Fig. 5(a). The loading function $\sigma_y^+(\beta)$ has a minimum, and unloading function $\sigma_y^-(\beta)$ a maximum, at

$$\beta_{\min}^+ = \frac{1}{2} \arctan(1/\mu), \quad (20a)$$

$$\beta_{\max}^- = \arctan \{1/[(1 + \mu^2 + \mu\sigma^*/\tau_c)^{1/2} - \mu]\}, \quad (20b)$$

defining yield points $\sigma_y^+(\beta_{\min}^+)$ and $\sigma_y^-(\beta_{\max}^-)$. The active angular ranges at any given applied stress σ are then determined as intersections between the horizontal heavy dashed line representing this stress and the appropriate $\sigma_y^+(\beta)$ and $\sigma_y^-(\beta)$ curves. The range β_1^+ to β_2^+ for forward sliding expands with increasing stress above $\sigma = \sigma_y^+(\beta_{\min}^+)$, to a maximum at $\sigma = \sigma^*$. Similarly, the range β_1^- to β_2^- for reverse sliding expands with decreasing applied stress below $\sigma = \sigma_y^-(\beta_{\max}^-)$, to a maximum at $\sigma = 0$. With the exception of the special case $\tau_c = 0$, the maximum range for reverse sliding is smaller than the maximum range for forward sliding. Note that in no case is the angular range of activity complete through the loading-unloading cycle.

For reloading, recall from Section 3.2 that (14) prevails, but with τ_c replaced by

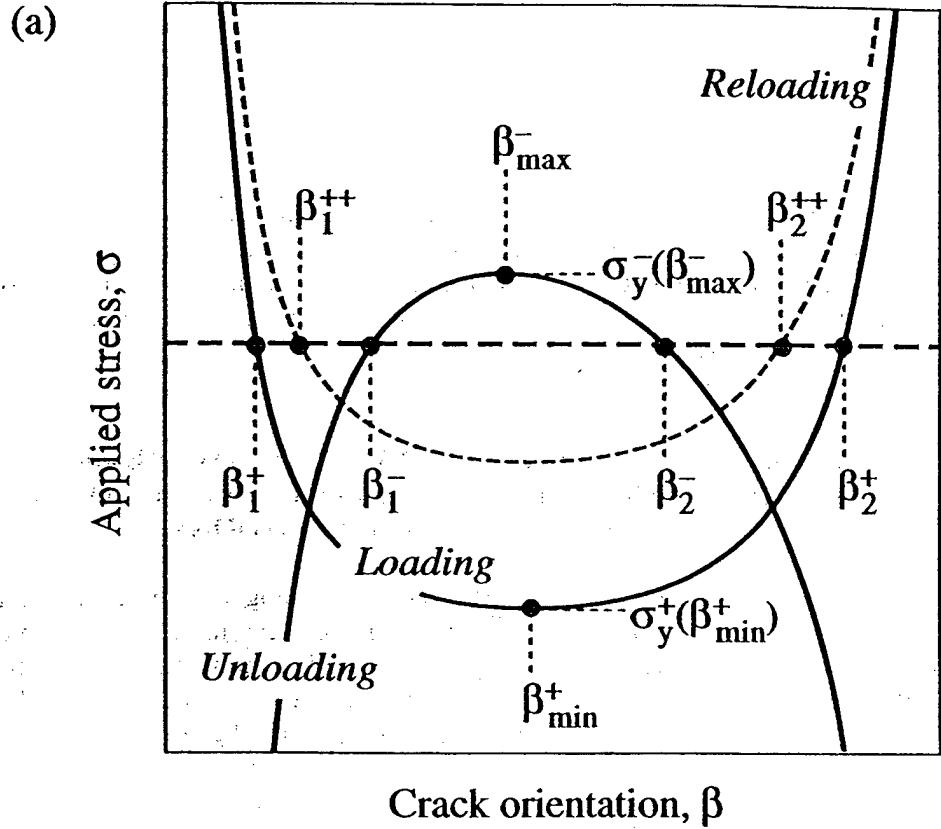


Fig. 5. Plots of loading $\sigma_y^+(\beta)$ and unloading $\sigma_y^-(\beta)$ functions in (14) and (15) (heavy curves). (a) Schematic plot, illustrating angular limits for crack-surface sliding at any specified applied stress σ (heavy horizontal dashed line). (b) Analytical plot, for indicated values of τ_c/σ^* , at $\mu = 0$. (c) Same as (b), but for $\mu = 0.5$.

$2\tau_c$. Hence, (20a) remains valid, and the appropriate $\sigma_y^+(\beta)$ curve is simply displaced upward on the stress axis by a factor of two, as indicated by the dashed curve in Fig. 5(a) (the unloading curves are unchanged). Accordingly, the active range β_1^{++} to β_2^{++} for reloading will be somewhat lower than for loading. At the same time, the maximum angular range for reloading (at $\sigma = \sigma^*$) is the same as the maximum range for reverse sliding (at $\sigma = 0$), resulting in a closed unloading-reloading hysteresis loop.

Also shown in Fig. 5 are plots of (14) and (15) for selected values of μ and τ_c (all stresses normalized to σ^*). For $\mu = 0$ [Fig. 5(b)] the extreme in these curves occur universally at $\beta = \beta_{\min}^+ = \beta_{\max}^- = 45^\circ$, regardless of τ_c . The forward yield stress $\sigma_y^+(\beta_{\min}^+)$ increases, and the reverse yield stress $\sigma_y^-(\beta_{\max}^-)$ decreases, with increasing τ_c . For $\mu = 0.5$ [Fig. 5(c)], the angular extrema shift to lower β . At the same time, $\sigma_y^+(\beta_{\min}^+)$ increases and $\sigma_y^-(\beta_{\max}^-)$ decreases still further. The net effect of increasing either of the friction parameters μ and τ_c is to diminish the angular range of crack sliding at any given stress level.

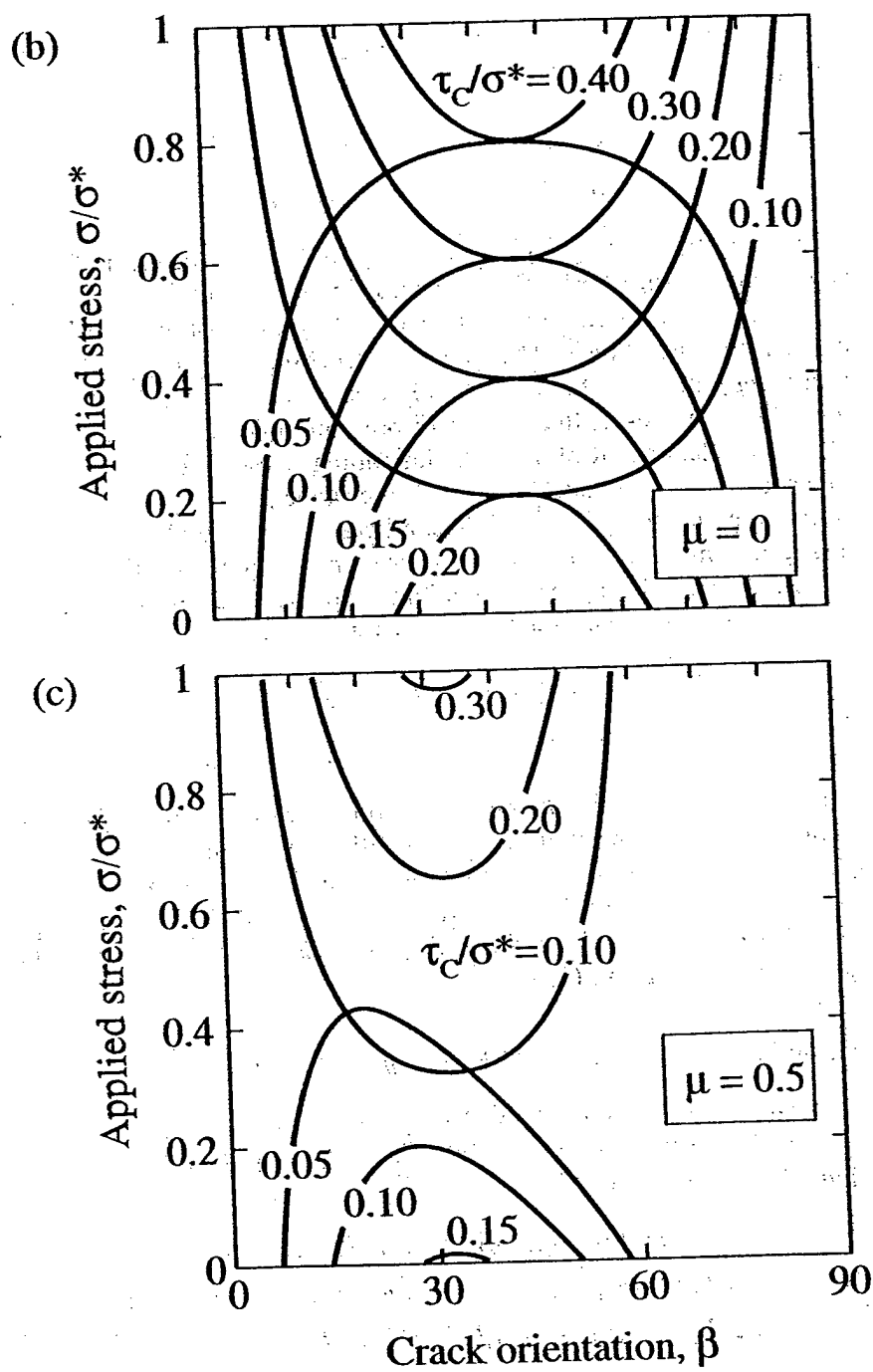


Fig. 5—Continued.

Generally, the limiting relations $\sigma = \sigma_y^+(\beta)$ and $\sigma = \sigma_y^-(\beta)$ in (14) and (15) must be solved numerically for β_1 and β_2 , but two special cases give explicit solutions:

- (i) *Zero cohesion stress*, $\tau_c = 0$, the case considered by Walsh (Walsh, 1965). We obtain

$$\beta_1^+ = 0, \quad \beta_2^+ = \arctan(1/\mu), \quad (21a)$$

$$\beta_1^- = 0, \quad \beta_2^- = \arctan[(\sigma^* - \sigma)/\mu(\sigma^* + \sigma)]. \quad (21b)$$

In this case, the loading angular range β_1^+ to β_2^+ is independent of σ . This stress independence, together with the proportional displacement-stress relation at $\tau_c = 0$ in (12), accounts for the linear loading stress-strain curve through the origin found by Walsh. The fact that the range β_1^+ to β_2^+ diminishes with increasing μ also accounts for the reduced modulus relative to the uncracked body. Note, however, that the corresponding unloading angular range β_1^- to β_2^- is not independent of σ , so the unloading stress-strain curve is necessarily nonlinear. Upon unloading to $\sigma = 0$, the range β_1^- to β_2^- in (21b) is identical to the range β_1^+ to β_2^+ in (21a)—i.e. all cracks which undergo forward sliding during loading ultimately restore at the completion of the full loading cycle to their initial state. In this case reloading simply retraces the loading curve.

- (ii) *Zero friction coefficient*, $\mu = 0$. In this case, we obtain

$$\beta_1^+ = \frac{1}{2} \arcsin(2\tau_c/\sigma), \quad \beta_2^+ = \pi/2 - \beta_1^+, \quad (22a)$$

$$\beta_1^- = \frac{1}{2} \arcsin[4\tau_c/(\sigma^* - \sigma)], \quad \beta_2^- = \pi/2 - \beta_1^-, \quad (22b)$$

where the angular ranges are dependent on σ , guaranteeing a nonlinear stress-strain curve. It follows that any combination of nonzero τ_c and μ will always result in nonlinear curves. Note that the range β_1^- to β_2^- at complete unloading, $\sigma = 0$ in (22b), is always less than the range β_1^+ to β_2^+ at peak loading, $\sigma = \sigma^*$ in (22a), so hysteresis with residual displacements is general. In reloading, τ_c is again replaced by $2\tau_c$ in (22a).

4.2 Energy and stress-strain curve: body with aligned cracks

Now consider a body containing a density N of non-interacting cracks of uniform size c , all aligned at some fixed orientation β . Then the energy density W in (2) is simply equal to Nw , with w from (17):

$$W(\sigma) = \begin{cases} (\rho/E_0)g^+(\beta)[\sigma - \sigma_y^+(\beta)]^2 & \text{(loading, } \sigma_y^+ \leq \sigma \leq \sigma^*), \\ (\rho/E_0)g^-(\beta)[\sigma_y^-(\beta) - \sigma]^2 & \text{(unloading, } 0 \leq \sigma \leq \sigma_y^-), \\ (\rho/E_0)g^+(\beta)[\sigma - 2\sigma_y^+(\beta)]^2 & \text{(reloading, } 2\sigma_y^+ \leq \sigma \leq \sigma^*), \end{cases} \quad (23a)$$

$$W(\sigma) = \begin{cases} (\rho/E_0)g^-(\beta)[\sigma_y^-(\beta) - \sigma]^2 & \text{(unloading, } 0 \leq \sigma \leq \sigma_y^-), \end{cases} \quad (23b)$$

$$W(\sigma) = \begin{cases} (\rho/E_0)g^+(\beta)[\sigma - 2\sigma_y^+(\beta)]^2 & \text{(reloading, } 2\sigma_y^+ \leq \sigma \leq \sigma^*), \end{cases} \quad (23c)$$

where we define a dimensionless parameter containing all the configurational information (size, shape, density) on the cracks,

$$\rho = \Omega\eta Nc^3. \quad (24)$$

For penny cracks and Poisson's ratio $\nu = 0.25$, $\rho = 2Nc^3$.

The assumption of fixed β in (23) leads to explicit expressions for the stress-strain curves from (3). Moreover, by defining normalized stress σ/σ^* and strains $\varepsilon E_0/\sigma^*$, these expressions take on universal forms. Then only three parameters are needed to describe the stress-strain curve completely: τ_c/σ^* , the normalized cohesion stress; μ , the friction coefficient; and ρ the crack configuration coefficient. All segments of the stress-strain curve for the cracked body remain linear (cf. Fig. 4), with slopes as follows: for the passive loading-unloading-reloading branches, unity (as for the reference uncracked body); for the sliding branches, reduced values [cf. (19)].

$$d(\sigma/\sigma^*)/d(\varepsilon E_0/\sigma^*) = \begin{cases} 1/[1+2\rho g^+(\beta)], & (\text{loading, reloading}), \\ 1/[1+2\rho g^-(\beta)] & (\text{unloading}). \end{cases} \quad (25a)$$

$$(25b)$$

Stress-strain curves for the special crack orientation $\beta = \beta_{\min}^+$, i.e. the configuration of maximum degree of sliding, are plotted in Figs 6–8, for selected values of τ_c/σ^* , μ and ρ . Various degrees of nonlinearity and hysteresis are evident (cf. Fig. 4 for notation):

- (i) *Effect of cohesion stress.* Figure 6 shows curves for $\tau_c/\sigma^* = 0, 0.1, 0.2$ and 0.3 , at fixed $\mu = 0.25$ and $\rho = 2$. In these plots the principal influence of τ_c is in the critical stresses $\sigma_y^+ = \sigma_y^+(\beta_{\min}^+)$ and $\sigma_y^- = \sigma_y^-(\beta_{\min}^+)$. At $\tau_c/\sigma^* = 0$, the loading curve is linear through the origin but with diminished modulus $E < E_0$, since all cracks within the active (load-invariant) angular range (Section 3.2) undergo immediate forward sliding at $\sigma = \sigma_y^+ = 0$. The cracks initially unload along a branch with modulus E_0 to σ_y^- , corresponding to the onset of reverse sliding, and thereafter along a branch with even more diminished modulus, ultimately returning to the origin. The system therefore absorbs energy in each cycle, but leaves zero residual strain. At $\tau_c/\sigma^* = 0.1$, initial loading occurs with modulus E_0 to a yield point σ_y^+ , and thereafter with reduced slope to σ^* . Unloading again occurs along two branches; but with a lower critical reverse sliding stress σ_y^- than at $\tau_c/\sigma^* = 0$. The hysteresis is accentuated, and the residual strain is no longer zero. At $\tau_c/\sigma^* = 0.2$, σ_y^+ is yet higher, but now $\sigma_y^- < 0$, so that while hysteresis remains pronounced, reverse sliding is suppressed. At $\tau_c/\sigma^* = 0.3$, σ_y^+ lies just below σ^* , and the hysteresis is substantially diminished.
- (ii) *Effect of friction coefficient.* Figure 7 shows curves for $\mu = 0, 0.5$ and 1 , at fixed $\tau_c/\sigma^* = 0.1$ and $\rho = 2$. Here, the effect of μ is felt both in the critical stresses σ_y^+ and σ_y^- and in the slopes of the nonlinear branches. The limiting case $\mu = 0$ is that of pure cohesion-type friction. In contrast with the case $\tau_c = 0$ in Fig. 6, a yield point σ_y^+ in the loading half-cycle (as well as σ_y^- in the loading half-cycle) is apparent, since a threshold stress must now be exceeded in order for forward sliding to occur. Hysteresis and residual strain are manifest. At $\mu = 0.5$, σ_y^+ increases and σ_y^- decreases, and the hysteretic loop is broader. At $\mu = 1$, $\sigma_y^- < 0$, so the unloading is completely elastic, and hysteresis is diminished.

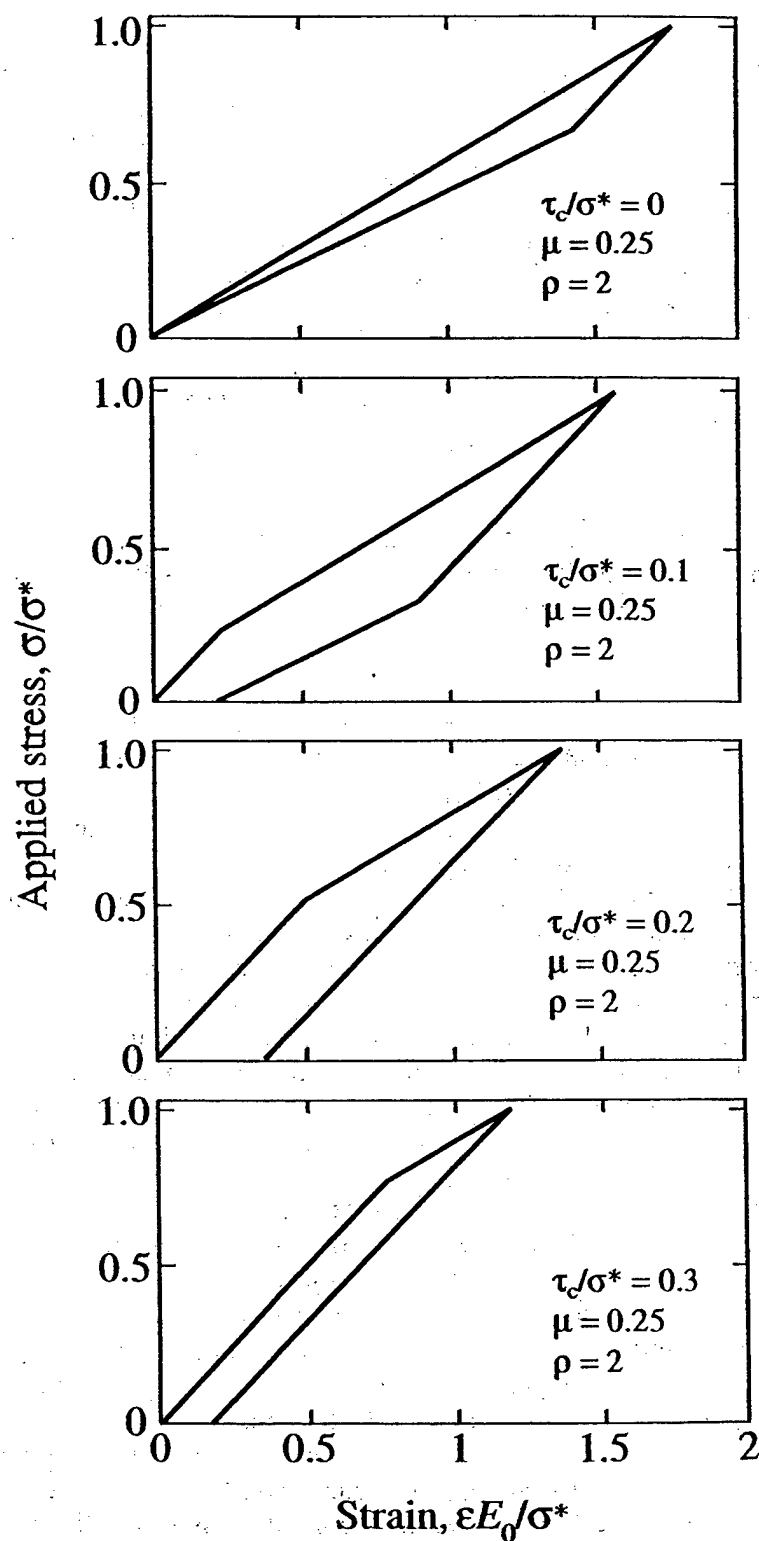


Fig. 6. Stress-strain curves for aligned cracks, evaluated from (3) and (23). Showing effect of cohesion stress: $\tau_c/\sigma^* =$ (a) 0, (b) 0.1, (c) 0.2 and (d) 0.3, at fixed $\mu = 0.25$ and $\rho = 2$.

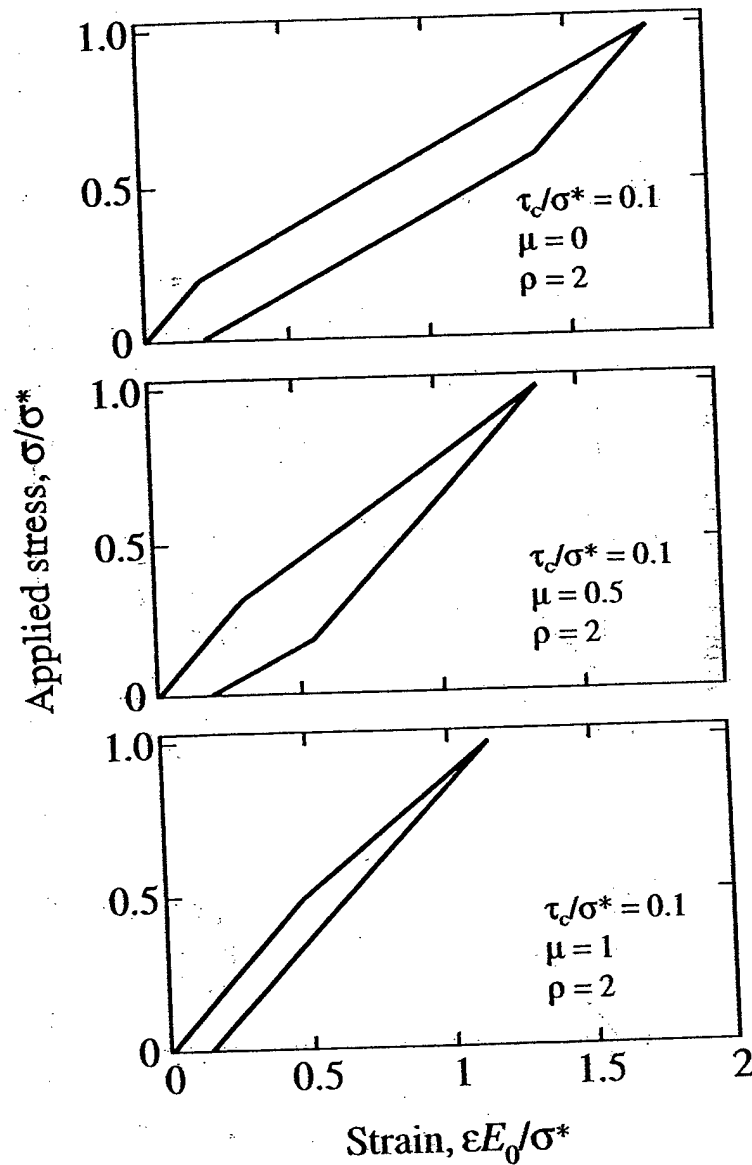


Fig. 7. Stress-strain curves for aligned cracks, evaluated from (3) and (23). Showing effect of coefficient of friction: $\mu =$ (a) 0, (b) 0.5 and (c) 1, at fixed $\tau_c/\sigma^* = 0.1$ and $\rho = 2$.

- (iii) *Effect of crack density.* Figure 8 shows curves for $\rho = 0, 1$ and 2 , at fixed $\tau_c/\sigma^* = 0.1$ and $\mu = 0.25$. Now it is only the slopes of the nonlinear branches that are affected, with σ_y^+ and σ_y^- invariant. The case $\rho = 0$ is trivial, corresponding to an ideally elastic response. Increasing ρ through 1 to 2 progressively decreases the slopes of the sliding branches, with attendant increasing hysteresis as the number of active sources increases.

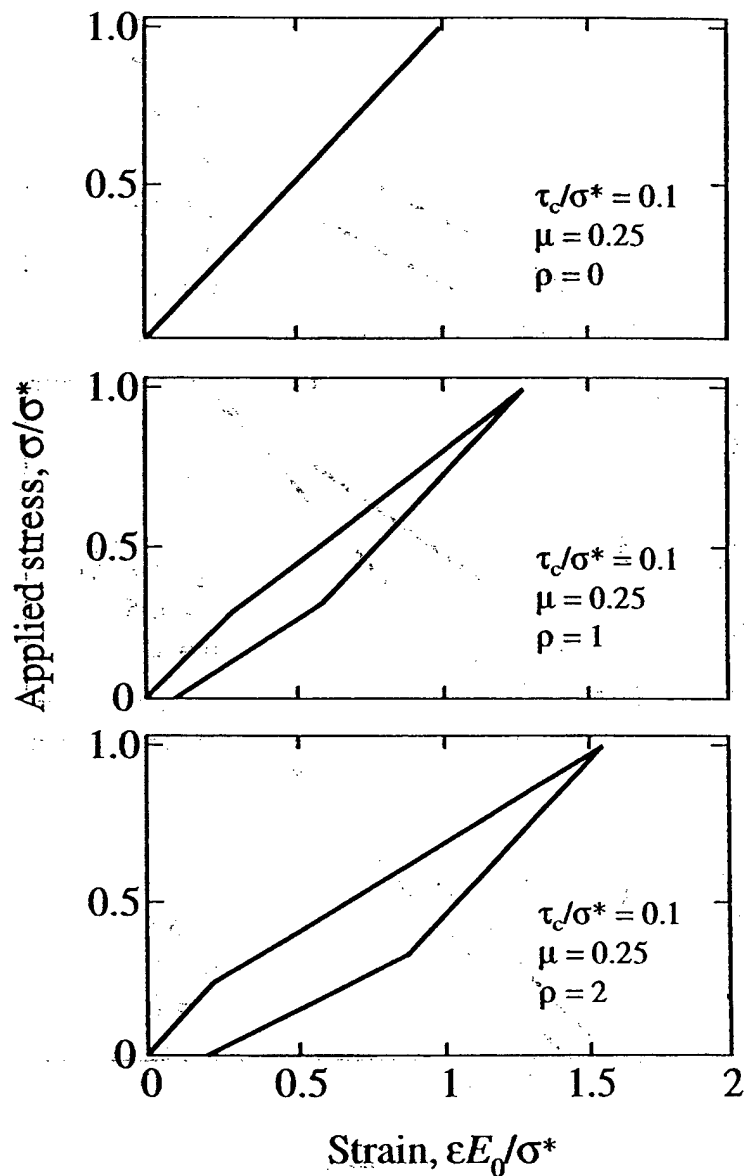


Fig. 8. Stress-strain curves for aligned cracks, evaluated from (3) and (23). Showing effect of crack density: $\rho = 0, 1$ and 2 , at fixed $\tau_c/\sigma^* = 0.1$ and $\mu = 0.25$.

4.3. Energy and stress-strain curve: body with randomly oriented cracks

For the same body containing a density N of non-interacting cracks of uniform size c , but now with the cracks randomly oriented, the energies in (7) and (17) must be integrated over all angles β within which sliding occurs [Fig. 5(a)]:

$$W(\sigma) = \begin{cases} (\rho/E_0) \int_{\beta_1^+}^{\beta_2^+} g^+(\beta) \cos \beta [\sigma - \sigma_y^+(\beta)]^2 d\beta & \text{(loading, } \sigma_y^+(\beta_{\min}^+) \leq \sigma \leq \sigma^*), \quad (26a) \\ (\rho/E_0) \int_{\beta_1^-}^{\beta_2^-} g^-(\beta) \cos \beta [\sigma_y^-(\beta) - \sigma]^2 d\beta & \text{(unloading, } 0 \leq \sigma \leq \sigma_y^-(\beta_{\max}^-)], \quad (26b) \\ (\rho/E_0) \int_{\beta_1^{++}}^{\beta_2^{++}} g^+(\beta) \cos \beta [\sigma - 2\sigma_y^+(\beta)]^2 d\beta & \text{(reloading, } 2\sigma_y^+(\beta_{\min}^+) \leq \sigma \leq \sigma^*), \quad (26c) \end{cases}$$

with the angular ranges determined in Section 4.1.

As in the previous subsection, it is convenient to introduce stress and strain normalizations σ/σ^* and $\varepsilon E_0/\sigma^*$. Substituting (26) into (3), we obtain the dimensionless stress-strain relations:

$$\varepsilon E_0/\sigma^* = \begin{cases} \sigma/\sigma^* + \rho \int_{\beta_1^+}^{\beta_2^+} g^+(\beta) \cos \beta [\sigma/\sigma^* - \sigma_y^+(\beta)/\sigma^*]^2 d\beta & \text{[loading, } \sigma_y^+(\beta_{\min}^+) \leq \sigma \leq \sigma^*], \quad (27a) \\ \sigma/\sigma^* + \rho \int_{\beta_1^-}^{\beta_2^-} g^-(\beta) \cos \beta [\sigma_y^-(\beta)/\sigma^* - \sigma/\sigma^*]^2 d\beta & \text{[unloading, } 0 \leq \sigma \leq \sigma_y^-(\beta_{\max}^-)], \quad (27b) \\ \sigma/\sigma^* + \rho \int_{\beta_1^{++}}^{\beta_2^{++}} g^+(\beta) \cos \beta [\sigma/\sigma^* - 2\sigma_y^+(\beta)/\sigma^*]^2 d\beta & \text{[reloading, } 2\sigma_y^+(\beta_{\min}^+) \leq \sigma \leq \sigma^*]. \quad (27c) \end{cases}$$

Since the limits β_1 and β_2 are themselves functions of σ/σ^* , τ_c/σ^* and μ (Section 4.1), the functions in (27) are again expressible entirely in terms of just three parameters, τ_c/σ^* , μ and ρ (Section 4.2).

Figure 9 shows a stress-strain curve computed from (27) using $\tau_c/\sigma^* = 0.1$, $\mu = 0.25$ and $\rho = 2$, for comparison with the corresponding plot for aligned cracks (dashed lines). The degree of quasi-plasticity is not so pronounced for the randomly oriented cracks, since only the most favorably aligned cracks will begin sliding at first yield.

5. DISCUSSION

In this study we have described a model for a body containing a distribution of closed cracks of uniform size in uniaxial loading. We have presented a general formalism for either tension or compression loading, with provision for frictional tractions at the crack interface. Special attention has been given to shear cracks in

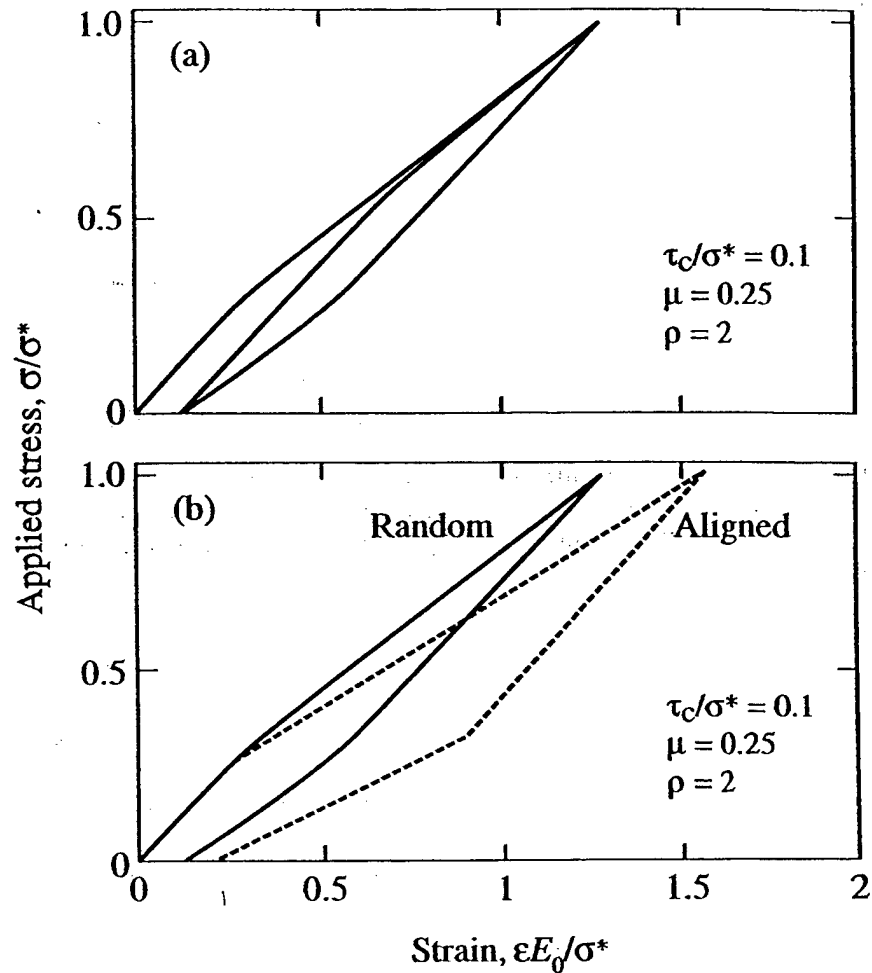


Fig. 9. Stress-strain curves for randomly oriented cracks evaluated from (3) and (26), for $\tau_c/\sigma^* = 0.1$, $\mu = 0.25$ and $\rho = 2$: (a) complete load-unload-reload cycle; (b) load-unload cycle, with corresponding result for cracks aligned at $\beta = \beta_{\min}^+$ (dashed lines).

compression loading with a crack-surface friction law of general form. The end result is a stress-strain response that is generally nonlinear, with well-defined yield stress and hysteresis in the loading-unloading-reloading cycle, as befits the real behavior of a wide range of quasi-plastic (quasi-brittle) solids. This formalism, expressible in terms of friction and crack configuration (and ultimately material microstructure—see below) parameters, may serve as a constitutive basis for analysis of damage accumulation in this interesting class of solids.

An element of the present analysis that warrants further comment is the provision for the existence of a well-defined macroscopic yield stress in compression loading, by virtue of inclusion of the cohesion term τ_c in the friction relation (10) (Sections 3 and 4). "Yield" above some initially elastic region is a distinctive feature of the stress-strain response in traditionally nonlinear materials like rocks (Jaeger and Cook, 1971) and concretes (Shah *et al.*, 1995), especially in compression testing. More recently,

quasi-plasticity has been demonstrated in tough ceramics above critical loads in Hertzian contact (Guiberteau *et al.*, 1993; Cai *et al.*, 1994a; Lawn *et al.*, 1994b), where a largely triaxial compression contact field suppresses classical cone fracture (Frank and Lawn, 1967) in these ordinarily brittle materials. This cohesion term could arise from any one of several mechanisms, whose character might alter in successive cycles: direct cohesive forces between the crack walls (chemical or van der Waals bonding); roughness of the crack walls (e.g. cleavage steps, grain boundary fractures), causing mechanical interlocking; or frictional debris trapped between the crack walls, causing residual compression stresses at the crack interface.

In quantifying this quasi-plasticity it has been found expedient to write the loading stress-strain relation in the sliding region in the empirical form (Fischer-Cripps and Lawn, 1996)

$$\sigma = Y + \alpha(\varepsilon E_0 - Y) \quad (\sigma > Y), \quad (28)$$

where Y defines the yield stress, such that $\alpha = 1$ represents the limit of full elasticity and $\alpha = 0$ full plasticity. Equation (28) has the same form as the results in Section 4.2 for aligned cracks. For cracks aligned at β_{\min}^+ , comparison with (14), (20a) and (25) gives

$$Y = \sigma_y^+(\beta_{\min}^+) = 2\tau_c h(\mu), \quad (29a)$$

$$\alpha = 1/[1 + \rho k(\mu)/2], \quad (29b)$$

with the friction-dependent functions

$$h(\mu) = 1/[(1 + \mu^2)^{1/2} - \mu], \quad (30a)$$

$$k(\mu) = [1 - \mu/(1 + \mu^2)^{1/2}]. \quad (30b)$$

Note that $Y = 0$ at $\tau_c = 0$ in (29a), confirming the necessity for τ_c to be nonzero in order for a yield stress to exist. Note also that $h(0) = 1 = k(0)$ in (30). Finally, note that for a specified peak stress σ^* there exists an upper limit to frictional resistance beyond which crack sliding cannot occur at all during the loading cycle, defined by the condition $Y > \sigma^*$, or $2\tau_c/\sigma^* > (1 + \mu^2)^{1/2} - \mu$, in (29a) and (30a). The locus of τ_c/σ^* and μ values that define this limiting condition is plotted in Fig. 10.

For the case of randomly oriented cracks, the stress-strain curve has a continuously varying slope beyond the yield point. However, since this variation is generally small (e.g. Fig. 9), we may closely approximate that portion of the stress-strain curve by a linear segment, similar to that for aligned cracks but with a greater slope. This linear segment may be represented by (28), but with an increased slope term α in (29b), corresponding to an "effective" crack density parameter ρ' . [Note this does not affect the yield point in (29a).] Table 1 lists best-fit ratios ρ'/ρ for various values of τ_c/σ^* and μ . Note that the values of this ratio become quite small for large friction terms.

At the fundamental microstructural level, the cracks envisioned in Fig. 1 (and especially in Section 3 and 4) originate as incipient defects within the material. In rocks and concretes, these defects are usually associated with pores, weak-phase inclusions, or pre-present cracks (Walsh, 1965; Jaeger and Cook, 1971; Paterson, 1978; Batzle *et al.*, 1980; Kranz, 1983; Zhang *et al.*, 1990; Kemeny and Cook, 1991;

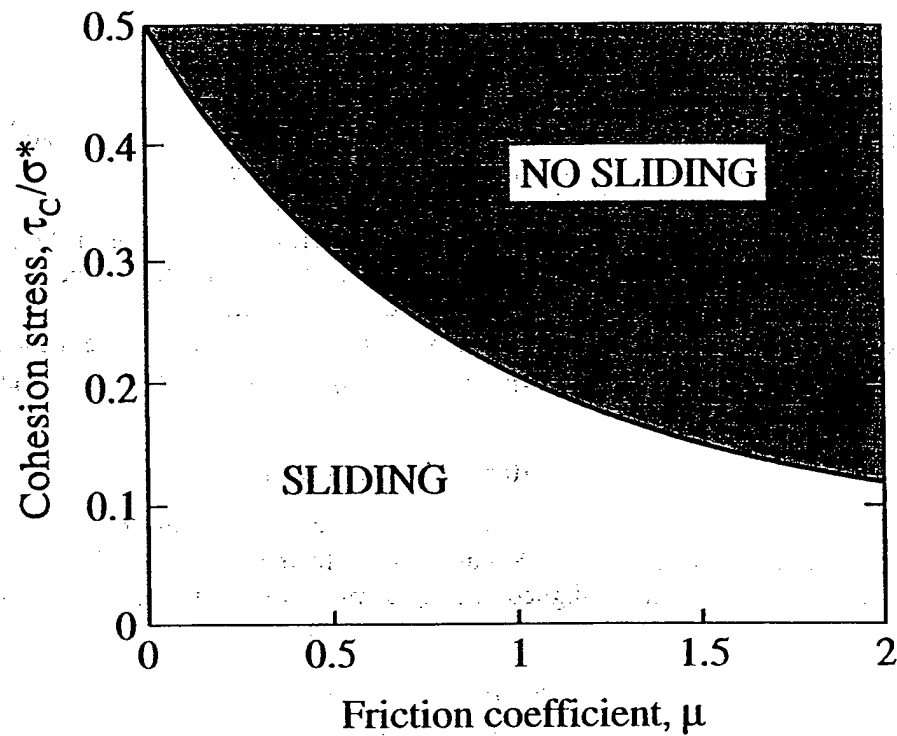


Fig. 10. Locus of τ_c/σ^* and μ values delineating domains of sliding and no sliding at crack surfaces.

Table 1. Values of ratio p'/ρ for selected friction terms

μ τ_c/σ^*	0	0.25	0.5	1
0	0.53	0.53	0.51	0.43
0.1	0.50	0.48	0.44	0.32
0.2	0.45	0.41	0.33	0.09
0.3	0.39	0.30	0.10	—

Meredith *et al.*, 1991; Wong *et al.*, 1992; Shah *et al.*, 1995). In dense ceramics, the defects are associated with weak interfaces in the microstructure, so-called "shear faults" (since they are shear-activated, exclusively in compression loading) (Lawn *et al.*, 1994b; Fischer-Cripps and Lawn, 1996). These shear faults may be twins [e.g. alumina (Guiberteau *et al.*, 1993, 1994; Wei and Lawn, 1996), silicon nitride (Xu *et al.*, 1995)], or weak grain or interphase boundaries [platelet or needle structures, e.g. in-situ toughened silicon carbide (Padture and Lawn, 1994; Padture and Lawn, 1995a, b), silicon nitride (Xu *et al.*, 1995), glass-ceramics (Cai *et al.*, 1994a, b), and particle-reinforced alumina composites (An *et al.*, 1996)].

It is through the crack configuration parameter $\rho = \Omega\eta Nc^3$ defined in (24), with its

embodiment of crack size (c), shape ($\Omega\eta$) and density (N), that we may connect the analysis most directly with the microstructure. As to shape, we have shown that $\Omega\eta = 2$ (Poisson's ratio 0.25) for the simplest case of penny cracks (Section 3.2). For the other factors, consider as an illustrative example a microstructure consisting of disk-like platelet inclusions with weak inclusion/matrix interfaces [as in several tough ceramics (Cai *et al.*, 1994a, b; Padture and Lawn, 1994, 1995a, b; An *et al.*, 1996)]; and suppose that each platelet slides along one of the large weak interfaces, i.e. one planar penny crack per platelet. The volume occupied by any one such platelet is $\pi c^2 d = \pi c^3/L$, where d is the platelet thickness and $L = c/d$ is the aspect ratio. The density N of cracks per unit volume is therefore determined by the volume fraction of platelets V_f , i.e. $N = V_f/(\pi c^3/L) = V_f L/\pi c^3$, so that $\rho = 2Nc^3 = 2V_f L/\pi$. Thus for a material in which the platelets grow uniformly at the expense of the matrix material during heat treatment (L constant), the crack density parameter is proportional to the volume fraction V_f . For a material in which the platelets grow without increasing the total concentration of platelet phase (V_f constant) [as is the case in some glass-ceramics (Fischer-Cripps and Lawn, 1996)], the crack density parameter depends only on the aspect ratio L .

Although we have treated just uniaxial loading, the analysis is readily extendable to more complex, triaxial stress states. It is necessary only to modify the expressions for σ_β and τ_β in (4) in terms of the orthogonally applied normal stresses. For the special case of superposition of a hydrostatic pressure p onto the uniaxial stress σ in Fig. 1, as pertains, for instance, to rock mechanics experiments under confining pressures (Jaeger and Cook, 1971; Paterson, 1978), the normal stress σ_β increases by p but the shear stress τ_β remains unaltered. Then (10) becomes $\tau_f = \tau_c + \mu p + \mu \sigma \sin^2 \beta$, which is equivalent to the same law as before but with an increased cohesion stress $\tau_c + \mu p$. The analysis may also be extended to inhomogeneous fields by using the stress-strain functions derived for uniform stress states in Section 3 as constitutive input into a finite element or other numerical algorithm, as has been done for Hertzian contacts in quasi-plastic ceramics (Fischer-Cripps and Lawn, 1996).

Our analysis has been restricted to non-interacting crack distributions. Strictly, allowance should be made for the fact that the energy w_i of any crack is affected by the presence of the other cracks in the distribution, through both the constitutive relation $\bar{v}(\sigma)$ of (12) and the local stresses experienced by the crack. Various approaches based on "effective medium" or "mean field" approximations have been devised to account for such interactions effects in linear systems (Budiansky and O'Connell, 1976; Horii and Nemat-Nasser, 1983; Aboudi and Benveniste, 1987; Hashin, 1988; Kachanov, 1992). Arguably, additional neighbor-neighbor ("two-body") interaction terms should become manifest in (26) as the separation between adjacent cracks approaches the crack dimension c itself. In the case of penny cracks this condition corresponds approximately to $\rho = 2Nc^3 \approx 2(1/4c^3)c^3 \approx 0.5$. On the other hand, computer simulations for various distributions indicate that elastic moduli for non-interacting, non-overlapping cracks remain accurate to surprisingly high densities, because of a tendency for cancellation of positive and negative interactions. For example, the difference in moduli for two-dimensional random arrays of cracks with and without interactions is $< 5\%$ for densities up to $\rho = 0.7$ (Kachanov, 1992). Accordingly, the present analysis may provide satisfactory approximations for high

densities of cracks. However, if in such systems overlap occurs, interaction effects can no longer be neglected.

The analysis also assumes that frictional sliding occurs at the crack surfaces without any extensile ("wing") cracking at the fault ends. Such extensile cracking has been considered widely in quasi-plastic solids under compression loading, most notably in rocks and concrete (Horii and Nemat-Nasser, 1985; Ashby and Hallam, 1986; Horii and Nemat-Nasser, 1986; Sammis and Ashby, 1986; Nemat-Nasser and Obata, 1988; Kemeny and Cook, 1991; Myer *et al.*, 1992; Nemat-Nasser and Deng, 1994). It has also been demonstrated to occur in some ceramics at Hertzian contacts, e.g. in alumina (Guiberteau *et al.*, 1993; Guiberteau *et al.*, 1994; Wei and Lawn, 1996) and silicon nitride (Xu *et al.*, 1995). In such cases, the fault dimension c increases progressively with loading, and in some cases also with unloading (Padture and Lawn, 1995a, b), further reducing the effective modulus. Where interactions become important, this can lead to strain softening, as reported in the rock and concrete literature (Jaeger and Cook, 1971; Horii and Nemat-Nasser, 1985; Horii and Nemat-Nasser, 1986; Shah *et al.*, 1995).

Finally, some implications concerning fatigue may be noted. We have made an issue of the existence of hysteresis in the loading-unloading-reloading cycles in Fig. 4. The degree of this hysteresis is governed by the friction parameters τ_c and μ (as well as the crack configuration parameter ρ) in the stress-strain formalism, as demonstrated in Figs 6-8. If these friction parameters are reduced by cyclic attrition at the sliding crack surfaces, the hysteretic loop in Fig. 4 contracts along the stress axis and expands along the strain axis, increasing the system compliance and therefore the degree of quasi-plasticity (Padture and Lawn, 1995b). Any accompanying extensile cracking from the ends of the shear cracks only exacerbates the effect (Lawn *et al.* 1994b). As has been demonstrated in repeat Hertzian contacts in ceramics, the result of such fatigue processes is a progressive damage accumulation that ultimately results in exaggerated strength loss and material removal (Padture and Lawn, 1995a, b).

ACKNOWLEDGEMENT

This work was funded by the U.S. Air Force Office of Scientific Research.

REFERENCES

- Aboudi, J. and Benvensite, Y. (1987) The effective moduli of cracked bodies in plane deformations. *Engng Fract. Mech.* **26**, 171-184.
- An, L., Chan, H. M., Padture, N. P. and Lawn, B. R. (1996) Damage-resistant alumina-based layer composites. *J. Mater. Res.* **11**, 204-210.
- Ashby, M. F. and Hallam, S. D. (1986) The failure of brittle solids containing small cracks under compressive stress states. *Acta Metall. Mater.* **34**, 497-510.
- Batzle, M. L., Simmons, G. and Siegfried, R. W. (1980) Microcrack closure in rocks under stress: direct observations. *J. Geophys. Res.* **85**, 7072-7090.
- Bowden, F. P. and Tabor, D. (1986) *The Friction and Lubrication of Solids*. Clarendon Press, Oxford.

- Budiansky, B. and O'Connell, R. J. (1976) Elastic moduli of a cracked solid. *Int. J. Solids Struct.* **12**, 81-97.
- Cai, H., Kalceff, M. A. and Lawn, B. R. (1994a) Deformation and fracture of mica-containing glass-ceramics in Hertzian contact. *J. Mater. Res.* **9**, 762-770.
- Cai, H., Kalceff, M. A. S., Hooks, B. M., Lawn, B. R. and Chyung, K. (1994b) Cyclic fatigue of a mica-containing glass-ceramic at Hertzian contacts. *J. Mater. Res.* **9**, 2654-2661.
- Cox, B. N. and Marshall, D. B. (1991) Stable and unstable solutions for bridged cracks in various specimens. *Acta Metall.* **39**, 579-589.
- Evans, A. G. (1990) Perspective on the development of high-toughness ceramics. *J. Am. Ceram. Soc.* **73**, 187-206.
- Fischer-Cripps, A. C. and Lawn, B. R. (1996) Indentation stress-strain curves for "quasi-ductile" ceramics. *Acta Metall.* **44**, 519-527.
- Frank, F. C. and Lawn, B. R. (1967) On the theory of Hertzian Fracture. *Proc. R. Soc. Lond.* **A299**, 291-306.
- Guiberteau, F., Padture, N. P., Cai, H. and Lawn, B. R. (1993) Indentation fatigue: a simple cyclic Hertzian test for measuring damage accumulation in polycrystalline ceramics. *Phil. Mag.* **A68**, 1003-1016.
- Guiberteau, F., Padture, N. P. and Lawn, B. R. (1994) Effect of grain size on Hertzian contact in alumina. *J. Am. Ceram. Soc.* **77**, 1825-1831.
- Hashin, Z. (1988) The differential scheme and its application to cracked materials. *J. Mech. Phys. Solids* **36**, 719-734.
- Horii, H. and Nemat-Nasser, S. N. (1983) Overall moduli of solids with microcracks: load-induced anisotropy. *J. Mech. Phys. Solids* **31**, 155-171.
- Horii, H. and Nemat-Nasser, S. (1985) Compression-induced microcrack growth in brittle solids: axial splitting and shear failure. *J. Geophys. Res.* **90**, 3105-3125.
- Horii, H. and Nemat-Nasser, S. (1986) Brittle failure in compression: splitting, faulting and brittle-ductile transition. *Phil. Trans. R. Soc. Lond.* **319**, 337-374.
- Jaeger, J. C. and Cook, N. G. W. (1971) *Fundamentals of Rock Mechanics*. Chapman and Hall, London.
- Kachanov, M. (1992) Effective elastic properties of cracked solids: critical review of some basic concepts. *Appl. Mech. Rev.* **45**, 304-335.
- Kachanov, M. (1994) Elastic solids with many cracks and related problems. *Adv. Appl. Mech.* **30**, 259-445.
- Kemeny, J. M. and Cook, N. G. W. Micromechanics of deformation in rock. In *Toughening Mechanisms in Quasi-Brittle Materials*, ed. S. P. Shah, pp. 287-311. Kluwer Academic Publishers, Dordrecht, The Netherlands.
- Kranz, R. L. (1983) Microcracks in rocks: a review. *Tectonophysics* **100**, 449-480.
- Lawn, B. R., Padture, N. P., Cai, H. and Guiberteau, F. (1994a), Making ceramics 'ductile'. *Science* **263**, 114-116.
- Lawn, B. R., Padture, N. P., Guiberteau, F. and Cai, H. (1994b) A model for microcrack initiation and propagation beneath Hertzian contacts in polycrystalline ceramics. *Acta Metall.* **42**, 1683-1693.
- Mai, Y.-W. and Lawn, B. R. (1987) Crack-interface grain bridging as a fracture resistance mechanism in ceramics: II. Theoretical fracture mechanics model. *J. Am. Ceram. Soc.* **70**, 289-294.
- Meredith, P. G., Ayling, M. R., Murrell, S. A. F. and Sammonds, P. R. (1991) Cracking, damage and fracture in stressed rock: a holistic approach. In *Toughening Mechanisms in Quasi-Brittle Materials*, ed. S. P. Shah, pp. 67-89. Kluwer Academic Publishers, Dordrecht, The Netherlands.
- Myer, L. R., Kemeny, J. M., Zheng, Z., Suarez, R., Ewy, R. T. and Cook, N. G. W. (1992) Extensile cracking in porous rock under differential compressive stress. *Appl. Mech. Rev.* **45**, 263-280.
- Nemat-Nasser, S. and Deng, H. (1994) Strain-rate effect on brittle failure in compression. *Acta Metall.* **42**, 1013-1024.
- Nemat-Nasser, S. and Obata, M. (1988) A microcrack model of dilatancy in brittle materials. *J. Appl. Mech.* **55**, 24-35.

- Padture, N. P. and Lawn, B. R. (1994) Toughness properties of silicon carbide with an in-situ-induced heterogeneous grain structure. *J. Am. Ceram. Soc.* **77**, 2518–2522.
- Padture, N. P. and Lawn, B. R. (1995a) Contact fatigue of a silicon carbide with a heterogeneous grain structure. *J. Am. Ceram. Soc.* **78**, 1431–1438.
- Padture, N. P. and Lawn, B. R. (1995b) Fatigue in ceramics with interconnecting weak interfaces: a study using cyclic Hertzian contacts *Acta Metall.* **43**, 1609–1617.
- Paterson, M. S. (1978) *Experimental Rock Deformation—The Brittle Field*. Springer-Verlag, Berlin.
- Sammis, C. G. and Ashby, M. F. (1986) The failure of brittle porous solids under compressive stress states. *Acta Metall.* **34**, 511–526.
- Shah, S. P., Swartz, S. E. and Ouyang, C. (1995) *Fracture Mechanics of Concrete: Applications of Fracture Mechanics to Concrete, Rock, and Other Quasi-Brittle Materials*. John Wiley, New York.
- Swanson, P. L., Fairbanks, C. J., Lawn, B. R., Mai, Y.-W. and Hockey, B. J. (1987) Crack-interface grain bridging as a fracture resistance mechanism in ceramics: I. Experimental study on alumina. *J. Am. Ceram. Soc.* **70**, 279–289.
- Walsh, J. B. (1965) The effect of cracks on the uniaxial elastic compression of rocks. *J. Geophys. Res.* **70**, 399–411.
- Wei, L. and Lawn, B. R. (1996) Thermal wave analysis of contact damage in ceramics: case study on alumina. *J. Mater. Res.* **11**, 939–947.
- Wong, T.-F., Szeto, H. and Zhang, J. (1992) Effect of loading path and porosity on the failure mode of porous rocks. *Appl. Mech. Rev.* **45**, 281–293.
- Xu, H. H. K., Wei, L., Padture, N. P., Lawn, B. R. and Yeckley, R. L. (1995) Effect of microstructural coarsening on Hertzian contact damage in silicon nitride. *J. Mater. Sci.* **30**, 869–878.
- Zhang, J., Wong, T.-F. and Davis, D. M. (1990) Micromechanics of pressure-induced grain crushing in porous rocks. *J. Geophys. Res.* **95**, 341–352.

APPENDIX A: CRACK ENERGY ANALYSIS FOR STRESS-STRAIN CURVES

In the following derivation the approach used by Budiansky and O'Connell (1976) to calculate stiffness changes in crack systems is generalized to allow for the imposition of nonlinear crack-surface tractions. Figure A1 depicts such a crack system (upper), with constitutive responses (lower), during loading to its final loaded state by two routes. An expression for the stress-strain relation follows by equating the changes in mechanical energy (potential energy of loading system plus strain energy of body) in the two routes.

To start, we restrict our consideration to just normal applied stresses, and leave inclusion of shear stresses until later. Consider first Route 1 in Fig. A1, where the body with nonlinear crack-surface tractions is loaded remotely by the applied stress σ (0 to σ_A), with attendant strain ϵ (0 to ϵ_A). The change in energy from application of the stress from zero to peak is

$$\begin{aligned}\Delta\phi_A &= -V\sigma_A\epsilon_A + V\int_0^{\epsilon_A}\sigma d\epsilon \\ &= -V\int_0^{\sigma_A}\epsilon d\sigma,\end{aligned}\tag{A1}$$

where V is the volume of the body.

Now consider Route 2 in Fig. A1, taken in two steps. In the first step, restraining tractions are applied to the crack surfaces to prevent relative displacement of the surfaces as the remote

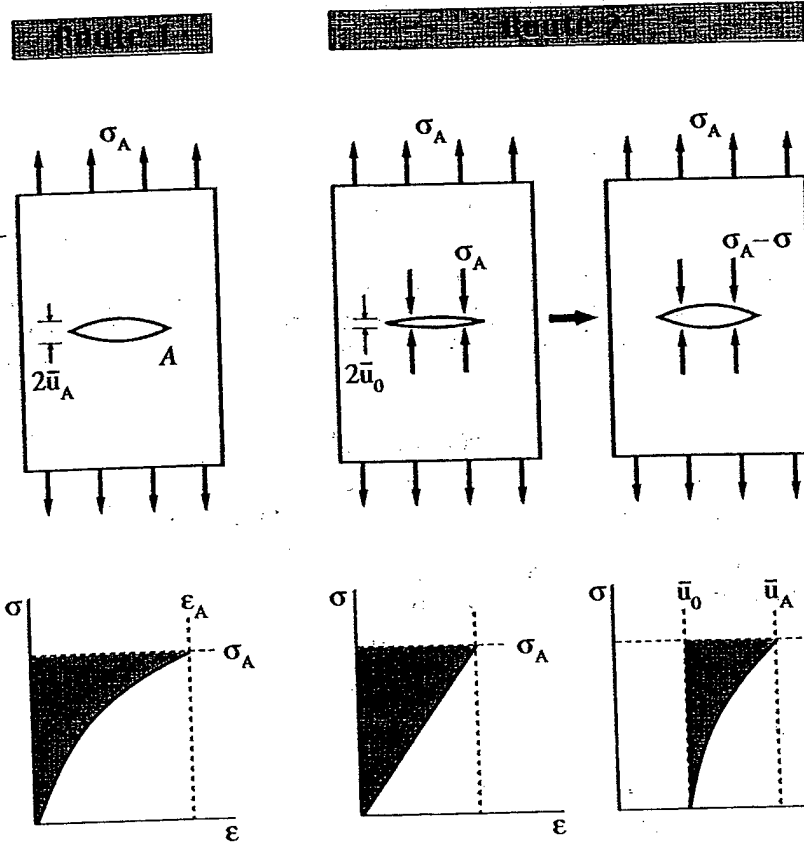


Fig. A1. Equivalent stress states for body containing crack with nonlinear tractions in normal loading. Shaded areas below indicate complementary energies in (A3).

stress σ is applied. (In general, the crack faces may be held open in the absence of any applied stress with average separation $2\bar{u}_0$, by residual stresses or wedging displacement.) The response is linear as shown, with change in energy

$$\Delta\phi_b = -V\sigma_A^2/2E_0. \quad (A2)$$

In the second step, the restraining tractions are relaxed by application of opening tractions σ on the crack surfaces (0 to σ_A), allowing the crack opening displacements to increase, thereby releasing energy w .

Since the final states in Routes 1 and 2 in Fig. A1 are identical, we may equate the energies $\Delta\phi_a$ and $\Delta\phi_b - w$ (equations A1 and A2):

$$\int_0^{\sigma_A} \epsilon d\sigma = \sigma_A^2/2E_0 + w/V. \quad (A3)$$

The three terms in (A3) correspond to the complementary energies shaded in Fig. A1. Differentiation of (A3) then gives

$$\epsilon_A = \sigma_A/E_0 + (1/V) dw/d\sigma_A. \quad (A4)$$

The energy release w associated with the crack-surface relaxation under the action of the normal applied stress σ is expressible in terms of the averaged displacement \bar{u} :

$$\begin{aligned} w &= 2A \int_{\sigma_0}^{\sigma_A} [\sigma_A - \sigma(\bar{u})] d\bar{u} \\ &= 2A \int_0^{\sigma_A} [\bar{u}(\sigma) - \bar{u}_0] d\sigma. \end{aligned} \quad (\text{A5})$$

(The factor 2 accounts for the definition of u as one half the total crack surface separation.)

If now the crack is inclined at an angle β to the applied stress, as in Fig. 1, the relaxation process can be carried out independently for the normal stress component σ_β and the resolved shear stress component τ_β :

$$w = 2A \left[\int_0^{\sigma_\beta} \Delta \bar{u}(\sigma_\beta) d\sigma_\beta + \int_0^{\tau_\beta} \Delta \bar{v}(\tau_\beta) d\tau_\beta \right], \quad (\text{A6})$$

with $\Delta \bar{u}(\sigma_\beta) = \bar{u}(\sigma_\beta) - \bar{u}(0)$ and $\Delta \bar{v}(\tau_\beta) = \bar{v}(\tau_\beta) - \bar{v}(0)$ normal and shear displacement changes, respectively.

For a body containing N cracks per unit volume, w in (A4) is replaced by the sum over all cracks contained in volume V . The crack energy density is

$$W = (1/V) \sum_{i=1}^{NV} w_i, \quad (\text{A7})$$

and (A4) becomes

$$\varepsilon_A = \sigma_A/E_0 + dW/d\sigma_A. \quad (\text{A8})$$

In the text we drop the subscript A notation in σ , ε and u , on the understanding there that these quantities denote final states.

APPENDIX B: CRACK SURFACE DISPLACEMENTS FOR ELLIPTICAL-FRONTED CRACKS

Consider an elliptical crack with semi-axes c and b parallel to the x and y axes in an infinite, homogeneous, isotropic, elastic body. A remotely applied shear stress $\tau = \tau_{xz}$ causes sliding displacements v_x . The average displacement \bar{v}_x over the crack plane can be found from a simple extension of an analysis given in Budiansky and O'Connell (1976). They pointed out that the sliding displacement can be written as

$$2v_x(x, y) = B(bc)^{1/2} (1 - x^2/c^2 - y^2/b^2)^{1/2}, \quad (\text{B1})$$

where B is a dimensionless constant (a result that follows directly from Eshelby's discovery that a homogeneous ellipsoidal inclusion under remote loading experiences uniform strain in its interior):

$$B = [4\tau_{xz}(1 - \nu^2)/E_0](b/c)^{1/2} \{k^2/[(k^2 - \nu)E(k) + \nu(1 - k^2)K(k)]\}, \quad (\text{B2})$$

with E_0 Young's modulus and ν Poisson's ratio, $k^2 = (1 - b^2/c^2)$, and $K(k)$ and $E(k)$ complete elliptical integrals of the first and second kind:

$$K(k) = \int_0^{\pi/2} (1 - k^2 \sin^2 \theta)^{-1/2} d\theta, \quad (\text{B3a})$$

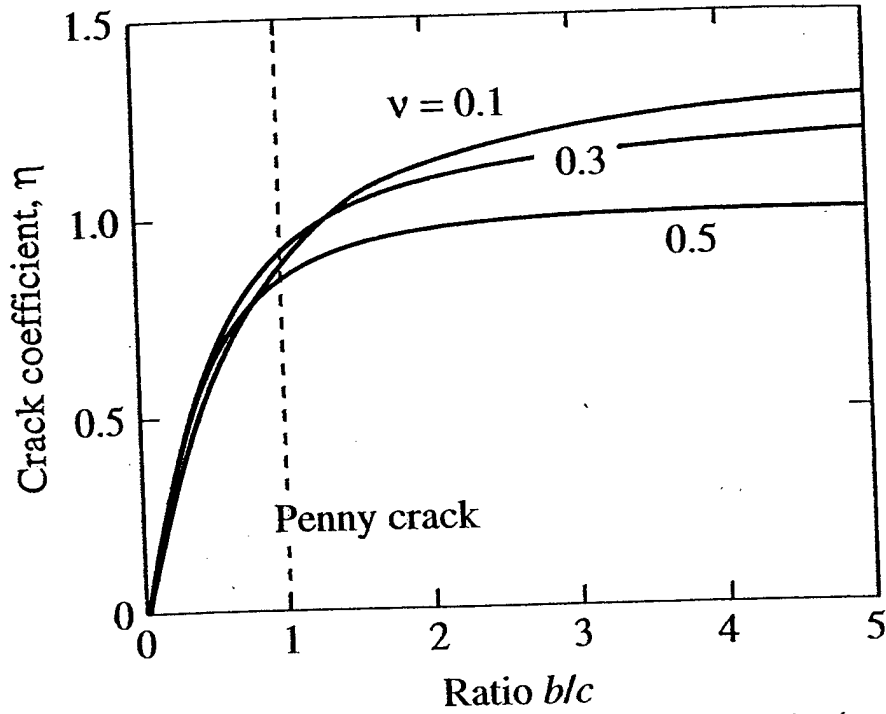


Fig. B1. Plot of elliptical integral function $\eta(b/c)$ for selected values of Poisson's ratio ν .

$$E(k) = \int_0^{\pi/2} (1 - k^2 \sin^2 \theta)^{1/2} d\theta. \quad (\text{B3b})$$

The average displacement is obtained by integration of (B1) over the crack area $A = \pi bc$:

$$\begin{aligned} \bar{v}_x &= (1/A) \int v_x(x, y) dA = (B/3)(bc)^{1/2} \\ &= (\eta c/E_0) \tau_{xz}, \end{aligned} \quad (\text{B4})$$

where we define the dimensionless constant $\eta(b/c) = (BE_0/3\tau_{xz})(b/c)^{1/2}$. The function $\eta(b/c)$ is plotted in Fig. B1, for selected values of ν . For a penny crack ($b/c = 1$), $\eta = 8(1+\nu)/3\pi$; for a plane strain crack ($b/c = \infty$), $\eta = 4(1-\nu^2)/3$.

Solutions for a shear stress in an arbitrary direction in the x - y plane can be obtained by superposition (with τ_{xz} obtained by interchanging c and b in the above relations). However, in that case the resultant displacement and the applied shear stress are in different directions, and the formulation requires tensor equivalents.

11.0 Analysis of Debonding at Interface Cusps

The following is a summary of a paper in preparation for publication in the Journal of the American Ceramic Society, by M. He and D. B. Marshall

Polycrystalline LaPO_4 coatings on single crystal fibers (sapphire and mullite) form cusps where the grain boundaries in the monazite intersect the fiber surface, by an interface diffusion process analogous to the surface diffusion that forms grain boundary grooves on free surfaces of polycrystalline bodies. Atomic force microscopy measurements have shown that the interfacial debond crack follows the interface faithfully along these cusps without deviating into the coating (Fig. 1).

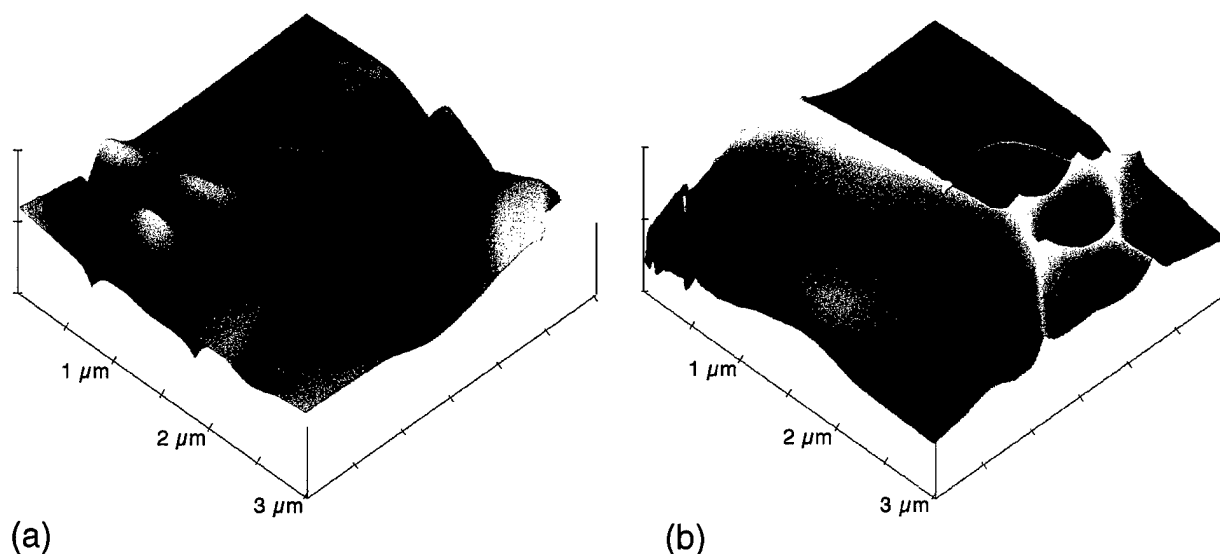
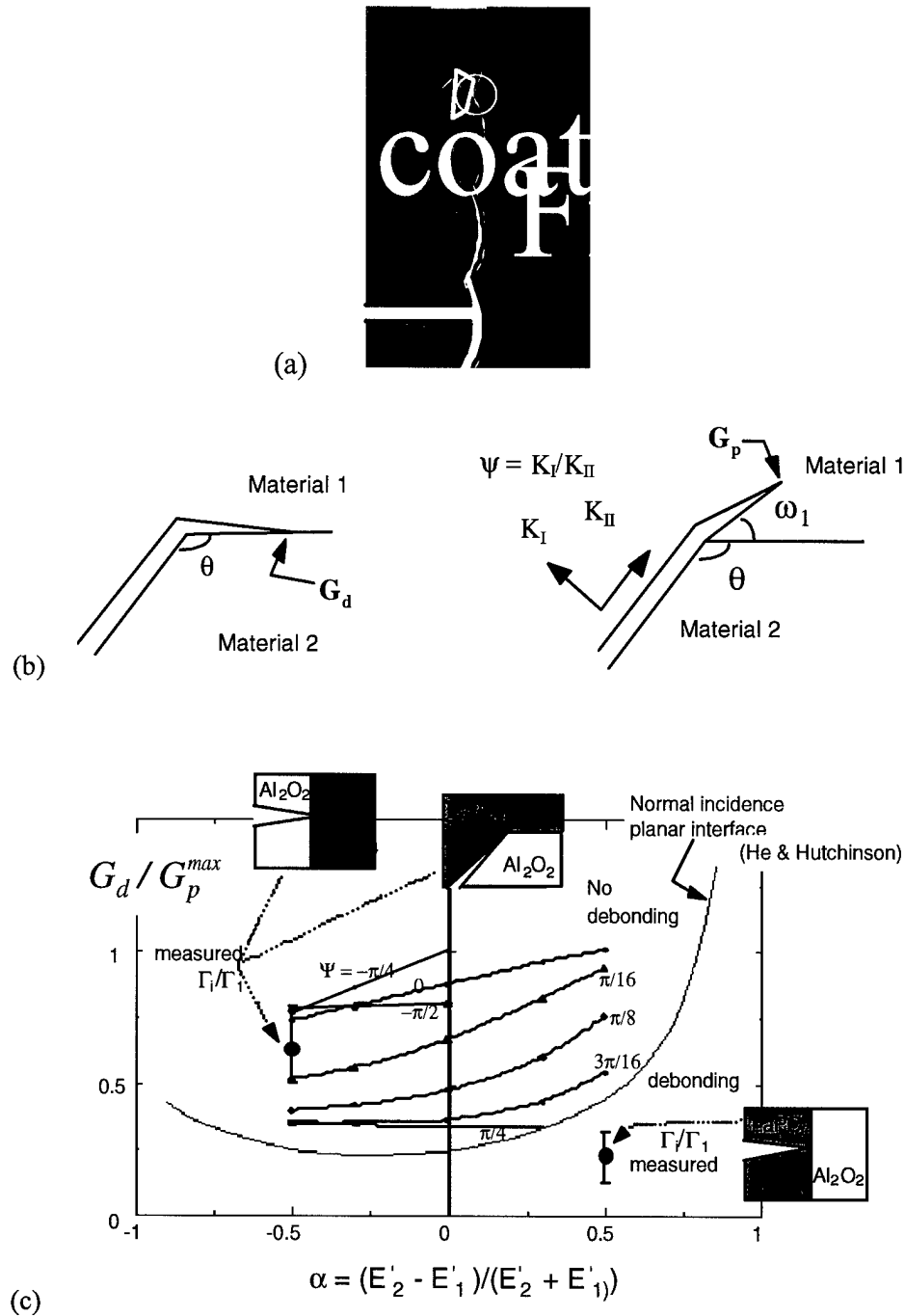


Fig. 1. Atomic force microscope images of matching regions of fractured interface of LaPO_4 and Al_2O_3 (sapphire): (a) LaPO_4 surface showing grain boundary grooves; (b) sapphire surface showing cusps corresponding to the grooves in (a) (From Marshall, Waldrop and Morgan, *Acta Mater.* **48**(2000)4471-74)

An analysis was carried out to define the range of interface toughnesses that would allow continued debonding at the tip of the cusp. This involved using finite element analysis to calculate the strain energy release rates G_d and G_p for a crack with its tip located initially at the tip of a cusp (Fig. 2(a)) then extending along the paths shown in Fig. 2(b). For the crack that deflects into the coating, the energy release rate, G_p , was calculated as a function of the deflection angle ω_1 : the favored path is given by the value of ω_1 , for which G_p is maximum (G_p^{\max}). The condition for debonding is then obtained by comparing the ratio G_d/G_p^{\max} with the ratio of the corresponding fracture toughnesses Γ_i and Γ_p of the interface and the coating: debonding occurs if

$$\Gamma_i/\Gamma_p < G_d/G_p^{\max}.$$

The critical condition is shown in Fig. 2(c), plotted as a function of the elastic mismatch parameter, α , for various values of the mode mix, Ψ , of the remote loading. Also shown is the well-known debond condition of He and Hutchinson for a crack at normal incidence to the interface, as well as measured values of the ratio Γ_i/Γ_p for the alumina-monazite system. The resulting predictions for this system are consistent with observations: the debond condition is satisfied for a crack growing at normal incidence from monazite to alumina and for a crack growing along the interface (close to mode II loading, $\Psi = -\pi/2$) at the tip of a cusp, but not for a crack growing from alumina to monazite at normal incidence to the interface.



12.0 Processing and Hardness of Single Crystal Al_2O_3 Films Containing Nano- ZrO_2 Inclusions Produced by Chemical Solution Deposition

by McNally, F. Lange, F. F. and Marshall, D. B.

The following section is a paper published in Phys. Stat. Sol. (a) 166 231 (1998) - Most of the work was supported at UCSB by contract F49620-96-1-003 (Prof. F. F. Lange); collaboration at Rockwell was supported by this contract.

phys. stat. sol. (a) 166, 231 (1998)

Subject classification: 68.55Jk; 68.60.Bs; S10.1

Processing and Hardness of Single Crystal Al_2O_3 Films Containing Nano- ZrO_2 Inclusions Produced by Chemical Solution Deposition¹⁾

F. McNALLY²⁾, F. F. LANGE, and D. B. MARSHALL³⁾

Materials Department, University of California, Santa Barbara, CA 93106, USA

(Received December 23, 1997)

Dedicated to Professor Dr. MANFRED RÜHLE on the occasion of his 60th birthday

Single crystal, homoepitaxial $\alpha\text{-Al}_2\text{O}_3$ films containing nanoscale ZrO_2 inclusions were grown on basal-plane, sapphire substrate. The substrates were coated with an aqueous solution containing aluminium nitrate and zirconium acetate and heat treated at 1200 °C. Powders were also prepared from these precursors by spray pyrolysis and heat treatment. XRD and TEM analyses confirmed the expected nonequilibrium phase evolution from an amorphous inorganic to $\gamma\text{-Al}_2\text{O}_3$ to $\gamma\text{-Al}_2\text{O}_3$ + tetragonal ZrO_2 to $\alpha\text{-Al}_2\text{O}_3$ + tetragonal ZrO_2 . Cross-sectional TEM of the films confirmed homoepitaxy and the random spatial distribution of spherical, tetragonal ZrO_2 inclusions approximately 20 nm in diameter. Nanoindentation studies show that these inclusions at 2, 5, and 15 vol% do not significantly affect the room temperature hardness of alumina.

1. Introduction

Chemical solutions can be used to synthesize inorganics. In this synthesis route, are mixed in a common solvent and treated with heat and/or pressure to produce desired phases. The viscosity of the precursor solutions can be tailored to give the properties necessary to form a variety of shapes including particles, films and fibers. Previous researchers have shown this processing route can be used to produce inorganic phase assemblies at low homologous temperatures where crystallization is kinetically constrained, resulting in the formation of nonequilibrium phases that can lead to novel microstructures [1, 2].

The crystallization of compositions in the ZrO_2 -rich portion of the $\text{ZrO}_2\text{-Al}_2\text{O}_3$ system from solution precursors has been studied by Balmer et al. [1]. They showed, for compositions up to 40 mol% Al_2O_3 , that the system crystallizes between 500 and 800 °C as a metastable single phase with a tetragonal ZrO_2 structure, while the equilibrium ZrO_2 phase should contain <2 mol% Al_2O_3 . Higher temperature heat treatment leads to the formation of another metastable phase assemblage by the partitioning of this initial crystalline phase into ZrO_2 with reduced Al content and the metastable $\gamma\text{-Al}_2\text{O}_3$ phase with Zr in solid solution. Increasing the heat treatment temperature further caused

¹⁾ Work supported by AFOSR Contract No. F49620-96-1-0003.

²⁾ To whom correspondence should be addressed. Phone: (805) 893-8056; Fax: (805) 893-8971; e-mail: mcnally@engineering.ucsb.edu.

³⁾ Also at Rockwell International Science Center, Thousand Oaks, CA, USA.

the $\gamma\text{-Al}_2\text{O}_3$ to transform to $\alpha\text{-Al}_2\text{O}_3$, with additional partitioning of ZrO_2 . Because of the low concentration of nuclei, the $\alpha\text{-Al}_2\text{O}_3$ grains grew very large to encompass many of the much smaller ZrO_2 inclusions, which appeared to be segregated into linear arrays [2].

Precursor processing lends itself to the production of films and can produce microstructure not readily achieved in processing of large bodies. Since nanoindentation allows the mechanical properties of thin films to be probed, it permits the examination of these unusual assemblages. Thus, the combination of precursor processing with nanoindentation makes possible the exploration of structure-property relations outside of the bounds of conventional ceramic microstructures.

In this study, we report the formation of single crystal Al_2O_3 films that contain ZrO_2 inclusions, from Al_2O_3 -rich composition in the $\text{ZrO}_2\text{-Al}_2\text{O}_3$ system. The hardnesses of these novel nano-composite films on sapphire substrates will be reported.

2. Experimental Procedure

Precursor solutions were prepared by mixing stock solutions of aqueous aluminium nitrate and zirconium acetate, assayed to contain the equivalent of 4.4 and 22 wt% of the two oxides, respectively. Mixtures were prepared to yield, after heat treatment, $\alpha\text{-Al}_2\text{O}_3$ containing 0, 0.02, 0.05, and 0.15 volume fractions of ZrO_2 .

Powders for phase and microstructural evolution studies were prepared by atomizing the precursor onto a Teflon coated aluminum sheet at 250 °C. Spray pyrolysis was used to avoid crystallization of aluminum nitrate during solvent evaporation. Electron and X-ray diffraction confirmed the amorphous nature of this powder. These powders were heat treated for 1 h in Pt crucibles in air to temperatures between 700 and 1400 °C. Heat treatments, except where noted, were carried out with a heating rate of 10 K/min. Other specimens were "upquenched", i.e. inserted to a furnace already at the treatment temperature. Powder specimens were prepared for transmission electron microscopy (TEM) by grinding, with a mortar and pestle, then dispersing the powder in ethanol and placing a drop of the suspension onto a carbon coated Cu grid; many of the particles were electron transparent. The sizes of zirconia inclusions within the particles were directly measured on TEM images using the average of two orthogonal major chords for each inclusion observed (≈ 24 inclusions within an area of $\approx 23\,000\text{ nm}^2$).

Films were produced by spin coating with the precursors described above at 5000 rpm for 30 s (Headway Research, Inc.) on a basal plane $\alpha\text{-Al}_2\text{O}_3$ substrate (Crystal and Coating Tech., Inc. and Materials Tech. Int., Inc.) previously heat treated at 1400 °C. The substrate and film was then heated at 700 °C for 5 min. This process was repeated until the substrate was coated 10 times, after which it was heat treated to 1200 °C for 1 h. Multiple spin coatings of the precursor solution, each coating heated to 300 °C before the next, produced films that contained cracks after 2 to 3 coats. It was observed that such cracking could be avoided by heating to 700 °C between each coating; films with 10 coats could be formed crack free.

To prepare cross section foils for TEM, samples were cut in half in cross-section, bonded to form a substrate/film/glue/film/substrate structure, and cut again to obtain an approximately 300 μm slice of this sandwich structure. These slices were thinned using a tripod polisher (Allied High Tech Products, Inc.) to form a shallow wedge wherein the film region could easily be made electron transparent by ion milling.

Surface roughness of films was assessed by tapping mode atomic force microscopy (AFM) (Nanoscope III, Digital Instruments, Inc.).

The hardnesses of the films were determined using a Nanoindenter® (Nano Instruments, Inc.) equipped with three-sided diamond pyramid indenter, in which the angle between the pyramid sides and the normal to the base is 65.3° . The indenter is attached to a rod and can achieve a depth resolution of ± 0.2 nm with a three plate capacitive sensor. During an experiment load is controlled by varying the current through a coil which interacts with a magnetic field. Loads from 0 to 12 g can be applied with a resolution as high as ± 20 μg . Indentation experiments where load versus displacement was recorded were performed using a constant load rate 0.03 g/s to a maximum load of 1, 5, or 10 g. These load-displacement curves were adjusted for thermal drift using data recorded during a hold period after partially unloading to 20% of the maximum load. Unlike conventional techniques, hardness determination is not based on imaging and measuring indentation dimensions after load removal (which can lead to overestimates of hardness due to elastic recovery). Instead the hardness (also elastic modulus) is determined from load-displacement data measured throughout the indentation. Conversion of load-displacement data requires knowledge of indenter geometry and elastic compliance obtained from the unloading curve. A full description of the nanoindentation process and the necessary calculations to extract a hardness versus depth curve from a load-displacement data is provided by Doerner and Nix whose methodology was applied [3].

3. Results

3.1 Phase selection and microstructural development

Phases identified by X-ray diffraction (XRD) and electron diffraction of powders containing 0.15 volume fraction of ZrO_2 heat treated for 1 h at temperatures between 700 and 1400 $^\circ\text{C}$ are listed in Table 1. These results indicate that the first crystalline phase to form was γ -alumina, which could only be identified by electron diffraction owing to its fine grain size. At 900 $^\circ\text{C}$, ZrO_2 was detected as a second phase, indicating that partitioning occurs at, or prior to, this temperature. The transformation of γ - to α -alumina was incomplete after a heat treatment of 1200 $^\circ\text{C}/1$ h, but appeared to be complete after heat treatment at either 1300 $^\circ\text{C}/1$ h or 1400 $^\circ\text{C}/1$ h. Further, after heat treat-

Table 1
Summary of diffraction results (am amorphous, γ $\gamma\text{-Al}_2\text{O}_3$, α $\alpha\text{-Al}_2\text{O}_3$, cub $\text{ZrO}_{2(c)}$, tet $\text{ZrO}_{2(t)}$ and mon $\text{ZrO}_{2(m)}$)

temperature ($^\circ\text{C}$)	XRD	TEM
700		am
800		γ
900		γ + tet or cub
1000		γ + tet or cub
1100	am + tet or cub	γ + tet or cub
1200	α + tet	γ + α + tet
1300	α + tet	α + tet + mon
1400	α + tet + mon	

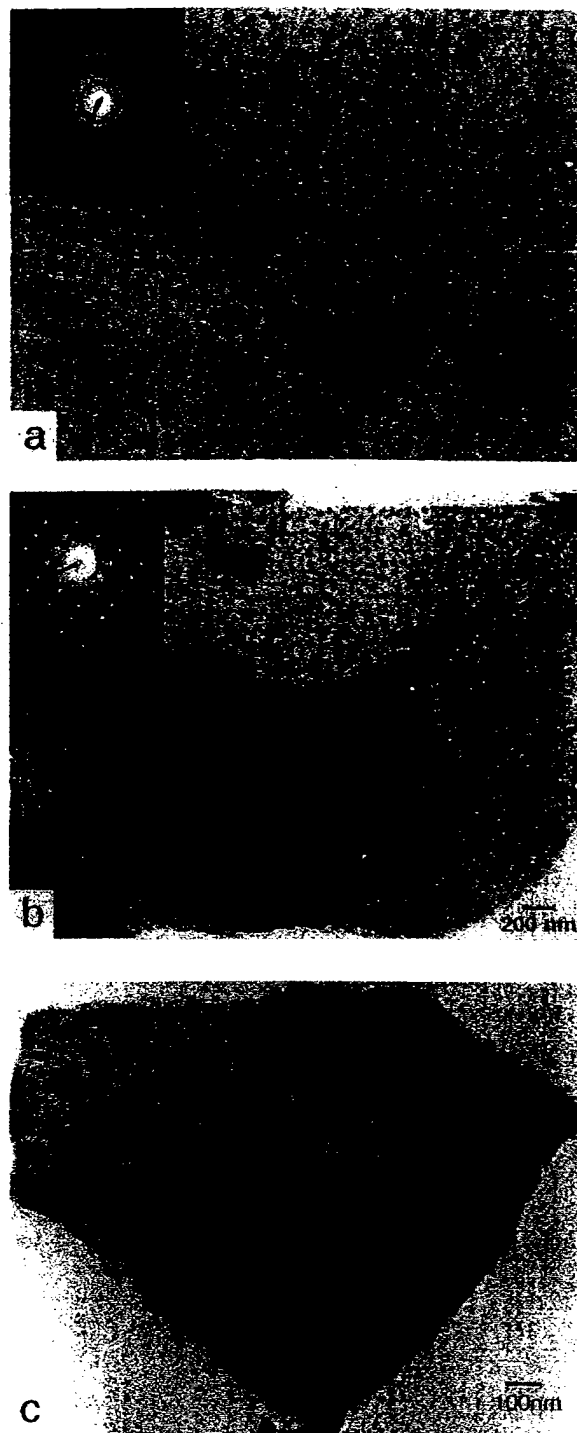


Fig. 1. TEM micrographs of $\text{Al}_2\text{O}_3\text{-ZrO}_2$ powders, containing 15 vol% ZrO_2 , heat treated for 1 h a) 1100, b) 1200, and c) 1300 °C

ment at either 1300 or 1400 °C, some of the ZrO_2 inclusions transformed during cooling from tetragonal to the monoclinic structure.

TEM micrographs of powders heat treated for 1 h at 1100, 1200, and 1300 °C are shown in Fig. 1a, b, and c, respectively. After 1 h at 1100 °C the material consisted of two phases, fine (<5 nm) zirconia particles in a matrix of similarly fine grained γ -alumina. In the TEM micrographs, the zirconia generally appears darker owing to its higher atomic weight. TEM observations confirmed XRD results showing the initiation of the γ -to- α transformation at 1200 °C/1 h. A partially transformed particle is shown in Fig. 1b. SAD, shown in the inset, reveals the presence of polycrystalline γ -alumina and tetragonal zirconia along with at least one large α -alumina grain. The particle, heat treated at 1300 °C/1 h, shown in Fig. 1c was identified by SAD as a single α -alumina crystal containing zirconia inclusions and porosity. Monoclinic zirconia inclusions can be identified in this micrograph by their lenticular twin bands produced during the constrained tetragonal-to-monoclinic phase transformation during cooling. Fig. 2 shows that the mean and width of the ZrO_2 inclusion size distribution increases with heat treatment period and temperature.

TEM micrographs of cross sections of thin films produced with 2, 5, and 15 volume fractions of ZrO_2 inclusions, all heat treated at 1200 °C/1 h, are shown in Figs. 3a to c. The inclusions are randomly distributed, roughly spherical, and approximately 20 nm in diameter. It should be noted that the volume fractions of ZrO_2 inclusions appear larger

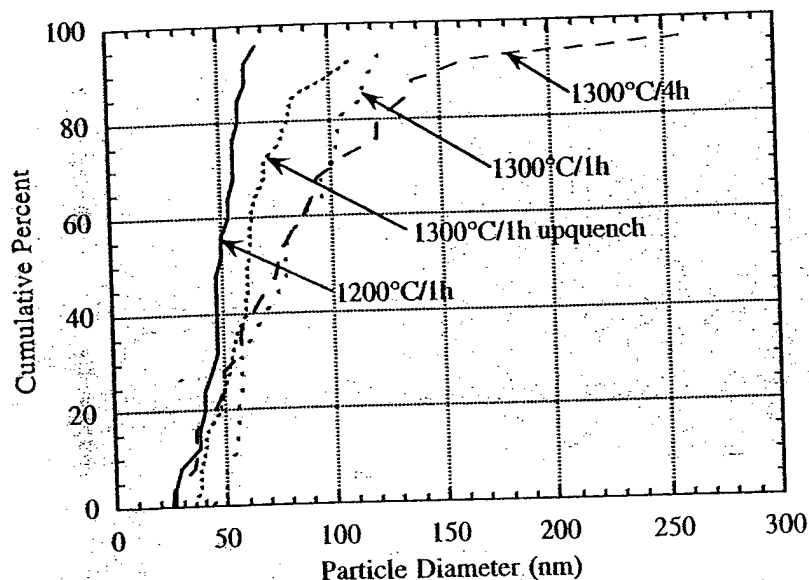


Fig. 2. Inclusion size distributions for Al_2O_3 - ZrO_2 powders, containing 15 vol% ZrO_2 , heated 10 K/min to 1200 °C/1 h, 1300 °C/1 h, and 1300 °C/4 h, or upquenched to 1300 °C/1 h. The curves show the percentage of inclusions smaller than a given diameter

than mentioned above because the cross section thicknesses are several times the inclusion diameter. In addition, the appearance that the volume fraction of inclusions is lower near the surfaces of the films is due to the wedge shape of the films produced during specimen preparation. The selected area diffraction (SAD) pattern in Fig. 3d ($[\bar{1}2\bar{1}0]$ zone axis, based on the hexagonal unit cell), shows that the α - Al_2O_3 portion of the film and the substrate have identical crystallographic orientations. The inset in Fig. 3d shows the area from which the SAD pattern was obtained. The diffraction pattern also contains low intensity rings, not visible in Fig. 3d, which correspond to tetragonal ZrO_2 and show that the inclusions are randomly oriented within the single crystal thin film. Diffraction patterns from many locations along the length of the film always showed epitaxy of alumina and no grain boundaries were observed. A small number of pores (<2 vol%) were also observed; these could be distinguished from inclusions by the presence of Fresnel fringes imaging slightly out of focus. Also, in films heat treated to 1200 °C/1 h, the γ - to α - Al_2O_3 transformation appears to be complete, unlike in powders where the transformation is incomplete after this heat treatment.

AFM examination of film specimens revealed surface features as large as 20 to 30 nm in height with local maxima (high points) separated in-plane by 200 to 400 nm. Root mean square (RMS) values for deviation from the average film height were 4 to 8 nm measured over in-plane distances of 10 μm . The sapphire substrates, however, have been shown to be an order of magnitude smoother (largest feature height \approx 2 nm and RMS roughness \approx 0.5 nm [4]).

3.2 Hardness studies

Films of 150 to 200 nm thickness, formed by 10 sequential coating/pyrolysis steps and heat treated at 1200 °C/1 h, were used to determine the effect of inclusions on hardness.

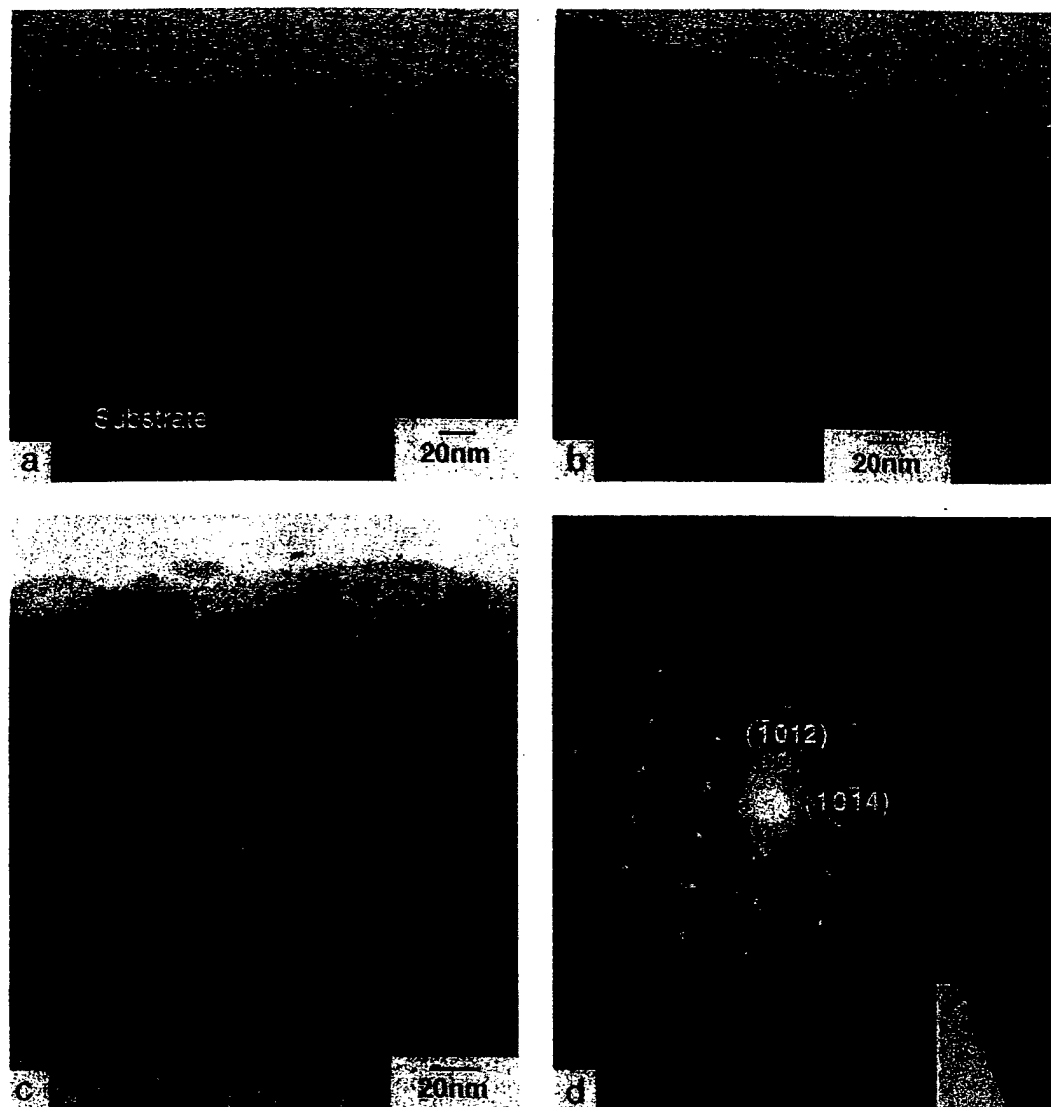


Fig. 3. TEM micrographs of cross sections of thin films heat treated at 1200 °C/1 h produced with a) 2, b) 5, and c) 15 vol% of ZrO_2 inclusions. Film and substrate location is indicated in a). d) SAD with $[\bar{1}2\bar{1}0]$ zone axis of the 15 vol% film confirms the homoepitaxial nature of the film; the diffraction area is shown in the inset

Nanoindentations made with loads 1 to 10 g produced clean, pyramidal impressions, with no evidence of cracks. Maximum penetration depths of approximately 100, 275, and 350 nm were achieved for loads of 1, 5, and 10 g, respectively, for all specimens, regardless of the volume fraction of ZrO_2 inclusions. Large data scatter was obtained using a peak load of 1 g, relative to data collected at 5 and 10 g peak loads. Hardnesses of a sapphire substrate and films containing the different volumen fractions (0, 2, 5, and 15%) of ZrO_2 inclusions are compared in Fig. 4a to e for indentations with peak loads of 5 g. This load provided shallower indentations than 10 g loads and therefore these indents are more sensitive to film properties. Each curve, five on each plot, corresponds to

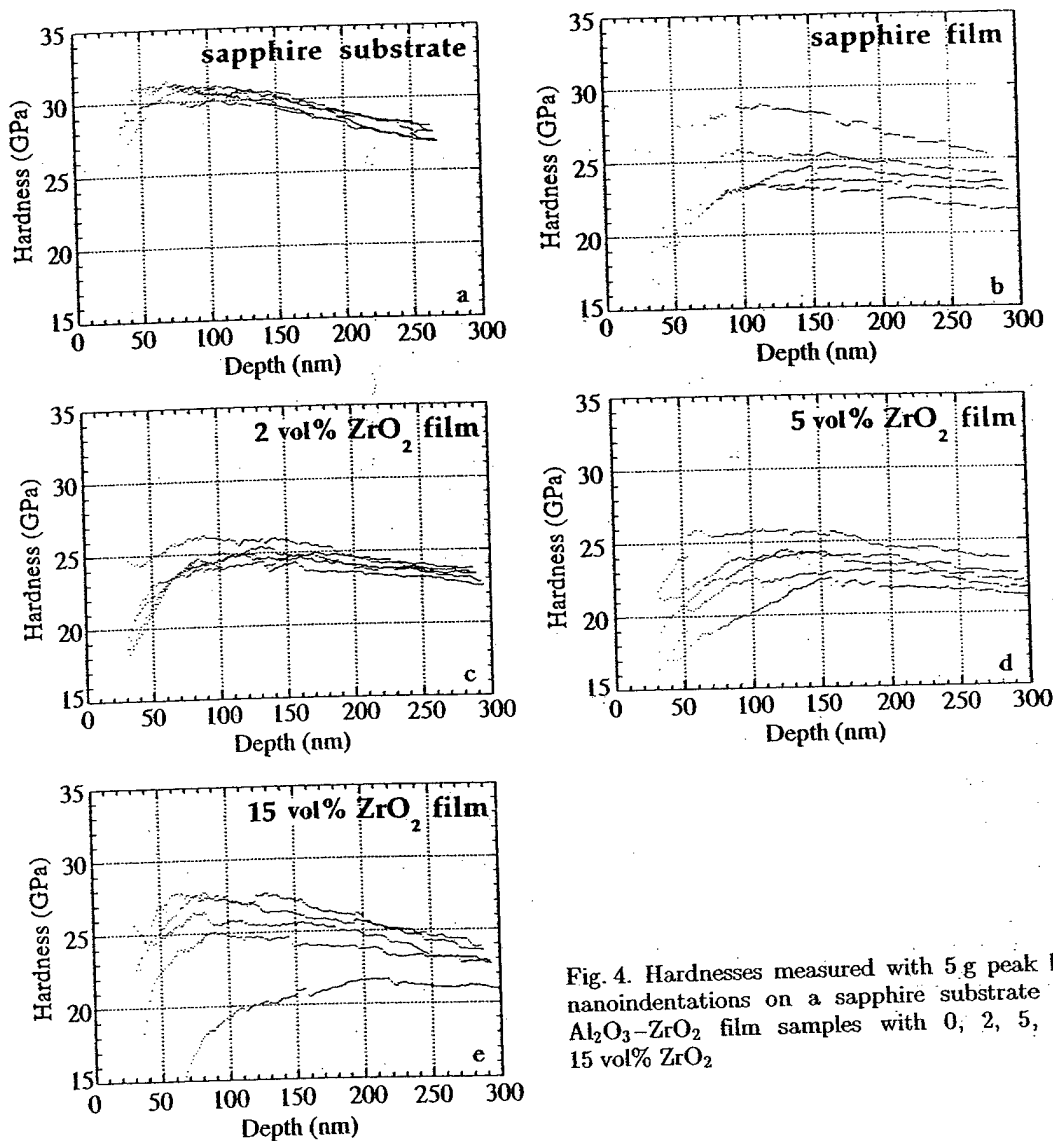


Fig. 4. Hardnesses measured with 5 g peak load nanoindentations on a sapphire substrate and Al_2O_3 - ZrO_2 film samples with 0, 2, 5, and 15 vol% ZrO_2

a single indentation experiment. The data show a broad maximum; hardness rises to a peak, then gradually decreases with increasing penetration depth. At a penetration depth of 150 nm, the uncoated substrate has an average hardness of 30 GPa. The epitaxial thin film without ZrO_2 inclusions, i.e. a sapphire film, has a lower average value of 25 GPa at the same depth. The hardnesses of epitaxial films are unchanged within the sensitivity of the nanoindentation measurements by the addition of ZrO_2 .

4. Discussion

4.1 Development of the two-phase-epitaxial film

The observation of crystallization of a single phase, $\gamma\text{-Al}_2\text{O}_3$, the partitioning of ZrO_2 from this phase, and the transformation of the γ - to $\alpha\text{-Al}_2\text{O}_3$ with increasing tempera-

ture is typical for the evolution for materials synthesized from chemical solutions. This sequence results because precursors pyrolyze at low temperatures where insufficient diffusion occurs to allow atoms to rearrange over long distances and form the equilibrium assemblage of phases. Instead, the pyrolyzed precursor forms metastable structures that tolerate more defects, and metastable phases with extended solid solubility. We observe the crystallization of a metastable solid solution phase, $\gamma\text{-Al}_2\text{O}_3$ containing 0.17 mole fraction (equivalent of 0.15 volume fraction) of ZrO_2 . Similar observations have been made for nearly identical compositions formed by rapid solidification [5]. Higher temperature heat treatment provides the atomic mobility for the long-range diffusion necessary for partitioning, leading to the nucleation and growth of ZrO_2 as a second phase. It is not clear from our TEM and XRD studies whether this zirconia is cubic or tetragonal for treatment temperatures below 1200 °C, because of line broadening due to the small grain size. At 1200 °C/1 h, $\gamma\text{-Al}_2\text{O}_3$ transforms to $\alpha\text{-Al}_2\text{O}_3$ and it is presumed that further expulsion of ZrO_2 occurs because of the lower solubility of zirconia in the α -alumina phase. Since this transformation is complete in thin-film specimens, but not in similarly treated powders, we conclude that the substrate provides a nucleation site. The lower temperature γ - to $\alpha\text{-Al}_2\text{O}_3$ transformation in films likely causes the smaller mean inclusion size in films (20 nm) than in powders (50 nm) after the same heat treatment (1200 °C/1 h), since the diffusivity of ZrO_2 is lower in $\alpha\text{-Al}_2\text{O}_3$ than in $\gamma\text{-Al}_2\text{O}_3$. Upon cooling to room temperature from 1200 °C these inclusions, owing to their small size [6], remain tetragonal rather than transforming to the monoclinic phase. Only upon further heating, which allows the ZrO_2 inclusions to coarsen, they transform to the monoclinic phase during cooling.

The inclusion of zirconia grains within the α -alumina grains and within the epitaxial Al_2O_3 occurs during the γ to α transformation. This entrapment results when a small number of α nuclei grow and the relatively immobile zirconia can neither pin, nor move with, the advancing boundaries. Porosity appears to be entrapped by the same phenomenon. Entrapment of porosity by such a process was previously observed [7] for the epitaxy of PbTiO_3 on SrTiO_3 (both perovskites), where the first phase formed during the crystallization of PbTiO_3 was not a perovskite, but a metastable fluorite. In both of these systems, the free energy change that drives the epitaxial growth is not only the free energy decrease due to the elimination of grain boundaries in the polycrystalline thin film, but also the free energy reduction of a phase transformation. Thus, the driving forces for epitaxy are larger than in systems not involving a phase transformation, and inclusions and pores should be less effective in hindering the epitaxy process.

4.2 Hardness

The 1 g loads were found not to give reproducible results. This is expected since the shallow indents barely extend past depths generally considered unreliable due to problems with indenter tip imperfection and surface roughness. For these reasons, data for depths < 30 nm was not considered. The initial portion of each of the hardness/penetration curves consists of a broad maximum and hardness gradually decreases with increasing penetration. The presence of higher hardness values for shallow depths is a common observation which has been the subject of much debate [8 to 11]. Less typical and apparently peculiar to depth sensing techniques is the observation of initially low hardness values [10 to 12]. In our measurements, this could be due to surface roughness. For the

purpose of comparing film hardness we have chosen the values at 150 nm depth, which generally lies beyond the maximum, in the region of gradual decrease. Since the depth of the plastic zone associated with the indentation should extend approximately three times the penetration depth [13], these hardness values reflect the hardnesses of both the film and substrate. Methods for extracting film hardness have been proposed by a number of workers [11, 14] but generally depend on an assumed knowledge of substrate and interface properties and were not deemed necessary to this investigation.

The purpose of the nanoindentation experiments was to examine any differences in hardness of the epitaxial films and sapphire substrates. The hardness data, in Fig. 4a, for the sapphire substrates agree well with data reported elsewhere [10]. The hardnesses of films with or without ZrO_2 inclusions were found to be $\approx 17\%$ lower. These films were more variable as well. These observed differences (lower magnitude and greater variability in the films) appear to be accounted for by the effects of surface roughness rather than variations in the intrinsic properties of the films. Roughness may be viewed as a surface layer of lower hardness than the underlying material, since material in such a layer is not fully constrained. If this hardness is negligibly small, the roughness effectively causes an overestimate of the penetration depth h of the indenter by an amount equal to the layer thickness. Since the measured hardness is inversely proportional to h^2 , the hardness is underestimated. For the films with a rough layer of 10 to 20 nm thickness, this underestimate is ≈ 13 to 25% at the indentation depth of 150 nm. In contrast, the surface roughness on the uncoated substrates, which is an order of magnitude smaller, has a negligible effect on the measured hardness.

The presence of ZrO_2 inclusions might be expected to affect the hardness of films by pinning dislocations. An upper bound estimate of the hardness increase due to the mechanism may be obtained from the increase in yield stress, $\Delta\tau_y$, given by [15]

$$\Delta\tau_y = Gb/(L - 2r), \quad (1)$$

where G is the shear modulus of Al_2O_3 (≈ 150 GPa), b is the absolute value of Burgers vector of the relevant slip plane, L is the inclusion spacing, r is the inclusion radius, f is the volume fraction of inclusions, and $L = 4r/3f$. If we assume slip on the basal plane, where $b = 0.476$ nm, the increases in yield stress obtained from Eq. (1) are 0.11 GPa, 0.28 GPa, and 1.0 GPa for volume fractions of inclusions of 0.02, 0.05, and 0.15, respectively. So, following the analysis for Johnson [16] for sapphire's ratio of Young's modulus/yield stress (≈ 40) then hardness is $< 2\tau_y$ and we should expect a maximum hardening effect of < 2 GPa. Since the measured values of the sapphire substrate were more than ten times this increment, the ZrO_2 inclusions should have little effect on the hardness of the thin films at room temperature. Further, the variability in our samples makes detection of this small effect unlikely.

5. Conclusions

Single crystal homoepitaxial α -alumina films containing nanosize ZrO_2 inclusions can be produced by the chemical solution deposition method. Cross section TEM confirmed the homoepitaxy of the matrix and the random spatial distribution of inclusions of ≈ 20 nm in diameter. These films, as well as similarly derived powders, follow a phase evolution path consistent with the principles of kinetically limited crystallization. XRD and TEM confirm the following sequence of non-equilibrium phase evolution: 1. amorphous inor-

ganic; 2. γ -alumina; 3. γ -alumina + tetragonal zirconia; 4. α -alumina + tetragonal zirconia. Nanoindentation studies show that these inclusions do not significantly affect the room temperature hardness of alumina.

References

- [1] M. L. BALMER, F. F. LANGE, and C. G. LEVI, *J. Amer. Ceram. Soc.* **77**, 2069 (1994).
- [2] MARI LOU BALMER, F. F. LANGE, VIKRAM JAYARAM, and CARLOS G. LEVI, *J. Amer. Ceram. Soc.* **78**, 14895 (1995).
- [3] M. F. DOERNER and W. D. NIX, *J. Mater. Res.* **1**, 601 (1986).
- [4] P. M. VERGHESE, private communication.
- [5] V. JAYARIM, C. G. LEVI, T. WHITNEY, and R. MEHRABIAN, *Mater. Sci. Engng. A* **124**, 65 (1990).
- [6] F. F. LANGE, *J. Mater. Sci.* **17**, 225 (1982).
- [7] A. SEIFERT, F. F. LANGE, and J. S. SPECK, *J. Mater. Res.* **10**, 680 (1995).
- [8] N. A. STELMASHENKO, M. G. WALLS, L. M. BROWN, and YU. V. MILMAN, *Acta Metall. et Mater.* **42**, 2855 (1993).
- [9] Q. MA and D. R. CLARKE, *J. Mater. Res.* **10**, 853 (1995).
- [10] S. M. M. RAMOS, *J. Mater. Res.* **7**, 178 (1992).
- [11] P. GRAU, G. BERG, H. OETTEL, and R. WIEDEMANN, *phys. stat. sol. (a)* **159**, 447 (1997).
- [12] L. BOUDOUKHA, S. PALETTO, and G. FANTOZZI, *Nuclear Instrum. and Methods B* **108**, 87 (1996).
- [13] D. TABOR, in: *Microindentation Techniques in Material Science and Engineering* ASTM STP 889, Eds. P. J. BLAU and B. R. LAWN, American Society for Testing and Materials, Philadelphia (Pennsylvania) 1986 (p. 129).
- [14] B. D. FABES, W. C. OLIVER, R. A. MCKEE, and F. J. WALKER, *J. Mater. Res.* **7**, 3056 (1992).
- [15] M. F. ASHBY and D. R. H. JONES, *Engineering Materials 1: An Introduction to Their Properties and Applications*, Pergamon Press, Oxford 1980.
- [16] K. L. JOHNSON, *J. Mech. Phys. Solids* **18**, 115 (1970).